University of Southampton

Faculty of Engineering and Physical Sciences

Institute of Sound and Vibration Research

On The Mechanisms of Leak Noise Generation in Water-Filled Pipes

By

Olusegun Adesina

ORCID ID: 0009-0004-2645-9087

Thesis for the degree of Doctor of Philosophy

October 2024

University of Southampton

Abstract

Faculty of Engineering and Physical Sciences

Institute of Sound and Vibration Research

Thesis for the degree of Doctor of Philosophy

On The Mechanisms of Leak Noise Generation in Water-Filled Pipes

by

Olusegun Adesina

This thesis investigates the generation and characterisation of leak noise in water pipes, with the aim of understanding its source and behaviour.

Knowledge of leak noise generation and characterisation could help in making informed decisions about detecting leaks and prioritising repair operations, which save time and money.

Numerical simulation of leaks on water pipes were carried out in 3-D, using Ansys-Fluent CFD software package and turbulent kinetic energy peaks, found around the edges of the leaks, were demonstrated to be largely responsible for leak noise in the pipes.

Flow data obtained from the leak holes of different shapes were incorporated into a derived semi-analytical model to predict leak noise spectra in the pipes.

The spectra were then characterised based on different shapes, leak sizes, line pressures, source strengths and leak mean flow velocities, to reveal distinct relationships between the leaks and their spectra.

Table of Contents

Contents

Table of Tables

Table of Figures

Table of Figures

Table of Figures

Research Thesis: Declaration of Authorship

Print name: Olusegun Adesina

Title of thesis: On the Mechanisms of Leak Noise Generation in Water-Filled Pipes

I declare that this thesis and the work presented in it are my own and has been generated by me as the result of my own original research.

I confirm that:

1. This work was done wholly or mainly while in candidature for a research degree at this University.
2. Where any part of this thesis has previously been submitted for a degree or any other qualification at this University or any other institution, this has been clearly stated;
3. Where I have consulted the published work of others, this is always clearly attributed;
4. Where I have quoted from the work of others, the source is always given. With the exception of such quotations, this thesis is entirely my own work;
5. I have acknowledged all main sources of help;
6. Where the thesis is based on work done by myself jointly with others, I have made clear exactly what was done by others and what I have contributed myself;
7. None of this work has been published before submission

Signature: ..... Date: 14/10/2024

Acknowledgements

I sincerely appreciate the support and encouragement of my advisors: Professor Phillip Joseph and Dr Jen Muggleton. You both supported me with your wealth of knowledge and experience in making sure this work was successfully delivered.

A special thank you goes to the Faculty of Engineering and Physical Sciences at the University of Southampton, Centre of Doctoral Training at the University of Southampton, EPSRC, UKRI, UKWIR and Portsmouth Water, for the funding opportunities.

To my family, I am forever grateful for your understanding and endless assistance.

Mom and Dad, you were here when I started this project but now, you are resting in peace. I am sure you are proud of the success. Thank you for your support and prayers.

You are all appreciated.

Chapter 1 Introduction

1.1 Overview

Pipelines have proven to be the safest and most economical means of transporting water and other fluid products (Fox, 2016). Since the last 15th century, the UK have been supplying potable water to the citizens (Farrow, 2016) and today, many pipes in the distribution network are now old, unhealthy, weak and prone to persistent leakages. About 2.6 billion litres of water is supplied to London and its environs every single day in the year 2022/23 but sadly, 24 % of the treated water is lost due to leakage, either from the water mains, customer supply pipes or even through unbilled consumptions (Thames-Water, 2023). Severe weather conditions have also caused water pipes to repeatedly expand and crack, which then lead to about 37 % increase in reported leaks and over 1000 busts in water mains (Thames-Water, 2023).

To minimise this huge water loss, UK Water Industry Research (UKWIR) launched an initiative termed: 'The Big Question; How Will We Achieve Zero Leakage in a Sustainable Way By 2050'. A lot of work is currently ongoing in the areas of research and development aimed at understanding the key research areas needed to produce a dynamic route map that will be instrumental to answering the Big Question (UK Water Industry Research, 2020).

To further reduce water loss, UK water companies, in agreement with The Office of Water Services (OFWAT), set annual leakage targets and devised a new approach of managing leakages called the sustainable economic level of leakage (SELL). The aim of SELL is to provide a much better way of effectively managing leakages by comparing the costs and benefits of fixing leaks to the costs and consequences of not fixing them. About ten leaks are fixed every minute of the day (Thames-Water, 2023) and a leak is fixed only if the cost of fixing it is cheaper than the cost of not fixing it. If the leak is not fixed because it is relatively more expensive, water companies will then have to bear the cost of compensating for the water loss and damages to the affected ecosystem. The decision to fix or not to fix leaks therefore largely depends on SELL strategy (CIWEM, 2020).

Leak noise correlation remains one of the most popular among the acoustic methods of locating leaks in water pipes (Y. Gao, Brennan, Joseph, Muggleton, & Hunaidi, 2004). The method involves mounting sensors on either side of the suspected leak, to record the signals given off at the orifice, due to the leak. The signals propagate through the pipe, contained fluid and surrounding medium until they arrive at the sensors. Leak noise correlator processes the signals and the sharp peak in the cross-correlation function is used to pin-point the leak (Y. Gao et al., 2004). The method works satisfactorily well for metallic pipe than for plastic pipe because leak noise in

plastic pipe often decays before reaching the sensors. However, it is important to understand the generation mechanisms as well as acoustic characteristics of leak signals in plastics pipes as these could be helpful in improving the effectiveness of acoustic methods to detect leaks in plastic pipes. In addition, prior knowledge of leak noise characteristics could help in making informed decisions about prioritising leak repair operations, which saves time and money.

1.2 Research aim

The aims of this research are to investigate the source of leak noise in plastic water pipes and how the noise behaves with different leak shapes, leak sizes, pressures, flow speeds and leak flow rates. Knowledge of generation and characterisation of the noise could potentially help in making informed decisions during leak detection and prioritisation of repair.

1.3 Objectives

To achieve the research aims, the following objectives have been established:

a) To review the body of literature in order to be current with the existing knowledge and to identify gaps in mechanisms of leak noise generation and characterisation in plastic water pipes.

b) To numerically simulate flow in water pipes with leaks of different shapes and collect flow data at the leak orifice.

c) To analyse the data so as to understand the source and behaviour leak noise.

d) To develop semi-analytical model for leak noise prediction.

e) To predict and characterise leak noise from different leak shapes and sizes under different leak flow rates.

1.4 Contributions of the thesis to knowledge

a. Flow in water pipes have been modelled, numerically simulated and leak noise were theoretically predicted from leaks of different sizes and shapes. A semi-analytical leak noise prediction model was developed to predict leak noise, using leak noise source

strength, pressure, leak flow rate, leak mean flow velocity, leak size, pipe diameter and radiation efficiency. Effects of the different leak shapes and sizes on leak noise and leak flow speed were investigated.

b. This study identified peaks of turbulent kinetic energy, found around the edges of the simulated leaks of different shapes and sizes, as a source of leak noise. Numerical data were used, alongside other flow parameters, to predict and characterise leak noise from different leak shapes and sizes. However, These theoretical findings require experimental validation

c. Comprehensive studies were carried out on turbulent kinetic energy as a leak noise source, mainly turbulence at the leak edge where, subject to experimental validation, most of the leak energy were believed to be concentrated, to establish the universal and distinct behaviours of the edge turbulence in relation to leak shear layer thickness, leak turbulence intensity, leak size, leak mean velocities and pressures.

d. Using the discharge coefficient semi-analytical model (Torricelli equation), leakage flow rate was estimated for different leak shapes of the same area, where transverse and circular leaks leak were found to produce the highest and lowest leak flow rate respectively.

Chapter 2 Literature review

2.1 Overview

When pipe leaks, it gives off leak noise, which contains important information that could be used to detect and pinpoint the leak (Allwright, 2001; Mashford, De Silva, Burn, & Marney, 2012; Xu et al., 2022). Other useful information such as the size and shape of the leak could also be potentially obtained from the leak noise characterisation (Allwright, 2001). The effectiveness of any adopted leak noise detection method will determine the amount of relevant information that could be extracted from the leak noise, and this could in turn influence the accuracy of leak detection and localisation. Consequently, published works regarding the most popular acoustic leak detection method, mechanisms of leak noise generation, leak noise modelling, simulation and characterisation were reviewed in the following sub sections.

2.2 Acoustic method of leak detection and localisation

Of all the methods of leak detection, acoustic method have been identified as the most accurate at detecting and localising leaks (Meng, Yuxing, Wuchang, & Juntao, 2012; Xiao, Hu, & Li, 2019). The method was first pioneered in the 1930s (Khulief, Khalifa, Mansour, & Habib, 2012) and today, leak noise correlation technique, otherwise known as cross correlation, is the most popular and most effective of all of the techniques of acoustic method and is used to detect and pinpoint leaks in many countries around the world (Brennan et al., 2018; Faerman, Sharkova, Avramchuk, & Shkunenko, 2022; J. Muggleton et al., 2023; J. M. Muggleton, Yan J., 2013; Xiao, Joseph, Muggleton, & Li, 2022).

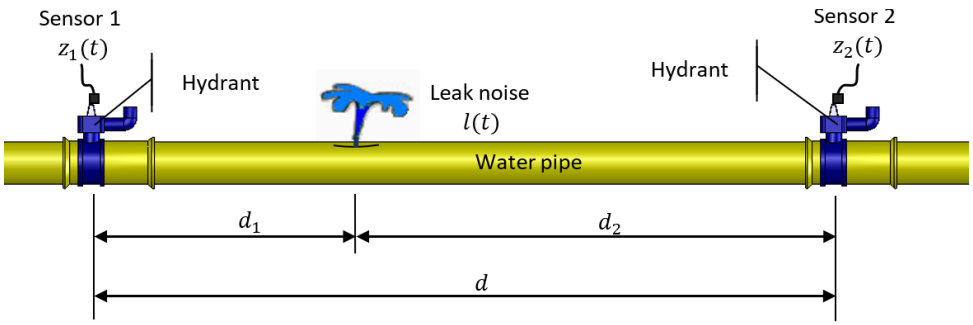

Figure 1 - Schematic of leaking water pipe with attached sensors (de Almeida, Joseph, Brennan, Whitfield, & Dray, 2013).

It works by placing acoustic or vibration sensors on either side of the suspected leaks (Figure 1). The sensors record the difference in the arrival times of the acoustic signals and cross correlation of the time delay between the two signals produces a sharp peak in the cross-correlation function, which is used to localise the leak, using a simple algebraic equation (1):

$$\boldsymbol{d_1 = \frac{d - c\tau_o}{2}} \quad (1)$$

where d_1 is the distance of sensor 1 from the leak position, d_2 is the distance of sensor 2 from the leak position, *d* is the distance between the sensors, τ_o is the difference in the arrival times of the signals at the sensors and c is the wave speed.

Leak noise correlators have been very effective at locating leaks on metal pipes. However, the effectiveness has been hampered by its inability to accurately locate leaks on plastic pipes. This is largely due to the existence of strong coupling between plastic pipes, water and soil which reduces the propagation of leak signals along the plastic pipes and irregularities in the speed of propagation (Brennan et al., 2018). To mitigate these challenges, many research have been carried out with the aim of improving the effectiveness of cross correlation technique especially in plastic pipes.

Acoustic listening devices are non-intrusive, portable, and cost-effective tools used in the acoustic method of leak detection in water pipes. These devices allow technicians to manually listen for leak-related sounds along the pipeline route. They work by amplifying the acoustic signals generated by the water escaping from the leak, enabling operators to identify the general area of the leak. Acoustic listening devices typically consist of a microphone, or a sensor designed to pick up and amplify the sounds produced by the escaping water from a leak. The device is held or placed near the pipe's surface or infrastructure, and the operator listens for any distinct sound patterns that indicate a leak. These sound patterns can include hissing, gushing, or rushing noises. When using an acoustic listening device, the technician moves along the pipeline route, listening for leak sounds at various points. The operator listens carefully to identify changes in the background noise, as leak sounds are typically distinct from the ambient noise of the surrounding environment. However, they require very well trained ears and the procedure can be time consuming (Hunaidi, Wang, Bracken, Gambino, & Fricke, 2004). Noise loggers are small, battery-powered devices that can be attached to the outside of the pipe or placed inside a valve chamber. They continuously monitor the pipeline for leak-related sounds. When a leak occurs, the noise logger records the data, and technicians can later retrieve and analyse the information to identify

the leak location. Hydrophone systems utilize underwater microphones to detect leak-related sounds in large water supply networks, such as mains and transmission lines (Hodasalu Sadananda, 2019; Midtun, 2011; Zohora, 2021). Hydrophones can be submerged in water bodies or attached to hydrants or valves to listen for leak noise and locate leaks. Digital acoustic sensors, when combined with advanced signal processing techniques, can enhance the accuracy of leak noise detection (Jin, Zhang, Liang, & Ding, 2014). Signal processing algorithms can filter out background noise and identify specific leak signatures, helping technicians to quickly detect and locate leaks in water pipes (Cody, 2020). Machine learning algorithms can be applied to analyse the acoustic signals from the pipeline and differentiate between normal operational sounds and leak-related noises (Ahmad, Ahmad, Kim, & Kim, 2022; Siddique, Ahmad, Ullah, & Kim, 2023; Zhao et al., 2022). By training models on a dataset of known leaks and non-leak events, these algorithms can help automate the leak detection process and improve accuracy. Acoustic fibre optic sensors are increasingly being used for continuous monitoring of long stretches of water pipelines (Prisutova, Krynkin, Tait, & Horoshenkov, 2022; Tran, Le, Yntema, & Havinga, 2021; Zhu, Liu, Wang, Su, & Shi, 2022). These sensors can detect acoustic disturbances caused by leaks, as the escaping water generates vibrations that affect the optical properties of the fibre. By analysing the signals from these sensors, leaks can be detected and located precisely.

Most water companies use a combination of different acoustic techniques such as noise loggers, listening devises and noise correlation to be able to detect and pinpoint leaks effectively (Cody, 2020; Fan, Tariq, & Zayed, 2022; Hunaidi et al., 2004; Xue et al., 2020). While listening devices are used to listen to the presence of the leaks, noise loggers and leak noise correlators are then used to pinpoint the leaks.

2.3 Sources and mechanisms of leak noise generation in fluid pipes

As the effectiveness of cross correlation technique depends largely on the magnitude of the leak noise recorded at the sensor position (Xiao, Joseph, & Li, 2020), many works have been done in the areas of leak noise propagation, sensing and processing but not a lot has been done in the area of understanding the mechanisms involved in the generation of leak noise (Liu, Li, Meng, Wang, & Zhang, 2014; J. M. Muggleton, Brennan, M. and Pinnington, R., 2002; J. M. Muggleton, Yan J., 2013; A. S. Papastefanou, Joseph, & Brennan, 2012; Scussel, 2020; Thompson, Chapman, Howison, & Ockendon, 2001a; Xiao et al., 2020). If the mechanism of leak noise generation is better understood, the knowledge could provide useful information needed to improve the

efficiency of leak noise correlation and other leak detection methods such as the computerised computational pipeline monitoring (CPM) systems.

It is very important to understand the processes of leak noise generation in water pipes as characterising the noise could potentially provide vital information about the leak, especially the size (Allwright, 2001; Thompson et al., 2001a) and location of the leak (J. D. Butterfield, 2018).

A study group (Allwright, 2001; Thompson et al., 2001a) conducted experimental study aimed at understanding leak noise generation mechanisms in water pipes. Circular holes of different diameters were drilled on ductile iron pipe of 100 mm diameter. The group observed as water was leaked into air and then into water; from vertical and inclined tubes attached to the leak area. It was found that the environment that water leaked into, could be a key factor in leak noise generation than the size of the leak. Turbulence at the leak hole was also suggested as a possible leak noise generation mechanism. In their work, turbulent jet was produced at the leak hole as normal flow pattern was disrupted, and this was suggested as a key contribution in the process of leak noise generation. In live leak scenarios, the turbulent jet from buried pipe leak creates a hollow which could either contain air and/or water. The presence of air entrainment and solid particle in swirling flow could generate noise by striking the pipe. As no bubbles were observed in the experiment, cavitation was ruled out as possible mechanism of leak noise generation and this finding was consistent with the experiments conducted by A. Papastefanou (2011) in which transparent plastic water pipe was used to visualise the presence (or absence) of bubble as water exited the leaks. However, it was mentioned in the works of J. D. Butterfield (2018) that bubbles were active sources of noise generation in nuclear pipes. Cavitation, as well as leak hole flow separation, was also reported as possible source of leak noise generation in water pipes by an independent comment (Allwright, 2001; Thompson et al., 2001a). Vortex shedding and shear layer pressure fluctuations were not considered as possible mechanisms of leak noise generation. Vortex shedding is usually formed at much higher frequencies while leak noise is generated at lower frequencies. Noise generated due to pressure fluctuation within the shear layer was not considered as a strong mechanism of leak noise generation as this is only an internal phenomenon. Although, the group made some reasonable suggestions on the possible mechanisms of leak noise, they were only theoretical as no experimental or numerical investigations were provided to validate these assumptions

A. S. Papastefanou et al. (2012) conducted an experimental study to determine the mechanisms of leak noise generation in plastic water pipes. To visualise flow as it exited the leak hole, a transparent plastic pipe with a leak hole was used in the test section of the rig. Similar to (Allwright, 2001; Thompson et al., 2001a), the study found no formation of bubbles in the vicinity

of the leak as water escaped and therefore ruled out the possibility of cavitation as a mechanism of leak noise generation. Moreover, the study measured the pressure levels of background noise in the pipe with no leak, as well as turbulent and laminar flows at the leak orifice. At 200 Hz, similar pressure levels were recorded for laminar flow and background noise while for turbulent leak orifice flow, the pressure level was higher by 30 *dB* hence turbulent jet flow at the leak orifice was suggested to be the mechanism of leak noise generation. This finding was in good agreement with the works of (Allwright, 2001; Thompson et al., 2001a).

Xiao et al. (2020) carried out theoretical and experimental studies on leak noise characteristics in gas pipelines. In their work, they suggested that turbulence was the main source of leak noise at the leak orifice and stated edge discontinuities, upstream turbulence migration and local shear layer generation, as the possible mechanisms of leak noise generation. Based on the assumption that leak noise spectrum in the pipe was related to the velocity spectrum at the leak orifice, analytical model was proposed, whereby velocity spectrum was generated from turbulent kinetic energy at the leak orifice and pressure spectrum in the pipe was estimated from the velocity spectrum. However, the generated velocity spectrum was reported by Xiao et al. (2020) to be erroneous because some turbulence parameters such as turbulence intensity and integral length scale, were arbitrarily assumed as constants for all leak sizes and the study thus recommended further work that will accurately quantify the leak orifice turbulence parameters and correctly predict the velocity / pressure spectra.

2.4 Importance of RANS models in predicting turbulence quantities

CFD transient and steady state simulations of pipe flow and leaks are relatively new tools used in aiding leak detection by providing useful numerical data that help to understand the behaviour and monitoring of fluid flow in pipes and leaks (Ali, Hawwa, & Baroudi, 2022; M. Jujuly, Thodi, Rahman, & Khan, 2016; M. M. Jujuly, 2016). They are very important engineering tools used to predict hydraulic behaviour of leakages in water systems using different pipe materials and operating conditions (Ferraiuolo, De Paola, Fiorillo, Caroppi, & Pugliese, 2020). The evolution of high performing computing has made CFD pipe flow simulations very popular and important engineering tool (Zeng & Luo, 2019). CFD uses numerical methods to analyse complex fluid flow challenges by using discretisation method to solve governing mathematical equations. It is relatively quicker, inexpensive and is used alongside analytical and experimental solutions to solve complex flow challenges. However, these models have certain limitations that affect their accuracy in predicting turbulence quantities. RANS models offer various turbulence model options, each with its own assumptions and limitations. The choice of the turbulence model has a significant impact on the accuracy of turbulence quantities predictions. It is challenging to identify

a universally suitable turbulence model that performs well across different flow regimes and applications (Yusuf, Asako, Sidik, Mohamed, & Japar, 2020).

The abilities of RANS models to capture key flow features at reduced costs makes them practical for analysing complex flow phenomenal in real-world applications (Yusuf et al., 2020). In addition, RANS models have a long history of development and validation. They have been extensively tested against experimental data and benchmark cases, providing a robust foundation for their application. This validation allows engineers and researchers to have confidence in the results obtained from RANS models (Yusuf et al., 2020). In industrial flow analyses, RANS models excel in analysing complex industrial flows (Absi, 2021) where emphasis is on overall flow behaviour and key features rather than capturing fine-scale turbulent structures. They are particularly suitable in situations where steady state or time-averaged results are sufficient for the analysis (Yusuf et al., 2020). Model uncertainties pose a significant challenge to the predictive capability of RANS simulations. To address this issue, recent studies have focused on quantifying and reducing model uncertainties in RANS simulations. The Navier-Stokes equations, which describe fluid flow, are complex and often require numerical techniques for their solution. RANS equations provide a reduced form of the general Navier-Stokes equations, separating the steady-state solution from the time-varying fluctuations in the system. This decomposition simplifies the equations and makes simulations more computationally efficient without sacrificing too much accuracy (CFD, 2023).

2.5 RANS turbulence model

Reynolds Averaged Navier Stokes (RANS) Equations are used to model turbulent flows where instantaneous Navier Stokes equations are decomposed into mean and fluctuating components (Alfonsi, 2009), as seen in equation (2),

$$U_i = \overline{U}_i + u_i' \tag{2}$$

U_i is the instantaneous velocity components, $\overline{U}_i$ is the mean velocity components and u_i' is the fluctuating velocity components in the x, y and z directions. Reynolds averaging process transformed the instantaneous continuity and momentum Navier Stokes equations to RANS equations in (3) and (4). The flow properties no longer change in time due to the averaging, they

become steady state, hence the RANS steady state solver used in this study. The Reynolds time averaging process has introduced unknown terms, Reynolds stress tensor, in the momentum part of RANS equations (4) and this has to be modelled, using eddy-viscosity-based turbulence model, to achieve closure. As no known turbulence model has superiority over the other (Ansys, 2006), the choice of turbulence model entirely depends on the user and the usage.

2.5.1 Governing equations

The time-averaged Navier Stokes governing equations for incompressible flows are given as:

2.5.1.1 Mass conservation (Continuity equation)

For homogeneous incompressible flows, mass is conserved:

$$\frac{\partial \overline{U}_i}{\partial x_i} = 0 \tag{3}$$

2.5.1.2 Momentum conservation

Momentum conservation follows Newton's second law of motion such that:

$$\frac{\partial}{\partial t}(\rho \overline{U}_i) + \frac{\partial}{\partial x_j}\left(\rho \overline{U}_i \overline{U}_j\right) = -\frac{\partial p}{\partial x_i} + \frac{\partial}{\partial x_j}\left[\mu\left(\frac{\partial \overline{U}_i}{\partial x_j} + \frac{\partial \overline{U}_j}{\partial x_i}\right) - \rho\overline{u_i' u_j'}\right] \tag{4}$$

where $\overline{U}_i$ is the mean (time averaged) velocity, u' is the fluctuating velocity and p is pressure. Reynolds averaging in equation (4) has introduced stress tensor, time-averaged fluctuating velocity components ($-\rho\overline{u_i' u_j'}$), which has to be modelled to achieve closure of the governing equations (Anderson Jr & Anderson, 1998; Ansys-Fluent, 2022; Ansys, 2006; Bais, 2021; George, 2021; NASA, 2021).

To solve RANS equations, Boussinesq hypothesis approach (eddy-viscosity-based turbulence model) was employed, which assumed that Reynold stress tensor was proportional to velocity gradient, with eddy viscosity, μ_t, as constant of proportionality.

$$-\rho\overline{u_i'u_j'} = \mu_t \frac{\partial \overline{U}_i}{\partial x_i} \quad (5)$$

For 3-D flow, Reynolds stress tensor have been simplified to:

$$-\rho\overline{u_i'u_j'} = \mu_t \left(\frac{\partial \overline{U}_i}{\partial x_j} + \frac{\partial \overline{U}_j}{\partial x_i} - \frac{2}{3}\frac{\partial \overline{U}_k}{\partial x_k}\partial_{ij}\right) - \frac{2}{3}\rho k \partial_{ij} \quad (6)$$

where ρ is fluid density, k (anisotropic turbulent kinetic energy) is $\frac{1}{2}(\overline{u'u'} + \overline{v'v'} + \overline{w'w'})$,

∂_{ij} is the Kronecker delta and μ_t is the eddy viscosity (SIMSCALE, 2023a).

2.5.2 Eddy viscosity based RANS turbulence models

To solve RANS equations, eddy viscosity based turbulence model was required to first solve transport equations and eddy viscosity. These will then provide solution for the unknown Reynold stresses in equations (4 & 5).

In the work of Yusuf et al. (2020), RANS turbulence models were reviewed and grouped into two categories: one-equation and two-equation models. In one-equation models, such as Spalart Allmaras (SA) model, only one transport equation is solved, making it a low cost and faster convergence RANS model (ANSYS, 2021). SA model is most suitable for aerodynamic and turbomachinery applications such as flow past wings and airfoils (Ansys, 2006; Yusuf et al., 2020). Main disadvantages of the model is that it is relatively new and its prediction of isotropic turbulence cannot be trusted (Ansys, 2006). Two-equation models solve two transport equations such as turbulent kinetic energy and either of the turbulence properties: dissipation rate (ε) and specific dissipation rate (ω). The famous and most extensively used two-equation models are the k-epsilon and k-omega turbulence models (Yusuf et al., 2020). k-epsilon model is known to be reasonably accurate and robust while k-omega model are accurate, robust and can be integrated to the wall without any need of wall functions (ANSYS, 2021). One of the issues of k-epsilon model is that its damping functions are insensitive for some flows and the model is inappropriate for flows with adverse pressure gradient and strong separation (ANSYS, 2021; F. R. Menter, 1994). For standard k-omega model, the asymptotic behaviour of turbulence closer to the wall was not accurately predicted (F. R. Menter, 1994).

The improved SST k-omega model is a 2-in-1 (k-ω/k-ε) model that does not require a damping function. SST k-omega model, unlike k-epsilon model, is capable of effectively predicting separation and resolving the near wall layers without any need of wall functions and because the model also has an in-built k-epsilon model, the outermost part of the boundary layer is resolved using the built-in k-epsilon model (Ansys, 2006; F. R. Menter, 1994).

The transport equations for k and ω Baseline Stress Transport (BST) model (Lansigan, 2021; F. R. Menter, 1994; NASA, 2021) are stated as:

$$\frac{\partial(\rho k)}{\partial t} + \frac{\partial\left(\rho \bar{U}_j k\right)}{\partial x_j} = \mathrm{P} - \beta^* \rho k\omega + \frac{\partial}{\partial x_j}\left[(\mu + \sigma_k \mu_t)\frac{\partial k}{\partial x_j}\right] \tag{7}$$

and:

$$\frac{\partial(\rho\omega)}{\partial t} + \frac{\partial\left(\rho \bar{U}_j \omega\right)}{\partial x_j} = \frac{\gamma}{\nu_t}\mathrm{P} - \beta^* \rho \omega^2 + \frac{\partial}{\partial x_j}\left[(\mu + \sigma_\omega \mu_t)\frac{\partial \omega}{\partial x_j}\right] + 2(1 - F_1)\frac{\rho\sigma\omega_2}{\omega}\frac{\partial k}{\partial x_j}\frac{\partial \omega}{\partial x_j} \tag{8}$$

where $F_1 = \tanh\left\{\left\{min\left[max\left(\frac{\sqrt{k}}{\beta^*\omega y'}\right), \frac{4\sigma_{\omega 2}k}{CD_{k\omega}y^2}\right]\right\}^4\right\}$, $CD_{k\omega} = max\left(2\rho\sigma_{\omega 2}\frac{1}{\omega}\frac{\partial k}{\partial x_i}\frac{\partial \omega}{\partial x_i}, 10^{-10}\right)$,

$P = \tau_{ij}\frac{\partial \bar{U}_i}{\partial x_j}$, $\tau_{ij} = \mu_t\left(2S_{ij} - \frac{2}{3}\frac{\partial \bar{U}_k}{\partial x_k}\delta_{ij}\right) - \frac{2}{3}\rho k\delta_{ij}$, $S_{ij} = \frac{1}{2}\left(\frac{\partial \bar{U}_i}{\partial x_j} + \frac{\partial \bar{U}_i}{\partial x_j}\right)$,

ν_t is the turbulent kinematic viscosity, μ = molecular dynamic viscosity and $\mu_t = \frac{\rho k}{\omega}$ is the turbulent eddy viscosity.

In equation (8), the term $(1 - F_1)$ is the blending function that allows the model to switch between k-omega and k-epsilon models. In the near wall region where k-omega model is required, F_1 equals 1 while in the free stream where k-epsilon model is required, F_1 equals zero. The main issue with the k-ω BST model was the overpredicting of wall shear in equation (8). To minimise the overprediction, k-ω BST model was modified to k-ω SST model, using the viscosity limiter (Lansigan, 2021; F. R. Menter, 1994) in the subsequent equation:

$$\mu_t = \frac{\rho a_1 k}{max(a_1\omega, \Omega F_2)} \tag{9}$$

where $F_2 = tanh\left[\left[max\left(\frac{2\sqrt{k}}{\beta^*\omega y'}, \frac{500\nu}{y^2\omega}\right)\right]^2\right]$, $\Omega = \sqrt{2W_{ij}W_{ij}}$ and $W_{ij} = \frac{1}{2}\left(\frac{\partial \bar{U}_i}{\partial x_j} + \frac{\partial \bar{U}_j}{\partial x_i}\right)$

The viscosity limiter in equation (9) was introduced to equation (8) such that in the near wall region, just like F_1, F_2 equals 1, for the viscosity limiter to correct the overprediction. However, in the free stream, where there is no wall shear over prediction issue, F2 equals zero and viscosity limiter is cancelled out.

SST k-ω model constants were listed below (Lansigan, 2021; F. R. Menter, 1994):

$$\gamma 1 = \frac{\beta_1}{\beta^*} - \frac{\sigma_{\omega 1} k^2}{\sqrt{\beta^*}} \qquad \gamma 2 = \frac{\beta_2}{\beta^*} - \frac{\sigma_{\omega 2} k^2}{\sqrt{\beta^*}} \qquad \sigma_{k1} = 0.85 \qquad \sigma_{k2} = 1.0 \qquad \sigma_{\omega 1} = 0.5$$

$$\sigma_{\omega 2} = 0.856 \qquad \beta_1 = 0.075 \qquad \beta_2 = 0.0828 \qquad \beta^* = 0.009 \qquad k = 0.41 \qquad a_1 = 0.31$$

2.5.3 Boundary layer theory in fluid flow

When fluid is entering into a bounded medium (pipe), the velocity profile of the fluid is uniform at the inlet and as the fluid started to flow into the pipe, portion of the fluid closest to the walls, under a no-slip boundary condition, is stuck to the walls with zero velocity. The adjacent layers of fluid also slow down and the centreline velocity, unaffected by wall shear stress and viscosity, is increased to balance the fluid's mass flow rate (Bhandari & Singh, 2012; K.A.U, 2004; KAHRAMANOĞLU, Sezen, & Bayraktar, 2017). The fluid is then divided into two types of flows: boundary layer flow (the part of the fluid affected by wall shear stress) and inviscid irrotational flow (part of the fluid not affected by the wall shear stress). Boundary layer thickness grows in the axial direction of the pipe and the inviscid flow slowly disappears until the pipe is filled with boundary layer flow. Beyond this point, the flow becomes fully developed and centreline velocity stabilised (Bhandari & Singh, 2012; K.A.U, 2004; KAHRAMANOĞLU et al., 2017).

Boundary layer in a wall bounded turbulent flow is made up of four regions (Figure 2): viscous sublayer, buffer, overlap and the turbulent layer (K.A.U, 2004).

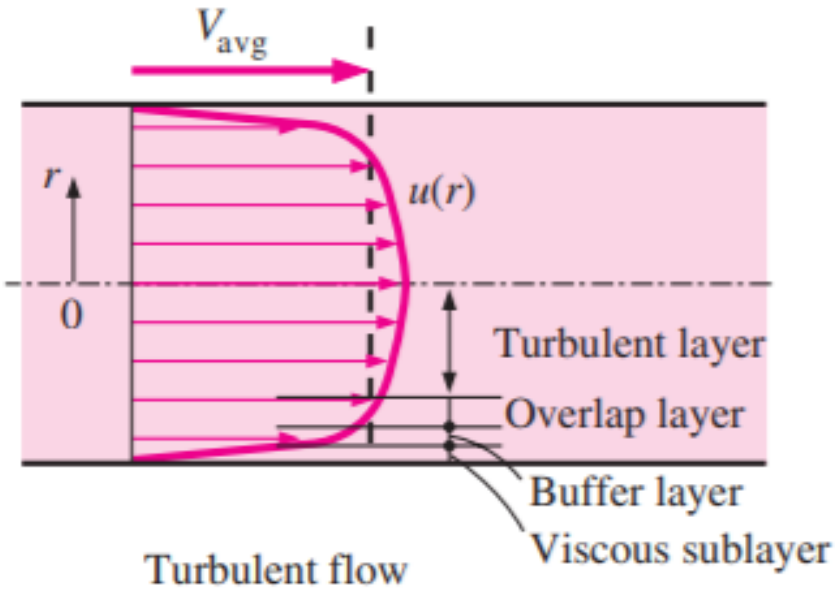

Figure 2 - Schematic of a velocity profile in a wall bounded turbulent flow (K.A.U, 2004).

In no-slip boundary condition, sharp velocity gradient develops close to the wall and velocity profile in the boundary layer must be accurately predicted for the CFD solutions to be reliable. To capture the important physics, turbulence and near wall flow behaviour in that region (Alauzet, Loseille, & Marcum, 2017), knowledge of y-plus concept is required. Y-plus is a dimensionless number that is used to determine the wall-normal distance (y) from the wall to the centroid of the first cell closest to the wall (ANSYS, 2021; Cengel & Cimbala, 2013; Mali & Dange, 2010).

$$y^+ = \frac{y\rho U_\tau}{\mu} \tag{10}$$

where y^+ is the dimensionless wall distance, y is wall-normal distance, μ is dynamic viscosity, ρ is fluid density and U_τ is friction velocity. Friction velocity, a very important velocity scale in the analysis of boundary layer flow, is given by (ANSYS, 2021; Cengel & Cimbala, 2013; Mali & Dange, 2010):

$$U_\tau = \sqrt{\frac{\tau_w}{\rho}} \tag{11}$$

where τ_w is wall shear stress. As fluid closest to the wall is slowed down due to no-slip condition, the force per unit area exerted on the wall by the fluid, due to the velocity gradient is called wall shear stress and is given by (Mali & Dange, 2010; Miedema, 2020):

$$\tau_w = \frac{1}{2} C_f \rho U_\infty^2 \tag{12}$$

where U_∞ is the mean flow velocity. The coefficient of skin friction, C_f, is a dimensionless parameter that is defined as the ratio of wall shear stress and local dynamic pressure in boundary layer flows (Pijush K. Kundu, 2016). It determines what fraction of local dynamic pressure is felt as shear stress on the wall (Johnson, 2016) and for turbulent pipe flow, skin friction coefficient is given by (Ansys, 2006, 2021; Mali & Dange, 2010):

$$C_f = 0.079\, Re_d^{-0.25} \tag{13}$$

where $Re_d = 30{,}000$ is Reynolds number of the turbulent flow in the pipe. It is very important to accurately resolve flow behaviour close to the wall as this defines velocity profile. To successfully predict wall bounded turbulent flows, it is very important to resolve accurately, the behaviour of the flow in the near-wall viscous sublayer region (Figure 2) and to do this, $y^+ < 5$ is required (ANSYS, 2021; Cengel & Cimbala, 2013; Johnson, 2016; Mali & Dange, 2010; Pijush K. Kundu, 2016; SIMSCALE, 2023b). Resolving the viscous sublayer region is often computationally expensive due to the placement of high mesh density in the region and to avoid this, wall functions are used to model the near-wall with y plus in the range of $30 < y^+ < 300$ (ANSYS, 2021; Cengel & Cimbala, 2013; Johnson, 2016; Mali & Dange, 2010; Pijush K. Kundu, 2016; SIMSCALE, 2023b).

2.6 CFD Numerical simulation methods

Acharya (2016) carried out numerical simulation study to investigate differences in Ansys Fluent solvers: CFX, ICEM and Fluent. In the study, three (3) turbulence models: k-epsilon, k-omega and SST k-omega were used to simulate Siemens SGT-800 burner model. Each of the solvers were used to simulate the model, using all the turbulence models. The studies found that, of the three

turbulence models, results from SST k-omega produced the least difference with the solvers and SST k omega was recommended for future studies involving any of the solvers.

Mangani, Sanz, and Darwish (2016), carried out numerical simulation study to compare the accuracy of pressure and density based solvers and SST k omega turbulence model was used in the study. Results from the two solvers were reported to be very similar and consistent with measured data. Although pressure based solvers are designed for subsonic incompressible flows with Mach number of less than 0.3 while density-based solvers perform better for supersonic compressible flow (Ansys, 2006; CFD-Online-1), however, modification operations have made it possible for solvers to be able to solve different kinds of flows (Mangani et al., 2016).

2.7 Numerical simulation solvers settings.

It is very important to understand solver settings and how to modify them as such competence can be used to improve convergence and accuracy of the solution. The two types of solvers available in Ansys Fluent are the pressure and density based solvers (ANSYS, 2010). For pressure based solver, the primary variables are velocity and pressure. Momentum equation (14) produces the velocity field but continuity equation (15) does not contain pressure, so pressure has to be estimated and incorporated into the continuity equation hence pressure correction (ANSYS, 2010; Elmekawi, 2012). The algorithms in pressure based solvers are: segregated and coupled. While segregated algorithm solves the momentum and pressure corrected continuity equations sequentially, coupled algorithm solved the equations concurrently. On the other hand, density based solver solves the equations simultaneously either implicitly or explicitly. As stated in the work of Mangani et al. (2016) and in Elmekawi (2012), pressure based solver have been modified to be applicable to different kinds of flow and coupled algorithm produces better performance than segregated algorithm.

To minimise numerical diffusion and enhance solution accuracy, the type of velocity formulation to adopt should be based on the flow velocity. If the flow is rotating but majority of the flow domain has the smallest velocity, the choice of absolute velocity formulation would enhance solution accuracy. On the other hand, if majority of the flow domain is rotating, relative velocity formulation is ideal (ANSYS_FLUENT, 2009a).

First order discretisation is suitable and more accurate for flows that align very well with mesh and geometry, especially when rectangular or tetrahedral cells are used for a rectangular geometry, this arrangement usually leads to faster convergence and better accuracy. In a

situation where the flow does not align well with the mesh or where unstructured mesh is used to model the flow, second order accuracy will provide much better accuracy (ANSYS_FLUENT, 2009b)

Gradient schemes are important in determining gradients of flow variables in each cell centroids and to also determine convective and diffusion terms in conservation equations (Ansys_Fluent, 2021) . The methods used in computing gradients are: Green-Gauss cell-based, Green-Gauss node-based and Least squares cell-based. Of all the gradient schemes, Green Gauss cell-based is the least intensive in terms of computational power but it may produce false diffusion. in their work, Green-Gauss node-based and Least squares cell-based have similar level of accuracy but the former is less expensive (Ansys_Fluent, 2021, 2023).

In single precision solver, floating point numbers are represented in 32-bit processor while in double precision solver, floating point numbers are represented in 64-bit processor. Double precision solver is usually slower, more accurate and requires more memory than single precision solver (Ansys_Fluent, 2023; Ansys_Fluent_precision_solvers_manual, 2021). Wieselquist (2002) in their work, compared results from single and double precision solvers, when simulating an expansion of gas as it enters a gas-cooled core of a reactor and found no difference in the results obtained from the two solvers, however, the study stated that single precision solver converged faster than double precision solver. In addition, Strasser (2007) used CFD to investigate gear pump mixing and found that the use of double precision solver did not increase the floating point numbers.

After each iteration of the numerical simulation, conservation equations are solved in each cell and due to numerical errors, there are imbalances, in the form of residuals, which are summed over the entire computational domain and then stored, for the purpose of convergence monitoring. The residuals decay to smaller values, tending towards zero, until convergence is achieved. In Ansys Fluent, convergence is judged by scaling the residuals and when the scaled residuals for each transport equation decrease to a set value, called convergence criterion and usually a default value of 10^{-3}, the solution is deemed to have converged, and simulation is automatically stopped (Ansys-Fluent_manual, 2023).

2.8 Applications of CFD solutions in the numerical simulation of fluid pipes and leaks

Ben-Mansour et al., (Ben-Mansour, Habib, Khalifa, Youcef-Toumi, & Chatzigeorgiou, 2012) conducted steady and unsteady-state CFD simulation studies of 3D turbulent flow in water pipe of

0.1 m diameter and 2 m long, with the aim of understanding the responses of leaks of different sizes to pressure and pressure gradient. A small square leak of 1mm by 1 mm was inserted at the middle of the pipe with pressure outlet boundary condition of zero (0) gauge. The pipe inlet was set as velocity inlet of 1 m/s while the outlet was pressure outlet of 1 Bar. Results from the simulation studies found kinetic energy to be highest in the leak region than at any other position along the pipe and unsteady-state DES simulation showed that turbulence was partly responsible for the generated leak noise that propagated through the fluid and walls of the pipe. The results agreed with the findings of this present study, where steady-state CFD simulation showed higher peaks of turbulent kinetic energy recorded only within the shear layer, around the edges of the leak holes than anywhere else. However, in the study of Ben-Mansour et al. (2012), magnitudes of the average PSDs reported for sensors positioned at 40 mm and 90 mm below the leak did not show any significant difference. It is expected that, in reality, sensors closer to the leak should have higher signal amplitudes than those positioned farther away from the leak location. The present study did not only estimate leak spectra from leaks of different sizes and shapes, it also went ahead of the work of Ben-Mansour et al. (2012) by modelling turbulence over the leak area and presented the variations of turbulent kinetic energy with leak area and mean velocity. This study also predicted leak noise in the pipe using turbulence at the leak and characterised these spectra based on leak sizes, flow rates, pipe dimension and pipe material.

In a similar study, M. Jujuly et al. (2016), conducted steady-state/unsteady-state CFD simulation study on subsea pipeline leaks using four different kinds of fluids: water, crude oil, nitrogen and methane; in order to predict the effects of different hole sizes and fluid types on local pressure and temperature contours as well as the generated acoustic signals, using unsteady Large Eddy Transient Simulation (LES). A pipe of 8 m in length with diameter 0.322 m and circular leak holes of sizes ranging from 4 mm to 8 mm were used for the study. The number of triangular cells used for the simulation were around 2.9 million with a finer mesh of only 32 cells at the leak hole. However, turbulence parameters in the 4mm leak hole was unlikely to be well resolved to be able to capture the fluctuating flow behaviour at the leak as only 32 cells were used at the orifice, whereas, in this present work, turbulence at the leak holes were adequately resolved with elements ranging from 5000 to 300000 cells for 1 mm and 8 mm diameter leaks respectively. M. Jujuly et al. (2016) also stated that although near wall mesh should ideally be fine enough to resolve the small turbulent eddies but claimed that the simulation could not adequately resolve the near wall region, where turbulent kinetic energy is normally generated from (Andersson, 2011; Harsha & Lee, 1970; T. Wei, 2018), due to high computational cost. Instead, a high Y plus value of 115 was used, which only captured the turbulent layer but missed the viscous sublayer in the near wall region; an area closest to the wall which is normally resolved with Y-plus value of

approximately 1 (Ansys, 2006). Nevertheless, the works of M. Jujuly et al. (2016), Ben-Mansour et al. (2012), O. Y. Wei and Masuri (2019) and this present study all maintained that high turbulent kinetic energy found near the vicinity leak area was due to the leak. Acoustic signals were simulated in the study using LES and the wall of leak hole area was chosen as the signal source while eight receivers were placed around the leak hole to capture the pressure behaviour. The receivers closest to the leak displayed higher peaks in their power spectral densities (PSDs) and magnitudes of the PSDs were strongly influenced by line pressures. The work pointed out that the maximum PSDs reported were masked by unwanted noise which could not be accounted for in their work. In this present study however, unwanted noise was carefully controlled by only considering, in the leak noise estimation, frequency spectrum within the region of high signal-to-noise ratio, as guided by literature (A. Papastefanou, 2011).

Ali et al. (2022) carried out numerical and experimental analyses to understand the effect of leak geometry on pressure and velocity distributions inside water pipes. In their work, three leak geometries were investigated: circular, square, and longitudinal slit-shaped leaks.

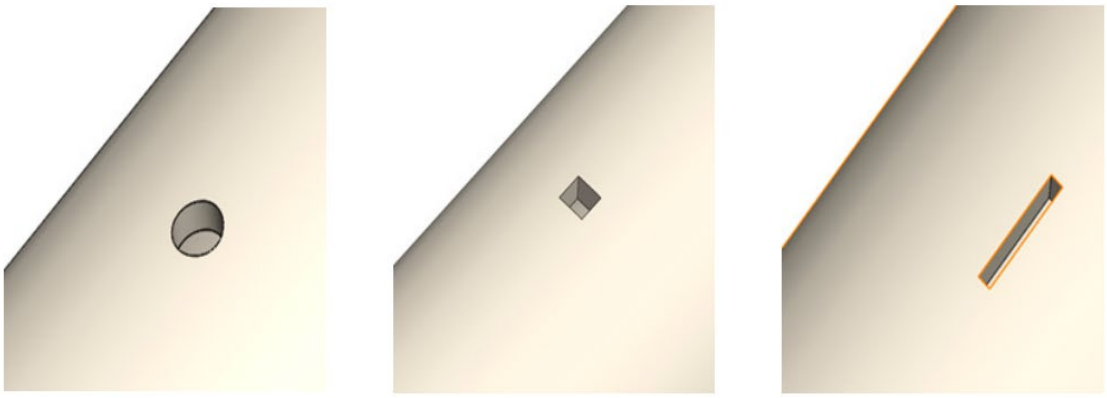

Figure 3 – Simulated leak geometries (Ali et al., 2022)

The study pointed out that variations in leak flow rates affect the distribution of velocity and pressure in the pipe. Circular and square-shaped leak geometries presented similar behaviours in their pressure and velocity distributions along the pipes while slit-shaped geometry resulted in pressure and velocity distributions different from the other geometries. The effect of leak size on circular leak geometry was found to be more pronounced in the pipe's velocity distribution than pressure distribution. The study concluded that, subject to further research, leak geometries could be estimated from pressure and velocity distributions along the pipe. The work of Ali et al. (2022) focussed more on velocity and pressure distributions only along the pipe and not in the leak orifice.

KAHRAMANOĞLU et al. (2017) carried out CFD study on the effects of surface roughness on hydrodynamic entry length in internal flows. Surface roughness of three different pipe geometries were considered in the investigation: square, circular, and triangular pipes of 50 m long and 0.6 m in hydraulic diameter. Roughness heights of these pipes were increased gradually, starting from smooth pipes and it was observed that, for the same Reynolds number, the axial velocities of the pipes increased when the roughness heights were increased. It was also observed that entry lengths were shorter in rough pipes but longer in smooth pipes and for the three pipe geometries, circular pipe had the shortest entry length. When the Reynolds number was increased, entry lengths were longer in all the pipe geometries and pipe with the least flow velocity had the shortest entry length. When flow velocity is increased, the boundary layers are suppressed by the increased flow, and it takes longer for the boundary layers to merge hence longer entry length. However, in order to avoid the computational expense of simulating flow with longer entry length for smooth pipes (KAHRAMANOĞLU et al., 2017), it could be computationally less expensive to import a fully developed velocity profile into a short symmetric circular pipe and simulate only the symmetric half of the pipe. This approach could be rather cheaper, relatively accurate, more effective, and time saving.

Ahsan (2014) conducted CFD study on fully developed turbulent flow using k-ε model with enhanced wall treatment to determine the effects of Reynolds number on turbulent intensity, shear stress and friction factor. The study also determined the maximum Reynolds number to obtain fully developed turbulent flow in a pipe length. Fluids with different Reynolds number were investigated to determine their entry lengths. The findings were similar to that of KAHRAMANOĞLU et al. (2017), which showed that fluids with higher Reynolds number had longer entry lengths than low Reynolds number fluids. Y-plus values of some fluids were also found to increase with increased Reynolds number. Fluids with low Reynolds number were found to have the highest turbulence intensity and this was in good agreement with the turbulence intensity expression (Ebrahimi-Moghadam, Farzaneh-Gord, Arabkoohsar, & Moghadam, 2018). Turbulence intensity is a very important flow parameter in simulating turbulent flows. It defines the extent of turbulence in fully developed turbulent flows. Although, turbulence intensity can only be accurately determined from experiments, it can also be estimated, in terms of percentages, based on degree of turbulence in the flow (Ansys-Fluent-4, 2021). For fully developed turbulent pipe flows, turbulence intensity can be estimated using the expression (Ansys-Fluent-4, 2021):

$$I = \frac{u'}{\overline{U}} = (0.16 Re_{DH})^{-1/8} \tag{16}$$

where I is the turbulence intensity, u' and $\overline{U}$ are fluctuating and mean velocities and Re_{DH} is the Reynolds number of the flow

In the study conducted by Ahsan (2014), the relationship between average wall shear stress and Reynolds number was found to be linear. Increase in fluid velocity led to increased Reynolds number and entry length to a fully developed flow but these eventually resulted in increased shear stress on the pipe wall. In addition, the relationship between friction factor, fluid's Reynolds number, and average flow velocity, was found to be non-linear and this was consistent with the analytical expression in Eq. (16).

Bhandari et al., (Bhandari & Singh, 2012) conducted CFD analyses on fully developed turbulent flow in a pipe. In their investigation, centreline velocity and skin friction coefficient of fluids (air and water) were obtained numerically, and the results were then compared with analytical expressions, in the body of literature, to validate the numerical results. Similarly, this present study validated the results of numerical simulations with the analytical expressions of centreline velocity, skin friction coefficient, wall shear stress and pressure-drop along the pipe (Cengel & Cimbala, 2013; K.A.U, 2004; Kudela, 2010).

O. Y. Wei and Masuri (2019) carried out CFD studies on submarine pipeline model with the aim of understanding the response of flow parameters to single leak and then compared the results with those obtained from double leaks. Two pipe models of 8m long and 0.322 m in diameter were used for the analyses. For a single leak study, a circular leak of 5 mm in diameter was placed on the pipe at 4 m from its inlet boundary while for double leak study, two circular leaks were placed at 4 m and 6 m away from the pipe's inlet boundary and the working fluid was water.

For a single leak pipe model, the results showed that inlet velocity and leak flow rate were directly related. For the same line pressure, an increase in the inlet velocity led to increased leak flow rate. On the other hand, increased inlet velocity had a little impact on the behaviour of pressure around the vicinity of the leak. This study, as well as previous studies (Ben-Mansour et al., 2012; M. Jujuly et al., 2016; Zeng & Luo, 2019), maintained that the complex behaviour of pressure in the vicinity of the leak hole was responsible for the sharp peak in the pressure gradient which can be used in detecting the leak. Also, turbulent kinetic energy was found to be strongest in the leak hole region but weakest everywhere else within the pipe. This behaviour could also be used to detect and pinpoint leaks.

For double leak pipe model, increase in inlet velocity resulted in increased leak flow rate at both leaks but the first leak hole experienced higher flow rate than the second leak hole. No explanation was given for this behaviour. The presence of the second leak hole had very little

impact in the flow rates at both holes. At the surface centreline and 50 mm below the leak, the pressure gradient at the second leak, located 2 m away from the first leak, displayed a much higher pressure amplitude and longer peak than that of the first leak. Comparing the two cases, there was no significant impact of the second leak on the pressure behaviour along the entire pipe cross section. Turbulent kinetic energy was higher in the first leak hole than in the second and higher leak velocity at the first leak hole was responsible for such outcome. This behaviour was similar to what was observed in this current work with a single simulated leak and the outcome can be used to explain what happened in the work of O. Y. Wei and Masuri (2019), even though, no deep explanation was provided about the drop in velocity and leak flow rate of the second leak. As water exited the leak, velocity dropped at the downstream of the leak and flow slows down. As a result of this, lower fluid velocity is received at the second leak and this leads to lower leak flow rate at the second leak compared to the first leak. Similarly, as velocity is higher and then lower in the first and second leak respectively, pressure is expected to behave in opposing manner hence the lower and higher pressure gradient in first and second leak respectively.

2.9 Pressure drop in circular pipes containing fully developed flow.

Pressure loss in fully developed internal turbulent flow of known viscosity and mean velocity can be quantified as (Cengel & Cimbala, 2013; K.A.U, 2004; Kudela, 2010):

$$\Delta P_L = f \frac{L}{D} \frac{\rho U^2}{2} \tag{17}$$

where $\frac{\boldsymbol{\rho U^2}}{\boldsymbol{2}}$ is the dynamic pressure due to the fluid, L is pipe length, ρ is fluid density, D is pipe diameter and U is the mean flow velocity.

$f =$ Darcy friction factor, a dimensionless number used in Darcy Weisbach equation (17) to estimate frictional losses in pipe flows. It is estimated either by reading from a Moody chart; a plot of relative roughness of a pipe against its Reynolds number, or by using theoretical expressions (Cengel & Cimbala, 2013).

For laminar flow, estimating friction factor is quite straightforward and is $\frac{\boldsymbol{64}}{\boldsymbol{Re}}$

For turbulent flow, it is calculated by using Colebrook-White equation (Cengel & Cimbala, 2013):

$$\frac{1}{\sqrt{\sqrt{f}}} = -2.0 \log\left(\frac{\varepsilon/D}{3.7} + \frac{2.51}{Re\sqrt{f}} \right) \quad (18)$$

where ε/D is the relative roughness, ε is the mean height roughness and D is the pipe diameter.

However, one major disadvantage of Colebrook-White equation (19) is that it is implicit and has to be solved iteratively.

A more convenient expression used in estimating friction factor for all flow regimes and pipe types is given as (Cengel & Cimbala, 2013):

$$f = \frac{8\tau_{\omega}}{\boldsymbol{\rho} U^2} \quad (20)$$

Wall shear stress, $\tau_w = \frac{1}{2} C_f \rho U_{\infty}^2$, is the shear deformation exerted on the fluid due to the viscosity in the boundary layer.

Fluid in direct contact with the wall have the highest shear stress but as velocity increases down to the free stream, the shear stress decreases.

Turbulent flow skin friction coefficient $C_f = 0.079\, Re_d^{-0.25}$, is a dimensionless parameter that is defined as the ratio of wall shear stress and local dynamic pressure in boundary layer flows (Pijush K. Kundu, 2016).

2.10 Pressure management systems in leakage control

In pressure management systems, discharge coefficient (C_d) is a dimensionless number that plays a crucial role in the estimation of leak flow rate, alongside other parameters such as pressure head and leakage area (Ekmekcioğlu, BAŞAKIN, & Özger, 2020; Ferraiuolo et al., 2020; Ferrante, Massari, Brunone, & Meniconi, 2010; Schwaller, Van Zyl, & Kabaasha, 2015). In practice, discharge coefficient, leakage exponent and leak flow rate can be estimated from the difference, in water volume, between an average night flow into the district metered area (DMA) and estimated

customer usage (Schwaller et al., 2015). Discharge coefficient can be estimated from the ratio of actual leak flow rate and theoretical leak flow rate (Fox, 2016):

$$C_d = \frac{Q_{actual}}{A\sqrt{2gh}} \tag{21}$$

It is a measure of how much the actual leak deviates from an ideal leak and accounts for various factors that may affect leak flow rate such as leak shape and size, leak exit velocity, pipe pressure and size, fluid viscosity and surrounding media.

In leakage studies, a number of researchers have assumed constant values for discharge coefficient while others thought that C_d should vary as some other parameters such as leak area, pressure, shape and Reynold's number (Braga, Fernandes, & Braga, 2018; A. Cassa, Van Zyl, & Laubscher, 2010; Ekmekcioğlu et al., 2020; Ferrante et al., 2010; Asaph M Kabaasha, Piller, & van Zyl, 2018; Schwaller et al., 2015) but these discrepancies might lead to erroneous estimation of leak flow rate and pressure loss in pipes. Schwaller et al. (2015) in their work, estimated discharge coefficient to be in the range of 0.5 to 0.8, with an average value of 0.65, in water network system. Similarly, A. Cassa et al. (2010) suggested discharge coefficient as a constant value of 0.67. However, (Lambert, 2001; Wu, Burton, & Schoenau, 2002) argued that the assumption of constant values for discharge coefficient might be invalid as it depends largely on Reynolds number and leak geometry. In this work, discharge coefficient was estimated from Torricelli equation (52) whereby leak area "*A*" was eliminated by using a simple expression (equation 53) and by doing so, the problem of leak area expansion in FAVAD equation could be avoided. This result was consistent with the works of Schwaller et al. (2015) and A. Cassa et al. (2010), who considered discharge coefficient as a constant rather than a variable.

In the water industry, a similar expression: N1 power equation (22), is used to manage pressure and thereby control leakage (Asaph M Kabaasha et al., 2018; Schwaller et al., 2015):

$$Q_{leak} = Ch^{N1} \tag{22}$$

where C is leakage coefficient and N1 is the leakage exponent. However, equation (22) was not universally acceptable as it was empirical and the exponent, as well as leakage coefficient, were

not constant but varied linearly with pressure (Ferraiuolo et al., 2020; Franchini & Lanza, 2014; Asaph M Kabaasha et al., 2018). Linear relationship between leak area and pressure has been reported in the literature (A. M. Cassa & van Zyl, 2013; Asaph M Kabaasha et al., 2018; Asaph Mercy Kabaasha, van Zyl, & Piller, 2016; Ssozi, Reddy, & Van Zyl, 2016) and can be expressed as:

$$A = A_0 + mh \tag{23}$$

where A is the expanded leak area due to increased pressure, A_0 is the initial leak area and m is the slope of the linear equation. By substituting equation (23) in equation (52), an alternative formulation named FAVAD (fixed and variable area discharges), was derived (Ferraiuolo et al., 2020; Franchini & Lanza, 2014; Asaph M Kabaasha et al., 2018; Schwaller et al., 2015):

$$Q_{leak} = C_d\sqrt{2g}(A_0 h^{0.5} + mh^{1.5}) \tag{24}$$

FAVAD equation (24) considers the area of the leak that expanded due to the effect of pressure. In the case of tiny leaks at low pressure, where the slope m = 0 (no expansion), FAVAD equation switches back to Torricelli equation and this implies that Torricelli equation is also applicable in pressure management (Franchini & Lanza, 2014) because Torricelli equation does not consider leal area expansion and when m equals zero, FAVAD equation (25) becomes Torricelli equation.

2.11 Analyses of field and laboratory measured leaks

An experimental study was carried out by J. Butterfield (2018), to investigate the factors that control leak signals. The experimental results showed that leak flow rate strongly influenced leak signal. Increasing leak flow rate led to increased leak noise amplitude regardless of leak shape, leak area and backfill types (J. Butterfield, 2018). The study suggested that it would be possible to predict leak flow rate from leak signal and vice versa due to their strong coupling.

Leak noise was measured internally in a laboratory experiment conducted by Khulief et al. (2012), to understand the practicality and challenges involved in in-pipe measurement of leak noise. In the experiment, hydrophone was inserted at the pipe centreline and leaks of different sizes were

placed at different distances from the sensor and under different pressure conditions. It was found that frequency bandwidth of leak noise varied as leak sizes within the same pipe set up. In addition, for larger leaks, most of the leak energy were concentrated on the upstream side of the leak and then decayed towards the downstream side. Smaller leaks were not affected by this attenuation of leak energy as most of the energy were rather found to be concentrated in the vicinity of the leak. This suggests that the larger the leak, the faster the attenuation of acoustic energy. Leak noise amplitude was found to also increase with pressure and leak size.

A study was carried out by Scussel (2020), using inverse approach to estimate the shape and level of leak noise spectrum at source location, from measurements made at access points, away from the leaks. In the study, a mathematical approach originally proposed by Y. Gao et al. (2004), was used, with the assumption that the noise generated at the leak was radiated into and propagated through the pipe. Data from three sites were analysed to obtain their power spectral densities, coherence, magnitudes and phases of cross spectral densities, frequency response functions and leak noise spectra of the signals from each sensor, measured away from the leak positions. The approach therefore focussed only within the frequency bandwidth of leak noise propagation. It was found that, for measurements obtained using pressure sensors, the shape and level of leak noise spectrum were estimated while for measurements obtained using accelerometers, only the shape of leak noise spectrum was estimated. The study found some evidence, that the leak spectrum did decay with a frequency of $\frac{1}{\omega}$ power law as stated in the work of (A. Papastefanou, 2011), but not for all the cases presented in Scussel (2020).

Xiao, Hu, and Li (2022) used experimental method to characterise leak noise generated from different leak shapes and sizes in gas pipelines. The aim of the study was to understand the effects of shapes and sizes of leaks on leak signatures, under different line pressures. A pipeline test bed consisting of steel pipe of 100 m in length, diameter of 150 mm and thickness of 4.5 mm, was used in the study. Leak shapes and sizes investigated were circular leaks of 1 mm, 3 mm and 5 mm diameter circular leaks and longitudinal leaks of dimensions: 2 × 1, 2 × 3, and 2 × 10 mm while pressures of 0.1 and 0.3 MPa were used to drive the flow. The dimensions of longitudinal leaks were planned to have the same leak areas to the circular leaks. Three acoustic sensors, used to record the signals, were mounted at distances: 0.7 m, 20.15 m and 70.15 m respectively, to the leak location. Cross-correlation technique was employed to detect and locate big leaks where the smallest leaks, under a very low line pressure, were difficult to detect. However, the use of cross correlation method to successfully detect the leaks in their work further validated the existing knowledge of the efficiency of acoustic method to accurately locate leaks in fluid pipelines. Their study found leak area to influence leak noise a lot more than leak shape and the effect of leak shapes were ignored in their finding (Figure 4).

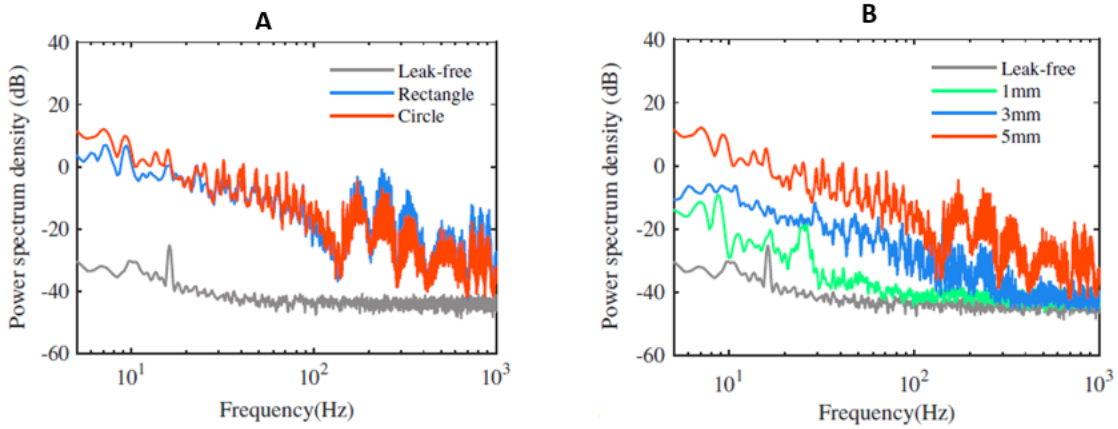

Figure 4 – Effects of leak shape (A) and size (B) on leak noise signatures (Xiao, Hu, et al., 2022)

The study also found leak noise to be concentrated at low frequencies with the capability of being transmitted to bends and junctions along the pipeline.

The experimental work was conducted by Xiao, Hu, et al. (2022) on gas pipelines, to investigate the effects of leak size and shape on leak noise. in the work, circular and square the leak shapes were considered and found that, contrary to the work of J. D. Butterfield, Meyers, Meruane, Collins, and Beck (2018), leak size, not its shape, influences leak noise.

Hunaidi and Chu (1999), studied the acoustical characteristics of leak signals in plastic water distribution pipes, with the aim of understanding the effectiveness of acoustic leak detection methods for plastic water pipes. Parameters investigated were: frequency content of leak signals, attenuation rate and propagation speed of the signals produced. The pipe rig used in the experiment consisted of 150 mm diameter pipe, with a length and burial depth of 200 m and 2.4 m respectively. Leaks investigated were longitudinal, joint and leaks from service connection pipes. Hydrophones and accelerometers were used to measure the leak signals. The study found that propagation speeds for the signals measured by both hydrophone and acceleroleter, were similar. In addition, the work also pointed out that most of the leak signals measured by accelerometers were of higher frequency contents than those meaasured by hydrophones. Signals measured by hydrophones were of low frequency content of as low as 50 Hz.

Xiao, Joseph, et al. (2022), in their work, developed a model of the cross correlation function of leak noise detection in gas pipelines, where, characteristics of wave propagation as well as the leak noise spectrum, are built into the model and effects of turbulence, pipe and flow parameters, on the model, are also considered. The model is able to describe the main features of the

correlation results in gas pipes and provide an estimation of leak noise detection limits, without the noise and this is important in the deployment of sensors in gas pipelines. Their findings provide theoretical insight and experimental evidence for optimizing the cross-correlation method when conducting leak detection and location in gas pipes

Khalifa, Ben-Mansour, Youcef-Toumi, and Choi (2011) conducted an experimental investigation aimed at characterising acoustic wave measured inside water pipe. To simulate leak noise, sound source was placed in the internal wall of the pipe, and frequency, as well as the amplitude of the sound, was being controlled at different conditions of the flow while hydrophone was position along the centreline of the pipe, to measure the generated sound. Findings revealed propagation and attenuation behaviours of low and high frequency signals. Low frequency signals, at frequencies below 400 Hz and at low pressures, attenuate slower than high frequency signals. Furthermore, wave propagation is evidently influenced by line pressure at frequencies, above 400 Hz, suggesting that source frequency and line pressure greatly influency the amplitude of the signals recorded at the sensor. This outcome was similar to the findings in this current study, where, leak noise was proportional square of the leak flow speed velocity. In addition, pressure and leak area, greatly influenced leak noise, as well as the leakage flow rate.

De Marchis and Milici (2019) conducted laboratory based experimental investigation by using leakage law to estimate leakage flow rate using different shapes and sizes of leaks in polyethylene pipes. Circular and rectangular-transverse leak shapes of the same area, were considered in the experiment. Their findings showed that, with the same pressure condition, circular leak produced a higher leak flow rate than rectangular transverse leak when effective area A_E was considered in the leak law. In the absence of the leak area deformation (A_E), circular leak and rectangular transverse leaks produced the same leak flow rates and according to De Marchis and Milici (2019), Torricelli equation is valid and effective in estimating leakage flow rates of different leak geometries. However, the study recommended further work by testing this outcome against different pipe materials and sizes. Ferrante, Brunone, Meniconi, Capponi, and Massari (2014) defined leak law as leakage flow rate and all of the physical parameters that influences the leakage flow rate. Using Torricelli equation:

$$Q_L = C_L A_L \sqrt{2gH} \tag{26}$$

where $C_L \; and \; A_L$ are discharge coefficient and leak area respectively, g is gravity acceleration and H is the total head. The product of discharge coefficient and leakage area in leak law is called effective area: $A_E = C_L A_L$ (De Marchis & Milici, 2019; Ferrante et al., 2014).

J. D. Butterfield et al. (2018) conducted an experimental investigation aimed at predicting leak shapes in water distribution systems from leak noise signatures by using signal processing technique. In the study, three leak shapes were considered: circular, longitudinal and electrofussion leaks, all designed to have the same leak area and flow rate, to remove the effects of leak area and flow speed from the investigation. The findings showed that all leak shapes behaved differently at different frequencies within the broad spectrum (Figure 5).

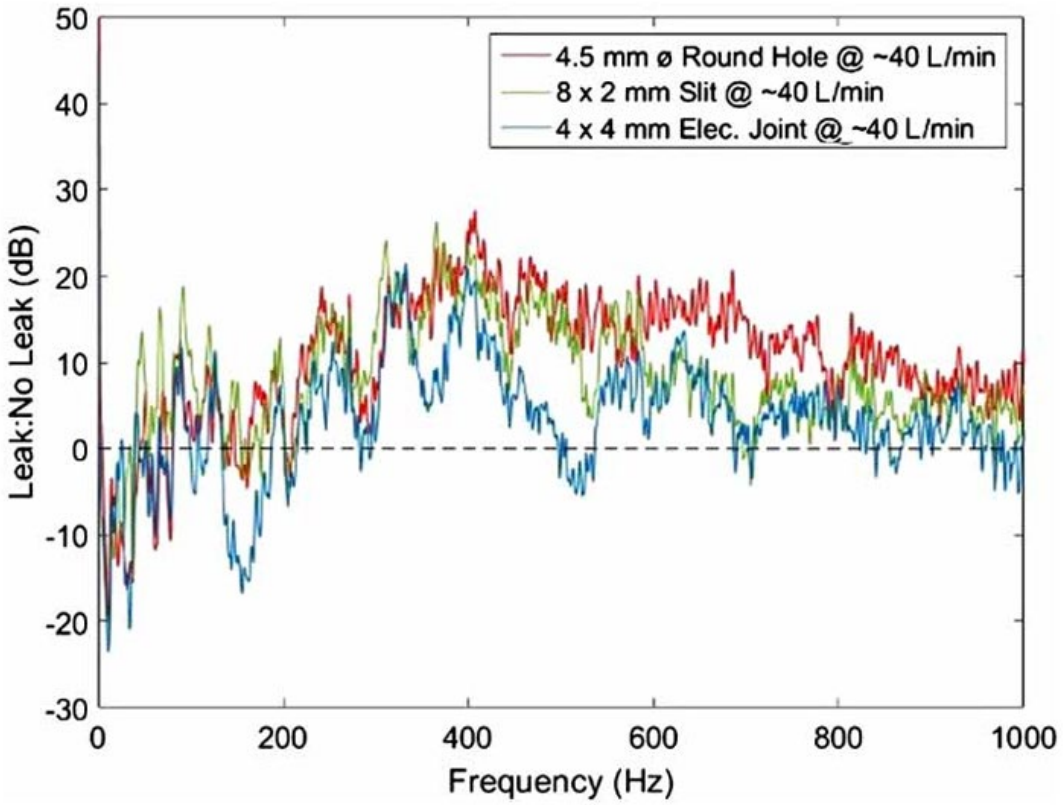

Figure 5 – Effect of leak shapes on leak noise signatures (J. D. Butterfield et al., 2018).

At frequencies below 200 Hz, longitudinal slit had the highest signal amplitude while electrofusion joint leak had the lowest. As frequencies increased and from 400 Hz specifically, circular leak was consistent at displaying the highest signal amplitude while electrofusion joint leak was lowest. However, longitudinal split and electrofusion joint leaks behaved in a similar pattern between frequencies 600 Hz to 700 Hz. The study however concluded that leak shape influences leak noise signatures and frequency contents. This behaviour was linked to the differences in jet angles of the different leak shapes as water exit the leak, resulting in different turbulence regimes, as suggested by A. Papastefanou (2011).

2.12 Sound source(s) at the leak

Fluctuating mass flux of velocity and pressure at the leak orifice generate acoustic source(s) which are radiated into the pipe and surrounding medium (Morse & Ingard, 1986); Reethof (1978); (Xiao et al., 2020).

2.12.1 Acoustic monopole

Monopole sound source is a pulsating or point source that radiate sound in all directions with dimensions much smaller than the wavelength (*ka<<1*) of the sound radiated, (Russell, Titlow, & Bemmen, 1999). The acoustic power of the omnidirectional monopole sound source is given by (Reethof, 1978; Russell et al., 1999):

$$W_m = \frac{\rho c k^2 |q^2|}{8\pi} \tag{27}$$

Where ρ is the fluid density, c is speed of sound, k is wave number and q is complex source strength, a product of surface area 'A' and surface volume velocity 'u', in (m^3/s).

For monopole sound source, source strength is real and is given by (microflown.com, 2023; Russell et al., 1999):

$$q_m = \pi a^2 u \tag{28}$$

where a is surface radius and $k = \frac{\omega}{c}$

by substituting for k, it was evident in equation (27) that the acoustic power varies as square of frequency, square of volume velocity and as fourth power of surface radius. This implied that monopole sound sources are less efficient at radiating low frequency sounds.

2.12.2 Acoustic dipole

Dipole sound source can be described as two monopoles of equal source strengths, radiating sound at opposite phase, and separated by a distance (d) less than the wavelength of the sound radiated. Acoustic power of dipole source is given by (Russell et al., 1999):

$$W_d = \frac{\rho c k^4 d^2 |q^2|}{6\pi} \quad (29)$$

By substituting for k, the acoustic power in equation (29) varies as ω^4 and this implied that, with the same source strength, monopole sound source radiates low frequency sounds better than dipole source.

2.12.3 Quadrupole sound source

Quadrupole sound source can be described as two dipoles of equal source strengths, radiating sound at opposite phase, and separated by a distance (d) less than the wavelength of the sound radiated. Acoustic power of quadrupole source is given by (Russell et al., 1999):

$$W_q = \frac{\rho c k^6 d^2 |q^2|}{6\pi} \quad (30)$$

In equation (30), acoustic power of quadrupole source varies as ω^6, and this implied that, with the same source strength, quadrupole source is the least efficient radiator of low frequency sounds.

Leak noise is generally a broadband frequency signal and the most significant energy in the frequency spectrum is concentrated in the low frequency range (Fuchs & Riehle, 1991; Y Gao, Brennan, Joseph, Muggleton, & Hunaidi, 2005; Y. Gao et al., 2004; Hunaidi, Wang, Bracken, Gambino, & Fricke, 2005; Kim & Lee, 2009; J. M. Muggleton & Brennan, 2004; Rucka, 2017; Xiao et al., 2020). Due to its low frequency nature, the sound source of leak noise can be ascribed to the aeroacoustic monopole sound source (A. Papastefanou, 2011; Xiao et al., 2020) since it is the only source that radiates sound at relatively low frequencies.

2.13 Pressure spectrum estimation; The semi-analytical model

Xiao et al., (Xiao et al., 2020) used Green's function to predict leak noise spectrum in a gas pipe model. In the model, total mean flow velocity (Figure 6) was assumed to consist of axial and normal components U_1 and U_2 and exited the hole at an angle of $cos^{-1}\frac{U_1}{U}$ (Xiao et al., 2020)

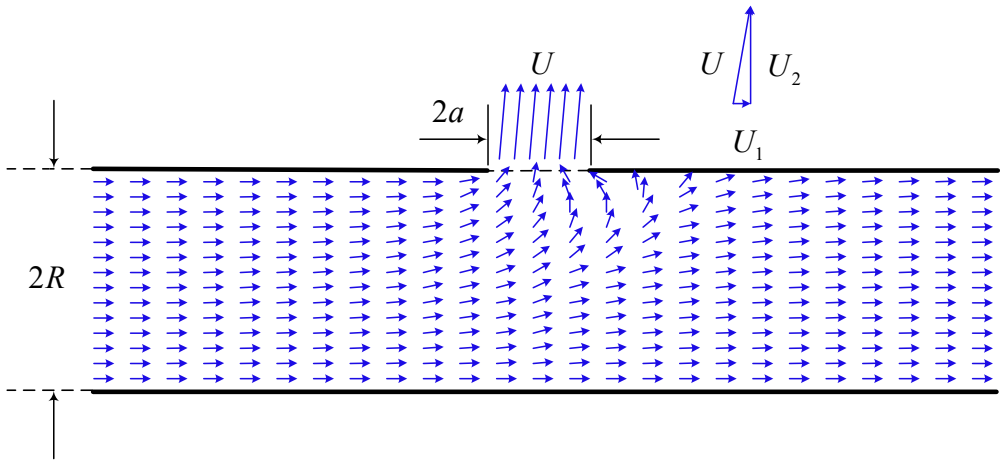

Figure 6 - Schematic of mean flow velocity U exiting the leak orifice of diameter 2a from a circular pipe of diameter 2R (Xiao et al., 2020)

The circular leak orifice of diameter 2a (Figure 7) was defined by surface area A, with axial and transverse components y_1 and y_3:

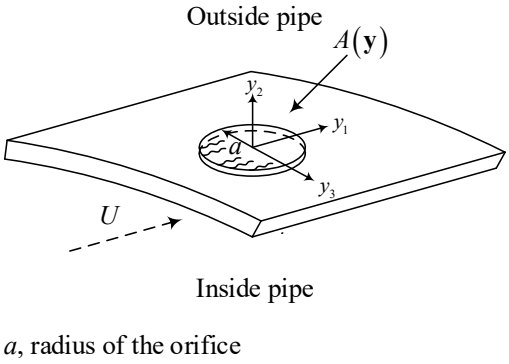

Figure 7 - Schematic of circular leak orifice of surface area A (Xiao et al., 2020)

Green's functions are fundamental solutions to homogeneous / inhomogeneous acoustic wave equations, particularly useful in solving acoustic problems where sound travels from point source location to observer position in an acoustic medium (Okoyenta, Wu, Liu, & Jiang, 2020). Green's functions provide that important link between the point source and observer position. To calculate acoustic pressure level at any position in the medium and away from the point source, the adopted Green's function must be able to satisfy the necessary boundary conditions of the acoustic problem (Okoyenta et al., 2020). Xiao et al., in their work (Xiao et al., 2020), proposed an acoustic pressure spectrum analytical model to predict leak noise in gas pipes where they

assumed that the velocity fluctuations at the leak orifice (source position) were responsible for the acoustic pressure spectrum in the pipe (observer position) and then predicted noise in the pipe by applying Green's function to link the velocity and pressure spectra:

$$p'(\boldsymbol{x},t) = \rho_0 \int_{-T}^{T} \int_{S} G(\boldsymbol{x},t;\boldsymbol{y},\tau) \frac{\partial u_j(\boldsymbol{y},t)}{\partial \tau} n_j dS(\boldsymbol{y}) d\tau \tag{31}$$

The acoustic pressure $p'(\boldsymbol{x},t)$ at any observer position and time (**x, t**) can be estimated from equation (31) where (**y**) and (**x**) are the coordinate of source and observer positions respectively, G(x,t:y,τ) is the time-domain Green's function, $\partial u_j\ (\boldsymbol{y},t)$ is the pipe wall-normal unsteady turbulence velocity, n_j is the unit vector normal to the wall, S is the cross sectional area of the duct, t and τ are observer and source time respectively.

Acoustic pressure PSD in the pipe was obtained by taking the Fourier Transform of equation (31).

$$S_{pp}(\boldsymbol{x},\omega) = \rho_0^2 \omega^2 \int_{S(\boldsymbol{y})} \int_{S(\boldsymbol{y}')} S_{u_2 u_2}(\boldsymbol{y},\boldsymbol{y}',\omega)\, \widehat{G}(\boldsymbol{x},\boldsymbol{y},\omega) \hat{G}^*(\boldsymbol{x},\boldsymbol{y}',\omega) dS(\boldsymbol{y}) dS(\boldsymbol{y}') \tag{32}$$

Where ρ is the density and ω is the angular frequency.

$S_{u_2 u_2}(\boldsymbol{y},\boldsymbol{y}',\omega)$ is the cross spectra density of the turbulent velocity component (u_2), normal to the pipe wall, and is given by:

$$S_{\hat{u}_2 \hat{u}_2}(\boldsymbol{y},\boldsymbol{y}',\omega) = \frac{1}{T} E\{\hat{u}_2(\boldsymbol{y},\omega) \hat{u}_2^*(\boldsymbol{y}',\omega)\} \tag{33}$$

where $\mathbf{y} = (r,\theta)\ and\ \mathbf{y}' = (r',\theta')$.

In a circular duct, the first high order mode has a cut-off frequency: $f_c = \frac{1.84c}{\pi D}$, where c is the speed of sound in the duct and D is pipe diameter (Eriksson, 1980). Leak noise is known to be of

low frequency signal and it thus propagates at frequencies far below the frequency f_c and this satisfies plane wave theory (Eriksson, 1980). Below the frequency f_c, plane wave theory is valid and plane-wave mode (m = 0, n = 0) can propagate. In plane wave mode, Green's function in frequency domain, $\hat{G}(\boldsymbol{x}, \boldsymbol{y}, \omega)$, in equation (32) can be re-written as (Xiao et al., 2020):

$$\hat{G}(\boldsymbol{x}, \boldsymbol{y}, \omega) = \frac{1}{2ikS} e^{ik|x_1 - y_1|} \tag{34}$$

where *k* the wave number and *S* is the cross-sectional area of the duct and cross spectrum of the turbulence velocity normal to the pipe wall, $S_{u_2u_2}(\boldsymbol{y}, \boldsymbol{y}', \omega)$, from equation (32), was further simplified as (Xiao et al., 2020):

$$S_{u_2u_2}(\boldsymbol{y}, \boldsymbol{y}', \omega) = Q_{u2u2}(\boldsymbol{y}, \omega) e^{iK_1(y_1 - y_1')} F(y_3 - y_3', \omega) \tag{35}$$

$Q_{u2u2}(\boldsymbol{y}, \omega)$ is PSD of the normal turbulent velocity component (u_2) over the leak and $F(y_3 - y_3', \omega)$ is the homogeneous transformation of cross spectrum in the transverse direction of the flow, which, in this case, was assumed to be 1, and K_1 = ω / U_1, is the wavenumber of velocity fluctuation in the axial direction of the flow and is obtained by assuming unchanged turbulence in the axial direction.

Equation (35) described the cross spectrum over the y_1 and y_3 plane of the leak hole, as depicted in (Figure 7).

By substituting equations (34 & 35) into equation (32), a solution of the acoustic pressure spectrum in the pipe was obtained (Xiao et al., 2020):

$$S_{pp}(\omega) = \frac{\rho_0^2 \omega^2}{4k^2 S^2} \int_{S(\boldsymbol{y})} \int_{S(\boldsymbol{y}')} Q_{u_2u_2}(\boldsymbol{y}, \omega) e^{iK_1(y_1 - y_1')} F(y_3 - y', \omega) dS(\boldsymbol{y}) dS(\boldsymbol{y}') \tag{36}$$

In their work, Xiao et al. (2020) assumed that the PSD of the normal velocity component over the leak in equation (36) was constant such that:

$$Q_{u_2u_2}(\boldsymbol{y},\omega) \;=\; Q_{u_2u_2}(\omega) \tag{37}$$

Based on the assumption of constant velocity spectrum over the leak orifice in equation (37), a new solution of acoustic pressure spectrum was proposed:

$$S_{pp}(\omega) = \frac{8\rho_0^2 c^2 a^4 Q_{u_2u_2}(\omega)}{\pi S^2} \tag{38}$$

where *c* is the speed of sound. The constant velocity spectrum at the leak orifice in equation (37) was now assumed to be in the streamwise direction and Liepman spectrum of isotropic turbulence (39) was adopted to simplify the velocity spectrum in the streamwise direction:

$$Q_{uu}(\omega) = \frac{\overline{u^2}\Lambda}{\pi U}\frac{1}{1+(\omega\Lambda/U)^2} \tag{39}$$

where $\overline{u'^2}$ is the mean square turbulent velocity fluctuations, U is the mean flow velocity and Λ is the integral length scale.

By substituting equation (39) in equation (38), the acoustic pressure spectrum with constant velocity spectrum in the streamwise direction was proposed:

$$S_{pp}(\omega) \sim \frac{8\rho_0^2 c^2 \overline{u^2}}{\pi^4}\left(\frac{a}{R}\right)^4 \frac{\Lambda}{U}\frac{1}{1+(\omega\Lambda/U)^2} \tag{40}$$

where *a* and *R* are leak and pipe radii respectively.

The 2D leak noise spectrum proposed in equation (40) was based on the assumptions that mean square turbulent velocity fluctuations from the velocity spectrum in equation (39) was only in the streamwise direction. However, results from the 3D numerical simulations in this work revealed that turbulent velocity fluctuations at the leak were never only in the stream-wise direction, they

vary radially and circumferentially over the leak and are particularly concentrated at the leak circumference (Figure 54). In addition, for all the different leak sizes and their leak mean velocities, a constant turbulent intensity of 0.5 % was chosen by Xiao et al. (2020), in order to obtain the mean square turbulent velocity fluctuations in equation (39) and this was incorrect because turbulence intensity varies with leak size and leak mean flow velocity (equation 49).

Numerical simulation solutions of leak mean velocity U, as shown in (Figure 47 & Figure 48), is more complex than it was assumed in the 2D model of Xiao et al. (2020). In the 3D domain as presented in this work, leak mean velocity U varies and is composed of axial, normal and transverse components as leak exited the hole in all the three directions (Figure 48) and not only in the normal and axial directions as assumed by Xiao et al. (2020).

Xiao et al. (2020) in their work acknowledged that the leak noise prediction analytical model proposed contained some assumptions, which could be incorrect. PSD of the turbulent velocity fluctuations was initially assumed to be normal to the pipe wall (equation 35) then it was later assumed to be constant over the leak orifice (equation 37), then it was again assumed to be constant in the streamwise direction (equation 38) and for all the leak holes, leak noise spectrum was estimated with the erroneous constant turbulent intensity and integral length scale.

2.14 Summary of literature review

Although the areas of leak noise characterisation and generation mechanisms have not been extensively researched, literature relevant to this current study have been reviewed and the following gaps have been identified.

1. Mechanisms of leak noise generation in fluid pipes have not been significantly researched and reported in the body of literature. This concept is still not clearly understood, due to the complex behaviour of fluid as it exits the leak, the interaction of fluid with the leak hole and surrounding environment, pipe material, pipe burial depth and soil type.

2. A. Papastefanou (2011), carried out experimental work on leak noise characterisation and generation mechanism using only circular leaks of different sizes but recommended that future works be carried out on other leak shapes and to validate the findings presented in their work.

3. J. D. Butterfield (2018), conducted experimental investigation into the influence of leak shape on leak noise signature in water pipes. However, there is no theoretical work in the literature that reported the effects of leak shapes on leak noise signature.

4. No theoretical work has been found in the literature, that investigates the behaviour of the components of the mean flow speed as water exit the leak. This could reveal the component that carries the most turbulent kinetic energy.

5. In the leak noise prediction model proposed by Xiao et al. (2020), turbulence intensity was assumed to be constant for all leak sizes and as this was incorrect, the researcher recommended future work to accurately measure or model turbulence intensities and validate variation of turbulence intensities to changes in leak sizes.

Chapter 3 Methodology

3.1 Introduction

This chapter presents general overview of the methodological approach employed in this research in order to fulfil the research aims and objectives that were previously described. In addition, methods used in generating the results for the investigations were also discussed.

This work employed CFD numerical simulation approach to investigate the mechanisms of leak noise generation in water pipes and then went ahead to predict leak noise in the pipes using turbulent kinetic energy, assumed to be the noise source at the leak orifice. A 3-D water-filled pipe with circular, square, longitudinal and transverse, leaks of different diameters were modelled and meshed using Steady-State Reynolds Averaged Navier Stokes (RANS) turbulence model in Ansys Fluent software.

The RANS turbulence model adopted in this work was the SST k-ω turbulence model. The turbulence model is very popular computational model for simulating industrial fluid flows and is known to only provide an approximation to the turbulence kinetic energy k and rate of dissipation ω, as the flow is steady state (flow parameters are not changing with time) and is particularly relatively better for adverse pressure gradients and separated flows (CFD-Online, 2021). However, the model is unable to capture the anisotropy of the turbulence flow but simply provides an estimate of its total kinetic energy, for the purpose of simplifying the modelling of turbulent flows (F. Menter, Lechner, & Matyushenko, 2021; F. R. Menter, 1994). Mean flow, as well as turbulent kinetic energy behaviours were studied as water exited the leak and their effects on leak radii, line pressure and flow speed were unravelled. Furthermore, leak noise was predicted in the pipe using the velocity spectrum obtained at the leak and the predicted noise was characterised using leak radii, line pressure, flow rate and flow speed.

3.2 Methods

This section delves into the research methodology by describing in detail, the specific methods and techniques employed to obtain and analyse data that were used to arrive at results presented in the following chapters. Methods used in this study have been split into the following sub sections:

1. Pipe modelling

2. Meshing of fluid domain inside the pipe
3. Mesh quality checks
4. Numerical simulation of fluid flow in pipes
5. Boundary conditions
6. Grid convergence study

3.2.1 Pipe modelling

Using ANSYS Fluent design modeller, two pipes of the same length of 0.1m and different diameters of 0.025 m and 0.05 m were modelled with 2 mm diameter circular leaks inserted at the top section of the pipes.

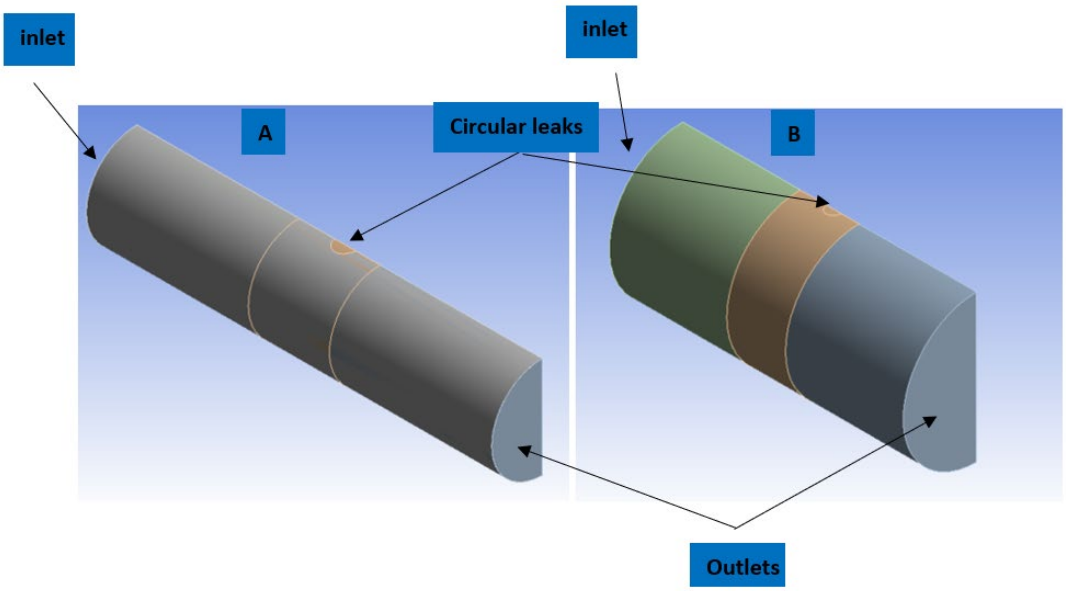

Figure 8 - Geometry of a symmetric halves of the pipe flow domains of 0.025 m (A) and 0.05 m (B) diameter pipes

To model a 3-D hydrodynamically fully developed pipe flow, a long pipe is often required, and numerical simulation of such model can be computationally expensive and time consuming (Bhandari & Singh, 2012; K.A.U, 2004; KAHRAMANOĞLU et al., 2017; Kudela, 2010). To minimise such expenses in this study, the axisymmetric pipe models were sliced into two symmetric parts, along their planes of symmetry and in the XY direction (Figure 8), such that only one half of the domains were required for the numerical simulations (Fluent, 2023).

In addition to circular leak, other leak shapes: square, longitudinal and transverse slit leaks were modelled, meshed and numerically simulated in this study. The leak shapes were modelled to have the same areas so that their results can be comparable.

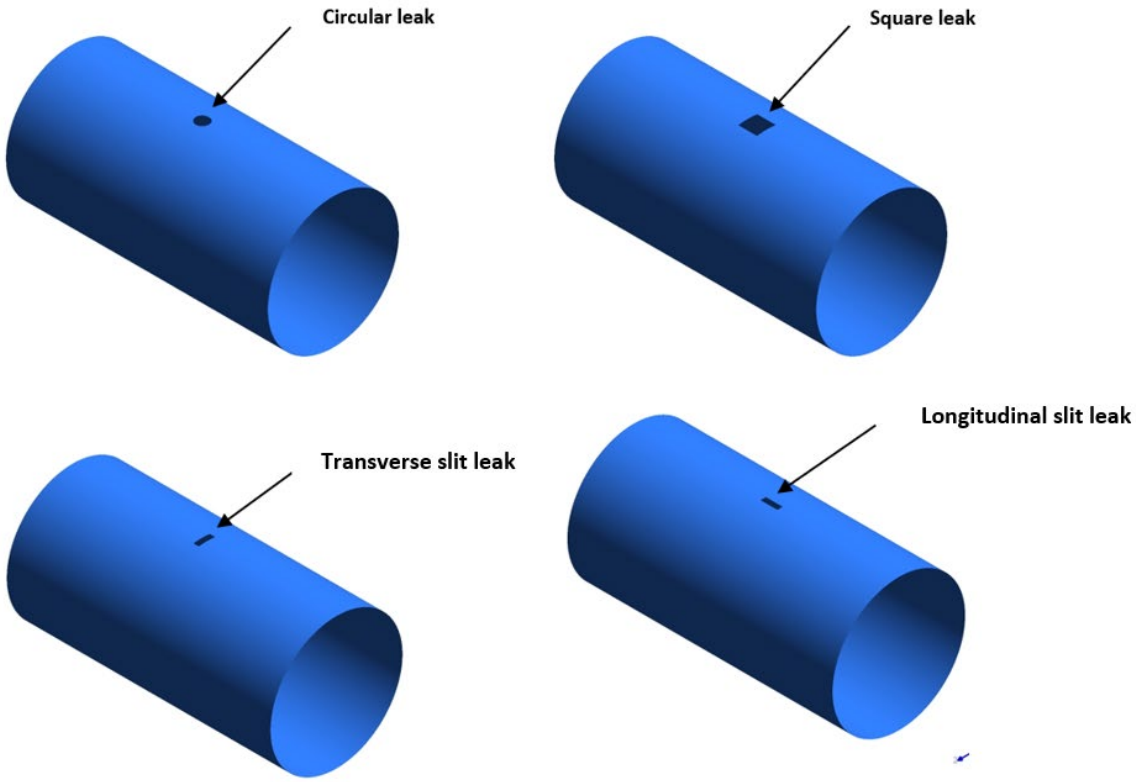

Figure 9 – modelled pipes containing different leak shapes of the same area.

3.2.2 Mesh generation

In this study, it is important to emphasise here that only the fluid domain of the pipes were meshed and numerically simulated. The pipe wall thicknesses and environment where the fluid leaked into, were not meshed and therefore not included in the RANS calculations, due to the huge number of mesh required to capture these boundaries and the limitation of computer memory available for this investigation. However, comprehensive meshing of the pipe wall thickness and leakage environment are recommended for future studies.

To accurately mesh the fluid domain of the pipes, meshing operation was split into three parts: boundary layer, bulk flow, and leak area meshing.

1. Boundary layer meshing

In boundary layer meshing (Figure 10), structured hexahedral mesh of twenty (20) inflation layers was used to resolve the boundary layers of the pipes so as to capture the sharp velocity gradients and preserve velocity profiles near the walls. The choice of twenty (20) inflation layers was adopted in the boundary layers so as to allow the hexahedral cells to grow gradually and transition into tetrahedral cells in the bulk flow.

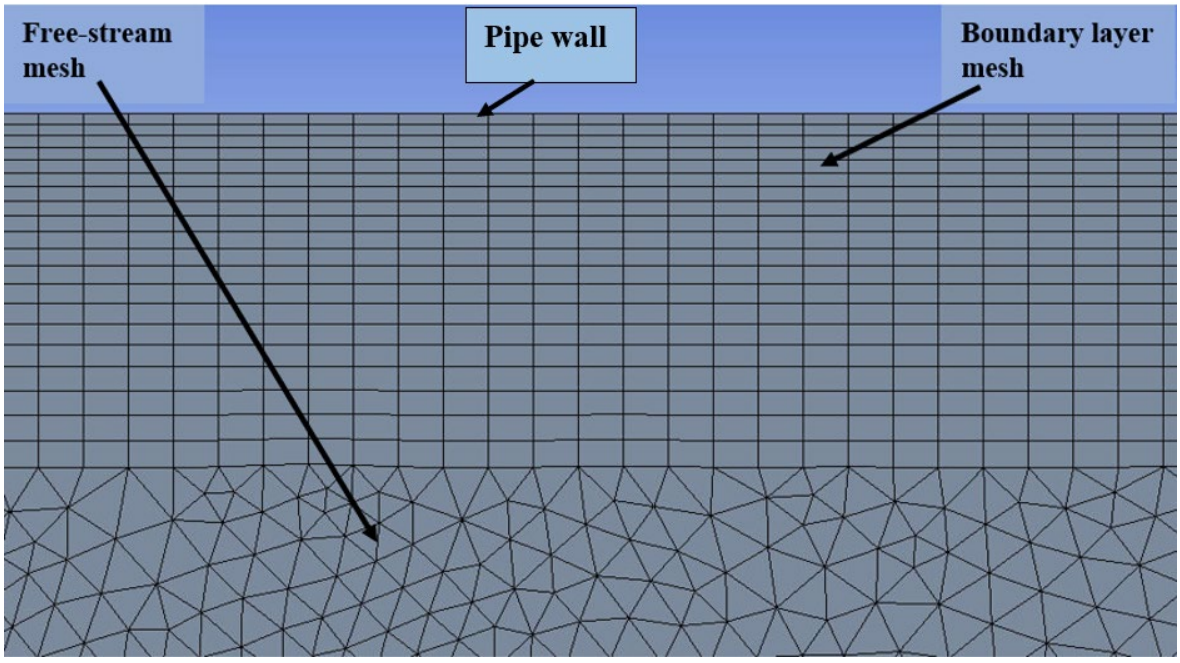

Figure 10 - Mesh transition in the boundary layer of the fluid

The concept of y^+ and the importance of meshing near wall region of fluid domain were reviewed in section (2.5.3). In this study, $y^+ < 5$, was adopted, so as to enable the use of very thin cells that will properly capture the velocity and pressure gradients near wall region. To achieve this, the closest mesh cell from the wall, has to be very short. Using equation (10), the vertical distance (y) from the wall to the first cell was calculated as 7e-05 m. To check that the y^+ value used to mesh the near wall flow was in the preferred range, y^+ result for the numerically simulated flow was measured and plotted. At the inlet, outlet and leak area, y^+ was found between 1, 1.2 and 4.75 respectively (Figure 11) and these fell within the acceptable range of $y^+ < 5$ (ANSYS, 2021; Cengel & Cimbala, 2013; Johnson, 2016; Mali & Dange, 2010; Pijush K. Kundu, 2016; SIMSCALE, 2023b). As presented in Figure 10, y^+ was close to 5, this has been reported to be acceptable as the cells still falls within the viscous sublayer region of the boundary layer (ANSYS, 2023).

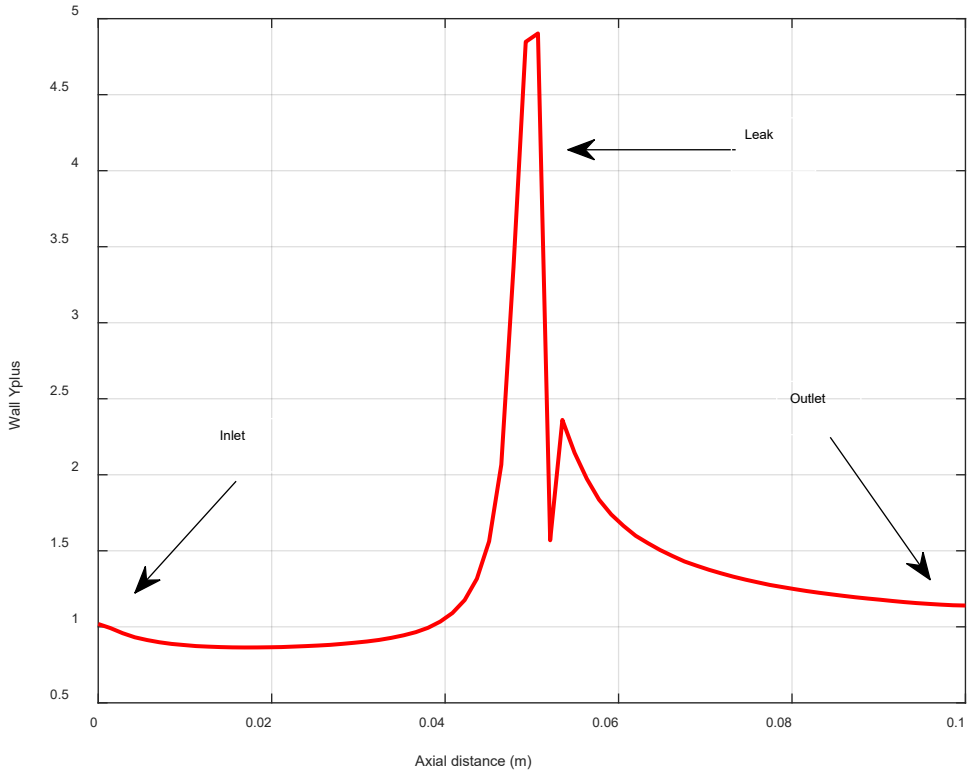

Figure 11 – Simulation of wall y plus for the 3-D pipe geometry with 2 mm diameter leak at 2 Bar

2. Bulk flow meshing

Unstructured tetrahedral mesh was used to resolve the bulk flow region of the fluid domains as there was no flow gradient in the axial direction of the flow and all the flow variables vary linearly between cell centroids. The unstructured mesh consisted of 3-D tetrahedral mesh with thickness of 3e-4 m. In the bulk flow, diameters of the two pipes were 0.025 m and 0.05 m and turbulence length scale, a quantity related to the size of the large energy-containing eddies (Ansys-Fluent-4, 2021; M. Jujuly et al., 2016; Xiao et al., 2020), was calculated from an estimated relationship that was based on mixing length maximum value in turbulent pipe flow (Ansys-Fluent-4, 2021; M. Jujuly et al., 2016; M. M. Jujuly, 2016):

$$l = 0.07L \tag{41}$$

where l and L are turbulence length scale and pipe diameter respectively. Using equation (41), turbulence length scales for small and large diameter pipes were calculated to be 1.8e-3m and 3.5e-3 m respectively and mesh size of 3e-4 m was deemed sufficient and fine enough to resolve

eddies of as small as 17 % and 8.6 % of the sizes of large eddies in the bulk flow of small and large diameter pipes respectively (M. Jujuly et al., 2016).

3. Leak area meshing

Similarly, using the y^+ calculation in equation (10), tetrahedral mesh size of 1e-5 m was used to capture local flow variables and resolve turbulence in 2e-3m diameter leak (Figure 12). The mesh is designed to grow at the rate of 1.2 from the edge to the centre of the leak. For 0.002 m diameter leak, turbulence length scale was calculated as 1.4e-4 m, using equation (41), and due to computational limitations, small eddies of as small as 7 % of the size of large eddies were deemed to have been resolved with the fine mesh size of 1e-5 m (M. Jujuly et al., 2016).

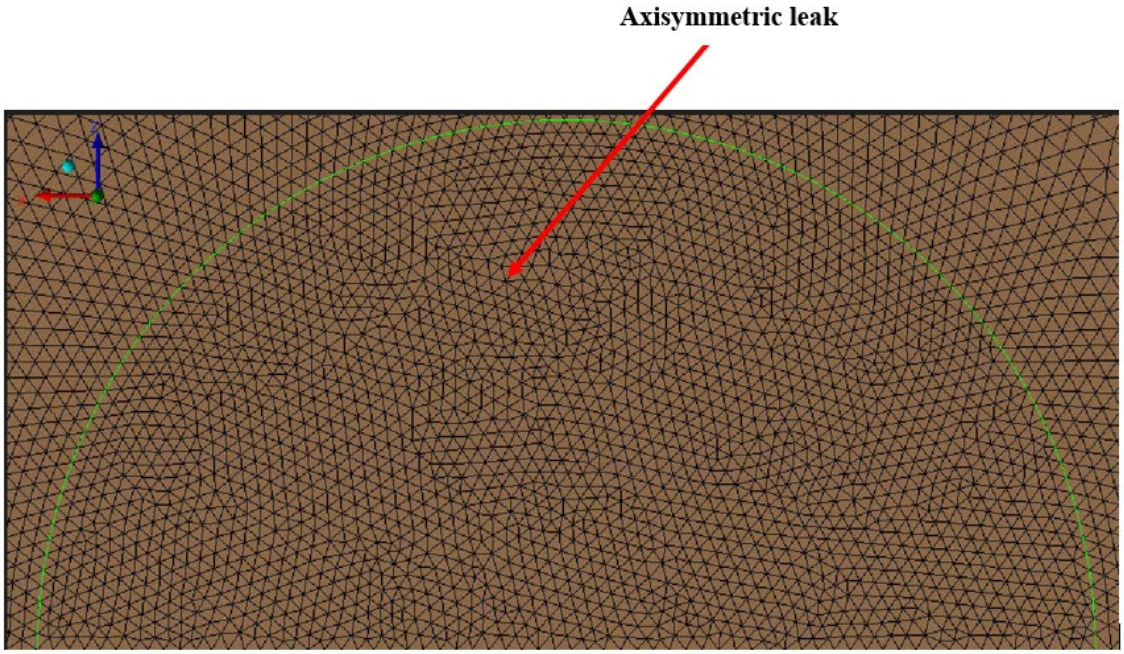

Figure 12 – Mesh in section view around 2e-3 m diameter leak

3.2.3 Mesh quality checks

To ensure stability of the numerical simulation and accuracy of the solutions, quality of the generated mesh was checked against certain quality metrics (Ansys, 2013; Fluent-Ansys, 2023). Aspect ratio, skewness and orthogonal quality of the cells were considered in the quality check study.

1. Aspect ratio

Aspect ratio measures the degree to which a cell is stretched, relative to an ideal shape and it is the ratio of the distance between cell centroid and node to the distance between cell centroid and face centroid (Fluent-Ansys, 2023). For an ideal shape, the aspect ratio is 1. However, aspect ratio of 1 to 5 is deemed acceptable in the bulk flow outside the walls as there is no flow gradient in this region (Ansys, 2013).

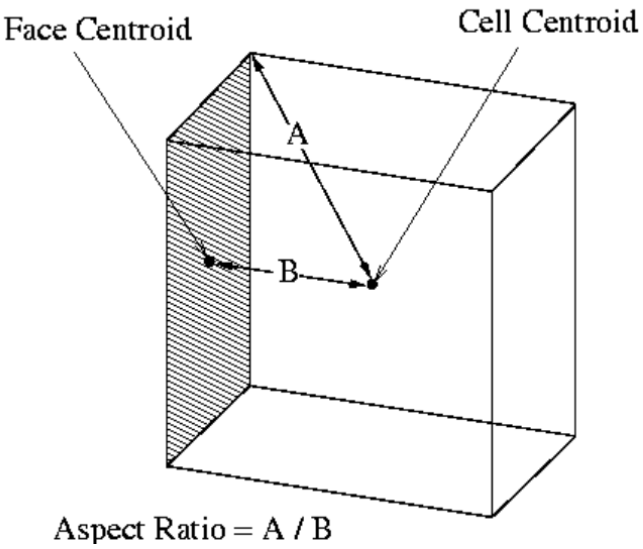

Figure 13 - Schematic of aspect ratio of a cube (Fluent-Ansys, 2023).

$$A.R = \frac{\mathrm{A}}{B} = \frac{3e-4\,m}{7e-5\,m} = 4.3 \tag{42}$$

where A.R is aspect ratio. For small y plus value in the range of $1<y^{+}<5$, having a perfect aspect ratio of 1, especially in the near wall region, is often hugely computationally expensive due to the placement very high mesh density in that region. In the boundary layer, aspect ratio of the first inflation layer closest to the wall was 4.3 (equation 42). This value fell within the acceptable range since aspect ratio of as high as 10 is allowed within the boundary layer (Fluent-Ansys, 2023). It is more important to have stretched cells with poor aspect ratio than having perfect cells with excellent aspect ratio at the walls because large velocity gradient in the boundary layer will be resolved and non-linear physics, as well as local turbulence, will be preserved (Alauzet et al., 2017;

Fluent-Ansys, 2023). As the inflation layer grew geometrically, from the first layer, at the rate of 1.05 % growth rate until twenty (20) layers were achieved, the effects of the inflation layer growth had reduced the aspect ratio to 1.67 in the last inflation layer, where mesh type changed from hexahedral to tetrahedral (Figure 12).

In general, about 29 million cells were generated in the computational domain containing 1e-3 m diameter leak (Figure 8), and only 14 % of that quantity consisted of hexahedral cells that were used in the near-wall meshing (Figure 11). About 70 % of the hexahedral cells (Figure 14) displayed aspect ratio in the range of 2.3 and 3.1 while the rest of the cells fell in the range of 4 to 4.8 aspect ratio.

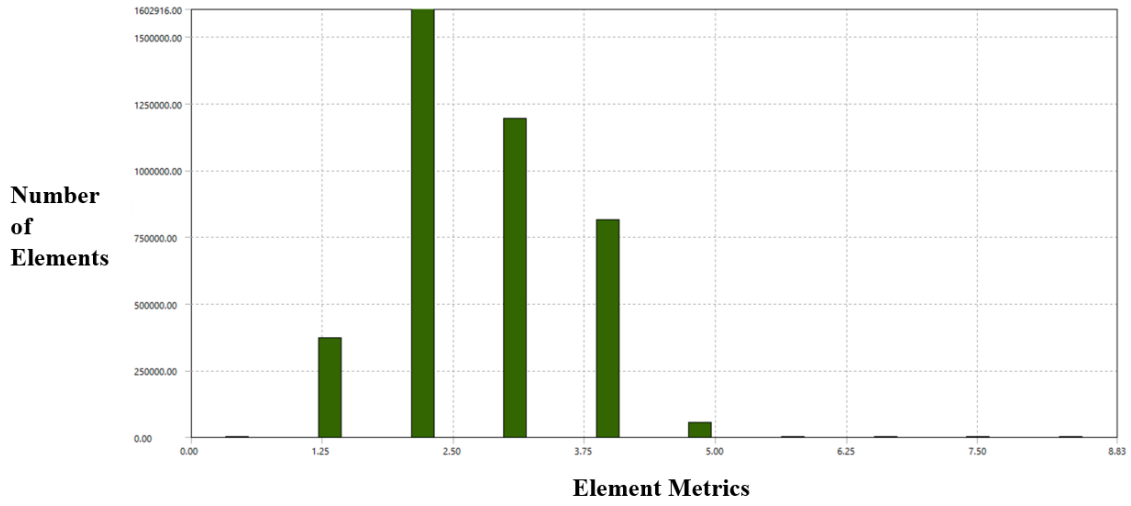

Figure 14 - Aspect ratio of hexahedral cells in near-wall region of the computational domain

In the free stream, away from the walls, and at the leak hole, aspect ratios of the tetrahedral mesh, with local mesh sizes of 3e-4 m and 1e-5 m respectively were estimated (Figure 15). About 63 % of the tetrahedral cells had aspect ratio of 1.45 and 35 % of the cells displayed aspect ratio of 2.3. The remaining tetrahedral cells had their aspect ratio in the range of 2.7 and 4.8. These values, therefore, fell within the acceptable range of $1<A.R<5$ (Fluent-Ansys, 2023).

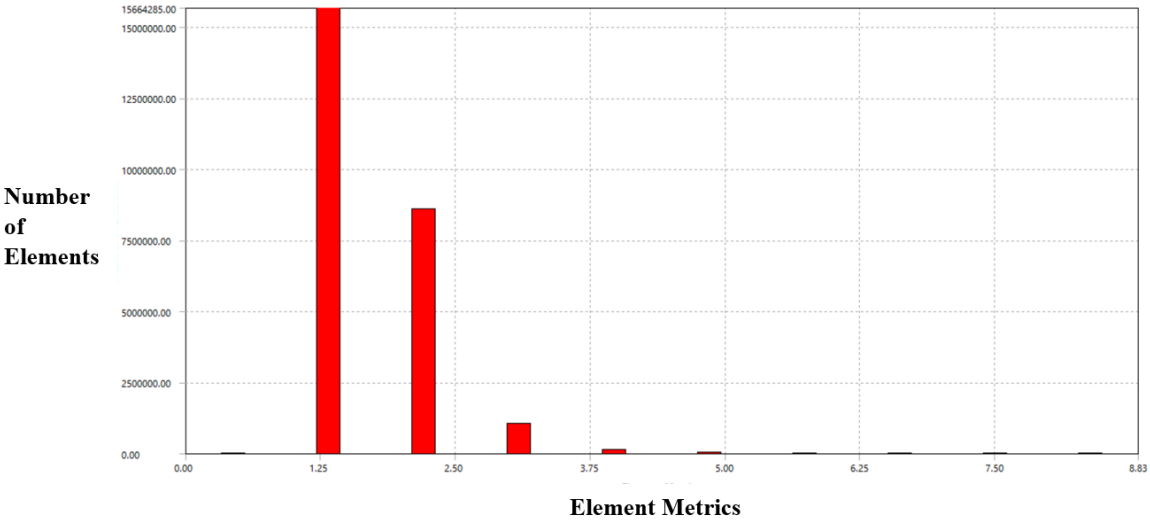

Figure 15 - Aspect ratio of tetrahedral cells in the computational domain

2. Skewness

Skewness is one of very important mesh quality metrics and is a measure of the closeness of a cell or face to an ideal shape (Ansys, 2013). Skewness of zero (0) shows that a cell matches perfectly with its ideal shape while skewness value of one (1) indicates a distorted cell that has deviated completely from its ideal shape (Table 1). However, for accuracy of numerical solutions, it is very vital that cells are close to equilateral or equiangular qualities as CFD equations assume these very excellent cell qualities in their calculations (Ansys, 2013; Fluent-Ansys, 2023).

The table below shows skewness values and their classifications (Ansys, 2013; Fluent-Ansys, 2023):

Table 1 – Skewness values and classifications

Skewness value	Quality of element
0	equilateral or equiangular (very excellent)
0 – 0.25	excellent
0.25 – 0.5	good
0.5 – 0.75	fair
0.75 – 0.9	poor
0.9 - < 1	bad
1	distorted

For equilateral cells, the volume-based skewness is measured as (Ansys, 2013):

$$Skewness = \frac{Ideal\ cell\ size - generated\ cell\ size}{Ideal\ cell\ size} \tag{43}$$

where ideal cell size is equilateral (triangular or tetrahedral) cell size of the same circumradius and generated cell size is the cell size obtained from mesh generator.

For equiangular cells (Ansys, 2013):

$$skewness = max\left[\frac{\theta_{max} - \theta_e}{180 - \theta_e}, \quad \frac{\theta_e - \theta_{min}}{\theta_e}\right] \tag{44}$$

where θ_{max} and θ_{min} are the maximum and minimum angles in the cell or face respectively and θ_e is the angle of the equiangular cell or face, which are 60° for a triangle and 90° for a rectangle or square.

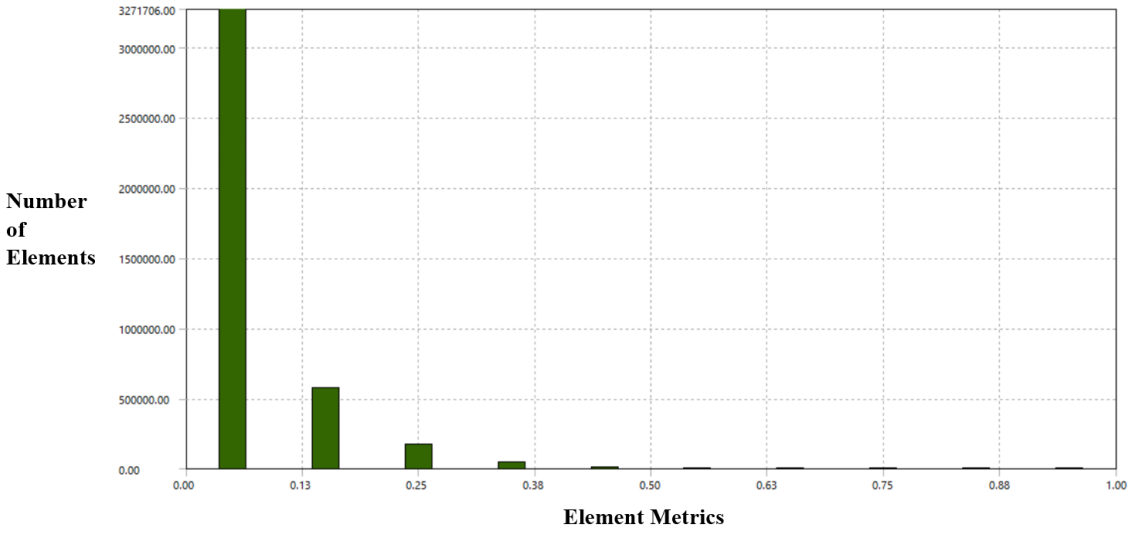

Figure 16 - Skewness of hexahedral cells in near-wall region of the computational domain

About 96 % of the cells in the near-wall (Figure 16) region fell within the range of excellent skewness quality while the remaining 4 % of the cells were classified in the range of good to poor skewness quality (Table 1). Having fair to poor cells in the near-wall region of the boundary layer is unavoidable, especially if the viscous sublayer is to be resolved, but good effort should be made to reduce the cells to the barest minimum (Fluent-Ansys, 2023). Tetrahedral of cells formed the remaining 86 % of the total cells in the computational domain and they were used mainly in the bulk flow and leak regions. About 80.7 % of the tetrahedral cells (Figure 17) fell within excellent range of skewness classification, 17.8 % could be classified as of good skewness and the remaining 1.5 % were within the range of fair to poor skewness classification (Table 1).

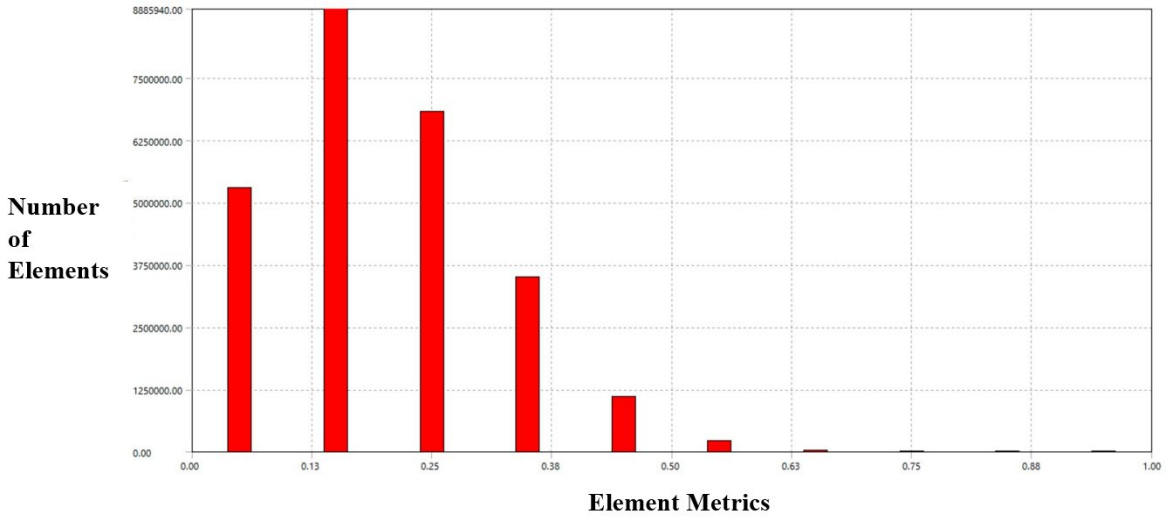

Figure 17 - Skewness of tetrahedral cells in the computational domain

3. Orthogonal quality

Orthogonal quality is a measure of how close the adjacent element faces are, to some optimal angle and it ranges from 0 to 1 for worst and best results respectively (Ansys, 2013; Fatchurrohman & Chia, 2017).

Table 2 - Values of orthogonal quality and their classifications (Fatchurrohman & Chia, 2017).

Orthogonal quality values	**Quality of element**
0 – 0.001	Unacceptable
0.001 - 0.14	Bad
0.15 - 0.2	Acceptable
0.2 - 0.69	Good
0.7 – 0.95	Very good
0.95 - 1	Excellent

There are two types of orthogonality in Ansys Fluent: cell-based and face-based orthogonality. In cell-based orthogonality (Figure 18), orthogonal quality can be calculated as the products of face normal vector $\vec{A}_i$ and the vector connecting the cell centroid of two adjacent cells $\vec{c}_i$, all normalised by their magnitudes (45):

$$C_{B1} = \frac{\vec{A}_i \,.\, \vec{c}_i}{|\vec{A}_i||\vec{c}_i|} \tag{45}$$

Orthogonal quality can also be calculated as the products of face normal vector $\vec{A}_i$ and the vector connecting the cell centroid to face centroid of a shared face $\vec{f}_i$, all normalised by their magnitudes (46):

$$C_{B2} = \frac{\vec{A}_i \,.\, \vec{f}_i}{|\vec{A}_i||\vec{f}_i|} \tag{46}$$

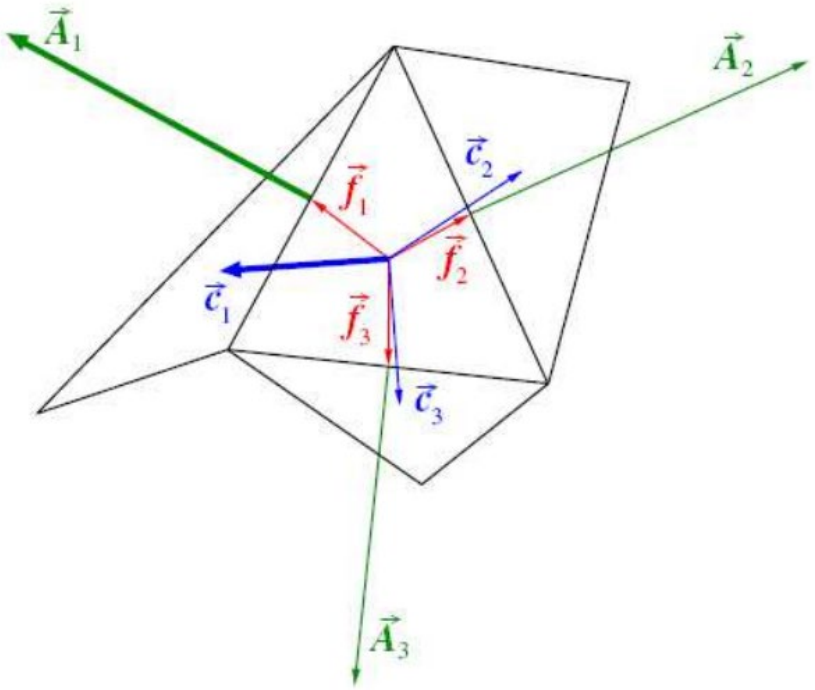

Figure 18 - Schematic of cell-based orthogonality

Final cell-based orthogonal quality is then calculated in Ansys-Fluent as the maximum value between the two forms of orthogonal quality calculations (47) described above (Ansys, 2013):

$$C_BO = max(C_{B1}, C_{B2}) \tag{47}$$

In face-based orthogonality (Figure 19), orthogonal quality can be calculated as the maximum of all the products between edge normal vector $\vec{A}_i$ and the vector connecting face centroid to edge centroid $\vec{e}_i$, all normalised by their magnitudes:

$$F_{Bmax} = \frac{\vec{A}_i \,.\, \vec{e}_i}{|\vec{A}_i||\vec{e}_i|} \tag{48}$$

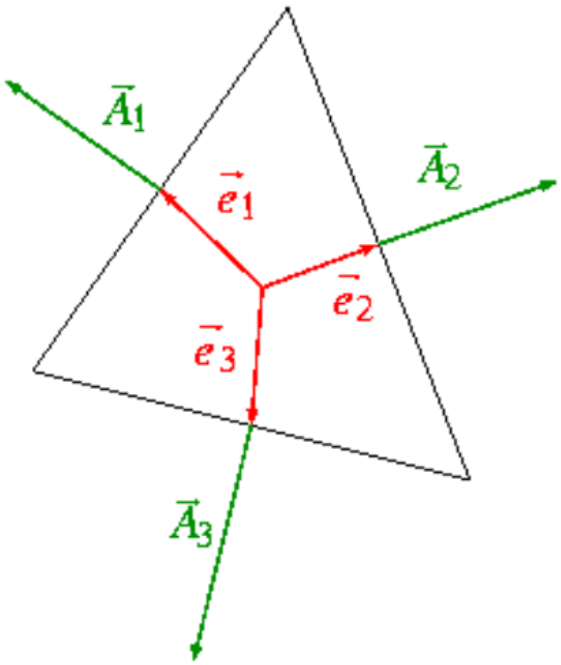

Figure 19 - Schematic of face-based orthogonality

As discussed in the previous section, hexahedral cells were used in the near-wall region, and these took about 14 % of the total cells in the domain. Using the classification chart (Table 2), about 81 % of the total cells in the near-wall region fell within the excellent orthogonal quality classification, 15 % were of very good classification and the remaining 4 % fell within good and acceptable classification range (Figure 20).

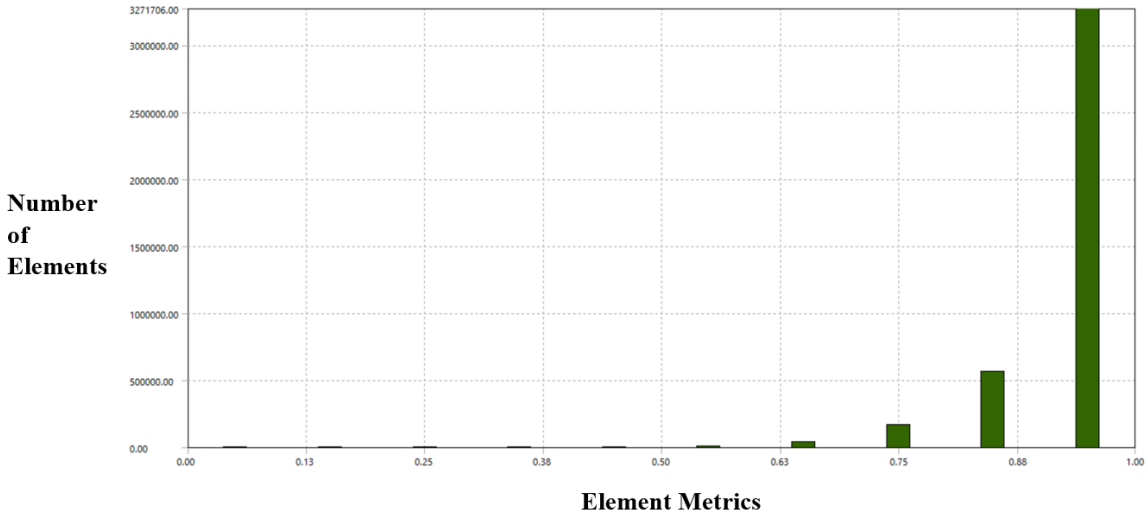

Figure 20 - Orthogonal quality of hexahedral cells in near-wall region of the computational domain

On the other hand, tetrahedral cells were used in the bulk flow region, including the leak area and about 21.2 % of these cells fell within the excellent orthogonal cell quality classification, 62 % were of very good classification, 16.4 % were of good classification and the remaining 0.4 % of the cells were within the range of acceptable and bad orthogonal quality classifications (Figure 21).

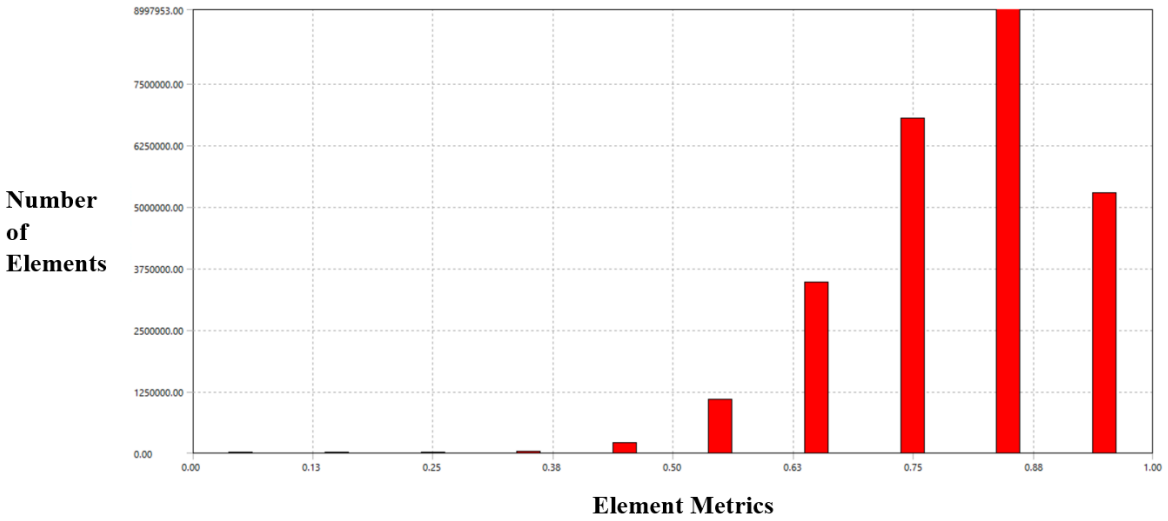

Figure 21 - Orthogonal quality of tetrahedral cells in near-wall region of computational domain

3.2.4 Numerical simulation of fluid flow in pipes.

In this study, the turbulence model adopted to simulate fluid flow in pipe containing leaks of different shapes was the shear-stress transport (SST) k-omega model, a two-equation model that efficiently resolves the near-wall and free stream regions of the flow (ANSYS, 2021; Yusuf et al., 2020). As discussed in the literature review section (2.5.2), SST k-omega model was preferred over other turbulence models because it was developed as an improvement to k-epsilon and BST k-omega turbulent models. The in-built blending function allows SST k-omega to be able to switch to BST k-omega at the walls and in the free stream, it has the capability to switch back to k epsilon model. In addition, the issue of wall shear over-prediction was corrected by the introduction of viscosity limiter.

As reviewed in section (2.7), coupled algorithm was adopted for this study because of the advantages it has over segregated algorithm. The single-phase implementation of steady state flow, derived from coupled algorithm is more efficient than that obtained from segregated algorithm (AnsysFluent, 2021). In addition, coupled algorithm converges faster than segregated

algorithm since coupled algorithm solves momentum and pressure-corrected continuity equations together while segregated algorithm solves the equations separately.

Absolute velocity formulation was chosen over relative, as the flow was not rotating inside the domain (ANSYS_FLUENT, 2009a). Steady-state solver was chosen as the flow parameters were not changing with time. The pipe was assumed to be horizontal (no gravity effect) and exposed (not buried).

To minimise numerical discretisation error (section 2.7), it would be more beneficial to adopt second order spatial discretisation if the flow is not in a very good alignment with the mesh, in a situation where tetrahedral mesh is used to model a cylindrical pipe, such that flow goes through the cell at angle(ANSYS_FLUENT, 2009b). In this study, accuracy of the numerical simulation is enhanced by adopting second order discretisation scheme as flow did not align well with the mesh due to the tetrahedral mesh used to model about 86 % of the computational domain, where the fluid was flowing through obliquely.

Least squares cell-based scheme was adopted over other schemes because it was efficient and computationally less expensive (section 2.7). Accuracy of the cell-based scheme has been improved by the introduction of weight factor to account for thin cells in the boundary layer, where aspect ratios are high (Ansys_Fluent, 2021).

Although it required more memory and relatively slower, double precision solver was chosen over single precision because it has more processing power and also, floating-point numbers are rather represented in 64-bit processor instead of 32-bit of single precision solver. Double-precision solver enhances processing power and precision of numerical simulation (Ansys_Fluent, 2023; Ansys_Fluent_precision_solvers_manual, 2021).

To judge convergence in pressure-based solver (section 2.7), residuals of conserved variables are summed up and stored each iterations and scaled by the scaling factor representative of the flow rate of conserved variables (Ansys-Fluent-11, 2023). The scaled residuals are normalised by a chosen number. In this study, convergence criteria for the transport equations was defined such that residuals of all conserved variables decreased to 10^{-6}, which was lower and closer to zero than the default 10^{-3}.

3.2.5 Boundary conditions

The computational domain of the model in Figure 8 was subdivided into the following boundaries and the set conditions at each boundary were discussed:

3.2.5.1 Velocity inlet boundary conditions

Velocity inlet boundary was assigned to the inlet of the computational domain (pipe model in Figure 8) and fluid of 0.5 ms^{-1} flow speed was simulated to enter the domain from the inlet. In accordance with the international standards, flow speed of not more than 2.5 ms^{-1} is allowed in water pipeline distribution systems (Ben-Mansour et al., 2012), in order to prevent wear and tear damage of the pipe.

For accuracy of results obtained from the numerical simulation of turbulent flow, it is important that flow in the computational domain is hydrodynamically fully developed as turbulent flow equations and expressions as well as CFD turbulent flow models and codes are only applicable to the hydrodynamically fully developed turbulent flows (KAHRAMANOĞLU et al., 2017).

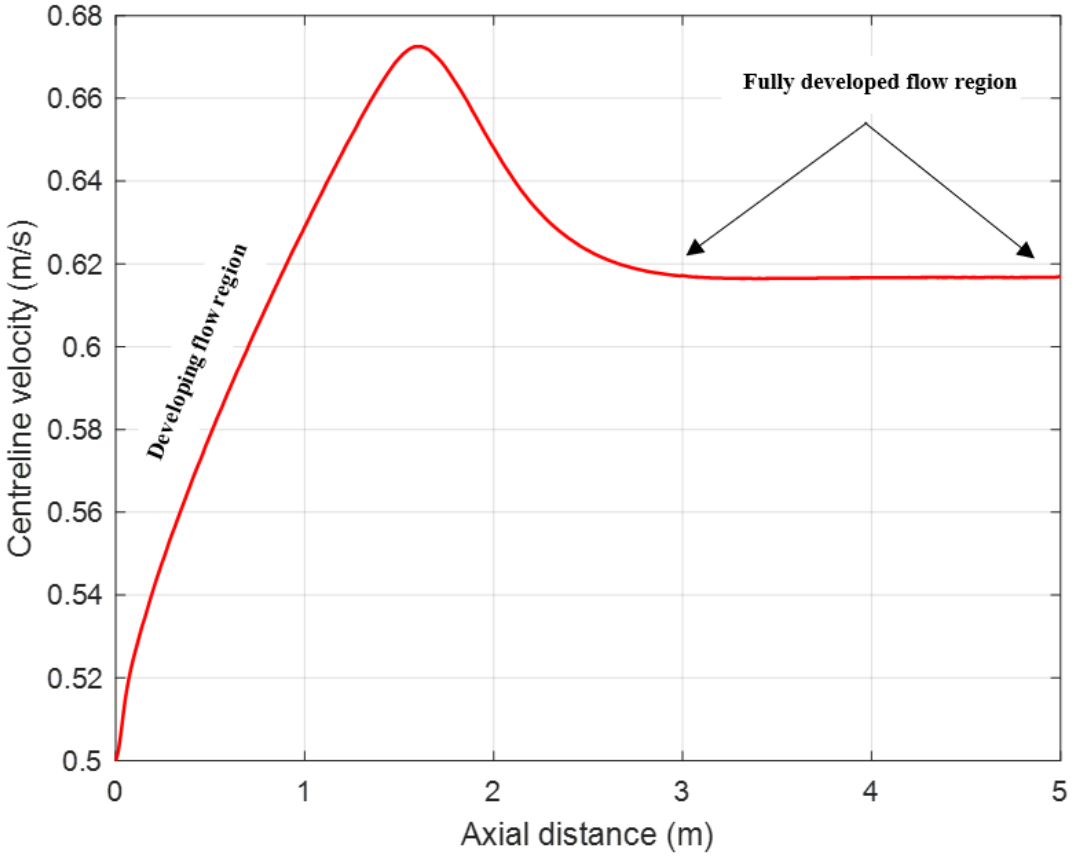

Figure 22 - Axial velocity profile of fluid flow in 0.05 m diameter pipe domain

To allow flow in the 0.1 m test pipes (Figure 8) to be fully developed prior to leak simulation, pipe domain lengths were scaled-up in the Ansys-Fluent to 2 m and 5 m for small and large diameter pipes respectively.

Fluid entered the domain at the inlet, with flow speed of 0.5 m/s and by the time the flow was fully developed, mean flow speed had increased to 0.617 m /s, due to viscous effects of fluids closest to the wall (Bhandari & Singh, 2012; K.A.U, 2004; KAHRAMANOĞLU et al., 2017). For a smaller diameter (0.025 m) pipe (Figure 8), the flow developed quicker (Figure 23), when compared to flow in larger diameter pipe (Figure 22) because the radial distance from the pipe wall to the centreline was relatively shorter for smaller diameter pipe and its boundary layer growth was faster (Bhandari & Singh, 2012; K.A.U, 2004; KAHRAMANOĞLU et al., 2017).

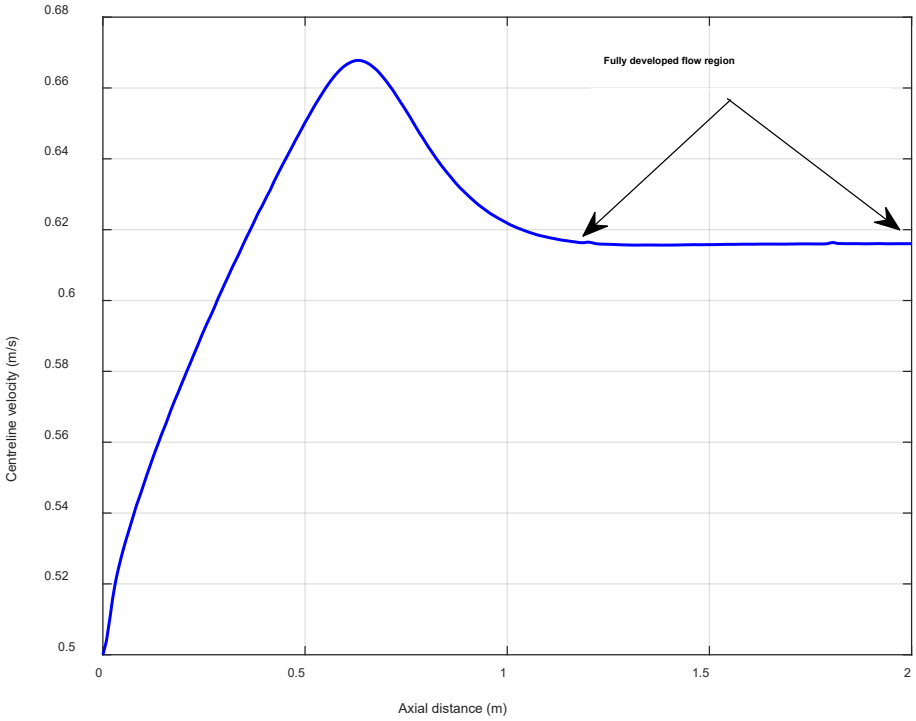

Figure 23 - Axial velocity profile of fluid flow in a 0.025 m diameter pipe domain

The axial velocity profile at the outlet of the fully developed flow from 5 m pipe in (Figure 22) was then exported and applied as inlet velocity of the 0.05 m diameter test pipe (Figure 8). Same procedure was carried out for smaller diameter test pipe (0.025 m) (Figure 8), where the axial velocity profile at the outlet of a fully developed flow (Figure 23) was exported and applied as inlet velocity. The rationale behind this procedure is to ensure that flow in the 0.1 m test pipes were hydrodynamically fully developed. To verify that flows in the test pipes (Figure 8) were actually fully developed, the velocity profiles were plotted at every 0.01 m intervals of the 0.1 m pipes, and all the 10 profiles for each test pipe showed very good collapse, which indicated that the flow in the pipes were fully developed (Figure 24 & Figure 25).

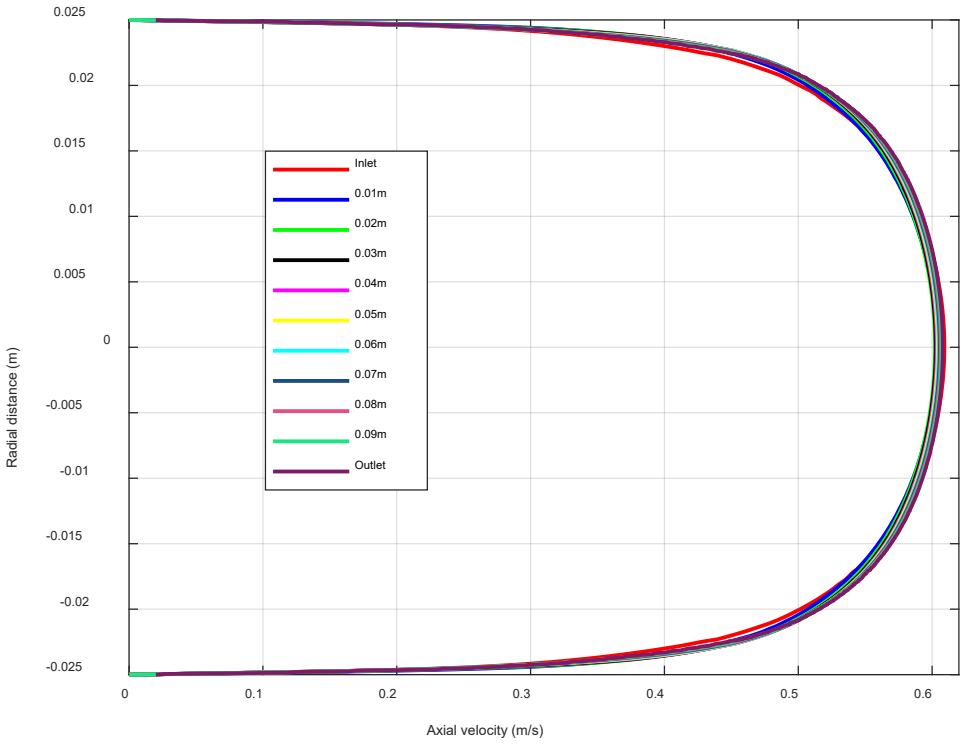

Figure 24 - Velocity profiles of fully developed flow in 0.05 m diameter pipe.

Development of fully developed flow in the smaller diameter pipe (section 3.2.1) was also verified by plotting the axial velocity profiles in the 0.025 m diameter pipe at 0.01 m intervals and the results indicated a very good collapse of the velocity profiles, which validated the development of a fully developed flow in the pipe (Figure 25). However, the shape of the velocity profiles for 0.025 m and 0.05 m diameter pipes were different (Figure 24 & Figure 25). The development of fully developed profiles in turbulent flows depend largely on various factors such as Reynold's number, pipe geometry and boundary conditions (Cengel & Cimbala, 2013; Salama, 2021). The two pipes were of different sizes and Reynolds numbers: R_e = 15,000 and R_e = 30,000 for 0.025 m and 0.05 m diameter pipes respectively, and it is expected that the shapes of their velocity profiles would be different. In addition, as mentioned previously, the flow was relatively quicker to fully develop in the smaller diameter pipe as pipe geometry played an important role in the process. Velocity profiles are generally fuller for turbulent flows and get even flatter as Reynolds number increases (Cengel & Cimbala, 2013). This was clearly evident in (Figure 24 & Figure 25) where the profiles of the 0.05 m diameter pipe were fuller and flatter than the profiles of the 0.025 m diameter pipe, due to Reynold's number difference. As Reynold's number increases, the fluid becomes more turbulent, and this enhances mixing of the fluid particles, reduction of velocity gradient and fullness of the velocity profiles (Salama, 2021).

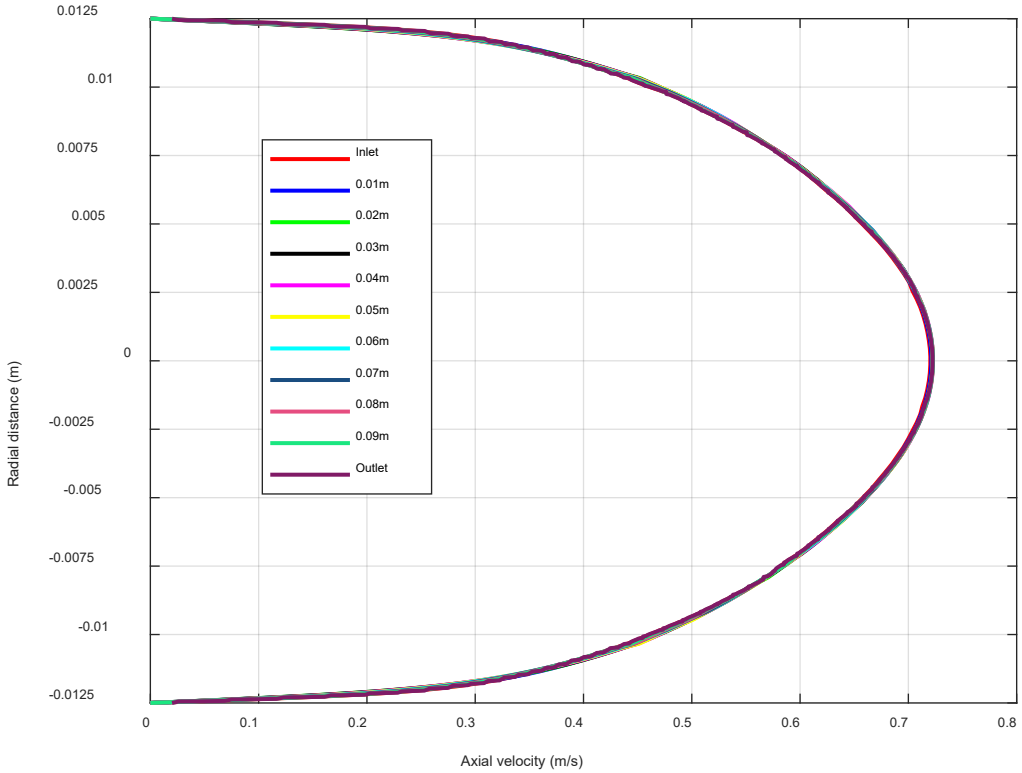

Figure 25 - Velocity profiles of fully developed flow in 0.025 m diameter pipe.

To further visualise the effect of Reynolds number on velocity profiles, fully developed profiles for 0.05 m and 0.025 m diameter pipes (Figure 24 & Figure 25) were normalised and plotted from the centreline. The plot in Figure 26 further confirmed that as Reynolds number increases, velocity profiles becomes fuller (Cengel & Cimbala, 2013; Salama, 2021)

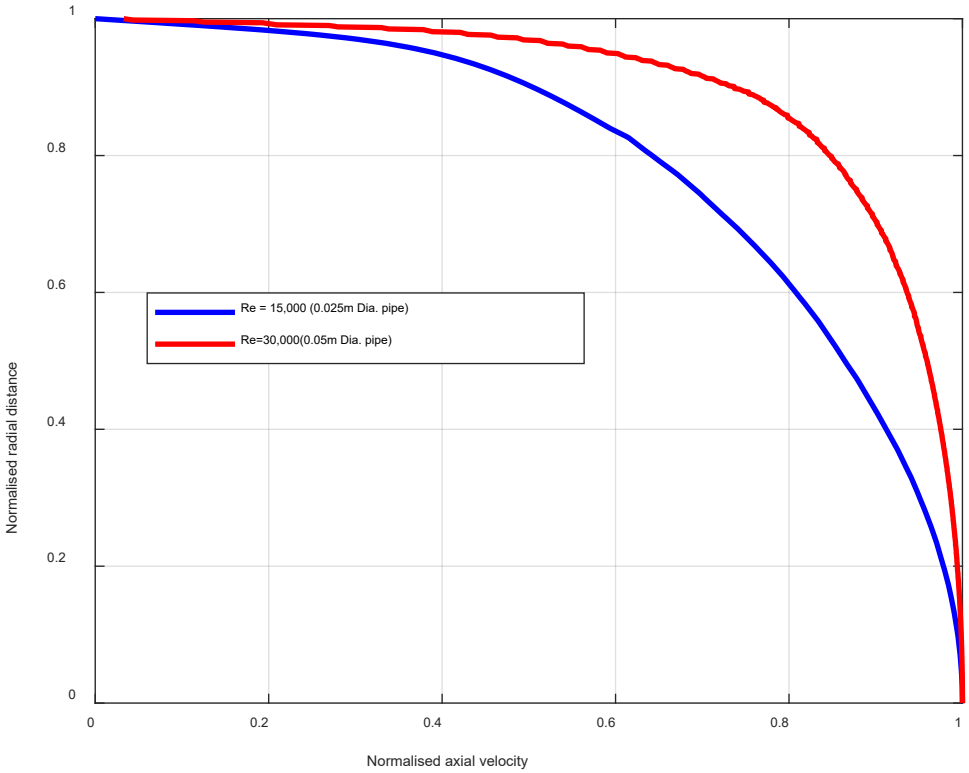

Figure 26 – Effect of Reynolds number on velocity profiles

As previously discussed in section 3.2.2 and using Eq. (41), turbulence length scales for 0.05 m and 0.025 m diameter pipes were 3.5e-3m and 1.8e-3m respectively. On the other hand, by using equation (49), turbulence intensities were calculated to be 4.4% and 4.8% for 0.05 m and 0.025 m diameter pipes respectively and these values were assigned to the inlet of the pipes (Ansys-Fluent-4, 2021; Cengel & Cimbala, 2013; Menge, 2015) .

$$I = 0.16 R_{e_{D_h}}^{\frac{-1}{8}} \tag{49}$$

where R_e is the Reynolds number and D_h is the hydraulic diameter of the pipe.

3.2.5.2 Pressure outlet boundary conditions

Pressure outlet boundary was assigned to the outlet of the pipes, using minimum gauge pressure of 1 Bar while the turbulence intensity and length scale were same as those used at the pipe inlet.

Similarly, the leak orifice was also set as pressure outlet boundary, using gauge pressure of 0 Bar, such that absolute pressure at the leak was the same as the atmospheric pressure: $P_{absolute\ (leak)} = P_{atm}$ (Ben-Mansour et al., 2012). Turbulence intensity of 4.85%, using equation (49), and turbulent length scale of 7e-5m (7% of the leak diameter), using equation (41), were assigned to the leak hole. In this study, the external environment where the water leaked to, was not investigated and subsequently not modelled due to limitation of computational power. This area is therefore recommended as a future work.

3.2.5.3 Symmetry boundary conditions

Symmetry boundary was adopted as the domain is axisymmetric and exhibit a mirror symmetry. Although, symmetry boundary was assigned to the plane of symmetry, no condition(s) were applied as all flow variables have zero normal gradients in the region (Fluent, 2023).

3.2.6 Grid convergence study

In order to capture the essential physics of the flow as it accelerates towards the leak orifice, the mesh size in the region of fluid in the close vicinity of the leak orifice must be sufficiently fine, to resolve the large velocity gradient responsible for turbulence generation. A schematic of the mesh geometry of the of the pipe containing the leak hole has been presented (Figure 12). To ensure that the solution obtained at the leak was independent of mesh resolution, grid convergence study was carried out on six (6) mesh sizes ranging from 3e-05m to 7.5e-06m (Table 3), where maximum turbulent kinetic energy was measured at the edge (edge turbulence) for each mesh sizes and the cases were compared to see how the solutions changed until convergence was achieved. The study was conducted for 5 mm diameter circular, square, longitudinal and transverse slit leaks.

Table 3 - Grid convergence study for 5mm diameter circular leak, comparing solutions of edge turbulence for different mesh sizes.

Mesh cases	Leak mesh sizes (m)	Leak node numbers	Edge turbulence (m^2s^{-2})
A	3e-05	13,264	1.13
B	2e-05	28,993	1.53
C	1e-05	114,195	2.1
D	9e-6	140,107	2.26
E	8e-6	186,436	2.1
F	7.5e-6	207,776	2.04

In Table 3, it was observed that as mesh sizes at the leak holes were reduced, node numbers increased, and turbulent kinetic energy levels also increased. The levels however stopped changing significantly from cases C to F, even as the node numbers and mesh sizes increased. At this point, the solutions obtained were deemed independent of mesh resolution. Subsequently, mesh size of 1e-05 m in case C was adopted to mesh leak holes of circular leaks in this study as it was computationally less expensive than mesh sizes in cases D, E and F.

To investigate variations of turbulent kinetic energy along the leak radii, radial profiles of turbulent kinetic energy were plotted, from the leak edge through to the leak centre, for the six mesh cases. Turbulent kinetic energy levels were found to increase, with highest values at the edge, as node numbers at the leak increased until convergence was attained from mesh sizes 1e-05 m to 7.5e-06 m. Turbulent kinetic energy (t.k.e) profiles for mesh cases A and B were clearly out of alignment with the rest of other cases (Figure 27).

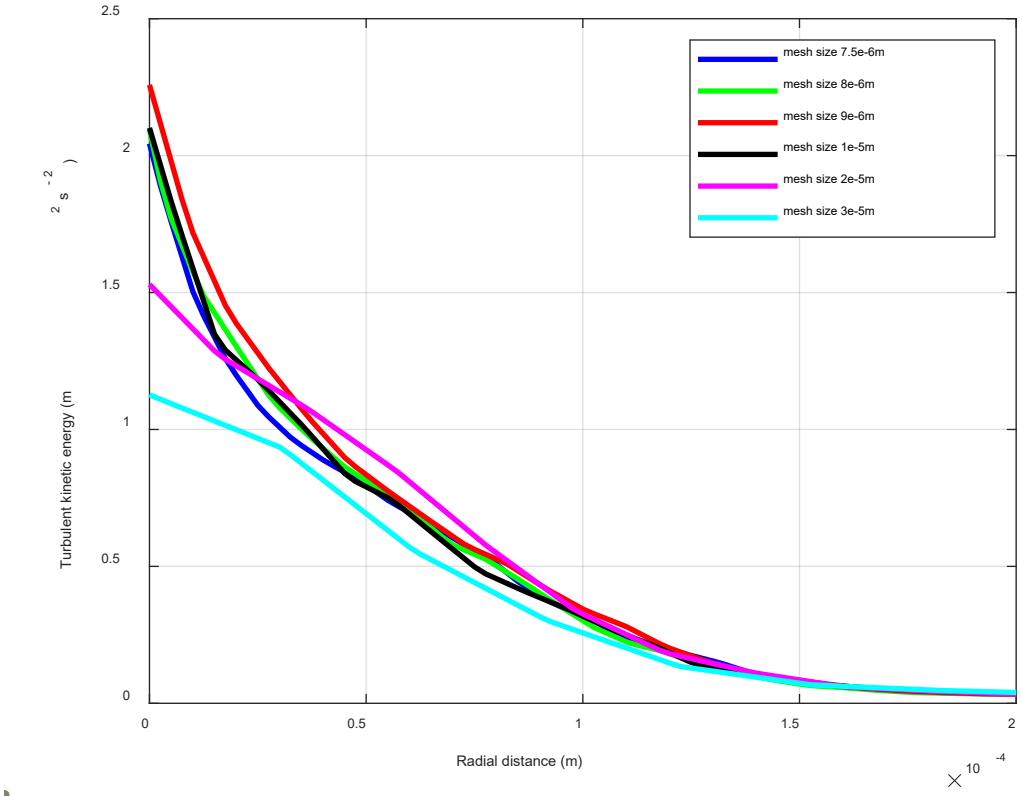

Figure 27 - Radial profiles of t.k.e for different mesh sizes on 5mm diameter circular leak.

however, as node numbers increased in cases C to F, the profiles became more converged and in better agreement.

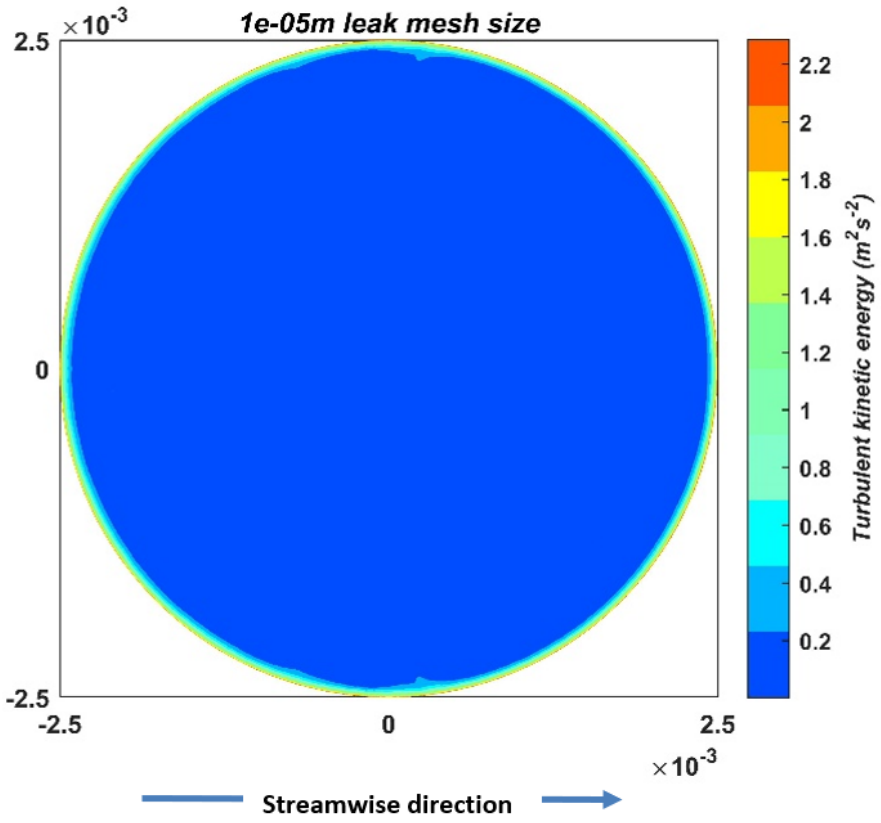

Figure 28 - Contour plot of turbulent kinetic energy for 5 mm diameter circular leak using mesh size of 1e-05 m.

Circular leak was meshed using mesh size of 1e-05m and then numerically simulated. High values of turbulent kinetic energy were concentrated around the edge of the leak and these values decayed down to the centre of the leak.

For square leak, solutions stopped changing significantly from mesh size of 1e-5m in case C (Table 4) and mesh size 1e-05m was adopted to mesh square leaks due to its low computational expense.

Table 4 - Grid convergence study for 5mm diameter square leak comparing solutions of edge turbulence for different mesh sizes

Mesh cases	**Leak mesh sizes (m)**	**Leak node numbers**	**Edge turbulence (m^2s^{-2})**
A	3e-05	12,635	1.34
B	2e-05	27,004	1.68
C	1e-05	86,803	2.3
D	9e-6	102,749	2.5
E	8e-6	122,843	2.46
F	7.5e-6	130,587	2.3

Radial profiles of the mesh sizes in Figure 29 showed that finer mesh sizes from 1e- 05 m to 7.5e-06 converged better than mesh sizes 2e-05 m and 3-05 m. Mesh size 1e-05m was consequently adopted as the representative mesh size for square leaks in this study.

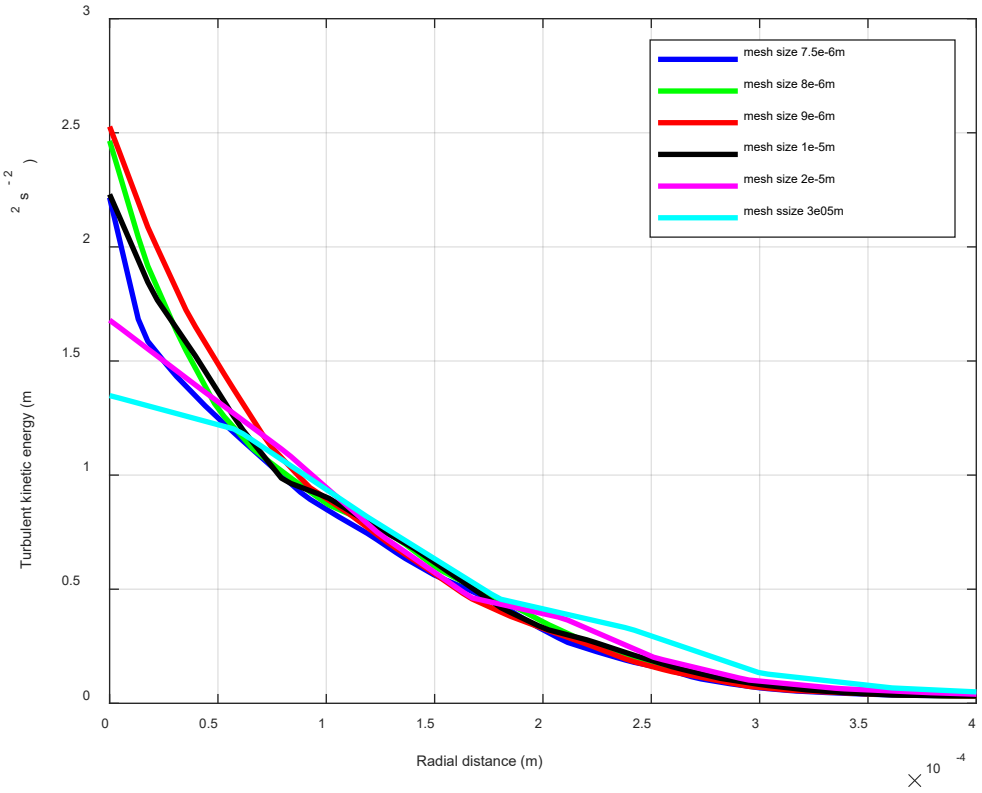

Figure 29 - Radial profiles of t.k.e for different mesh sizes on 5mm diameter square leak.

Square leak was meshed using mesh size 1e-05m and numerically simulated. Similar to circular leak, higher values of turbulent kinetic energy were concentrated at the edge of the

leak and the values decayed down to the centre (

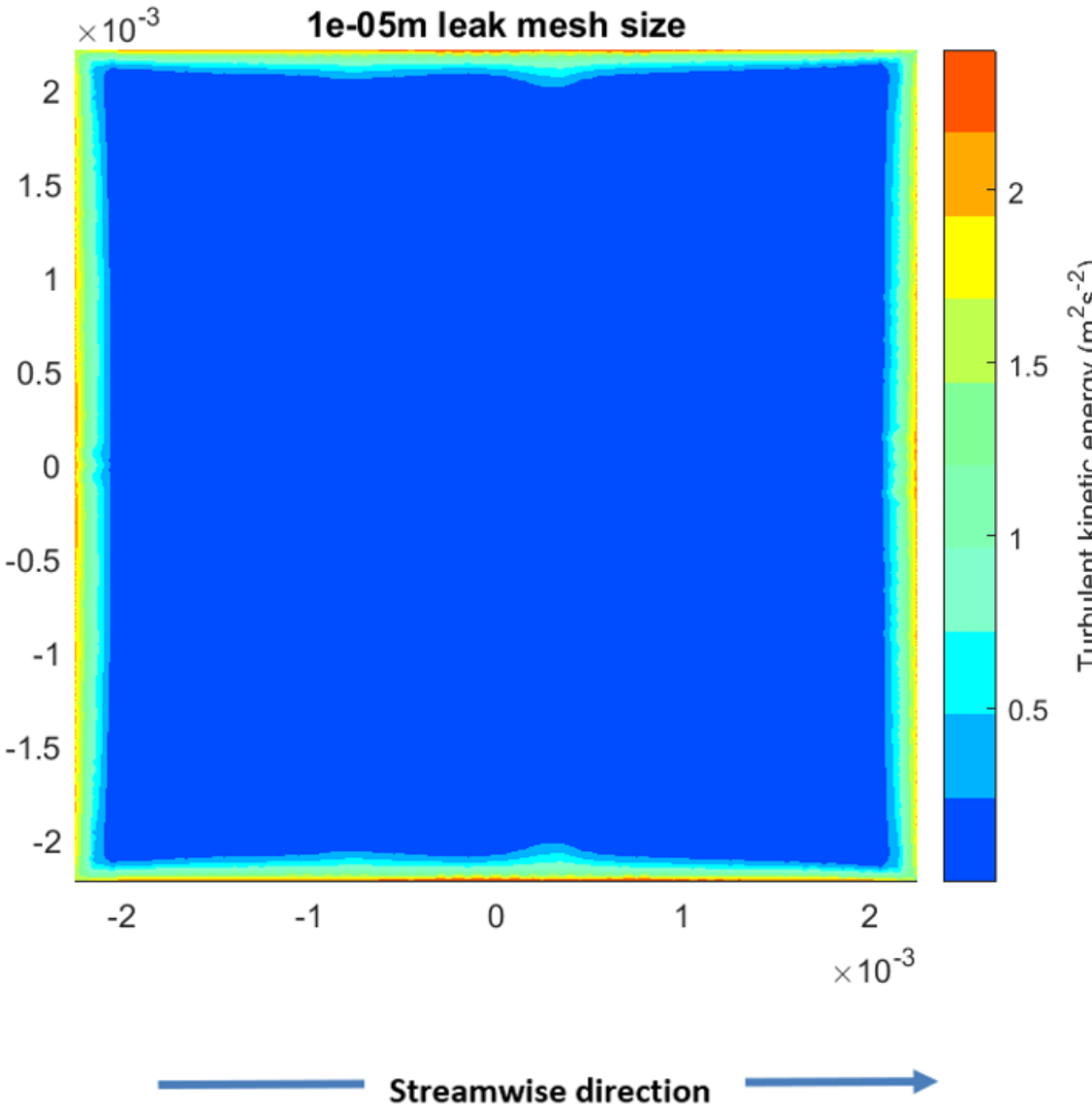

Figure 30).

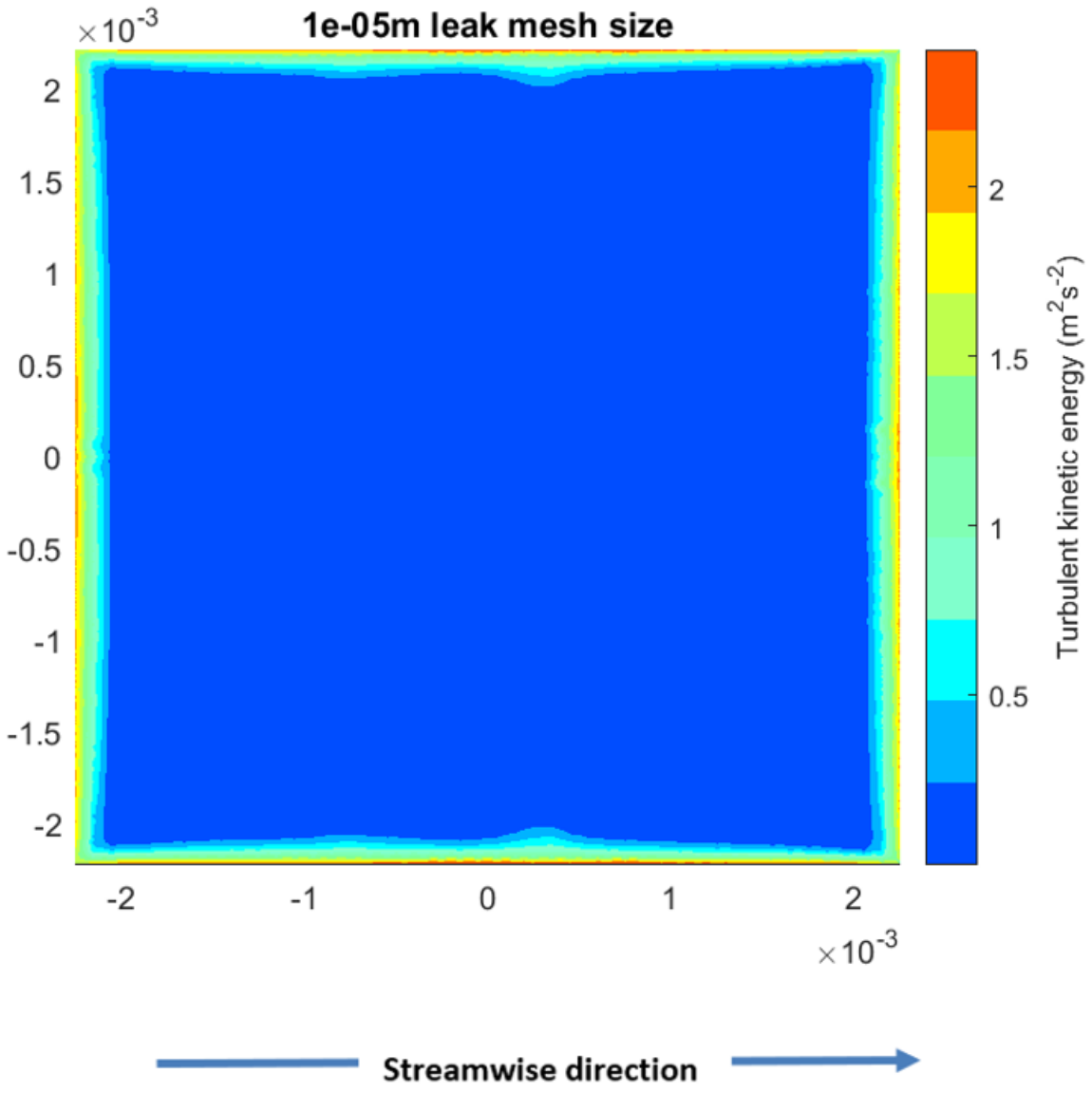

Figure 30 - Contour plot of turbulent kinetic energy for 5 mm diameter square leak using mesh size of 1e-05 m.

Longitudinal leak was modelled as elongated rectangle with the longer sides positioned in the streamwise direction (Figure 9). To obtain mesh independent numerical solutions, gird convergence study was carried out on mesh sizes ranging from 3e-05m to 7.5e-06m in cases A to F (Table 5).

Table 5 - Grid convergence study for 5mm diameter longitudinal slit leak, comparing solutions of edge turbulence for different mesh sizes

Mesh cases	**Leak mesh sizes (m)**	**Leak node numbers**	**Edge turbulence (m^2s^{-2})**
A	3e-05	13,208	1.1
B	2e-05	29,016	1.38
C	1e-05	111,779	2.36
D	9e-6	135,700	2.31
E	8e-6	169,541	2.37
F	7.5e-6	193,485	2.46

Convergence study for longitudinal slit leak was investigated by plotting line profile of turbulent kinetic energy (Figure 31), from leak edge to the centre, for all cases with different mesh sizes. Edge turbulence changed as meshes got finer but not significantly from cases C to F and mesh size 1e-05m in case C was chosen to mesh longitudinal slit leaks in this study.

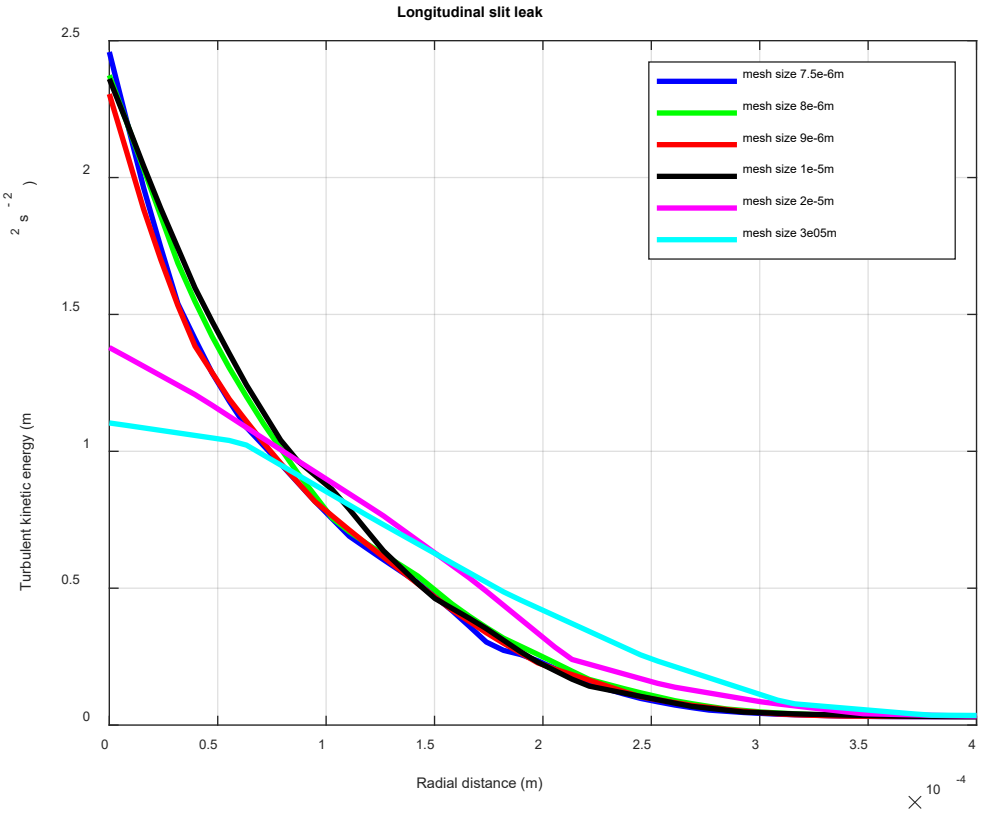

Figure 31 - Radial profiles of t.k.e for different mesh sizes on 5mm diameter longitudinal slit leak.

The contour plot of longitudinal slit leak (Figure 32) also showed higher points of turbulent kinetic energy distributed around the edge of the leak and this decayed towards the leak centre.

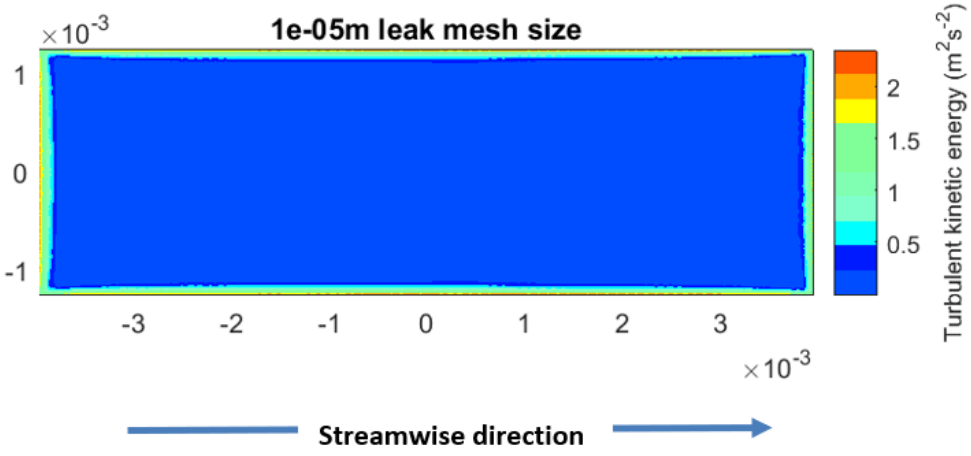

Figure 32 - Contour plot of turbulent kinetic energy for 5 mm diameter longitudinal slit leak using mesh size of 1e-05 m.

Transverse slit leak was modelled as elongated rectangle with the longer sides positioned in a direction perpendicular to the bulk flow. To obtain numerical solutions that are independent of mesh sizes, convergence study was carried out on mesh sizes ranging from 7.5e-06m to 3e-05m, and edge turbulence was measured for each of the cases (Table 6).

Table 6 - Grid convergence study for 5mm diameter transverse slit leak, comparing solutions of edge turbulence for different mesh sizes

Mesh cases	**Leak mesh sizes (m)**	**Leak node numbers**	**Edge turbulence (m^2s^{-2})**
A	3e-05	9,334	1.08
B	2e-05	17,442	1.47
C	1e-05	42,610	1.9
D	9e-6	48,513	1.88
E	8e-6	55,835	2
F	7.5e-6	58,562	1.9

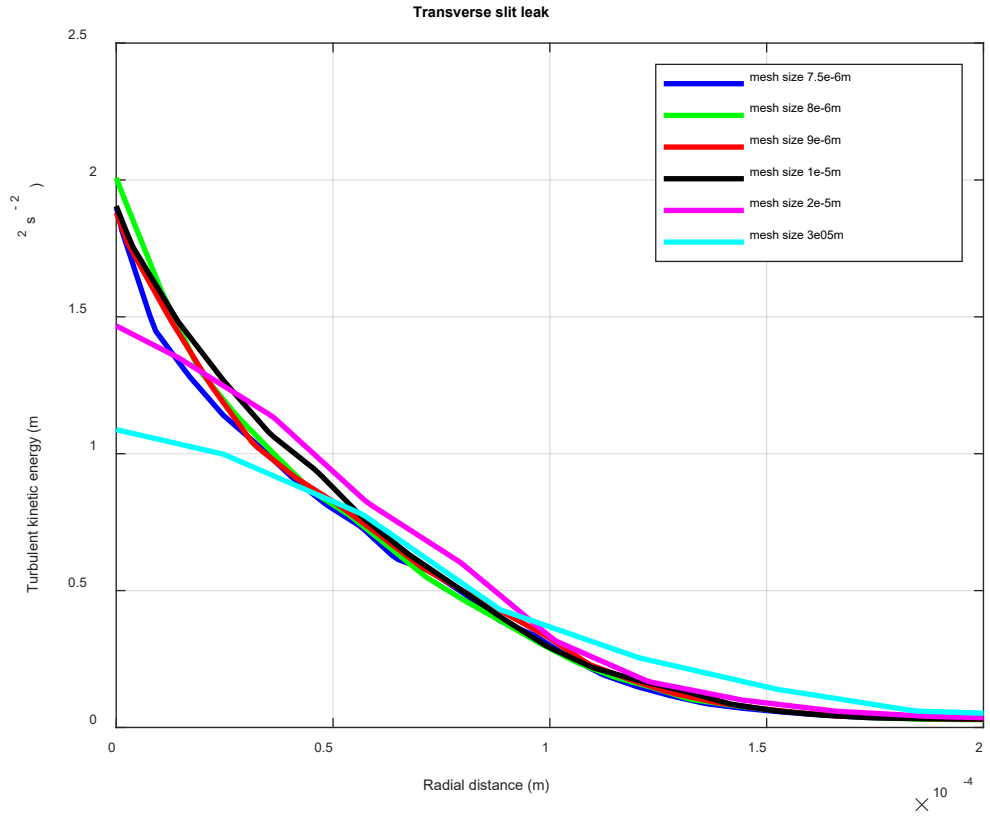

Figure 33 - Radial profiles of t.k.e for different mesh sizes on 5mm diameter transverse slit leak.

Turbulence kinetic energy increased as mesh sizes were reduced until the percentage increment fell within 10 %, from cases C to F. Mesh size in case C was however adopted to mesh transverse slit leaks in this study. Radial profiles of the mesh cases (Figure 33) also showed good collapse from cases C to F.

Contour plot of transverse slit leak, just like the other leak sizes considered in this study, showed turbulent kinetic energy to be concentrated at the leak edge and decayed down to the leak centre

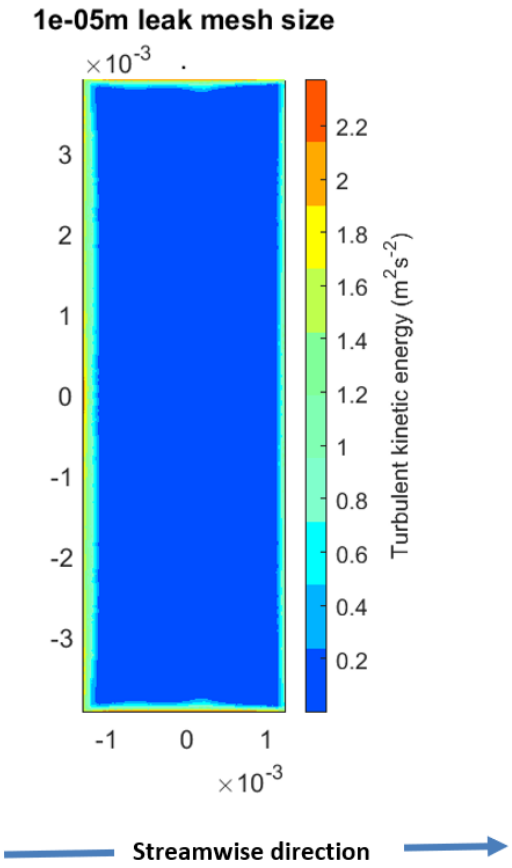

Figure 34 - Contour plot of turbulent kinetic energy for 5 mm diameter transverse slit leak using mesh size of 1e-05 m.

Chapter 4 Results and discussions

4.1 Overview

This chapter presents the results obtained from numerical simulation of flow in the pipes and leaks of different diameters and shapes respectively. To ensure accuracy, numerical simulation results were validated against their analytical solutions. Leaks of different shapes and diameters and under different line pressures were modelled and numerically simulated. The behaviours of turbulent kinetic energy, mean flow velocity and other flow parameters in the vicinity of the leak area were investigated and variations of these flow parameters with different pipe sizes, leak shapes, pressures and flow rates were established.

4.2 Validation of results from symmetric (half) pipe with full pipe

As discussed in section (3.2.1), to minimise computational cost, the computational domain of the test pipe was sliced into two symmetric parts and only one half of the pipe was used in the numerical simulations. To ensure accuracy of this approach, numerical simulation of a full test pipe (Figure 35) was conducted and the results at the leak were compared with those obtained from the leak orifice of the half pipe in (Figure 8).

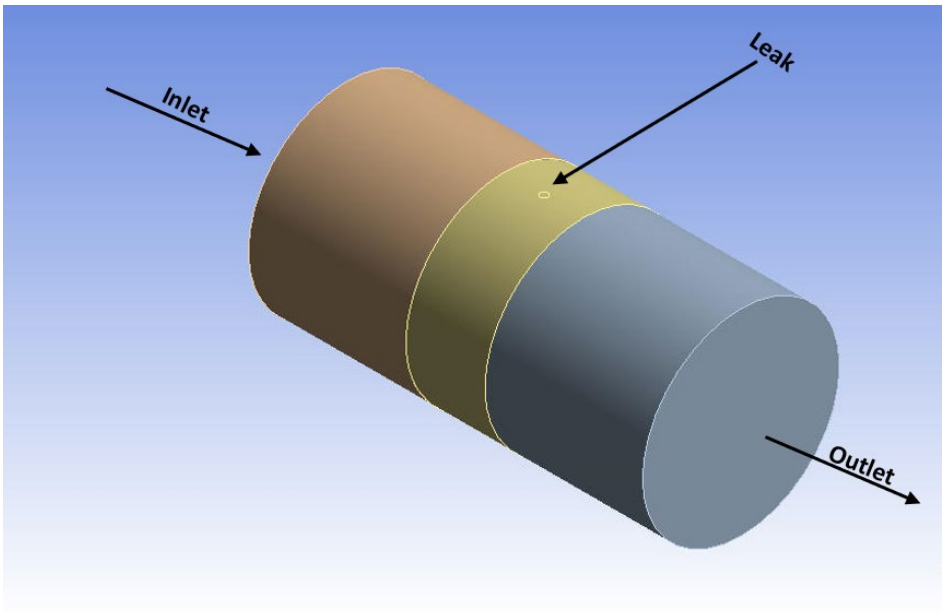

Figure 35 – Computational domain of a full test pipe

Turbulent kinetic energy contour plot at the leak orifice of 2 mm diameter circular leak from half pipe was compared with that of a full pipe (Figure 36).

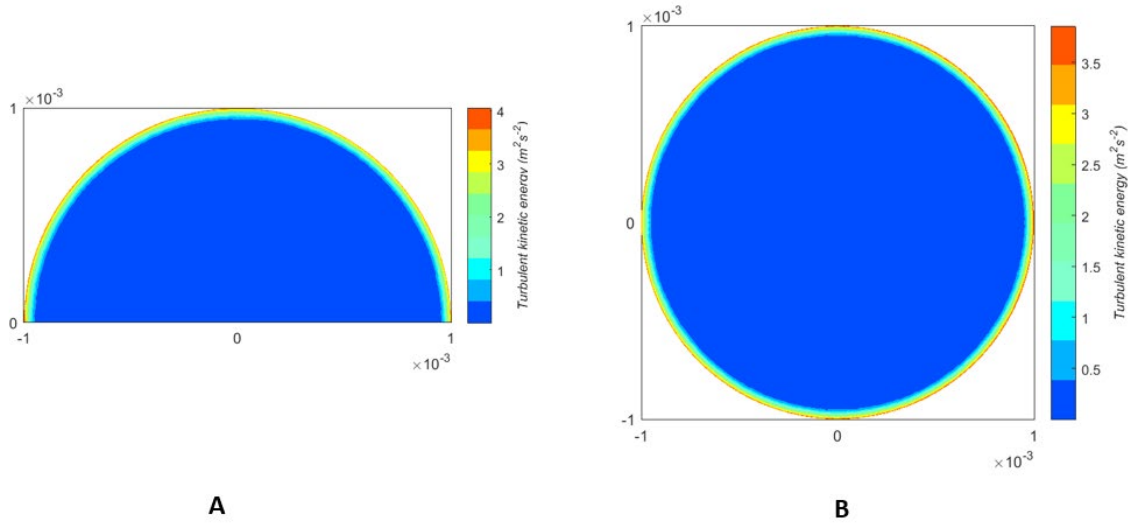

Figure 36 – Turbulent kinetic energy contour at 2mm diameter leak orifice of half pipe (A) and the leak contour a full pipe (B)

The contour plots in (Figure 36) indicated a very good agreement in the maximum values of turbulent kinetic energy (edge turbulence) for the two pipes, with only a percentage error of 3.1 %, from the half pipe. To transform the t.k.e contour plot at the leak orifice of the half pipe to a full circle, negative values of the t.k.e in (Figure 36A) were plotted and this indicated that solutions of turbulent kinetic energy at the leak holes of the two pipes were axisymmetric (Figure 37).

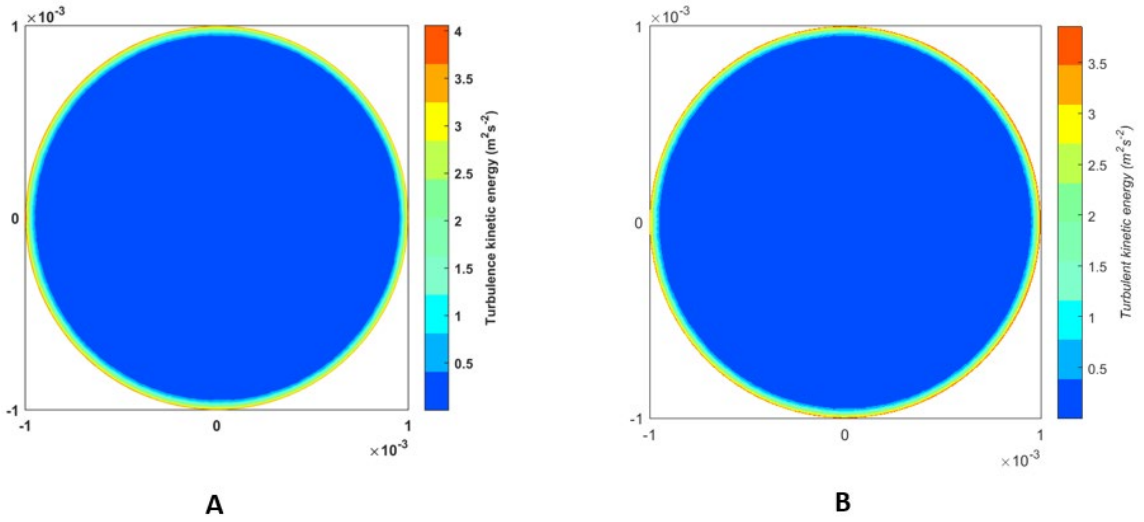

Figure 37 – Transformed turbulent kinetic energy contour at 2mm diameter leak orifice of half pipe (A) and the leak contour of a full pipe (B)

The behaviours of turbulent kinetic energy along the radii of the two leak holes were investigated and it was found that turbulent kinetic energy, in the radial direction, at the leak holes of the two pipes did not differ much. For the two leak holes, high values of turbulent kinetic energy were concentrated at the edges, and then decay down to zero, at the centre of the holes (Figure 38). This indicated a similar behaviour of turbulent kinetic energy at the leak holes of the two pipes and thus provided a good justification for adopting the half pipe approach.

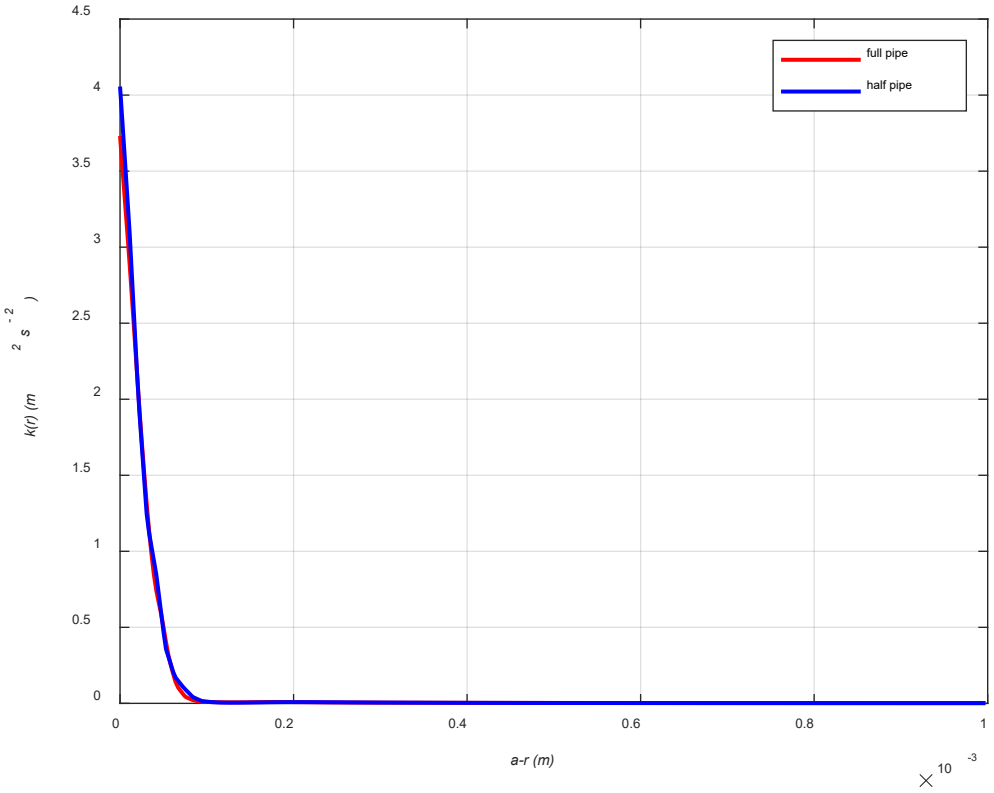

Figure 38 – Radial variations of turbulent kinetic energy at the leak orifice of the two pipes

Similarly, the contour (transformed) plot of total leak mean velocity at the orifice of a 2 mm diameter leak from a half pipe was compared to the leak velocity contour from a full pipe (Figure 39). A very good agreement was attained for the maximum values of total leak mean velocities of the two pipes. For the two pipes, velocity magnitudes at the edges of the 2 mm diameter leak sizes were zero, due to no slip boundary conditions. The velocity magnitudes gradually rose to maximum values of 20.0812 m/s and 20.0566 m/s at their leak centres, for full and half pipe respectively with only a percentage error of 0.12 %, from the half pipe.

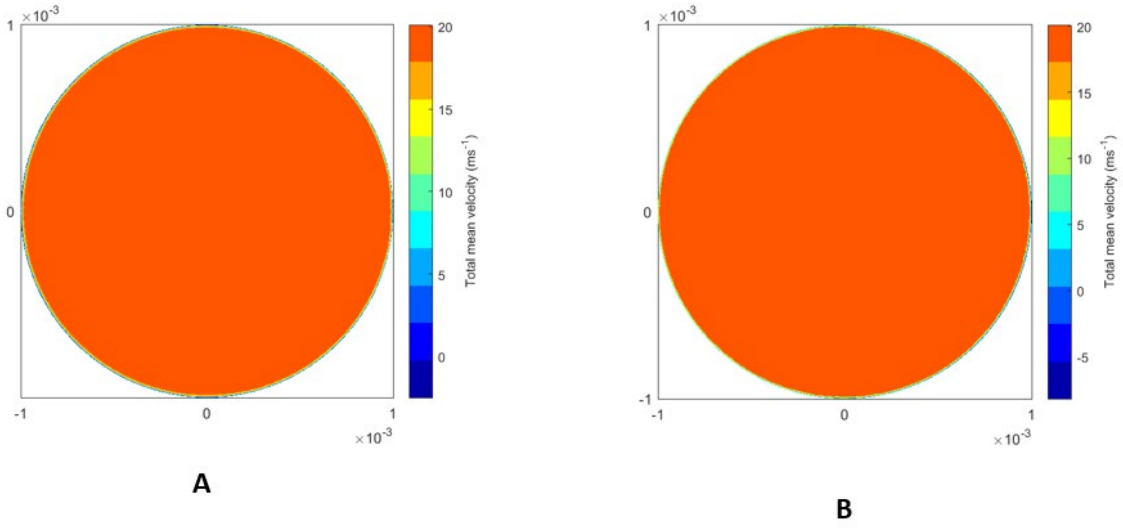

Figure 39 - Transformed total leak mean velocity contour at 2mm diameter leak orifice of half pipe (A) and the leak contour of a full pipe (B)

In the radial direction, velocity profiles of the two leaks did not vary much. There existed a very good similarity in their radial velocity profile behaviours (Figure 40) and this substantiated the justification for the adoption of half pipe modelling and simulation approach in this study.

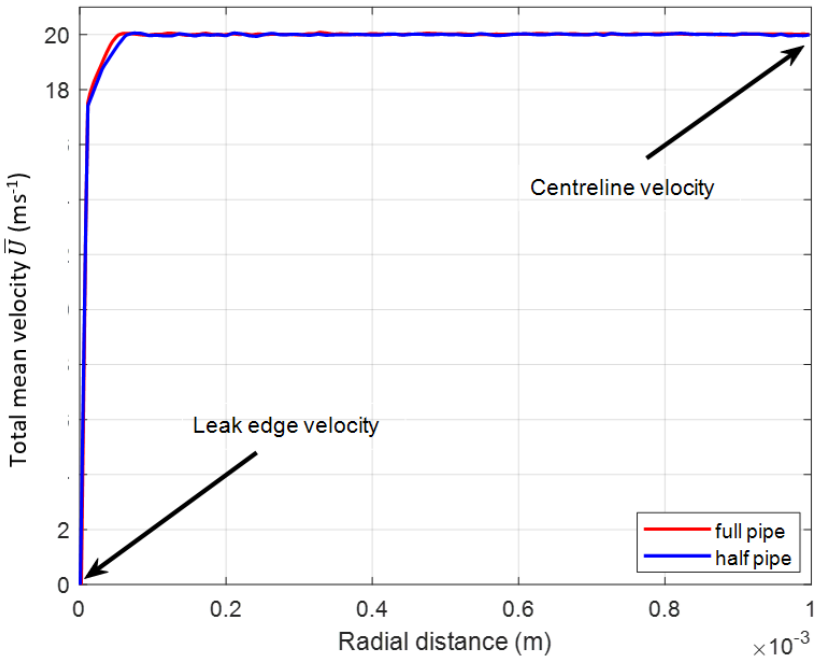

Figure 40 – Comparison of radial velocity profiles of 2 mm diameter leaks from full and half pipes

4.3 Validation of numerical simulation results

The accuracy of results obtained from numerical simulations were verified with the following analytical solutions:

4.3.1 Pressure drop

Reynolds number $Re_d = \frac{\rho UD}{\mu}$ for flow in 0.05 m diameter smooth pipe is 29910 and average fluid velocity in this study was 0.5 m/s.

By using the pressure drop analytical expression in equation (17), analytical solution for pressure-drop in the 0.05 m diameter pipe was calculated as 6.28 Pa**.**

L is the pipe length = 0.1 m

D is the diameter of the pipe = 0.05m

Using Eqn. (50), Darcy friction factor f = 0.0251

Wall shear stress calculation, using τ_w expression (2.9) = 0.785 Pa

Turbulent flow skin friction coefficient calculation, using C_f expression (2.9) = 0.0063

This was in good agreement with the solution of numerical simulation (Figure 41) where the pressure drop was 6.4 Pa, and the percentage error was less than 2%.

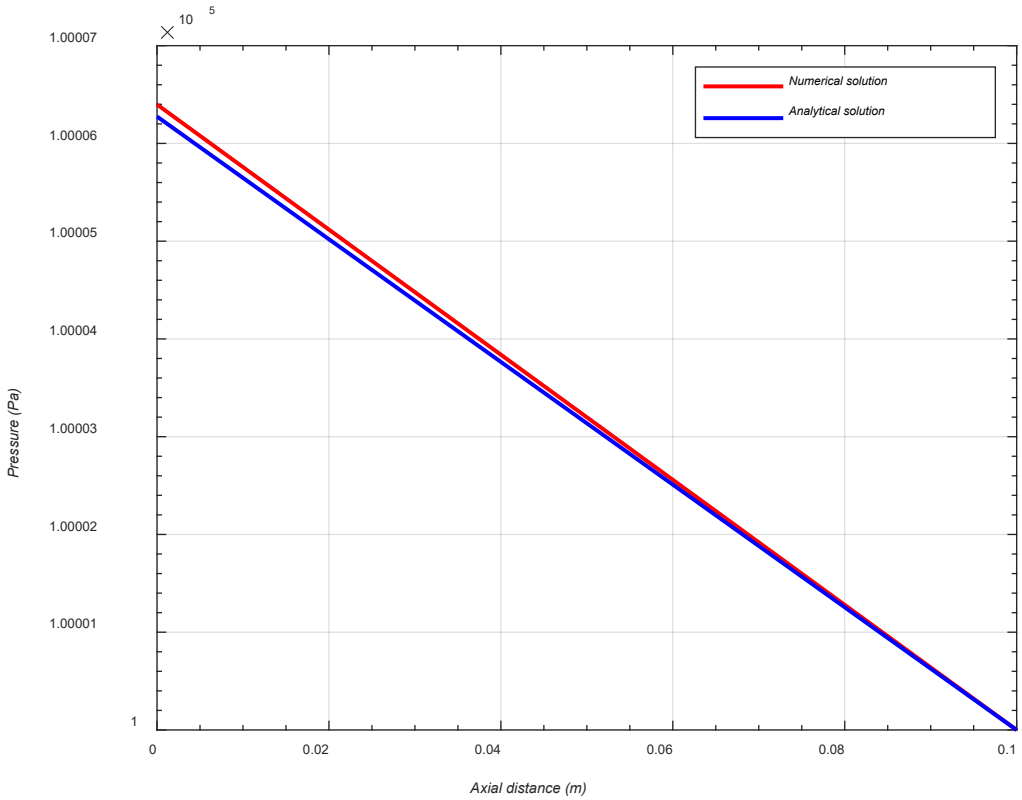

Figure 41 - Comparison of pressure drop for analytical and numerical solutions

4.3.2 Centreline velocity

Analytical expression for estimating centreline velocity in equation (51) was obtained from the integration of power law velocity profile (Bhandari & Singh, 2012; Kudela, 2010) and this expression has been used to validate the solution of centreline velocity in 3D numerically simulated flows (Bhandari & Singh, 2012).

$$\frac{U_x}{U_{max}} = \frac{2n^2}{(n+1)(2n+1)} \tag{51}$$

Where U_x is the mean velocity and U_{max} is the centreline velocity which is maximum velocity at the centreline of the pipe while n is a value that depends largely on Reynolds number (Bhandari & Singh, 2012; Kudela, 2010) and can be obtained from a chart (Figure 42).

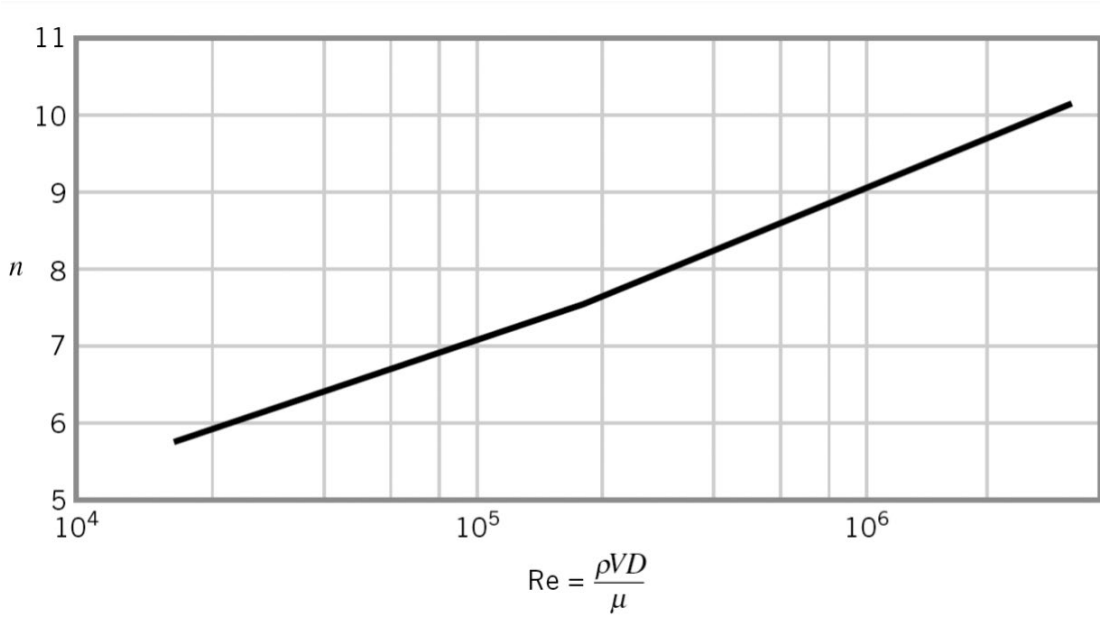

Figure 42 - Linear relationship between 'n' and Re (Bhandari & Singh, 2012; Kudela, 2010).

As noted in the previous subsection, Reynolds number for 0.05 m diameter pipe was 29910 and using the chart in (Figure 42), n was estimated to be 6.1. By substituting 6.1 for "n" in equation (51), centreline velocity was analytically estimated as 0.6297 m/s and this was in good agreement with the numerically simulated centreline velocity solution of 0.617 m/s (Figure 22), where the percentage error was about 2 %.

4.3.3 Leak flow rates

The leak flow rates obtained from different leak diameters were plotted against line pressures (Figure 43). In their work, (Ben-Mansour et al., 2012; M. Jujuly et al., 2016) have used analytical expression of leak flow rate and pressure relationship (Torricelli law) in equation (52), to validate the accuracy of their CFD models.

$$Q_{leak} = C_d A\sqrt{2gh} = C_d A\sqrt{2P/\rho} \tag{52}$$

where Q_{leak} is the leak flow rate, C_d is the discharge coefficient, A is the leak area, g is gravity acceleration, ρ is fluid density and h is the pressure head.

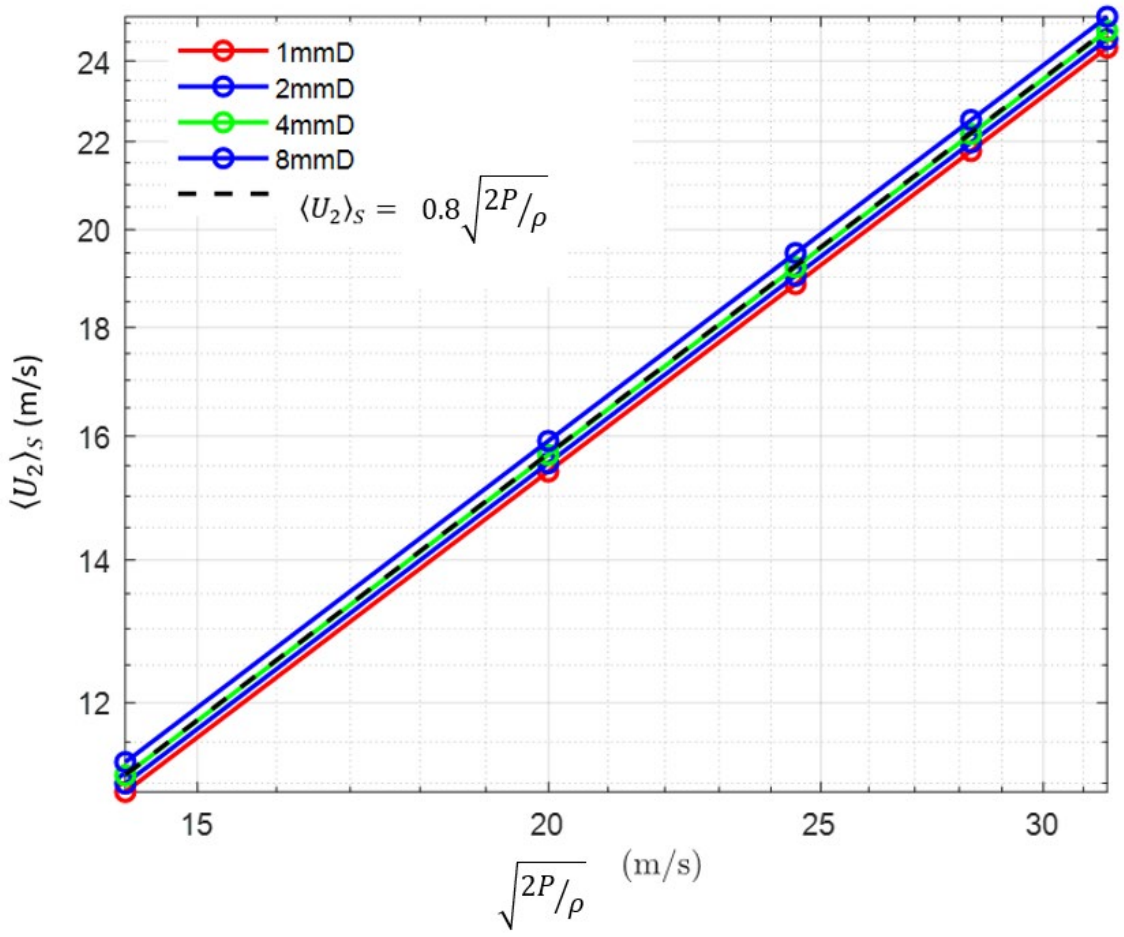

Figure 43 - Volumetric leak flow rate and pressure relationship

Radial component of the mean velocity $\overline{\langle U_2 \rangle_S}$ was numerically integrated over the leak orifice and normalised by the leak area such that Torricelli expression (equation 52) becomes:

$$\langle U_2 \rangle_S = C_d \sqrt{2P/\rho} \tag{53}$$

Note that in both sides of equation (53), leak area A has been cancelled out. A clear linear relationship therefore existed between $\langle U_2 \rangle_S$ and $\sqrt{2P/\rho}$ showing good collapse of the data and this agreed with Torricelli's equation: $\langle U_2 \rangle_S = C_d\sqrt{2gh} = C_d\sqrt{2P/\rho}$ (Ben-Mansour et al., 2012; A. Cassa et al., 2010; Ferraiuolo et al., 2020; Franchini & Lanza, 2014; M. Jujuly et al., 2016). The gradient in Figure 43 represents the discharge coefficient C_d, given by $C_d \approx 0.8$.

In addition, a universal profile, independent of the sizes of the leaks, can be observed in the plot, suggesting that with this approach, size of the leak might not necessarily be required in estimating discharge coefficient, at least in this study and subject to experimental validation. The leak area expansion in Eqn. (54) is usually caused by pressure increase, which results in the expansion of the size of the original leak area A_0.

4.3.4 Leak shape studies

In this work, four different leak shapes were modelled, namely: square-shaped, transverse slit, longitudinal slit, and circular leaks (Figure 44). Only the fluid domain was modelled, meshed, numerically simulated and analysed for leak noise prediction. Wall thickness was not considered in this study due to the huge mesh density involved, which was too computationally expensive for this study. However, mesh invariance for different leak shapes have been carried out and discussed in grid convergence study in section (3.2.6). Y plus at the leak in this study have been kept below 5 so as to be able resolve all fluid layers, from the viscous sublayer region, where velocity gradient was highest, to the leak centre.

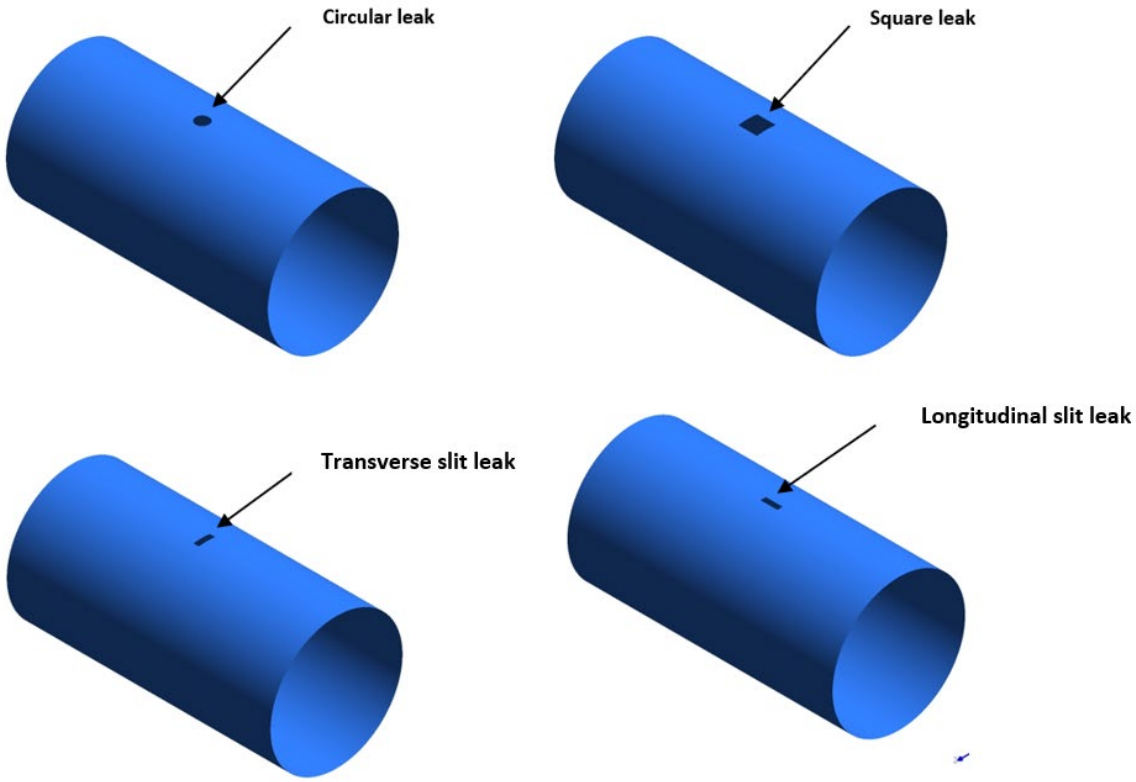

Figure 44 – Modelled pipes with different leak shapes

Numerical simulation of fluid-flow in the pipes and leaks showed that for all the four leak shapes, the generation of turbulent kinetic energy was maximum in the shear layer region, very close to the edges of the leaks, where velocity gradient was largest, and then decayed towards the centre of the leak (Figure 45). This was in perfect agreement with what is already known in the literature (Andersson, 2011; Harsha & Lee, 1970).

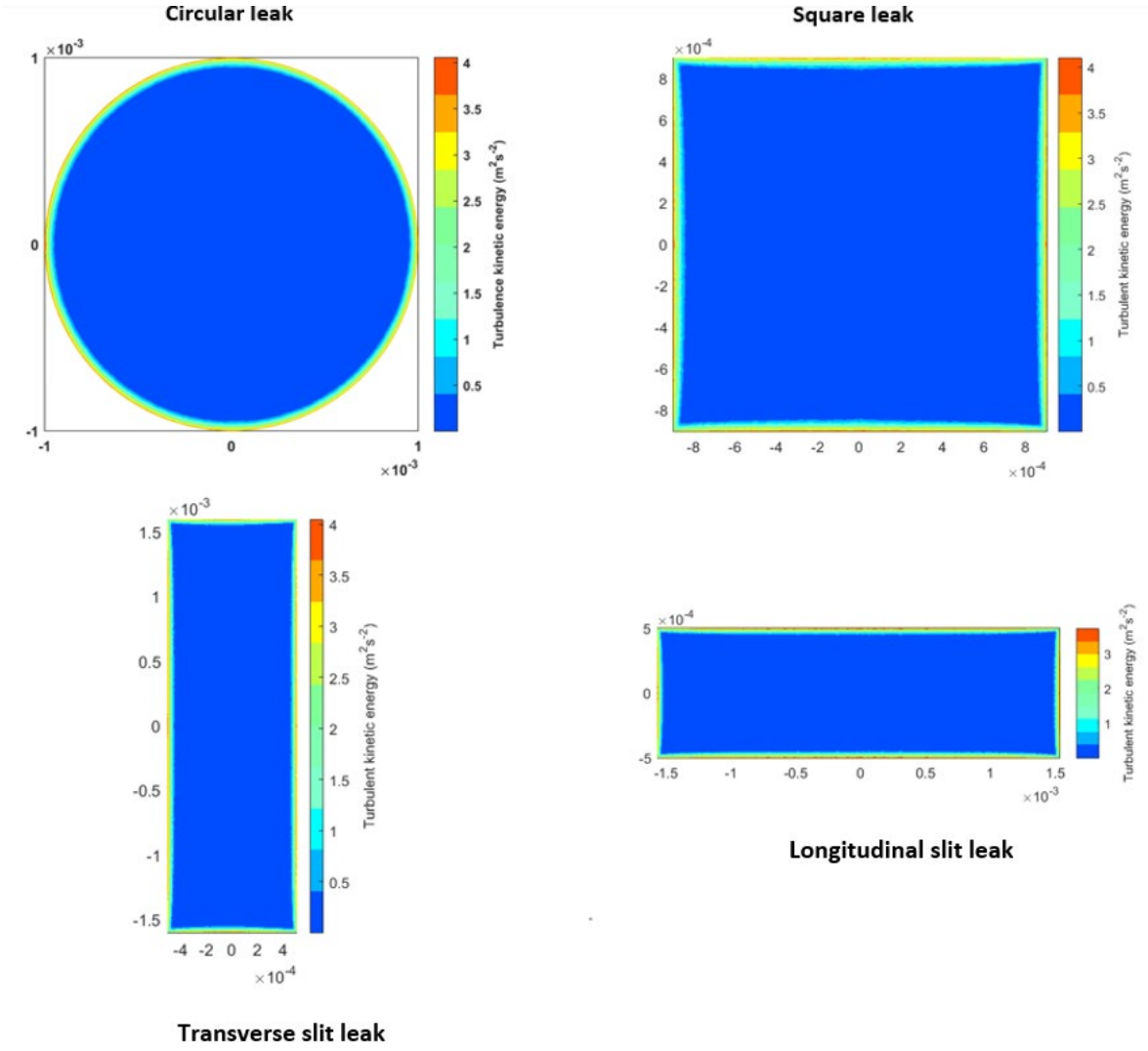

Figure 45 – Turbulent kinetic energy contours for different leak shapes

4.4 A comprehensive qualitative and quantitative analyses of mean flow velocity behaviour at the orifice of circular leak

Prior to investigating the characteristics of the turbulence generated at the leak orifice, which is suggested to be the dominant source of leak noise, it is important to first discuss the behaviour of mean flow velocity. As water exits the leak at a high velocity, due to pressure differential at the

orifice, the interaction between the mean flow velocity at the orifice, velocity gradient in the shear layer, shear stress and the wall bounding the leak (edge) are responsible for turbulence generation (Andersson, 2011; Harsha & Lee, 1970). Mean flow velocity therefore plays an important role in turbulence generation. The velocity vector of the flow as it approached the leak orifice was shown in (Figure 46), where water was flowing from the left of the pipe at mean flow speed and as it approaches the leak, flow accelerated towards the leak, resulting in turbulence generation at the leak, due to increased velocity and reduced pressure.

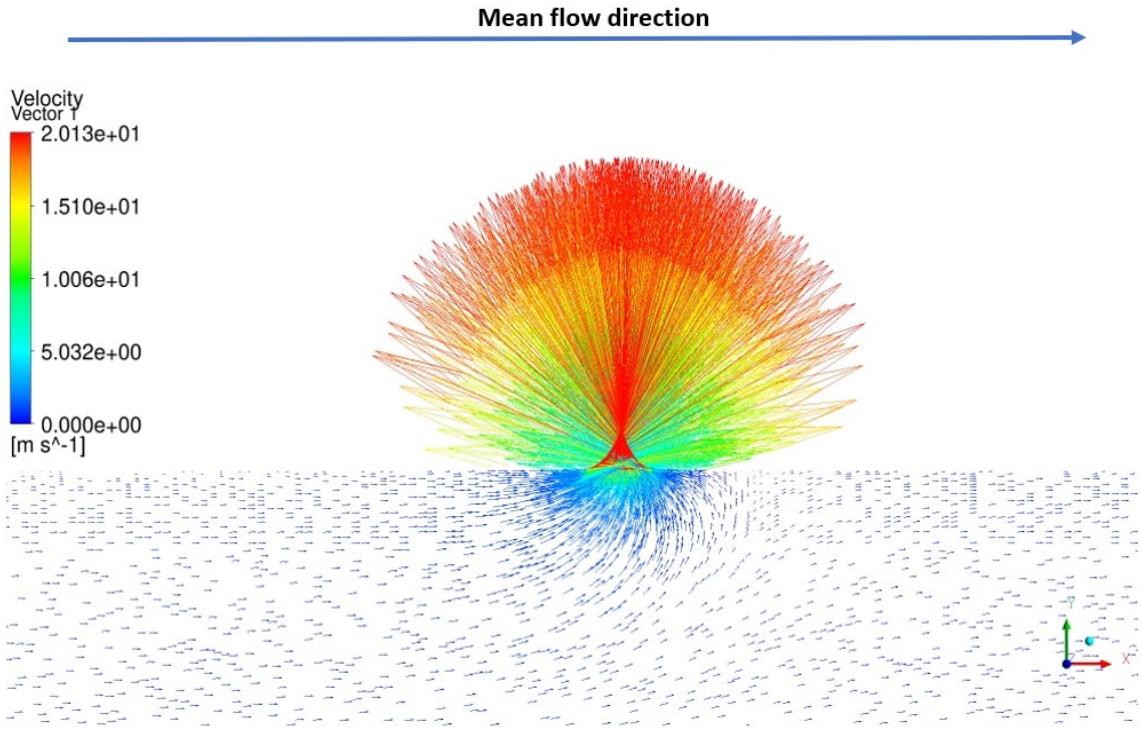

Figure 46 - Velocity vector of fluid along the pipe and in the leak orifice for a leak radius of 2 mm driven by pressure difference of 2bar.

4.4.1 Total mean flow velocity behaviour at the leak holes of two pipe sizes

The mean flow velocity of fluid in the 0.025 m and 0.05m diameter pipes increased gradually from 0.6 m/s in the pipe (Figure 22, Figure 46 & Figure 47) to 20 m/s as the fluid approached a leak opening with much smaller diameter and this behaviour followed Bernoulli's principle which stated that the speed of fluid increases as its pressure drops (Ben-Mansour et al., 2012; A. Papastefanou, 2011).

In the numerically simulated leaks, the mean flow velocity of fluid exiting the hole is turbulent (A. S. Papastefanou et al., 2012; Thompson, Chapman, Howison, & Ockendon, 2001b; Yang, Wen, & Li, 2008) and follows Bernoulli expression in equation (55):

$$\overline{U}_{leak} = \sqrt{\frac{2P}{\rho}} \tag{55}$$

where $\overline{U}_{leak}$ is the mean flow velocity at the leak, P is pressure drop and ρ is the fluid density. Using equation (55), in 0.025 m and 0.05 m diameter pipes, total mean flow velocity at the exit of 2 mm diameter leaks, with pressure drop of 2 Bar, was 20 m/s, for both pipes (Figure 46 & Figure 47).

Numerically simulated total mean flow velocity, $\overline{U}(r, \theta)$, was presented in (Figure 47). Due to no slip boundary condition, the velocity at the edge of the leak was zero and this increased towards the centre as the fluid became less viscous.

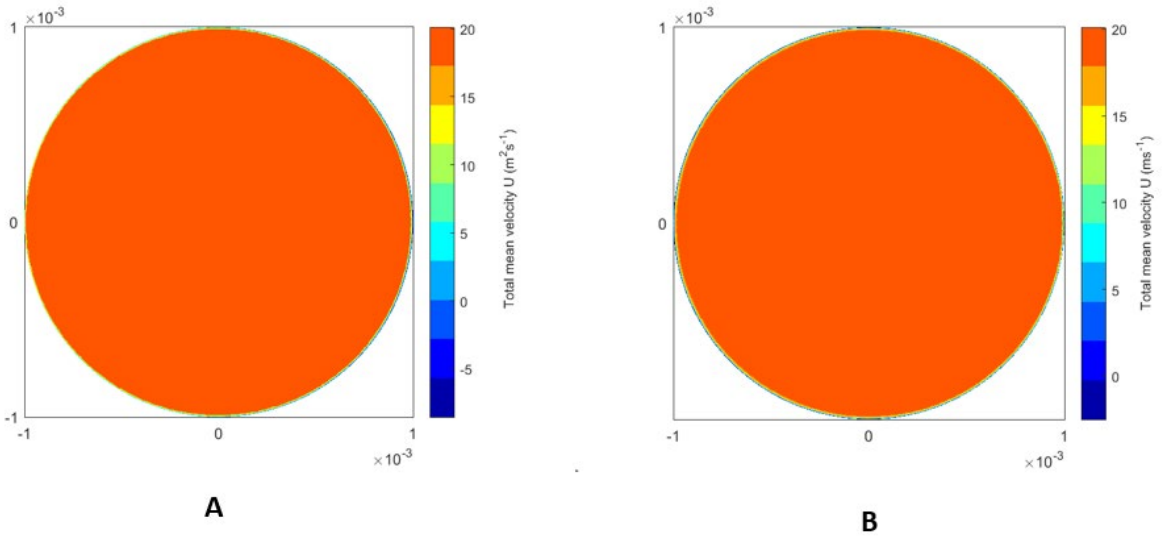

Figure 47 - Total mean velocity at the exit of 2 mm diameter leak for 25 mm (A) and 50 mm (B) diameter pipes

As discussed in the previous chapter, Figure 47 showed that total mean velocity at the leak holes of 0.025 m and 0.05 m diameter pipes were similar, regardless of their pipe sizes. Consequently, pipe of 0.05 m in diameter was chosen as the representative pipe, of which leaks were comprehensively studied.

4.4.2 Distinct behaviours of the components of total mean flow velocity at the leak

The total mean velocity at the leak is comprised of the sum of the radial, circumferential and axial mean velocity components, as shown in equation (56):

$$\overline{U}_{Total} = \sqrt{\overline{U}_r{}^2 + \overline{U}_\theta{}^2 + \overline{U}_x{}^2} \tag{56}$$

where $\overline{U}_r$, $\overline{U}_\theta$, and $\overline{U}_x$ are the radial, circumferential and axial components respectively.

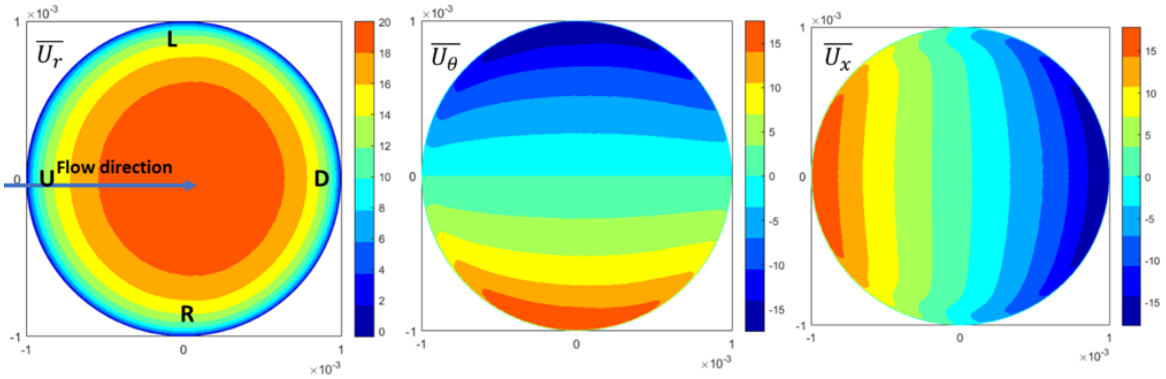

A. Distribution of radial velocity components over the leak area (a=2mm, P=2bar).

B. Distribution of circumferentia velocity components over the leak area (a=2mm, P=2bar).

C. Distribution of axial components over the leak area (a=2mm, P=2bar).

Figure 48 – Total mean flow velocity components.

It was demonstrated in Figure 48 that the flow leaving the leak orifice is highly directional. However, the total mean flow exiting the leak orifice is relatively uniform (Figure 47). This study thus explored the behaviour in detail. Flow velocity distribution at the leak is split into 3 parts:

i. at the leak centre, (Figure 48 A),
ii. right to left of the leak (Figure 48 B),
iii. Flow velocity distribution from upstream to downstream of the leak (Figure 48 C).

In general, flow at the leak centre displayed the highest velocity magnitude while flow in the two other parts of the leak displayed equal velocity but in opposite directions.

As shown in Figure 48 A, B and C, the distribution of the individual mean flow velocity components over the leak orifice for a case of the 2mm diameter leak at 2 Bar pressure, whose total mean velocity was observed in (Figure 47) was relatively uniform. The following conclusions were therefore drawn from the behaviour of total mean velocity components:

i. Each of the three velocity components showed a strong variation across the leak area, unlike the total velocity plotted in (Figure 47).
ii. The radial (leak centre) component of flow variation in (Figure 48A) showed a clear downstream shift, due to convection effects. This implies that, as flow in the pipe moves downstream, flow at the leak is also tilted towards the downstream direction.
iii. Figure 48B showed evidence of symmetry, suggesting that the flow leaving on opposite sides (right to left) of the leak are equal in magnitude but in opposite directions.
iv. The variation in distribution of axial velocity component (upstream to downstream) plotted in (Figure 48C) can be observed to be identical to that of the circumferential velocity component (right to left) when rotated by 90^0.

4.4.3 The effects of leak size and pressure on total leak mean flow velocity

Area-averaged total mean velocity for all leaks were plotted against their leak radii and it was found that regardless of leak size, total leak mean velocity is largely influenced by pressure (Figure 49 & Figure 50). This suggests that given the same pressure, small and large leaks will produce the same leak velocity as leak velocity is driven mainly by pressure. However, leak flow rate is driven by both leak size and pressure (Figure 43) hence the significance of pressure in leakage management. The arrow in Figure 49 indicated pressure increase from 1Bar to 5Bar.

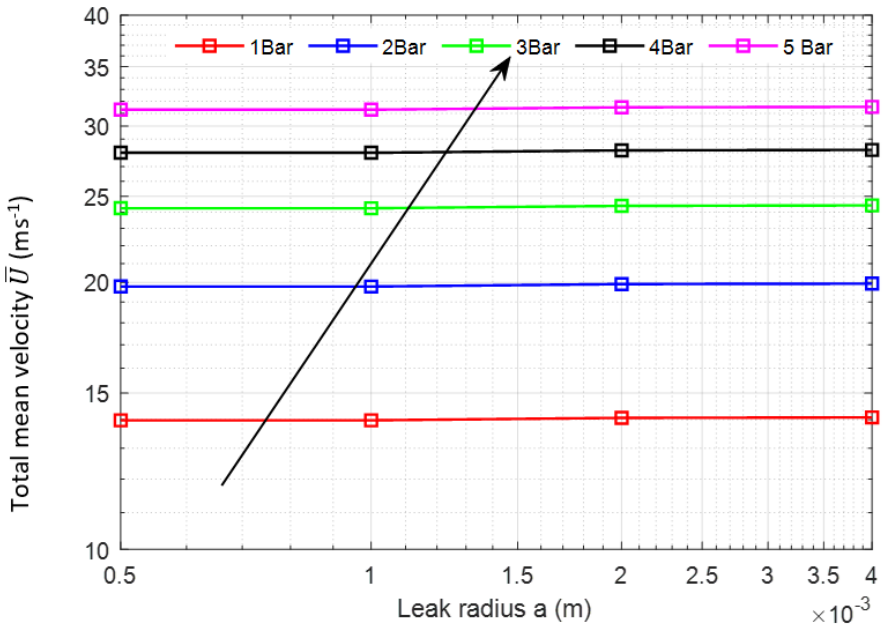

Figure 49 – The effect of pressure on total mean flow velocity at the leak.

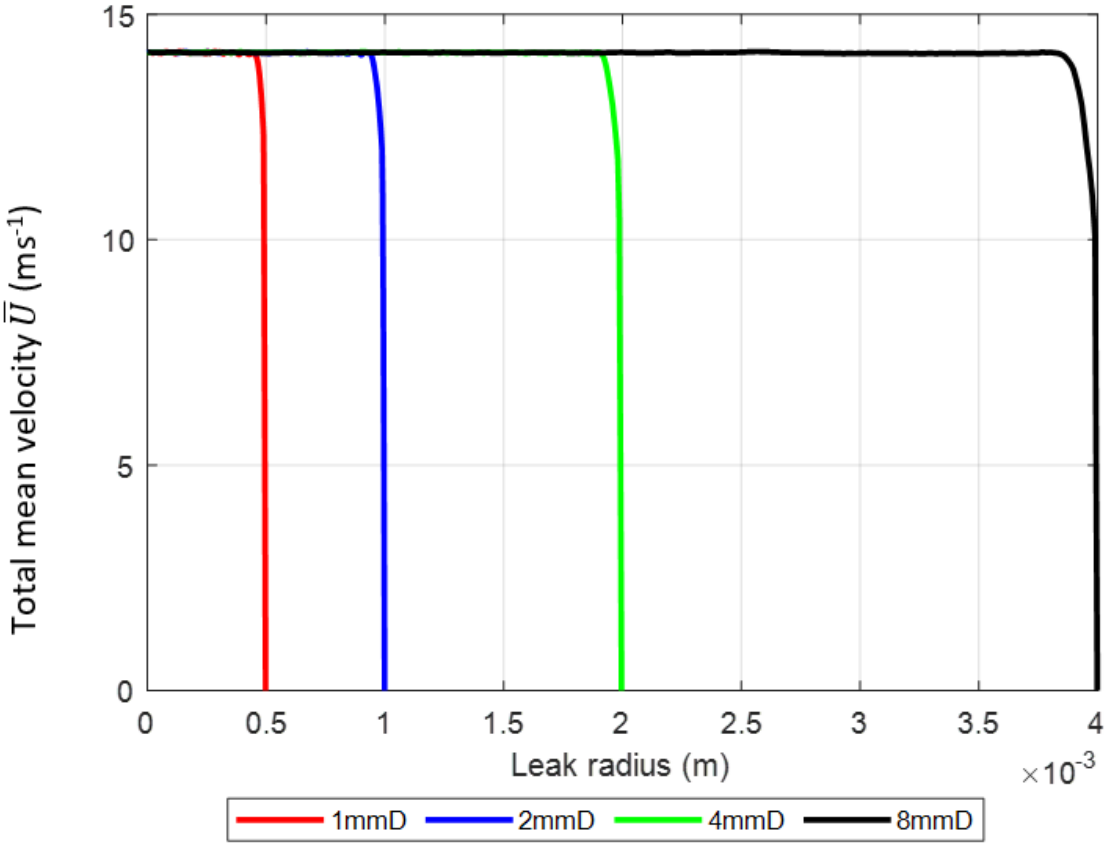

Figure 50 - The effect of leak size on total mean flow velocity at the leak.

Numerical simulation results showed that power law relationship existed between total leak mean velocity and exit pressure (Figure 51) where mean velocity varied as square root of pressure and this relationship agreed perfectly with the analytical expression in equation (55).

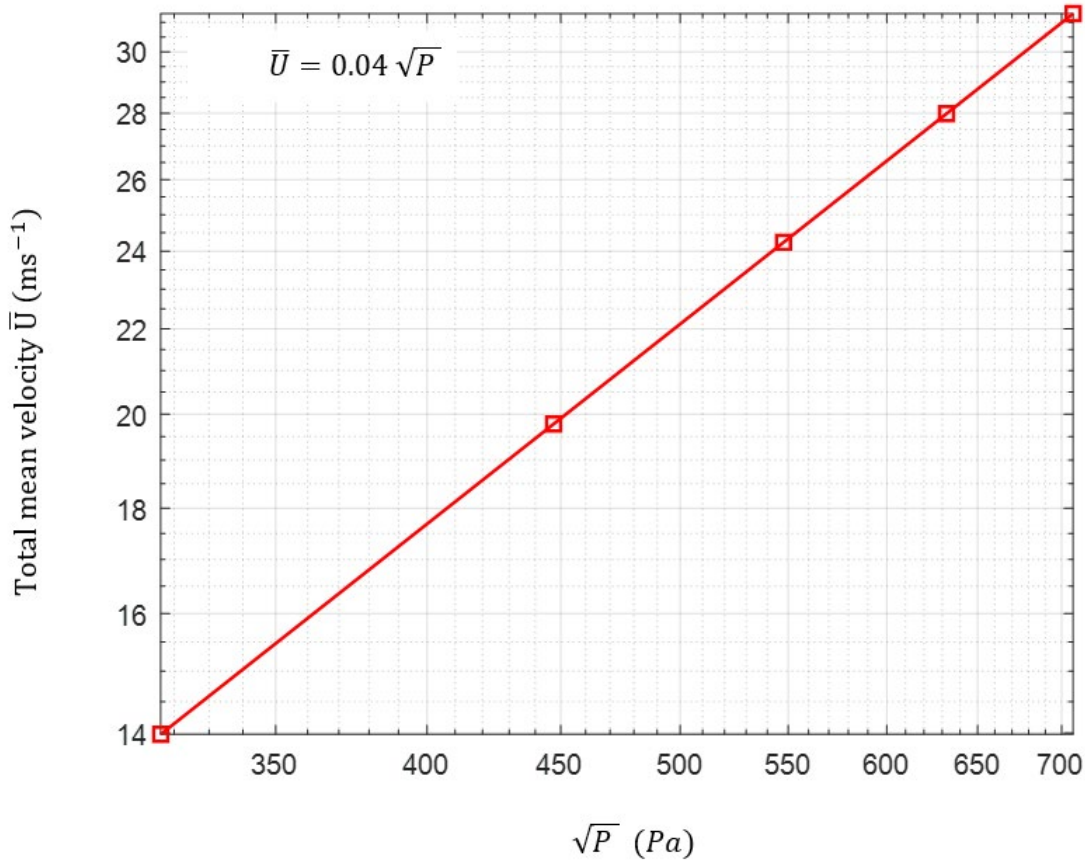

Figure 51 – Total mean flow velocity and pressure relationship for 2 mm diameter leaks

Evidence of universal profile of total mean leak flow velocity, independent of pipe size (Figure 47), pressure and leak size, was observed when the radial profile of total mean velocity, normalised by the circumferential variation, was plotted against normalised radial distance, from the edge of the leak (Figure 52 A). This suggested that regardless of pipe size, pressure and leak size, the shape and behaviour of mean flow velocity at the leak remains the same. When radial profile of total mean flow velocity was un-normalised and plotted against normalised radial distance, universal profiles existed for all leaks, as long as pressure is kept constant (Figure 52 B). The applicability of this finding in real leak scenario is that, in the event of suspected leak, pressure should be kept low and constant such that, regardless of the leak size, total mean leak flow velocity would remain the same and water loss could be minimised. This is another interpretation of pressure management in leakage control by using different pressure reduction schemes such as the

installation of pressure reducing valves (PRV), pressure reduction at the outlet of a pump and establishment of DMA in a low pressure area. In the event of a leak, increasing pressure would increase leak flow rate, it could result in pipe burst and then expand leak area of existing leak or cause more leaks and the associated increase in leak flow speed could also result in water quality issue.

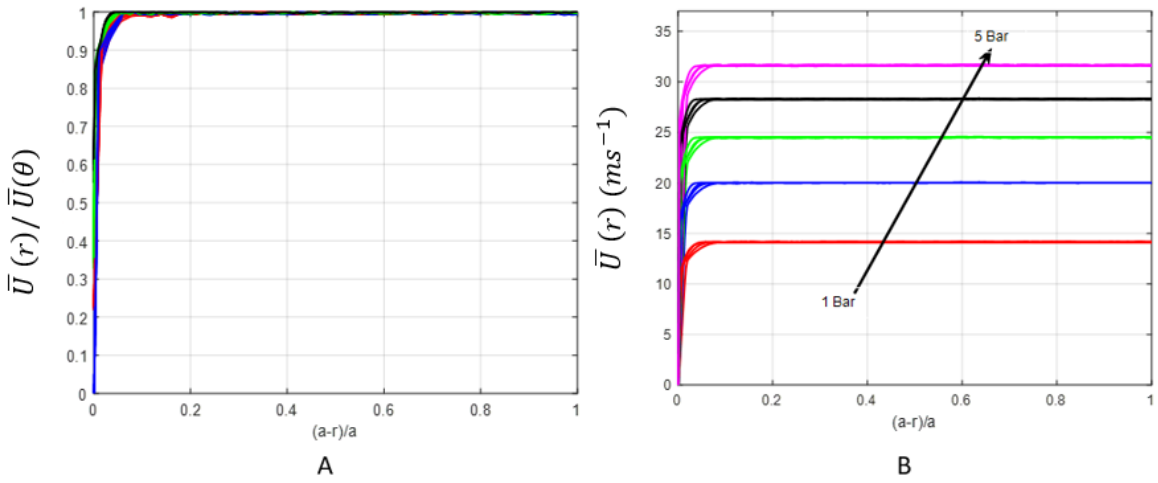

Figure 52 – Circumferentially averaged (A) and non-averaged (B) radial variations of total mean velocity of all leaks at all pressures

4.4.4 Relationship between turbulent kinetic energy, area-averaged rms velocity, area-averaged mean velocity and turbulence intensity

As mentioned in section (3.1), SST k-ω model was used in this study and one of the key assumptions in the model was the adoption of isotropic turbulence, for the purpose of simplifying the modelling of turbulent flows (F. Menter et al., 2021; F. R. Menter, 1994). Isotropic turbulence refers to a turbulence state where the statistical properties of turbulence are independent of the direction. In other words, it assumes that the turbulence is statistically the same in all directions. In the numerical simulations, turbulent kinetic energy is obtained from turbulent velocity fluctuations u' (Andersson, 2011; ANSYS, 2021), using the expression:

$$k = \frac{1}{2}\left(\left(\overline{u'}_1\right)^2 + \left(\overline{u'}_2\right)^2 + \left(\overline{u'}_3\right)^2\right) \tag{57}$$

where $(\overline{u'}_1)^2$, $(\overline{u'}_2)^2$ and $(\overline{u'}_3)^2$ are the mean of the squares of turbulent velocity (mean square velocity) fluctuations in all of the three directions. Assuming isotropic turbulence, where: $(\overline{u'}_1)^2 = (\overline{u'}_2)^2 = (\overline{u'}_3)^2 = (\overline{u'})^2$, equation (57) becomes:

$$\sqrt{(\overline{u'})^2} = \sqrt{\frac{2}{3}k} \tag{58}$$

where $\sqrt{(\overline{u'})^2}$ is the root-mean-square (RMS) turbulent velocity fluctuations and *k* is the turbulent kinetic energy.

For all leaks sizes and at all pressures, area-averaged rms velocity fluctuations and leak mean velocity components normal to the leak orifice, were plotted (Figure 53), to investigate the relationship between the fluctuating rms radial velocity and mean radial velocity components at the leak.

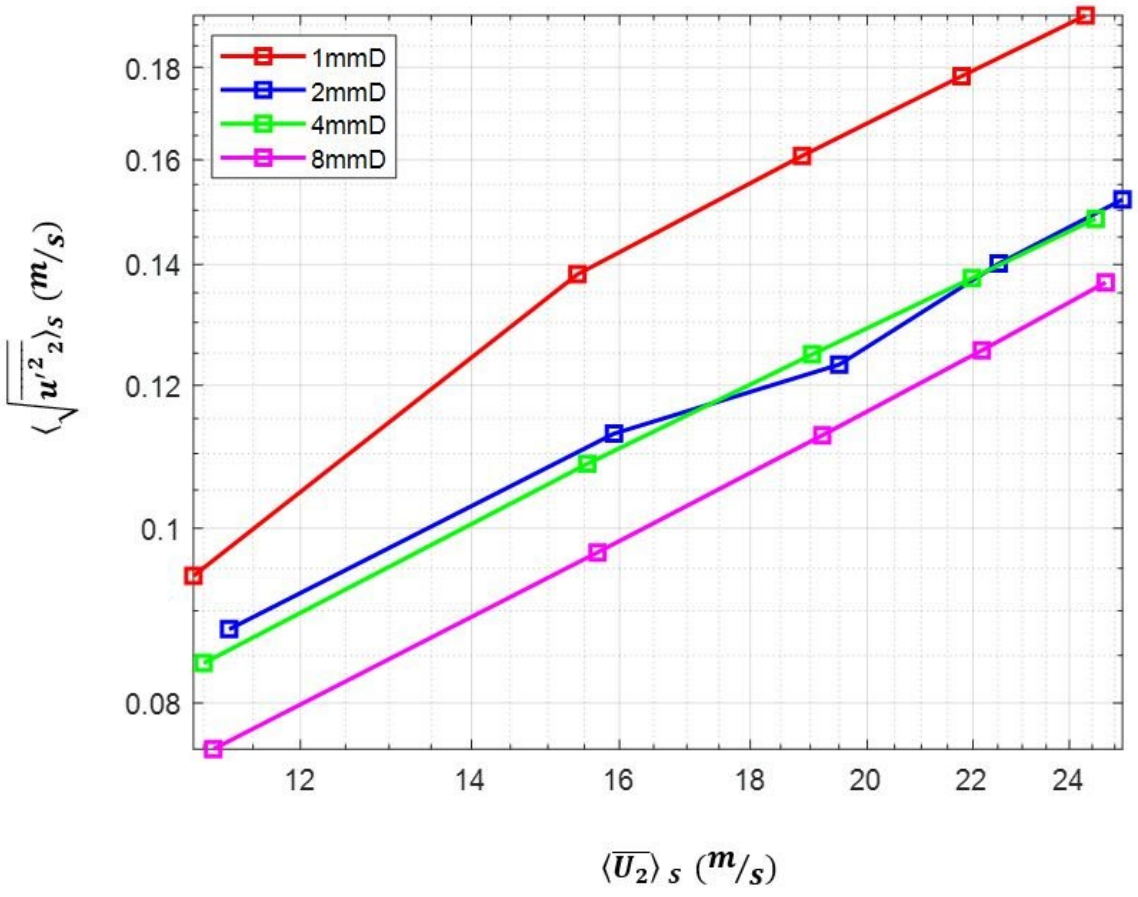

Figure 53 – Relationship between area-averaged mean flow and fluctuating velocity

The relationship between rms fluctuating velocity and mean velocity can be described by the RANS decomposition in Equation 59, which separates the instantaneous velocity into mean and fluctuating components. By decomposing the instantaneous velocity into mean and fluctuating components (Alfonsi, 2009), it becomes possible to study and analyse the statistical properties of the fluctuations, such as their intensity, spatial distribution, and temporal behaviour (Piest, 2018). The knowledge is crucial for turbulence modelling and in predicting the behaviour of turbulent flows in various engineering and scientific applications.

For simplicity, the relationship between $\langle\sqrt{\overline{u^2}}\rangle_S$ and $\langle\overline{U_2}\rangle_S$ (Figure 53) was assumed to be proportional in this study and the ratio of $\frac{\langle\sqrt{\overline{u^2}}\rangle_S}{\langle\overline{U_2}\rangle_S} \approx I$, where I is the turbulence intensity and it is assumed to be 0.007, suggesting an average turbulence Intensity of less than 1 %. This relationship clearly follows the analytical expression of estimating turbulent intensity (Ansys-Fluent-4, 2021; ANSYS, 2021; Xiao et al., 2020). With this relationship, if the mean leak flow speed is known, rms velocity can be estimated and vice-versa.

4.5 A comprehensive qualitative and quantitative analyses of the production and behaviour of turbulent kinetic energy at the leak orifice

This section investigated the production, behaviour, distribution, and variation of turbulent kinetic energy with other important flow parameters at the orifice of a leaked water pipe. As discussed in section (4.4), production of turbulent kinetic energy was as a result of the interaction between the mean flow velocity, velocity gradient in the shear layer, shear stress and the wall bounding the leak (Andersson, 2011; Harsha & Lee, 1970). Turbulent kinetic energy is understood to be produced in the near-wall region (y+ < 20) through different scales of dynamic events of near wall eddies, which are responsible for momentum transfer within the region (Absi, 2021). Consequently, to capture the near wall turbulence, mesh resolution in the near wall region is expected to be suitably fine. It can be observed from the contour and profile plots in (Figure 54) that peak values of turbulent were concentrated in the near wall region, around the edge, where mean velocity gradient was highest, and then decayed towards the centre of the leak.

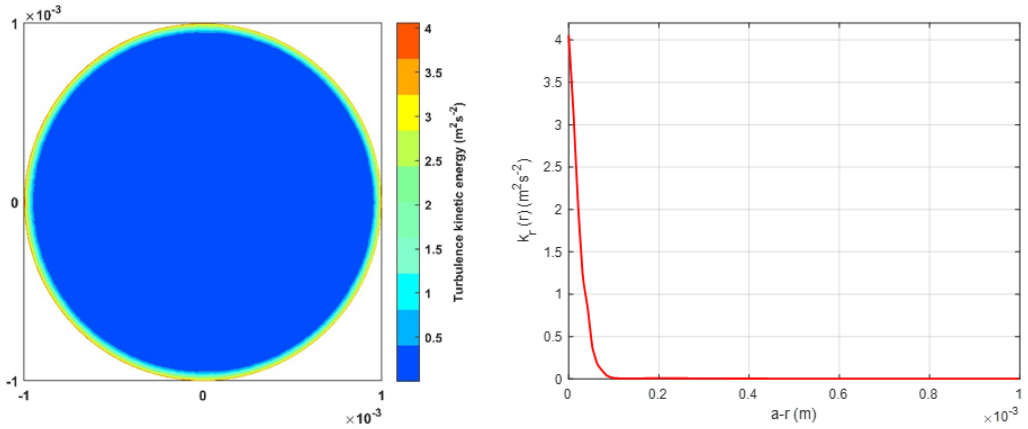

A. Turbulent kinetic energy contour for 2 mm diameter circular leak at 2 Bar.

B. Radial variation of turbulent kinetic energy for 2 mm diameter circular leak at 2 Bar.

Figure 54 – contour plot and radial variation profile for 2 mm diameter leak at 2 Bar.

4.5.1 Variation of turbulent kinetic energy distribution with leak size and pressure

The sensitivity of the turbulent kinetic energy, *k (r, Θ)*, to leak radius and pressure is investigated and much attention is focussed on the radial variation of turbulence kinetic energy, *k(r)*, since turbulent kinetic energy does not change much in the theta (Θ) direction. In Figure 55, a is leak size, *Θ* is circumferential distance and r is the radial distance of the leak.

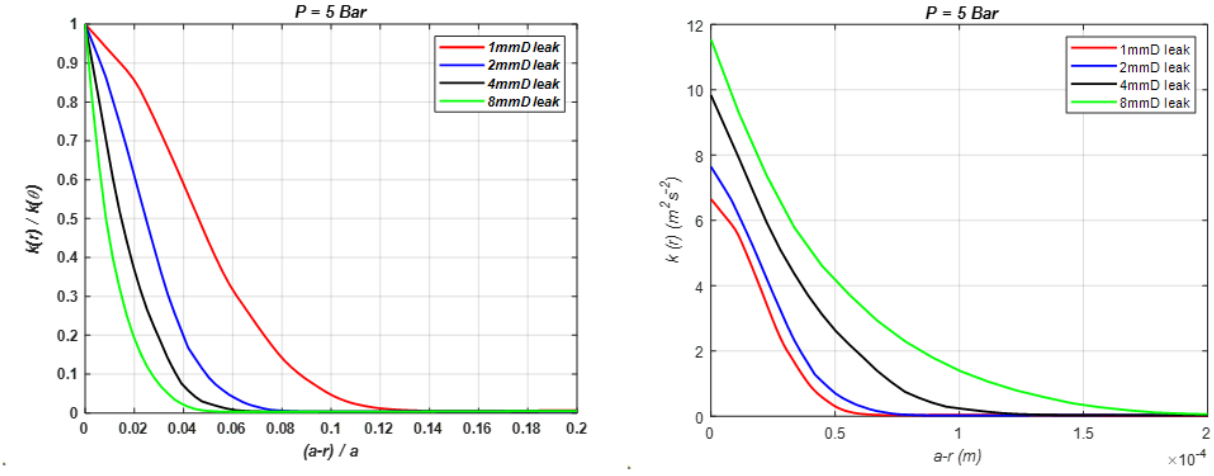

A B

Figure 55 - Radial variations of turbulent kinetic energy at 5 Bar

As previously discussed, for all leak sizes, all of the turbulent kinetic energy were concentrated around the edges (*Θ*) and then decayed towards the leak centre (Figure 54). Evidence of global behaviour of turbulent kinetic energy with leak size and pressure was investigated (Figure 55). It

was found that, for circumferentially averaged turbulent kinetic energy, the larger the leak, the smaller the shear layer is, relative to its radius. However, when radial variation of turbulent kinetic energy was not averaged, shear layer increases just as leak size increases. In both cases, turbulent kinetic energy is therefore sensitive to, and increases with, leak size and pressure.

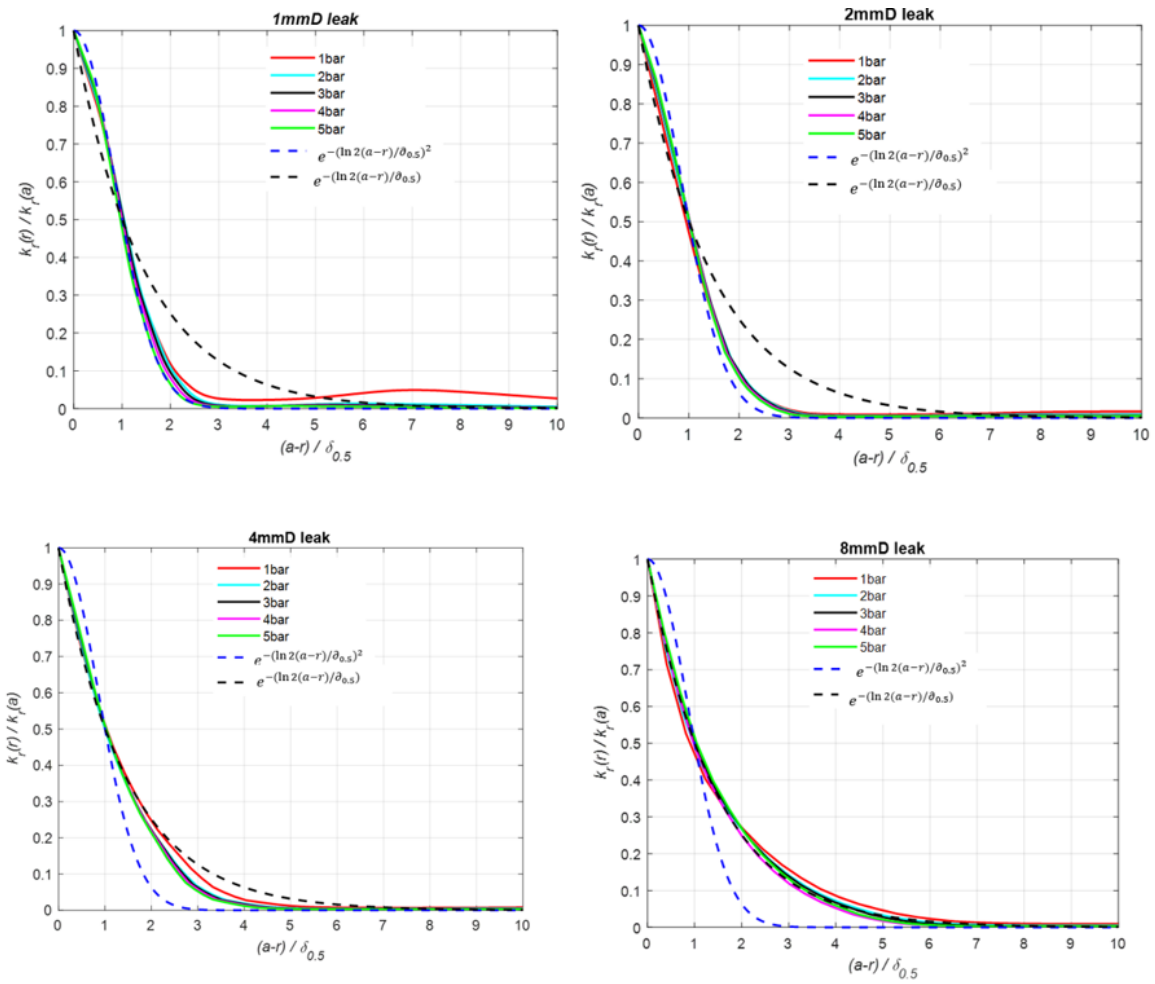

Figure 56 – Radial variations of turbulent kinetic energy in 1 mm to 8mm diameter leaks

To further investigate evidence of uniformity in turbulent kinetic energy behaviour, radial variations of normalised turbulent kinetic energy, *k(r) / k(a)*, was plotted against normalised distance from the wall, $(a-r)/\delta_{0.5}$, for 1mm, 2mm, 4mm and 8mm diameter leaks, driven by pressure differentials of 1 Bar to 5 Bar, with exponential functions and Gaussian functions: $e^{-\ln 2(a-r)/\delta_{0.5}}$, $e^{-(\ln 2(a-r)/\delta_{0.5})\wedge 2}$ respectively; where $\delta_{0.5}$ is shear layer thickness (Figure 56). As shear layer is a thin layer where velocity gradient is highest, in this study, shear layer thickness was estimated as the distance from the leak edge to the point where turbulent kinetic energy has decayed to half of its maximum value:

$$\frac{k(r)(a-\delta_{0.5})}{k(a)} = 0.5 \tag{60}$$

It was found that when the leak size is fixed, evidence of universal behaviour existed for the smallest leaks 1mm and 2mm diameter leaks, which aligns with Gaussian function, $e^{-(\ln 2(a-r)/\delta_{0.5})\text{^}2}$ (Figure 56) and this suggests that, given the same leak size and when turbulent kinetic energy is normalised by its edge turbulence, the generation of turbulent kinetic energy is insensitive to, and independent of pressure. However, as the leaks got bigger, the behaviour of the numerical data clearly changed gradually from Gaussian to exponential, indicating the existence of a universal profile for large leaks of 4mm and 8mm diameter, which follows an exponential curve: $e^{-\ln 2(a-r)/\delta_{0.5}}$ (Figure 56). Whilst the degree of collapse of the data for the different pressures remain the same for the smallest leak ($e^{-(\ln 2(a-r)/\delta_{0.5})\text{^}2}$), there is poor agreement with the exponential curve distribution ($e^{-\ln 2(a-r)/\delta_{0.5}}$) of the largest leaks. Strong universal behaviour for the turbulent kinetic energy distribution therefore appears to exist for large leaks but begins to break for very small leaks. The reason for this behaviour could not be evidenced in this study and is thus recommended for future work.

4.5.2 Variation of edge turbulence with leak size and pressure

In the previous sub-section, it was demonstrated that for the same leak size, universal behaviour of turbulent kinetic energy existed and is independent of pressure. For larger leaks, radial variation in turbulent kinetic energy closely follows an exponential function that breaks down as leaks get smaller, where smaller leaks agree with Gaussian function. Therefore, turbulent kinetic energy at any radial position *r* from the centre of the leak may be expressed in the form:

$$k_r(r) = k(a)e^{-(\ln 2(a-r)/\delta_{0.5}))^n} \tag{61}$$

where $\begin{matrix} n \to 2, & a \to 0 \\ n \to 1, & a \to \infty \end{matrix}$

Equation (61) showed that the radial variation of turbulent kinetic energy is determined only by its value at the leak edge $k(a)$ and the shear layer thickness $\delta_{0.5}$. In this section variations of edge turbulence $k(a)$ and shear layer thickness $\delta_{0.5}$ with leak size *a* and pressure *P* were explored.

Edge turbulence for all leaks were plotted against leak radii and pressures and two scenarios were investigated. In the first scenario, edge turbulence was found to increases with leak radii to the power of 0.3 ($a^{0.3}$) (Figure 57). This suggests that turbulent kinetic energy is a weak function of leak size as it is less sensitive to leak size and that the size of a leak might not be responsible for the maximum generation of turbulence at the orifice.

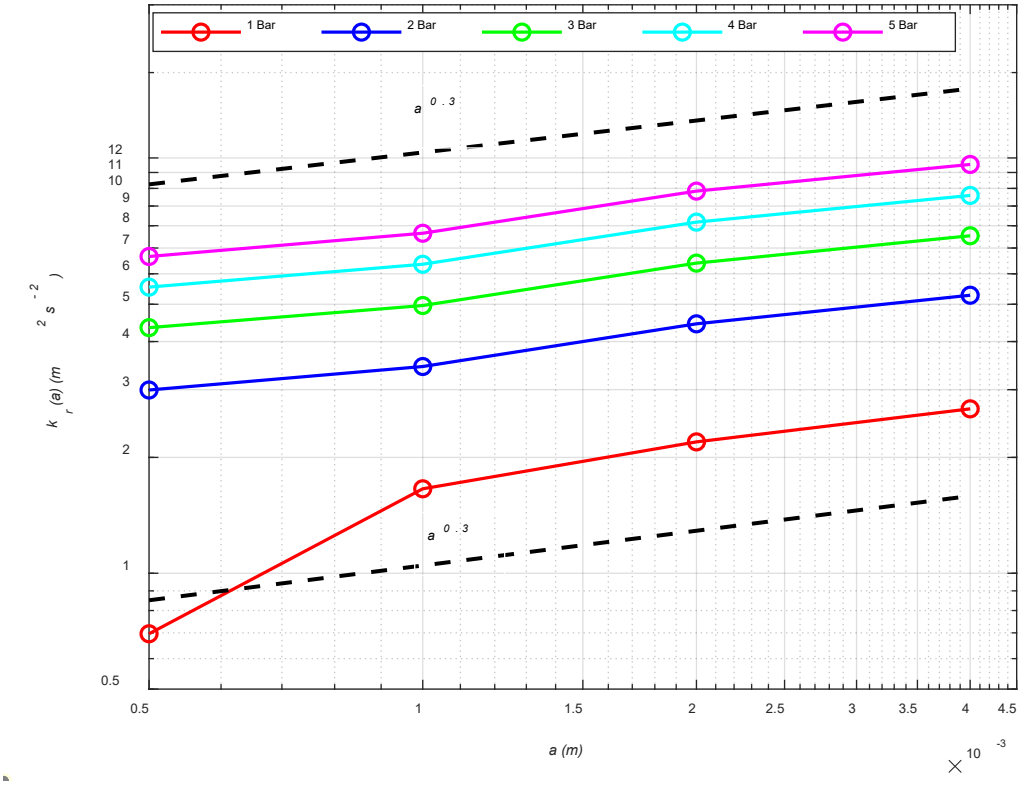

Figure 57 – Effects of leak size on edge turbulence

In the second scenario, edge turbulence was found to increase as pressure increases to the power of 0.9 (Figure 58). This gave a strong indication that edge turbulence might be more sensitive to pressure than the size of a leak. As the total speed of water out of a leak is proportional to the square root of pressure $\left(U = \sqrt{P}\right)$ (equation 55) and $k_r(a) \approx P$ (Figure 58), squaring both sides of equation (55) yields $U^2 = P$ and this indicated that $k_r(a) \approx U^2$. The edge turbulence and leak mean velocity scaling relationship however indicated that maximum turbulent kinetic energy, concentrated at the edge of a leak is strongly driven and greatly influenced by the speed of water out of the leak. As discussed in section (4.4), generation mechanism involved in turbulence

production is due to the interaction of mean flow velocity, velocity gradient and shear stress. The edge turbulence scaling with mean flow velocity further confirms the crucial role played by mean flow velocity in turbulence generation.

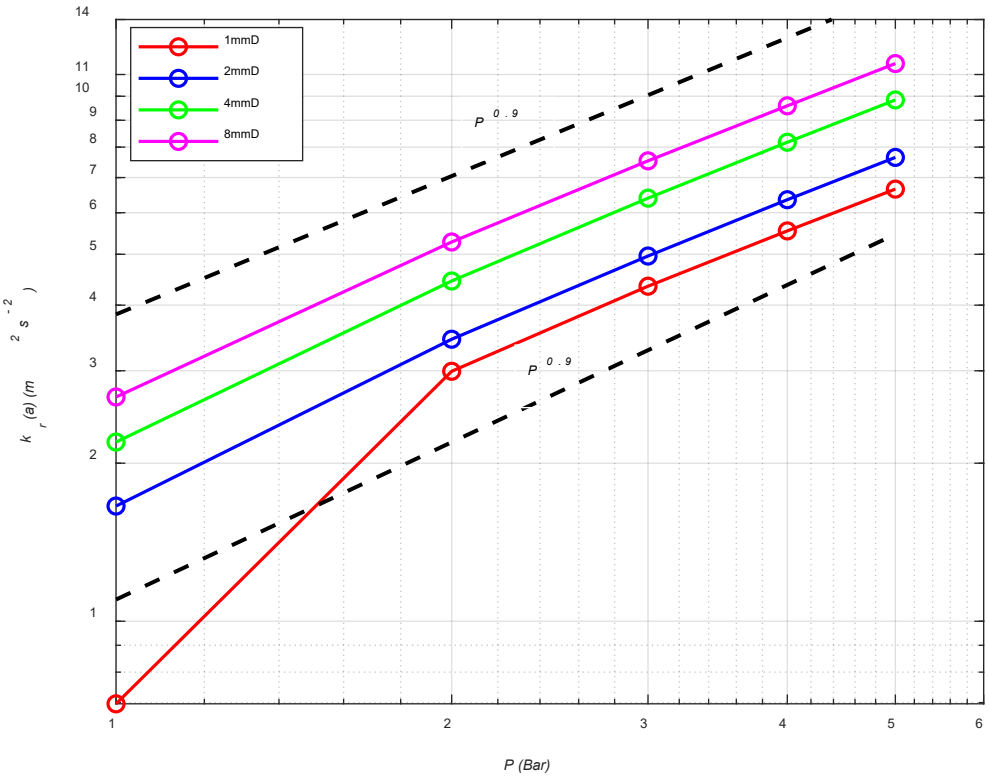

Figure 58 – Effects of pressure on edge turbulence

4.5.3 Variation of shear layer thickness with leak size and pressure

As previously discussed, most of the generated turbulent kinetic energy is concentrated in the shear layer, around the edge of the leak, and shear layer has been defined as the distance from the leak edge to the point where turbulent kinetic energy is reduced to half its original value (equation 60). The shear layer thickness $\delta_{0.5}$ was obtained from the value that provides best fit of $e^{-(\ln 2(a-r)/\delta_{0.5}))^n}$ to the computed radial variation of turbulent kinetic energy for leak diameters 1 mm to 8 mm and at line pressures of 1 to 5 Bar. To understand how shear layer thickness would behave when leak size increases, a plot of shear layer thickness against leak radii was produced and presented (Figure 59). It was found that, when pressure is kept constant, shear layer thickness increases as leak sizes increased. In this situation, the viscous effects within the

boundary layer is not disrupted as pressure and velocity are kept constant. On the contrary, when leak size is fixed, shear layer gets thinner as pressure, hence velocity, is increased.

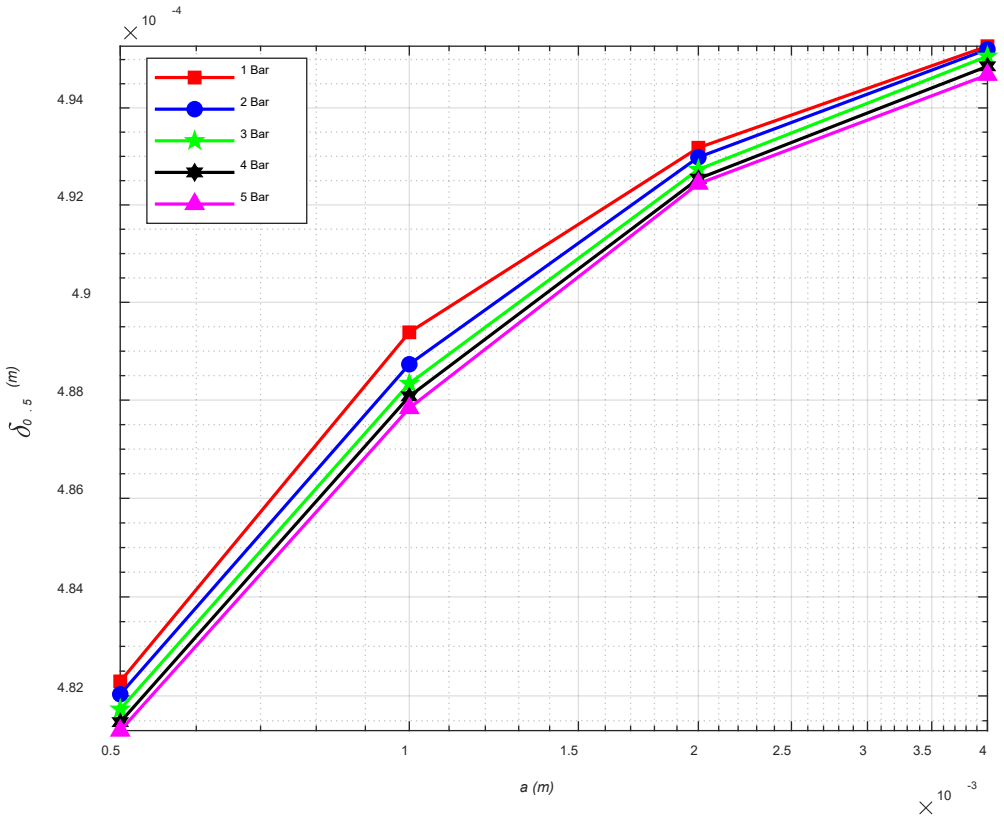

Figure 59 – Effect of leak size on shear layer thickness

Higher flow velocities generally lead to thinner boundary layers (Schlichting, Gersten, Schlichting, & Gersten, 2000). This relationship can be attributed to the impact of velocity on momentum and viscosity. As flow velocity increases, the momentum of the fluid particles becomes more dominant, reducing the influence of viscosity. This results in fluid particles within the boundary layer remaining closely attached to the surface, leading to a compact and thin boundary layer. A study by Schlichting et al. (2000) outlines the fundamental principles of boundary layer behaviour and its dependence on velocity. This dependence on mean flow velocity is a general characteristic of boundary layers, which become thinner with increasing flow speed (Figure 60). As flow speed

continues to be increased, boundary layer will be eventually depleted, leading to flow separation and reversal.

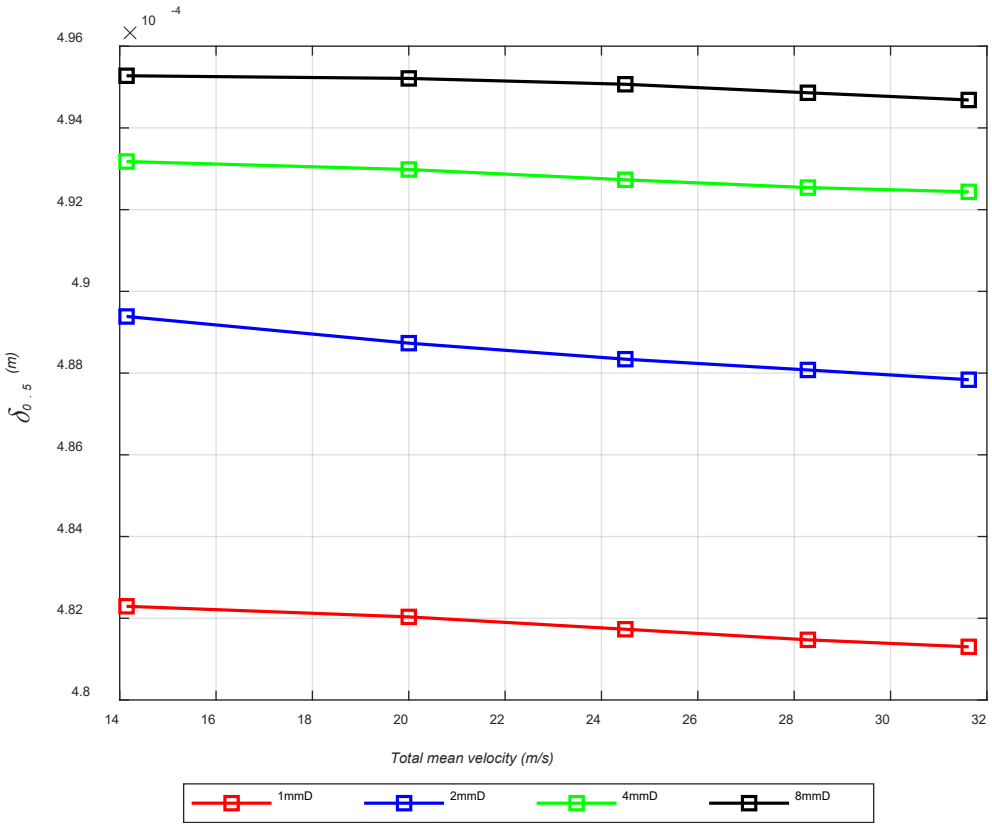

Figure 60 - Effect of leak flow speed on shear layer thickness

In addition, increase in pressure when leak size is fixed, assists in accelerating the flow within the boundary layer, resulting in a reduced thickness (Figure 61).

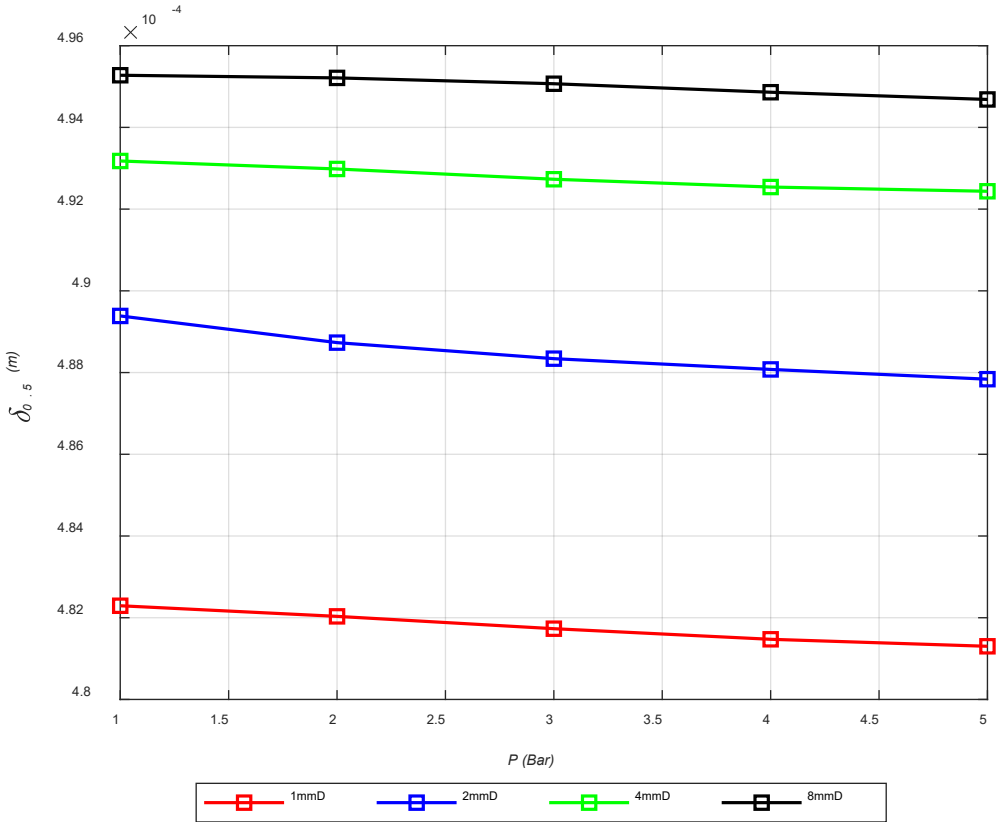

Figure 61 - Effect of pressure on shear layer thickness

4.5.4 Source strength estimation and its relationship with leak flow rate

This section presents an analytical model for source strength estimation. Prior to estimating the source strength at the leak, it would be beneficial to understand the relationship between pressure, mean flow velocity and rms velocity. These relationships were clearly explained in sub-sections (4.3.3) and (4.4.4). Using these relationships, if pressure and mean flow velocity are known, it would be possible to estimate discharge coefficient and if rms turbulent velocity is also known, it would be possible to estimate leak turbulent intensity.

From Figure 53, $\langle\sqrt{\overline{u^2}}\rangle_S$ was obtained as:

$$\langle\sqrt{\overline{u^2}}\rangle_S = I\langle\overline{U_2}\rangle_S = 0.007\langle\overline{U_2}\rangle_S \tag{62}$$

where I is the turbulence intensity: the slope of equation (62) and was already estimated in section (4.4.4) as 0.007.

Similar to the analytical expression in equation (28), source strength was numerically obtained as a product of area-averaged rms turbulence velocity, and leak area:

$$q_{rms} = \pi a^2 \langle \sqrt{\overline{u^2}} \rangle_S \tag{63}$$

where a is the leak radius, πa^2 is the leak area and $\langle \sqrt{\overline{u^2}} \rangle_S$ is the rms turbulence velocity fluctuations at the leak area.

Equation (63) described source strength as a function of rms turbulent velocity fluctuations ($\langle \sqrt{\overline{u^2}} \rangle_S$).

Sensitivity of the source strength to leak size was investigated and it was found that, at constant pressure, source strength *q* scaled approximately as a square of leak radii ($q \approx a^2$).

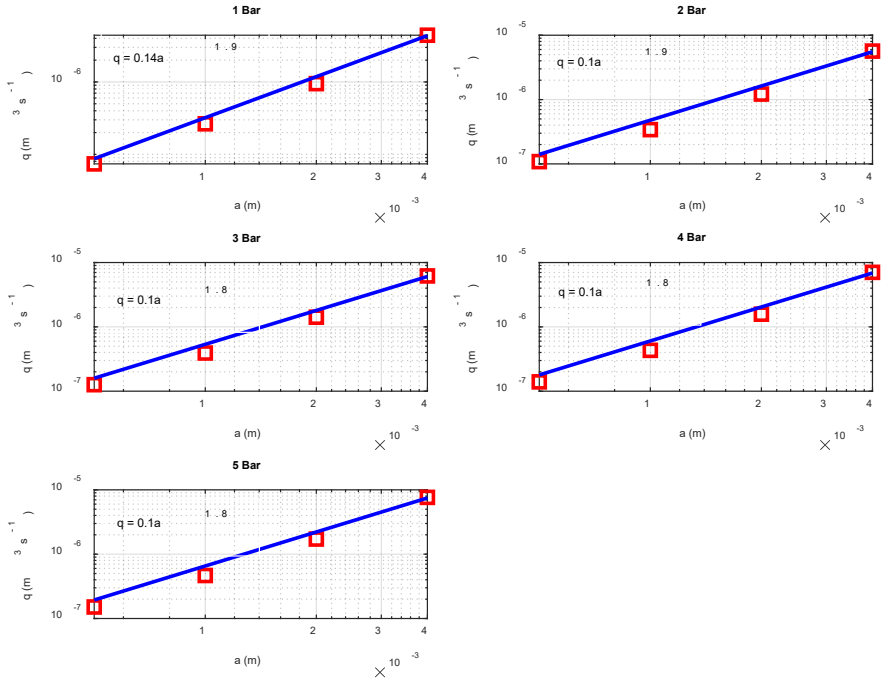

Figure 62 – Variation of source strength with leak size

as shown in (Figure 62). The power law relationship was consistent with the analytical expression in equations (28 & 63) and indicated that if pressure was kept unchanged, strength of noise source at the leak is sensitive to leak radii and increases as leak radii scales to the power of ≈ 2. (it was previously shown in Figure 58 that edge turbulence increases with pressure to the power of

0.9). Whilst surface area plays a crucial role in source strength generation (equations 28 & 63), bigger leaks will produce much stronger noise source than smaller leaks (Xiao et al., 2020).

Using the important analytical relationships between rms velocity, mean velocity, pressure, intensity and discharge coefficient (Figure 43, Figure 53 and equation 53), source strength could be analytically derived as a function of mean flow velocity when rms velocity in equation (62) was substituted in equation (63) as:

$$q_{rms} = 0.007\pi a^2 \langle \overline{U_2} \rangle_S \tag{64}$$

Variation of source strength with mean velocity was investigated with the purpose of understanding the relationship between leak mean velocity and leak noise source strength. In addition, this study was interested in knowing the scale of contributions of the mean flow velocity and pressure to the source strength.

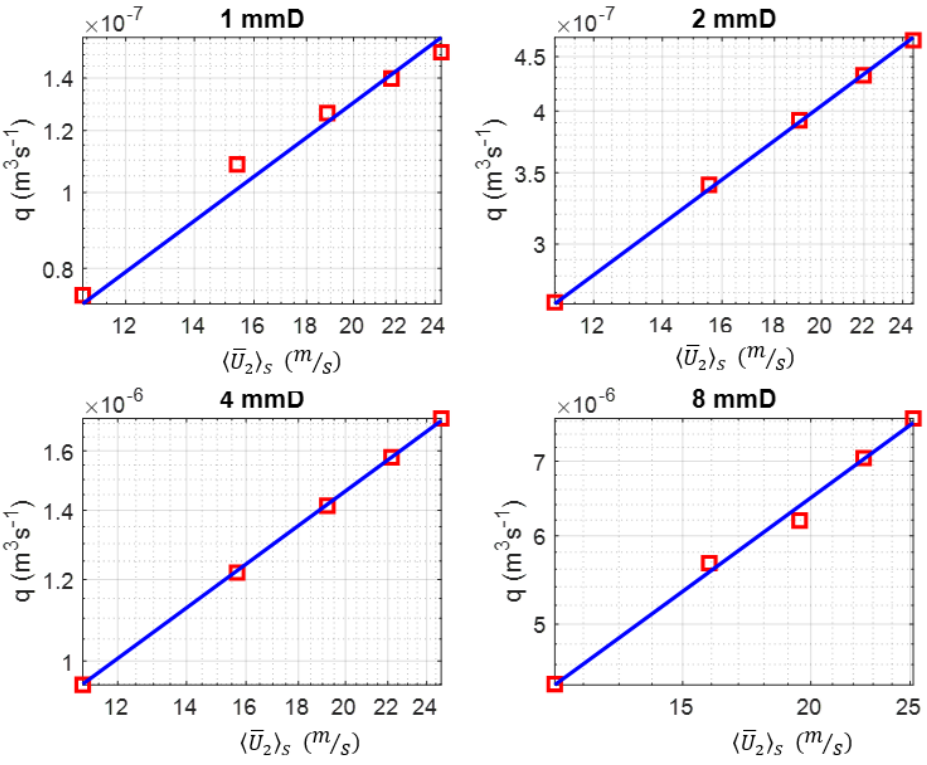

Figure 63 – Variation of source strength and mean velocity at the leak

If leak size was kept constant, source strength at the leak, clearly increases with pressure and mean flow velocity and the relationship between source strength and mean velocity at the leak was found to be approximately linear (q ≈ U), with a weak power of U (Figure 63), and the slopes

in (Figure 63) are also comparable to the analytical expression in equation (64). This suggests that leak noise source strength would proportionately increase if mean flow velocity or volumetric leak flow rate was increased. As the leak mean flow velocity increases, volumetric flow rate increases accordingly, which subsequently result in higher level of turbulence at the leak orifice and noise in the pipe. This finding agrees with the experimental work of J. D. Butterfield (2018) and Joseph D Butterfield, Collins, Krynkin, and Beck (2017); which reported that increase in leak flow rate significantly increases the amplitude of leak noise.

Similarly, using the relationships explained in Figure 43, Figure 53 and equation (65), source strength was also derived as a function of leak flow rate by substituting $C_d\sqrt{2P/\rho_0}$ for $\langle\overline{U_2}\rangle_S$ in equation (66) to become:

$$q_{rms} = 0.007\pi a^2 C_d\sqrt{2P/\rho_0} = 0.007Q \tag{67}$$

where $\langle\overline{U_2}\rangle_S$ (area averaged mean flow velocity) = $C_d\sqrt{2P/\rho_0}$

and $\pi a^2 C_d\sqrt{2P/\rho_0}$ = leak flow rate Q

q_{rms} = $0.007Q$ as derived in Eqn. (67) seems universal, based on the range of leak sizes and flow speeds investigated, at least, in this study.

The choice of turbulence model will certainly have an effect on the source strength / flow rate relationship. However, this change cannot be established or quantified without first running new simulations, which are not possible at this time, due to constraints of time and resources. Nonetheless, as extensively discussed in section (2.5.2), SST k ω model was chosen over other turbulence models because it is an improved version of k epsilon and k ω models. SST k ω model has an in-built blending and viscosity limiter functions that enable it to be able to resolve the near wall and free stream parts of the flow better than other models. To enhance the accuracy of the solutions, some of the suitable turbulence models for fluid flow in pipes were properly researched and their strengths and weaknesses were taken into consideration before choosing the preferred turbulence model for this study.

The value of the turbulence intensity of 0.7% is based on a limited set of RANS-based simulations. Further work is needed to establish whether this turbulence intensity value is universal for all leak geometries or is only valid for the current set of simulations.

Equation 67 and Figure 64 showed an approximated linear relationship between source strength and volumetric flow rate where the slope of the line represents turbulence intensity of 0.7 percent (0.7 %). As leak noise is proportional to the square of source strength (A. Papastefanou, 2011; Xiao et al., 2020), leak noise is also proportional to the square of volumetric flow rate.

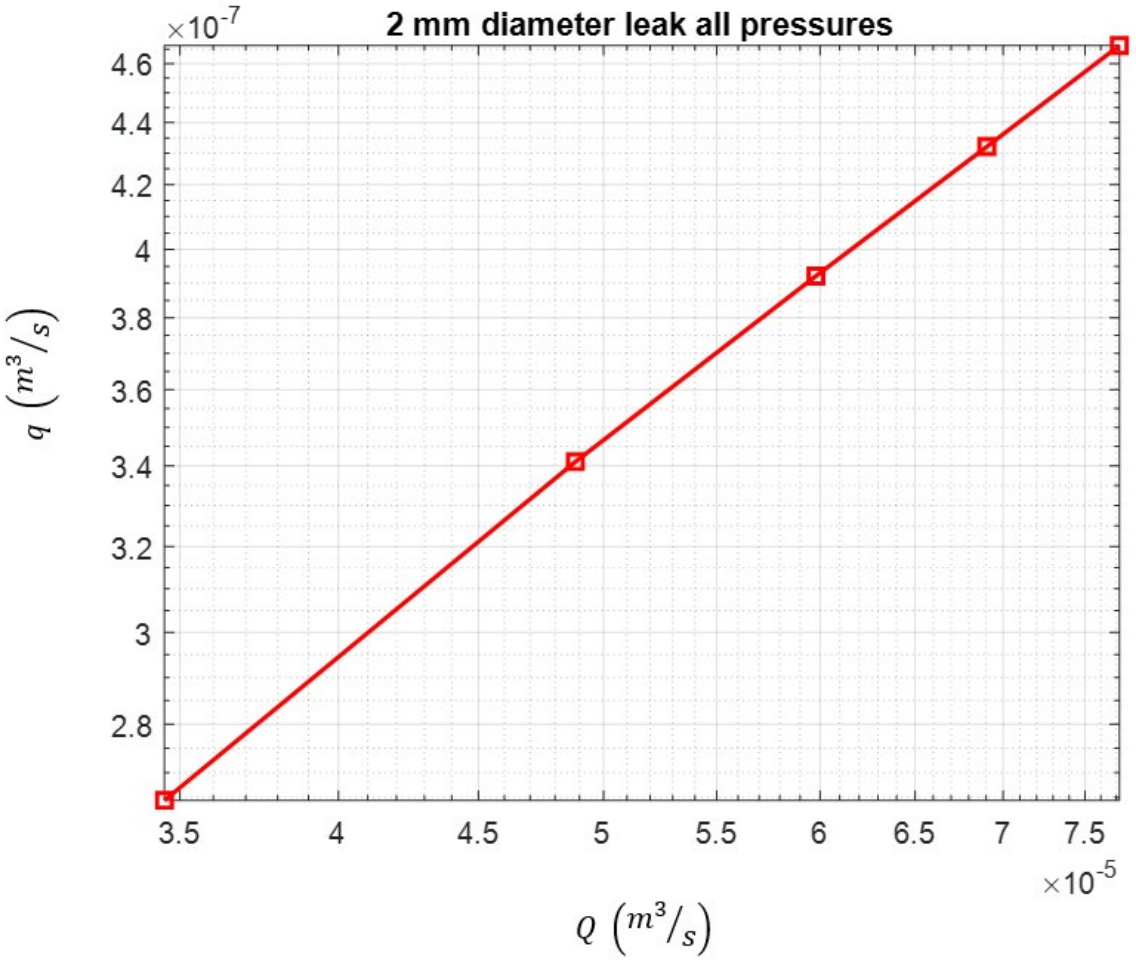

Figure 64 – Relationship between source strength and volumetric flow rate for circular leak

Power law relationship was also found to exists between leak source strength and pressure. At a fixed leak size, source strength was found to vary as a weak power of pressure (Figure 65) and this suggests although source strength increases with pressure, the strength of leak noise source is not significantly influenced by pressure. At a fixed leak of 1 mm diameter size, for instance, a hundred percent (100 %) increment of pressure from 1 Bar to 2 Bar has only resulted in 47 % increment of source strength. Alternatively, for the same leak size, a hundred percent (100 %) increment of

leak velocity, from 11 m/s to 22 m/s (Figure 63), has resulted eighty-nine percent (92 %) increment of source strength. This was a strong indication that mean flow velocity greatly influenced the strength of leak noise source, relative to pressure.

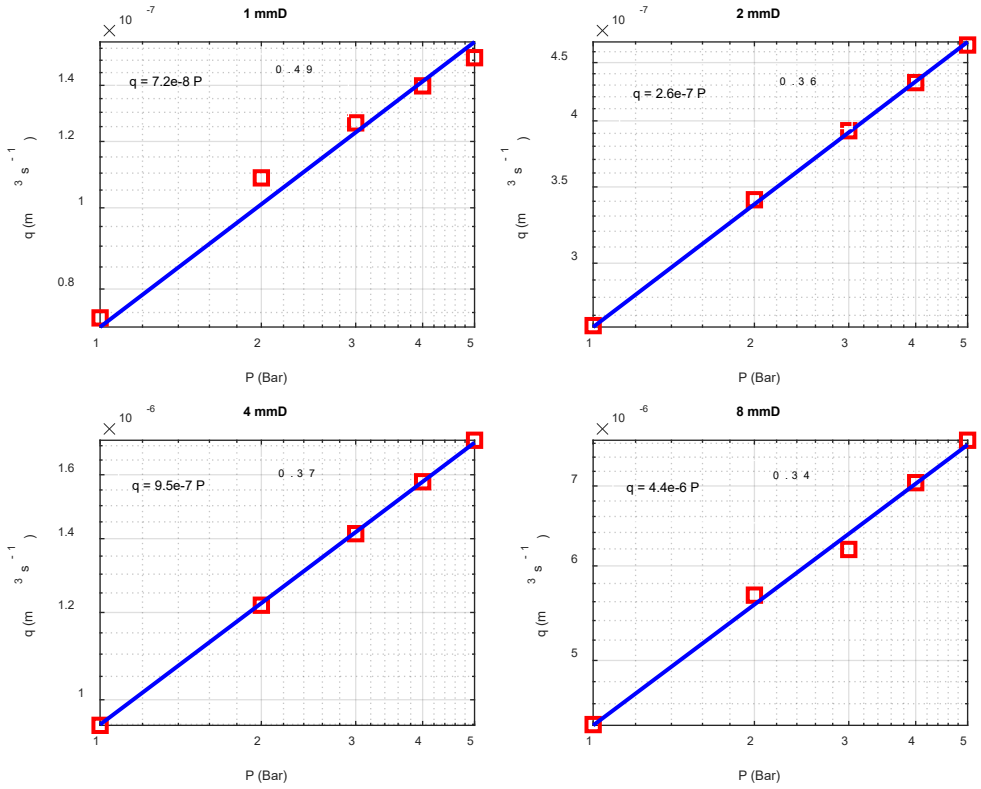

Figure 65 – Variation of source strength with pressure

As it was reported that leak noise is proportional to a square of source strength (A. Papastefanou, 2011; Xiao, Hu, et al., 2022; Xiao et al., 2020; Xiao, Joseph, et al., 2022), the source strength and the analytical expressions discussed in this sub-section would be useful in deriving an expression for leak noise, later in this study.

Chapter 5 Modelling, simulation, and numerical analyses of other leak shapes

5.1 Overview

There were very few studied reported in the body of literature about how the shape of leak could affect or influence its leak noise. In this chapter, modelling, simulation, and analyses of noise generation mechanisms of leaks from square, longitudinal slit and transverse slit shapes were discussed. Modelling and analyses of noise generation mechanisms of leaks from circular shapes has already been extensively discussed in the previous chapters. Also, It has already been shown in the previous chapter that, when pipe leaks, regardless of the shape of the leak, turbulent kinetic energy is generated within the leak area, with peak values around the edge of the leak and then decays towards the centre of the leak (Figure 45). Although turbulent kinetic energy does not vary much at the edges of the leaks, significant variation was observed from the edge to the centre of the leaks. Each of these leaks (square, longitudinal slit and transverse slit leaks) have been modelled to have the same area as circular leaks so as to eliminate the effect of leak area from leak shape investigation outcome. Furthermore, numerical simulation results from all the leak shapes will be compared so as to investigate the effects of leak shapes on the results obtained, especially leak noise signatures and leak flow rates.

5.2 Modelling simulation and numerical analyses of square leaks

Square leaks were modelled, meshed and simulated using the same boundary conditions similar to the simulation of circular leaks, as presented in the previous chapter. Area of the square leak is made equal to that of a circular leak such that length *B* of each side of the square leak is obtained by using the expression:

$$B_{square\_leak} = r\sqrt{\pi} \tag{68}$$

where r is radius of the circular leak. Using the expression in equation (68), the area of a square of side length of 1.8 mm corresponds to the area of a 2 mm diameter circular leak. Numerical simulation results comparing contours of turbulent kinetic energy and that of total leak mean flow velocity from square and circular shaped leaks are presented in Figure 66 and Figure 67.

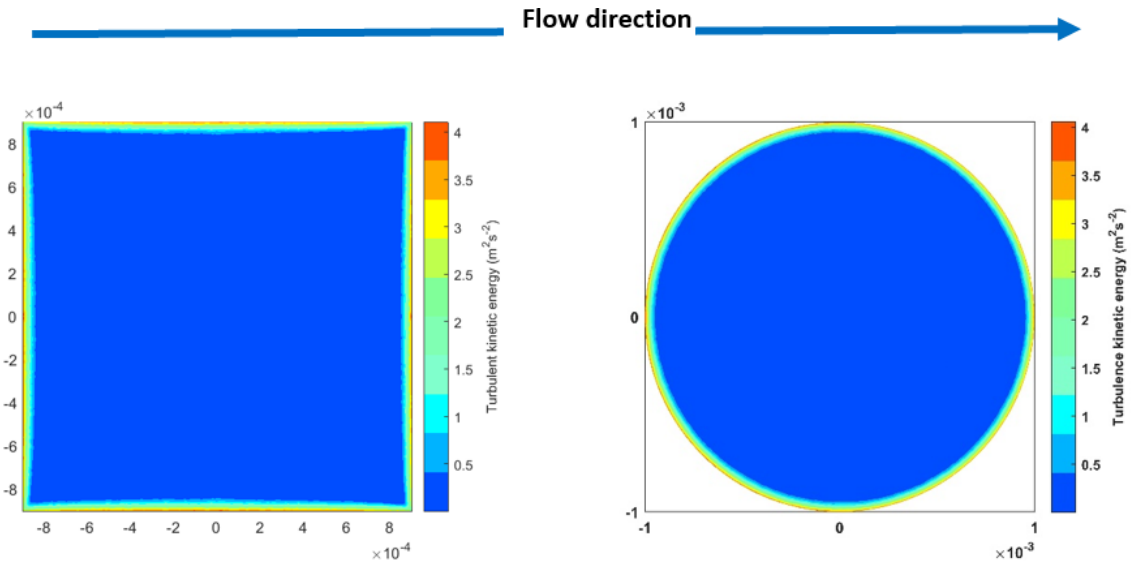

Figure 66 – Comparison of turbulent kinetic energy contours of square leak and a 2 mm diameter circular leak with the same area

As mentioned previously, highest peaks of turbulent kinetic energy was generated at the edges of the leaks, and then decay down to the centre (Figure 66). It was found that, regardless of their shapes, models of the two leaks displayed have similar levels of turbulent kinetic energy and total mean velocity contours (Figure 66 & Figure 67). This suggests that the generation and dissipation of turbulent kinetic energy and total mean velocity are unaffected by shapes of the leaks, at least in the numerical models presented in this work. This finding is in agreement with the experiment conducted by Xiao, Hu, et al. (2022) in gas pipes.

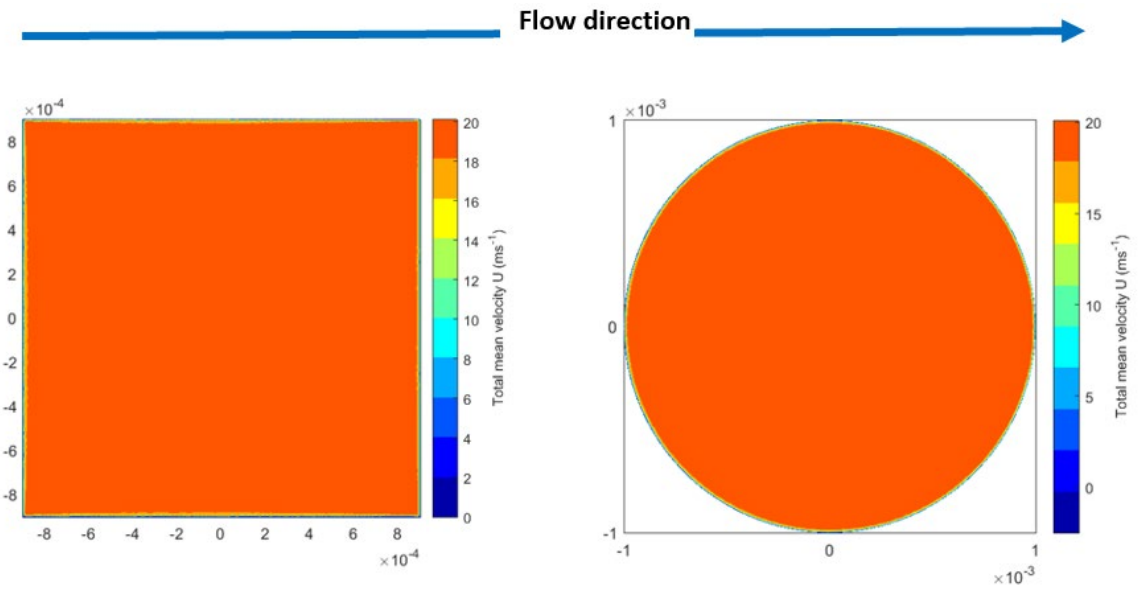

Figure 67 - Comparison of total mean velocity contours of square leak and a 2 mm diameter circular leak with the same area

5.3 Modelling, simulation and numerical analyses of longitudinal slit leak

Similarly, longitudinal slit leaks were modelled such that their areas were made similar to the areas of circular leaks. For example, longitudinal leak of 3.1 mm X 1 mm length and width respectively, corresponds to the area of a 2 mm diameter circular leak. Numerical simulation results comparing contours of turbulent kinetic energy and that of total leak mean flow velocity from longitudinal slit and circular shaped leaks are presented in Figure 68 and Figure 69.

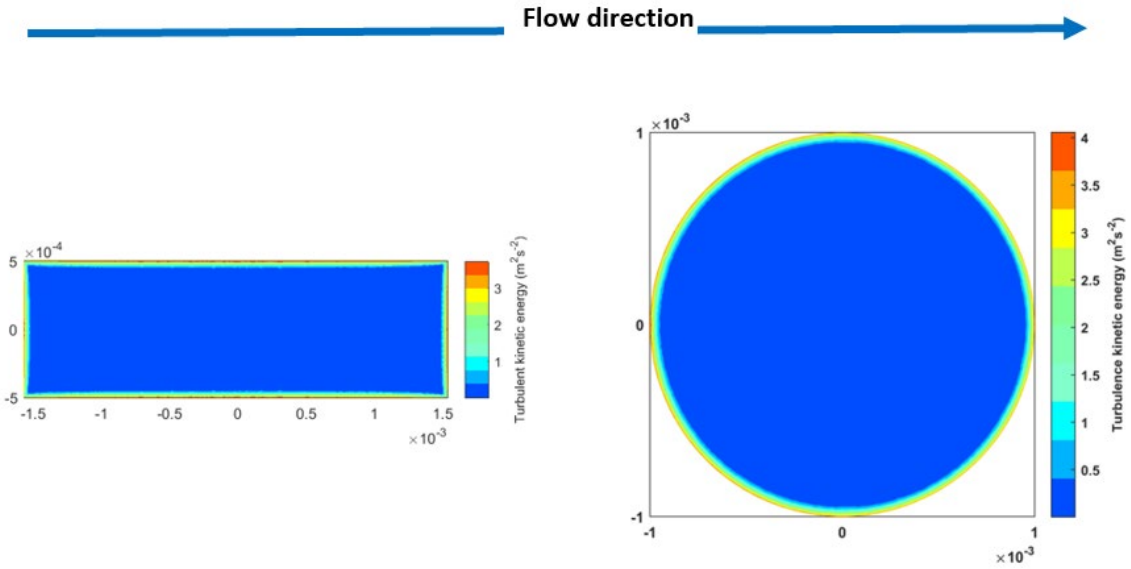

Figure 68 - Comparison of turbulent kinetic energy contours of longitudinal slit leak and a 2 mm diameter circular leak with the same area

Numerical simulation results of turbulent kinetic energy contour showed that the edge turbulence of longitudinal slit leak was slightly lower than that of circular leak. The reason could be linked to the edge length of the leak that is in contact with the upstream flow. As water is flowing in the pipe, beneath the leak, from left to right hand side through the pipe and also in the radial direction out of the leak, the edge length of the longitudinal slit leak that is exposed to the flow that is coming from the upstream direction is shorter when compared to the edge exposed by circular, square and transverse leaks. However, results of total mean leak velocity contours for longitudinal slit and circular leaks are similar (Figure 69). This could be as a result of the generation mechanism of mean flow velocity, where, due to no slip boundary condition, velocity at the edge of the leak is zero and increases in the boundary layer until it reaches maximum level, at the centre of the leak.

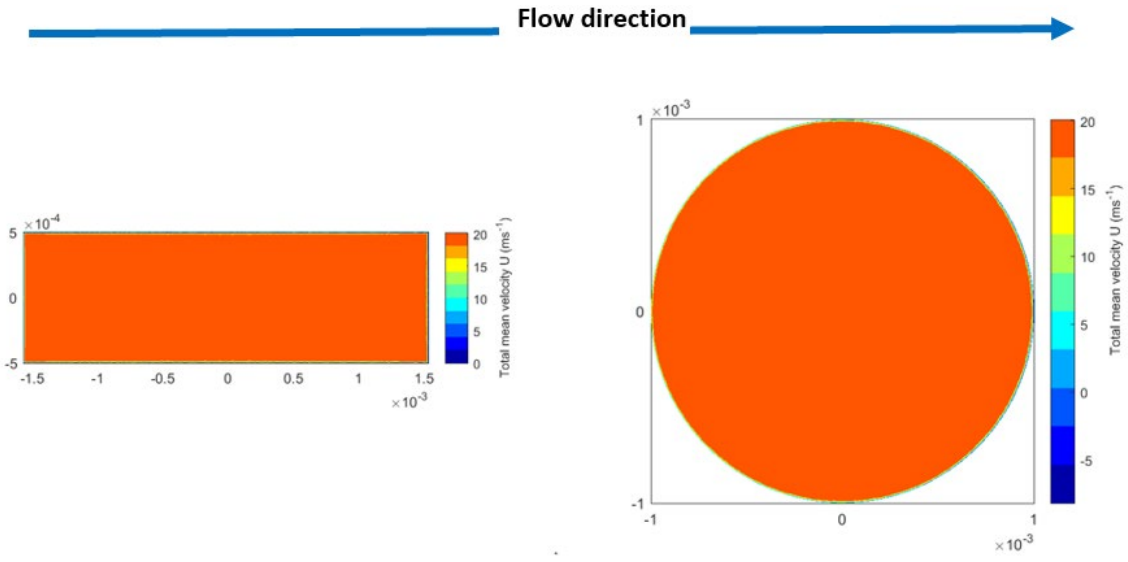

Figure 69 - Comparison of total mean velocity contours of longitudinal slit leak and a 2 mm diameter circular leak with the same area

5.4 Modelling, simulation and numerical analyses of transverse slit leak

Transverse slit leaks were also modelled to have the same area as circular leaks such that transverse slit leak of 1 mm X 3.1 mm length and width respectively, is equivalent to the area of a 2 mm diameter circular leak. Unlike longitudinal leak, contours of turbulent kinetic energy and total mean leak velocity for transverse slit and circular leaks were similar (Figure 70 and Figure 71), thereby allowing the generation and dissipation of turbulent kinetic energy to be the same, regardless of the shape of the leaks.

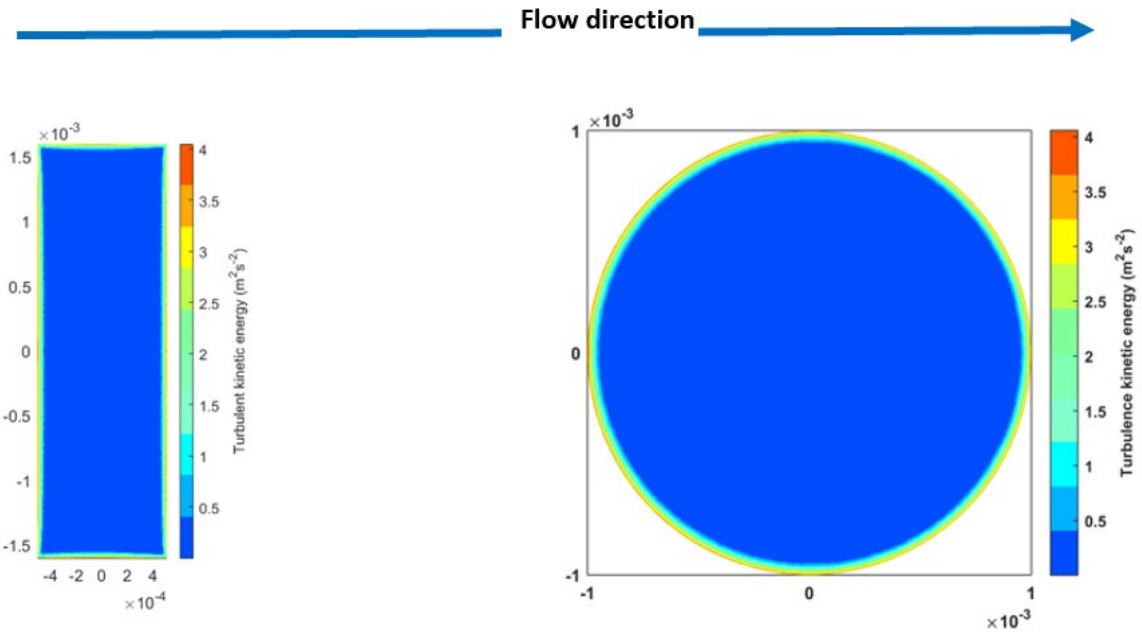

Figure 70 - Comparison of turbulent kinetic energy contours of transverse slit leak and a 2 mm diameter circular leak with the same area

The flow approaching transverse slit leak from the upstream was in contact with the longer edge of the leak geometry, making the maximum turbulence at the edge of the leak to be comparable to that of circular leak.

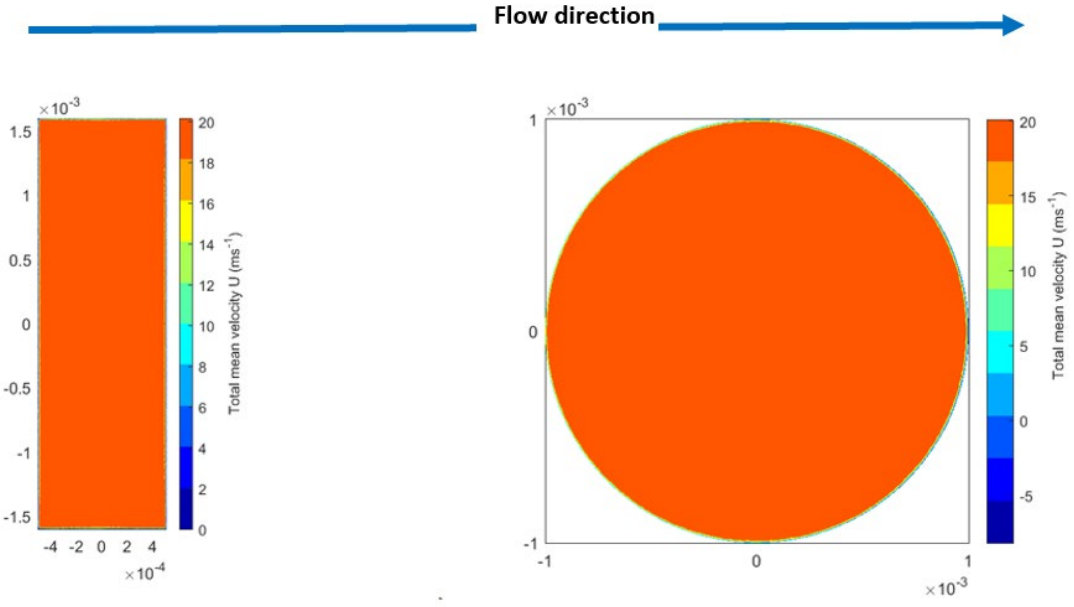

Figure 71 - Comparison of total mean velocity contours of transverse slit leak and a 2 mm diameter circular leak with the same area

5.5 Effect of leak shape on leakage flow rate estimation

To investigate how leak flow rate is affected by leaks shapes, leak flow speeds were simulated from circular, square, longitudinal slit and transverse slit leaks, using a semi-analytical expression obtained from the modification of Torricelli equation (53). Although, all the leak geometries were modelled to have the same leak area as a 2 mm diameter circular leak, as explained previously, the modified semi analytical expression allowed for the elimination of leakage area from Torricelli equation so that the contribution of leak shape in the leakage flow speed estimation can be adequately predicted. It was found that the slit leaks produced the same leakage flow speeds. This result was however not surprising because the two shapes were of the same dimensions but positioned in different directions. However, leakage flow speed estimated from circular leak was the same as the slit leaks, but square shaped leak produced the highest level of leakage flow speed. The results indicated that square leak would produce more leak flow than other leak shapes, although the difference in flow speed was only 0.37 m/s apart, which is very insignificant and has very minimal effect and it could be concluded that the, considering the same leak size and pressure, the shape of the leak has very minimal effect on leak flow rate (Figure 72).

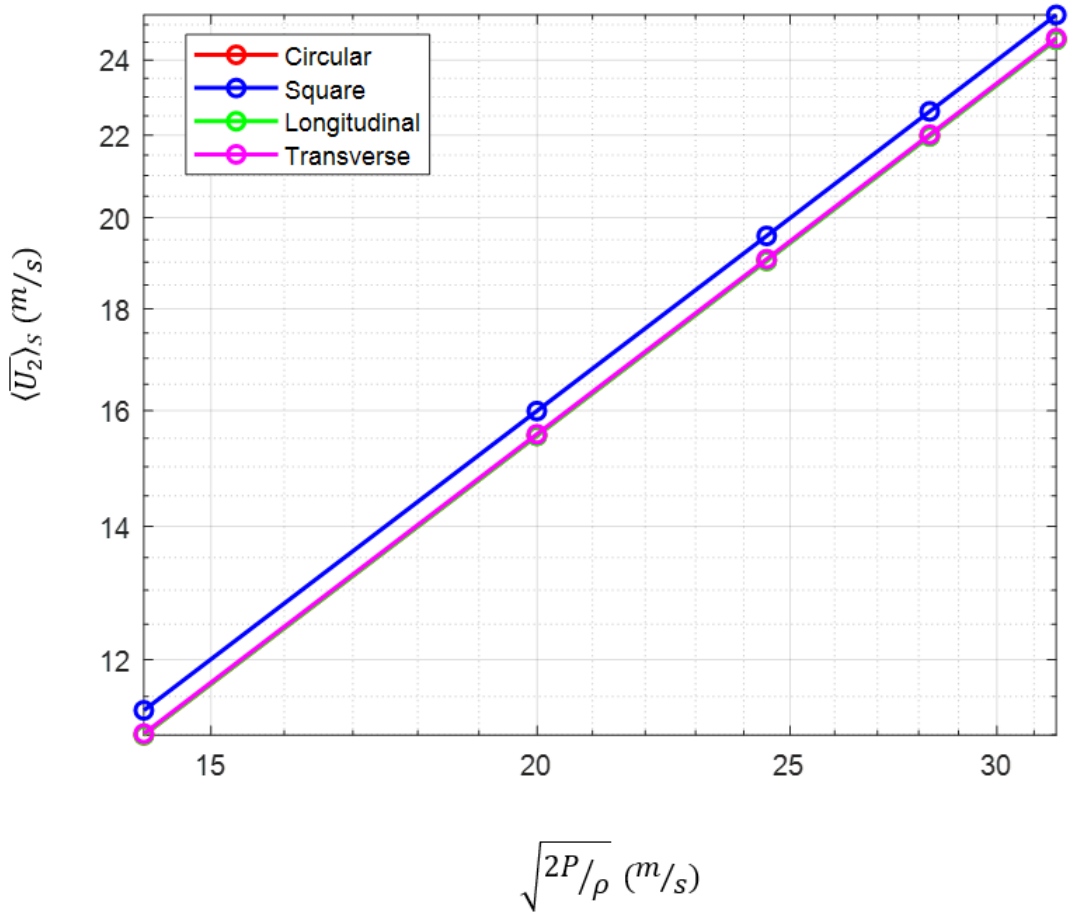

Figure 72 – Effect of leak shape on leakage flow rate

This finding was similar to the work of Xiao, Hu, et al. (2022). Although Xiao, Hu, et al. (2022) measured leak noise from circular and rectangular leaks of the same area, it was reported that leak noise signatures from the two shaped were similar. In the following chapter, leak noise from the leak shapes under investigation in this work will also be measured and their results will be compared.

5.6 Effect of leak shape on leak noise source strength

As discussed in the previous chapter, monopole sound source is an effective radiator of low frequency signals, including leak noise. It was reported in the work of J. D. Butterfield et al. (2018) that leaks of different shapes exit water at varying angles and this could be responsible for the differences in their turbulence generation mechanisms. This investigation is very important because we know from the literature that leak noise is proportional to the square of the source strength at the leak orifice, $S_{ll} \propto q^2$ (A. Papastefanou, 2011; Xiao et al., 2020). Knowledge of the source strength gives a very good estimate of what the leak noise would be. To find out if different leak shapes could lead to differences in source strength at their leak holes as well as noise levels in the pipes, the strength of leak noise source in a 2 mm diameter circular leak at different pressures, was obtained from area-integration of rms turbulent velocity fluctuations and results were compared with source strengths from other leak shapes with the same area as the circular leak (Figure 73).

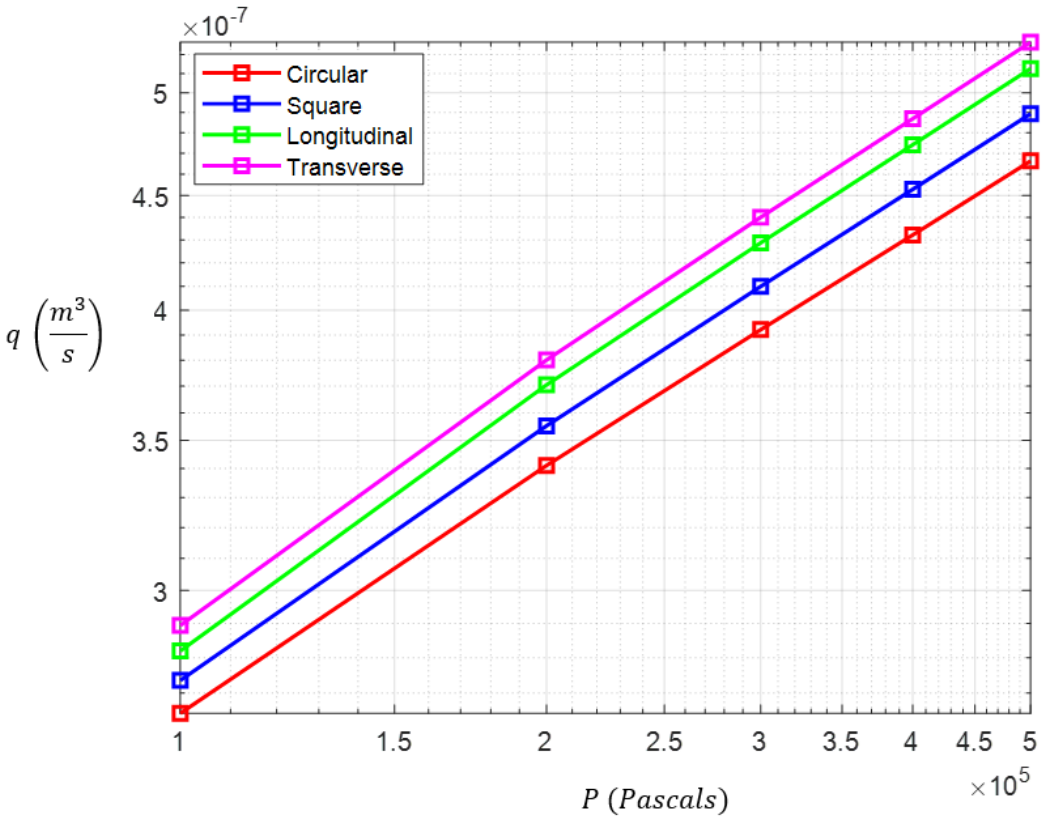

Figure 73 – Effect of leak shape and pressure on leak noise source strength

It was found that as pressures increased, source strengths also increased for all of the leak shapes with circular leak having the lowest source strength while transverse slit leak have the highest magnitude of source strength. This finding showed that, given the same leak area, increase in pressure results in corresponding increase in source strength for all the leak shapes, with transverse and circular leaks having the largest and smallest source strengths respectively. Differences in the values of the source strengths of leaks of different shapes could be linked to the differences in their jet angles as water exit the holes, leading to different turbulence generation mechanisms, as suggested by J. D. Butterfield et al. (2018). This finding could also be linked to the differences in the perimeters of the leak geometries.

Leak shapes	Leak perimeter / 2πa a = leak radius = 0.001 m	Results
Slits	$1 + \frac{1}{\pi}$	1.32
square	$2\left(\sqrt{\pi}\right)/_{\pi}$	1.13
circle	1	1

Table 7 – Leak perimeters for different leak geometries

It was shown in Table 7 that, transverse and longitudinal slit leaks have the largest perimeter followed by square leak, while circular leak has the smallest leak perimeter. In Figure 73, transverse leak with the largest perimeter displayed the largest source strength while circular leak with the lowest perimeter produced the lowest source strength. This suggests that leak perimeter plays an important role in the estimation of source strength hence leak noise. The larger the leak perimeter, the larger the source strength and the louder the leak noise. However, longitudinal slit leak, which has the same leak perimeter as transverse leak, was expected to be of the same source strength level as transverse leak but it dropped below transverse leak. The reason for the discrepancy could be due to differences in their jet angles as water exits the leaks (J. D. Butterfield et al., 2018). In addition, reason for the discrepancy could also be as a result of the shorter edge length of longitudinal leak that was in contact with the upstream flow, which was ascribed to the lower edge turbulence of the leak shape, compared to other leak shapes of the same size.

5.7 Effects of source strength and volumetric flow rate on leak shapes

It is important to understand the effect of volumetric leak flow rate on source strength for all the leak shapes because it will be beneficial to know how water exiting the leak contributes to the strength of the leak noise source and leak noise. It was found that, in leaks of different shapes having areas equivalent to the area of a 2mm diameter circular leak, pressure increases with source strength and volumetric leak flow rate (Figure 74). This suggests that, for all the leak shapes, the higher the amount of water exiting the leak, the higher the source strength and the louder the leak noise. However, for the same leak area, transverse leak would be losing the most water and therefore producing the loudest noise while circular leak would be producing the least noise. This result can also be linked to leak perimeter, as explained in section (5.6), Figure 73 and

Table 7, where, transverse leak produced the largest source strength as pressure increases, due to its largest perimeter. The finding in this section therefore suggests that leaks with the largest perimeter will lose the most water and produce the loudest noise than leak with the smallest perimeter. As pressure is proportional to square of exit velocity, increasing pressure results in bigger increase in exit velocity and consequently the volumetric flow rate. The findings in this section further validated the analytical expressions of source strength in equations (64 & 67), where source strength is 0.7 percent of volumetric leal flow rate (0.7 % Q) and the slopes of Figure 74 represent turbulence intensity and is approximately 0.7 %. As leak noise is proportional to the square of source strength ($S_{ll} \propto q^2$) and source strength is proportional to volumetric leak flow rate ($q \propto Q$), so leak noise is also proportional to the square of volumetric leak flow rate ($S_{ll} \propto Q^2$).

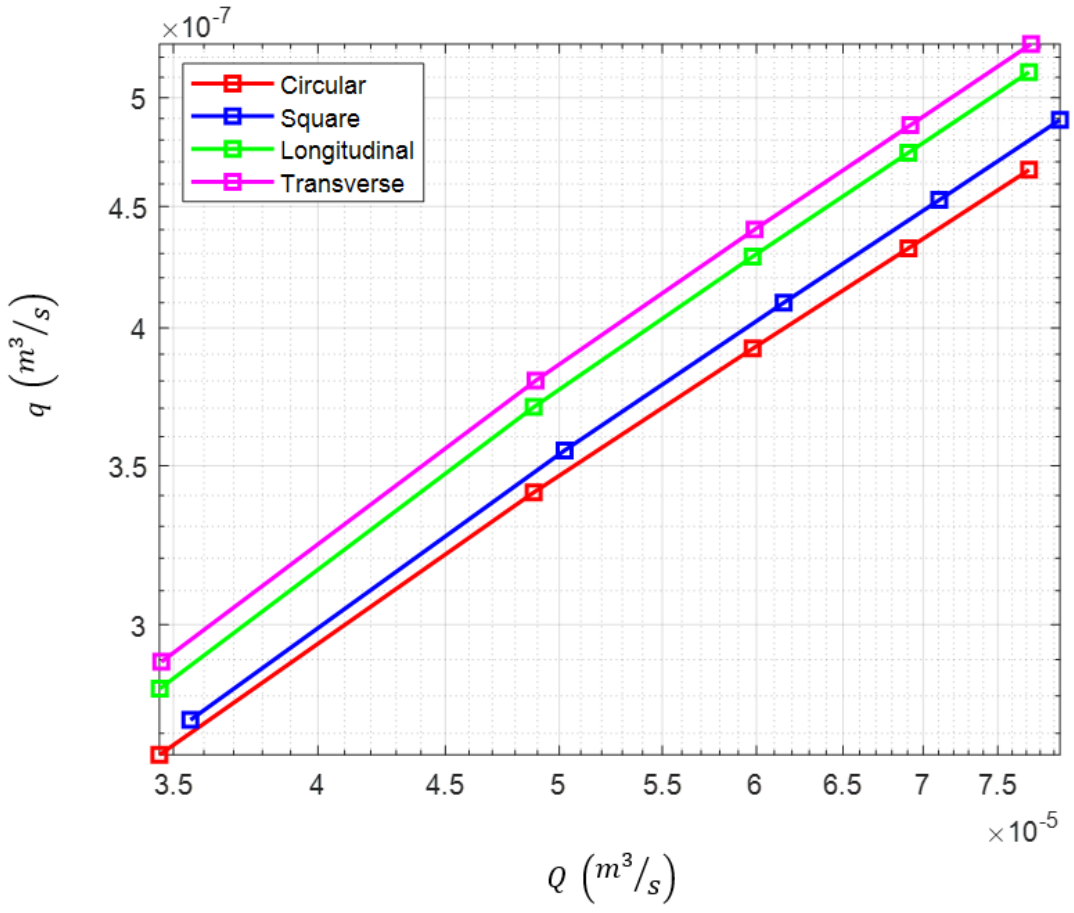

Figure 74 – Effect of volumetric leak flow rate on source strength.

5.8 Effects of source strength on leak area

To understand how source strength is affected by the size of the leak, at a fixed pressure of 2 Bar, source strength was predicted for all the leak shapes at different sizes.

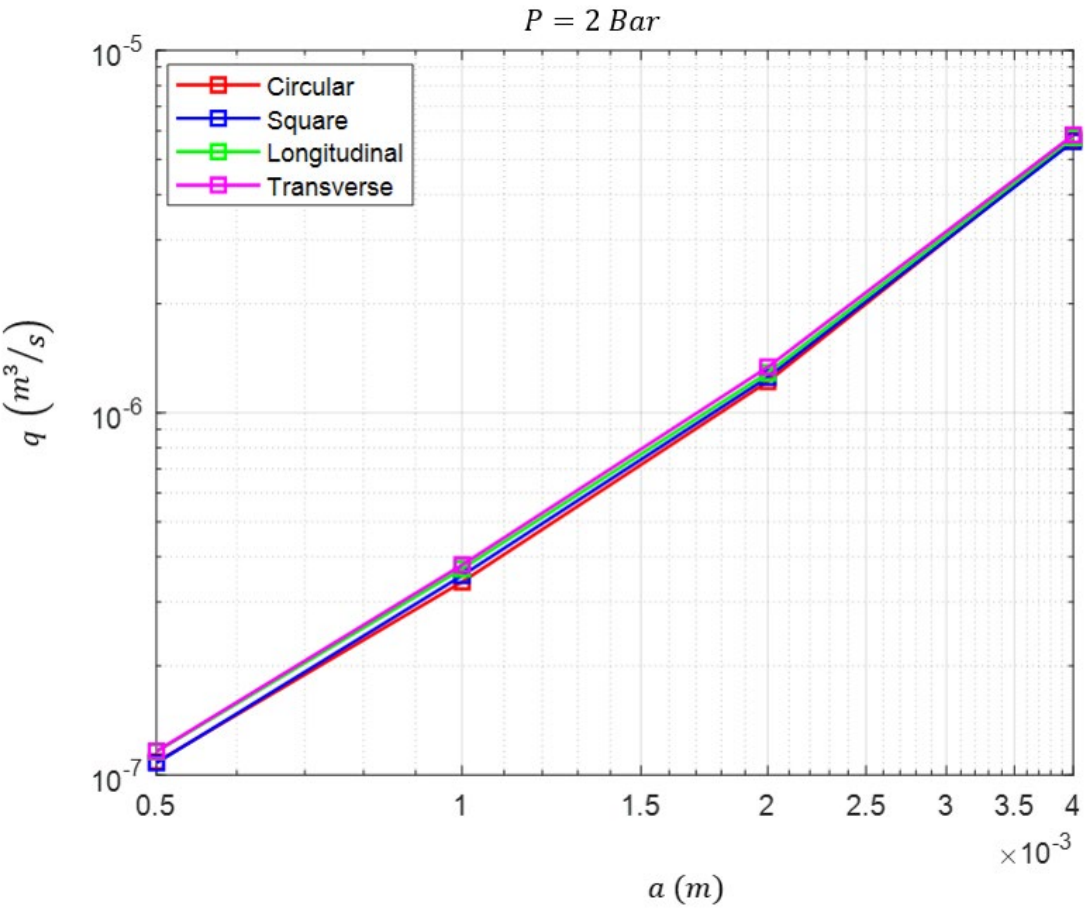

Figure 75 – Effects of leak size on source strength

Results (Figure 75) showed a universal profile of source strength as a function of leak size, that is independent of leak shape. This indicated that at a fixed pressure, source strength increases with increasing leak size. However, leaks of the same area, regardless of their shape, would produce the same source strength, hence noise, if pressure was kept constant. Besides, Figure 73 showed that the effect of leak shape on source strength was very minimal even when pressure was increased and this indicated that different leak shapes of the same size would behave similar if pressure (and leak noise) was increased.

Chapter 6 Leak noise modelling, prediction, and characterisation

6.1 Overview

Turbulent kinetic energy has been modelled and identified as a source of leak noise in the water pipes, with maximum production at the edge of the leak, and its relationship to leak size, mean flow velocity, pressure, shear layer thickness and source strength have been discussed. In this chapter, a semi-analytical model that estimates the pressure spectrum in the pipe from the velocity spectrum at the leak orifice, was developed. Flow data obtained from the leaks was incorporated into the model in order to predict the pressure spectrum for all leaks and pipe sizes. Leak noise was then predicted and characterised, based on the semi analytical model, using turbulent kinetic energy, line pressures and leak mean flow velocities, to reveal distinct relationships between the leak noise and other flow parameters such as leak size, leak shape, mean flow speed, volumetric flow rate and source strength.

6.2 Leak noise prediction: The velocity cross spectra model

This study aimed to minimise the assumptions in the work of Xiao et al. (2020), by proposing a velocity spectra model that will show that the turbulent velocity fluctuations, responsible for noise generation is concentrated at the edge of the leak and decay down to the leak centre, as modelled in Figure 45.

Based on the numerical modelling and simulation of turbulent kinetic energy (Figure 45), where high magnitude of turbulent kinetic energy were concentrated at the circumference of the leak, the source distribution adopted in the noise model will be represented as a ring of monopole sound sources located around the edge of the leak orifice of the form:

$$u(r,\theta,\omega) = \tilde{u}(\omega)a\delta(r-a) \tag{69}$$

which is independent of θ and $\tilde{u}(\omega)$ is the effective velocity whose amplitude and phase is frequency dependent, δ is the Dirac delta function and the factor of leak radius "a" has been introduced to maintain consistent dimensions since $\delta(r-a)$ has dimensions of m^{-1}. The velocity $\tilde{u}(\omega)$ is chosen so that the form of the velocity distribution in equation (69) preserves the volume velocity $q(\omega)$ of the leak, corresponding to the total monopole source given by:

$$q(\omega) = \int_0^a \int_0^{2\pi} u_{rms}(r,\theta,\omega) r dr d\theta = \tilde{u}(\omega) 2\pi a \int_0^a r\delta(r-a) dr \tag{70}$$

Solving of $\tilde{u}(\omega)$ therefore becomes:

$$\tilde{u}(\omega) = \frac{1}{2\pi a^2} \int_0^a \int_0^{2\pi} u_{rms}(r,\theta,\omega) r dr d\theta \tag{71}$$

Equation (71) could be readily interpreted as the area-averaged leak velocity. The area-averaged rms velocity is therefore simply related to the leak volume velocity source strength by:

$$\tilde{q}(\omega) = 2\pi a^2 \tilde{u}(\omega) \tag{72}$$

A form of velocity cross spectrum in equation (33) was assumed and is given by:

$$S_{u_2 u_2}(\mathbf{y}, \mathbf{y}', \omega) = \frac{1}{2} |\tilde{u}(\omega)|^2 a^2 \delta(r-a) \delta(r'-a) e^{-a|\theta-\theta'|/l_\theta} e^{iK_1(y_1 - y_1')} \tag{73}$$

and the spectrum therefore has the following properties:

a. The spectrum is equal to zero unless both receiver positions are located at the edge of the leak such that $r = a, r' = a$.

b. It decays exponentially with increasing circumferential separation distance around the leak edge $a[\theta - \theta']$, whose rate of decay is controlled by the turbulence length-scale l_θ in the θ direction and when $\theta - \theta' > \pi$, $\theta - \theta' - \pi$ is substituted in the exponential in equation (73), since the correlation decay is determined by the closest distance between the observers.

c. It has a phase variation that is determined by $\omega(y_1 - y_1^{'})/U_c$ corresponding to the time taken for the turbulent flow to convect as a frozen pattern across two points with streamwise separation distance $y_1 - y_1^{'}$. Since the sources are assumed to be located along the edge of the leak, $y_1 - y_1' = a(\cos\theta - \cos\theta')$.

By substituting equations (72 & 73) into equation (36), the expression for the acoustic pressure PSD in the pipe was proposed, whose frequency range was below the duct's first high order mode cut off frequency and therefore dominated by plane wave propagation:

$$S_{pp}(\omega) = \frac{\rho_0^2\omega^2}{4k^2S^2\pi^2a^2}\int_{\theta=0}^{2\pi}\int_{\theta'}^{2\pi}\int_{r=0}^{a}\int_{r'=0}^{a} q_{rms}^2\,\delta(r-a)\delta\left(r^{'}-a\right)e^{-a|\theta-\theta'|/l_\theta}\,e^{iK_1(rcos\theta-rcos\theta')}rr'drdr'd\theta d\theta \tag{74}$$

By performing the integration over r and r', equation (74) becomes:

$$S_{pp}(\omega) = \frac{q_{rms}^2(\omega)\rho_0^2c^2}{S^2}\sigma_{rad}(K_1a, a/l_\theta) \tag{75}$$

where $\sigma_{rad}(K_1 a, a/l_\theta)$ may be regarded as radiation efficiency term in the range ($0 \leq \sigma_{rad} \leq 1$) that determines the efficiency by which the leak can radiate energy into the pipe of the form:

$$\sigma_{rad}(K_1 a, a/l_\theta) = \frac{1}{(4\pi)^2} \int_{\theta=0}^{2\pi} \int_{\theta'=0}^{2\pi} e^{-a|\theta-\theta'|/l_\theta} e^{iK_1 a(\cos\theta - \cos\theta')} d\theta d\theta' \quad (76)$$

and can be observed to be a function of the two non-dimensional factors of frequency $K_1 a$ and the ratio of leak radius to length-scale a/l_θ . However, there is no closed form of solution for this function and must therefore be computed numerically. As radiation efficiency term cannot be accurately predicted with RANS numerical simulation approach employed in this work, it was assumed to be 1.

6.3 The frequency power law model

In a controlled laboratory experiment conducted by A. S. Papastefanou et al. (2012), it was reported that in plastic water pipes, leak noise spectra, for all the leak nose measured with hydrophones, decayed with a characteristic slope of frequency power law of $\frac{1}{\omega}$. Above certain higher frequency called critical frequency, the spectra decayed further with a power law of $\frac{1}{\omega^n}$ where n is a positive integer between 6 and 16. The study thus proposed analytical model for predicting leak noise in a 50 mm diameter plastic pipe with two hydrophone sensors mounted on either side of circular leaks:

$$S_{ll}(\omega) = \frac{S_{x1x1}(\omega)}{H^*(\omega, d_1)H(\omega, d_1)} = \frac{S_{x2x2}(\omega)}{H^*(\omega, d_2)\, H(\omega, d_2)} = \frac{S_{x1x2}(\omega)}{H^*(\omega, d_1)\, H(\omega, d_2)} \quad (77)$$

where $S_{x1x1}(\omega)$ and $S_{x2x2}(\omega)$ are the power spectral densities (PSDs) of the signals recorded from sensors 1 and 2 respectively, while $S_{x1x2}(\omega)$ is the cross spectral density (CSD) between the two signals on either side of the leak. The distances d_1 and d_2 are distances from the leak to the two sensor positions while $H^*(\omega, d_1)$ and $H(\omega, d_2)$ are transfer functions between the leak and the two sensor positions (Figure 76).

The model was based on the work of Y. Gao et al. (2004), where cross spectral density was obtained from leak noise spectrum and transfer functions between two signals on either side of the leak.

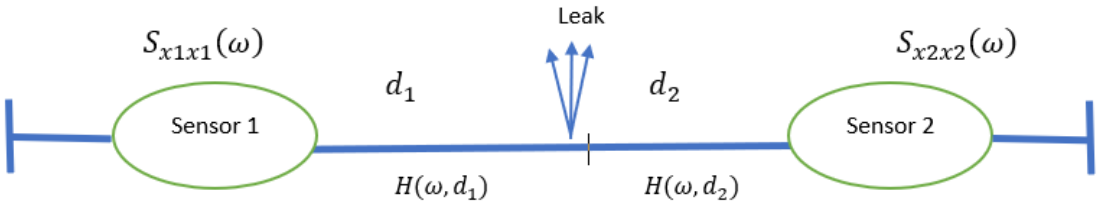

Figure 76 - Schematic of the key parameters involved in leak noise modelling.

The study stated that the accuracy of the leak spectrum in equation (77) largely depends on maximising the strength of the recorded PSDs and minimising the pipe response. However, due to wave reflections in the pipe, caused by pipe response, estimating leak noise spectrum by dividing PSD with the pipe response introduces additional peaks in the leak noise spectrum. To prevent this, the study assumed that there were no reflections between the leak and the sensors and pipe response functions were represented by:

$$H(\omega, d_1) = e^{-jkd_1} \tag{78}$$

$$H(\omega, d_2) = e^{-jkd_2} \tag{79}$$

By adjusting equation (77) with equations (78 & 79), leak noise spectrum model was proposed as:

$$S_{ll}(\omega) = S_{x1x1}(\omega)e^{\frac{\omega\eta}{c}d_1} = S_{x2x2}(\omega)e^{\frac{\omega\eta}{c}d_2} \tag{80}$$

where *c* is the wave speed *k* is the acoustic wave number, ω is the angular frequency and η is the loss factor of the pipe.

Estimating leak noise spectrum using equation (80) introduced a characteristic slope of ω^{-1}, within the frequency range of 50 Hz to 4 kHz, to the spectral shape of all the measurements (A. Papastefanou, 2011; Scussel, 2020). The characteristic frequency power law slope ω^{-1} was also observed in the work of (Scussel, 2020) where it was reported that some real leak noise spectra in plastic pipes decayed with the characteristic slope. However, this behaviour was not common to all the estimated spectra.

To accommodate the typical characteristic slope of ω^{-1} in the acoustic pressure PSD, the analytical model of equation (74) was modified by including an assumed spectrum *A/ω*, such that the integration of A/ω, within the limits of 50 Hz and 4 kHz, equals 1 (equation 81). The region of high signal-to-noise in leak noise measurement for plastic pipes, as reported by A. S. Papastefanou et al. (2012) and Scussel (2020), was within the range of 50 Hz to 4 kHz.

$$\int_{\omega_0}^{\omega_1} \left(\frac{A}{\omega}\right) d\omega \ = 1 \tag{81}$$

where A is a constant, and by integrating equation (81) over the frequency range of high signal to noise ratio, the constant A was obtained as:

$$A = \frac{1}{\ln \frac{\omega_1}{\omega_o}} \tag{82}$$

By including the solution of equation (81) in equation (75) acoustic pressure spectrum, typical of plastic water pipes was proposed as:

$$S_{pp}(\omega) = \frac{q_{rms}^2(\omega)\rho_0^2 c^2}{\ln(\omega_2/\omega_1)\,\omega S^2}\,\sigma_{rad}(K_1 a, a/l_\theta) \tag{83}$$

The semi-analytical model for acoustic pressure PSD prediction in equation (83) clearly showed that the pressure spectrum is proportional to the square of source strength and this finding validated the works of (A. Papastefanou, 2011; A. S. Papastefanou et al., 2012; Xiao et al., 2020).

6.4 Relationship between acoustic pressure spectrum in the pipe with pressure and mean flow speed at the leak hole

To establish the relationship between acoustic pressure spectrum and mean flow speed as well as pressure, the semi-analytical acoustic pressure PSD model in equation (83) is re-written so as to reflect these relationships. The source strength analytical expression as a function of volumetric leak flow rate in equation (67) was squared and incorporated in equation (83) to become:

$$S_{pp}(\omega) = \frac{2(0.007)^2 C_d^2 \rho_0 c^2 P}{\ln(\omega_2/\omega_1)\,\omega}\left(\frac{a}{R}\right)^4 \sigma_{rad}(K_1 a, a/l_\theta) \tag{84}$$

Equation (84) presented a semi-analytical expression for acoustic pressure PSD as functions of pressure and discharge coefficient. This means that if pressure, discharge coefficient, leak and pipe sizes are known, the acoustic pressure spectrum and leak noise in the pipe could be estimated. To derive the expression for acoustic pressure PSD as a function of mean flow speed at the leak, the area-averaged mean flow speed expression in equation (53) is re-written such that:

$$\frac{1}{2}\rho_0^2 \langle \overline{U_2} \rangle_S^2 = C_d^2 \rho_0 P \tag{85}$$

By substituting $\frac{1}{2}\rho_0^2 \langle \overline{U_2} \rangle_S^2$ in equation (85) for $C_d^2 \rho_0 P$ in equation (84) and assuming radiation efficiency term, $\sigma_{rad}(K_1 a, \frac{a}{l_\theta}) = 1$, the acoustic pressure PSD as a function of mean flow speed was proposed and converted from omega frequency to Hertz frequency by using the identity: $S_{pp}(f) = 2\pi S_{pp}(\omega)$ in the work of Xiao et al. (2020).

$$S_{pp}(f) = \frac{2\pi(0.007)^2\rho_0^2\langle\overline{U_2}\rangle_S^2 c^2}{\ln(\omega_2/\omega_1)\,\omega}\left(\frac{a}{R}\right)^4 \tag{86}$$

Equation (86) further validated the findings of A. Papastefanou (2011), A. S. Papastefanou et al. (2012) and Xiao et al. (2020), where they reported that leak noise is proportional to the square of mean flow speed at the leak and to the fourth power of leak radius ($S_{pp} \propto (\overline{U})^2 \propto a^4$). If the mean flow speed, leak and pipe radii are known, by applying the analytical expression in equation (86), acoustic pressure PSD and leak noise can be predicted.

To derive an expression for an acoustic pressure PSD divided by volumetric leak flow rate, the source strength and leak flow rate relationship in equation (67) is squared to become:

$$q^2 = (0.007Q)^2 \tag{87}$$

By substituting q^2 in equation (87) for $(0.007Q)^2$ in equation (83), acoustic pressure PSD model divided by volumetric flow rate was obtained as:

$$\frac{S_{pp}(f)}{Q^2} = \frac{(0.007)^2\rho_0^2 c^2}{\ln(\omega_2/\omega_1)\,\omega S^2} \tag{88}$$

The semi-analytical model in equation (88) further proved that acoustic pressure PSD is proportional to the square of volumetric leak flow rate as already discussed in section (5.7). Furthermore, equation (88) also indicated that as the size of the pipe gets bigger, the ratio of leak noise to leak flow rate gets smaller and this suggests that leak noise is louder in smaller pipes.

6.5 Leak noise prediction

Using the predicted acoustic pressure PSD data obtained from the semi-analytical model proposed in equation (86), leak noise was estimated for different pipe and leak sizes, under varying pressures and mean flow speeds. The model was able to capture the shape of leak noise spectra typical of plastic water pipes, and the results were compared with measured leak noise spectra in the work of A. Papastefanou (2011). In the following sub-sections, effects of pressure,

pipe size, leak size, exit velocity, leak flow rate and source strength, on the estimated leak noise spectra were investigated.

6.5.1 Effect of line pressure, leak, and pipe sizes on leak noise spectrum

To validate accuracy of the predicted acoustic pressure PSD results from the proposed model, leak noise spectra from the predicted model in this study were compared with the measured leak noise spectra in the experimental work of A. Papastefanou (2011), where leak noise were measured for 1mm, 2mm and 4mm diameter circular leaks from 50 mm diameter pipe. It was found that at 100 Hz and for the same pipe and leak dimensions, leak noise amplitude from the estimated spectra were higher than that of measured spectra by about 12 dB for 1 mm, 14 dB for 2 mm and by 18 dB for 4 mm diameter circular leak (Figure 77). However, in all the cases, ω^{-1} leak noise decay shape was evident.

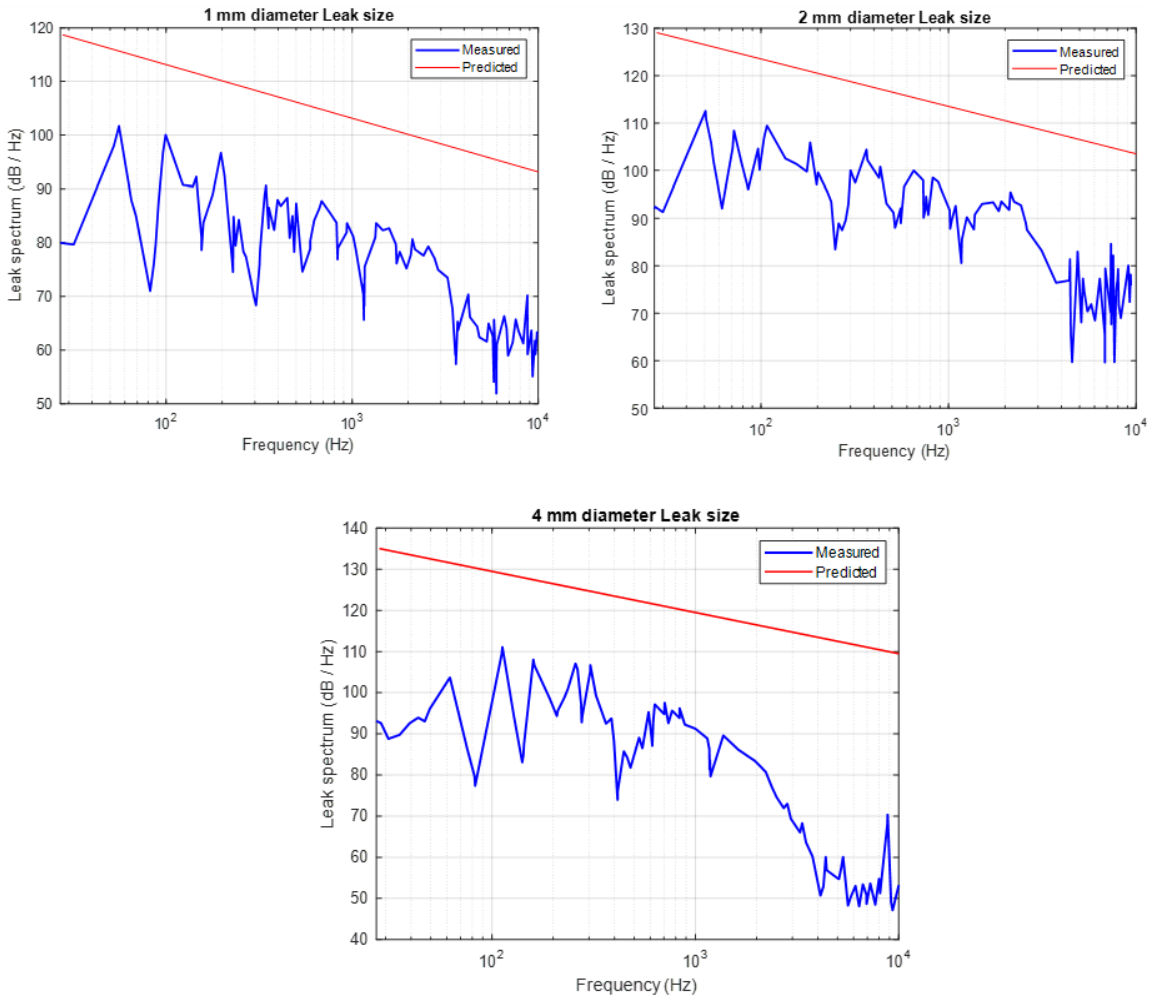

Figure 77 – Comparison of measured and predicted spectra for 1mm, 2mm and 4mm diameter leaks in a 50mm diameter pipe.

Figure 77 showed that the predicted noise spectra failed to capture accurately, noise levels from the experimental data. The current model used in this study over predicted noise levels by 20dB to 30dB, when results were compared to measured data. Possible reasons for the discrepancy are suggested below:

a. Over-prediction of turbulence levels in the RANS simulations

It is well known that the prediction of turbulence levels are less accurate when using Reynolds Averaged Navier Stokes equations (RANS) because the solutions are time averaged, thereby failing to capture turbulence anisotropy (F. Menter et al., 2021; F. R. Menter, 1994). Predictions are particularly so in the case where the flow is separated as the fluid accelerates from inside the pipe towards the leak orifice.

As presented in Figure 77, predicted spectra were 20dB to 30dB higher than the measured spectra, which means that the pressure square (P^2) of the predicted spectra were 100 times bigger than those of the measured spectra. As leak noise is proportional to the square of source strength (Eq. 75), it follows (Eqs. 62, 63, 64 & 83) that:

$$P^2 = q^2{}_{rms} = (0.007\pi a^2 \langle \overline{U_2} \rangle_S)^2 \tag{89}$$

Therefore, turbulence intensity (TI) of the predicted spectra may be 10 times bigger than that of the measured spectra. In the predicted spectra, turbulence intensity was obtained as 0.7 % (Eq. 62) and to obtain a perfect agreement with the measured spectra, turbulence intensity has to be 0.07 %, which is 10 times smaller than what was originally predicted.

With the adoption of the lower turbulence intensity of 0.07%, the modified leak noise prediction model is presented as:

$$S_{pp}(f) = \frac{2\pi(7e^{-5})^2 \rho_0^2 \langle \overline{U_2} \rangle_S^2 c^2}{\ln(\omega_2/\omega_1)\,\omega} \left(\frac{a}{R}\right)^4 \tag{90}$$

Future work should aim to verify the validity of the current RANS simulations by the use of time-resolved simulations, such as LES and DES, in which large scales of turbulence are resolved.

b. Accuracy

Another reason for the discrepancy observed between measured and predicted spectral levels is uncertainty over the calibration of the hydrophones used to obtain the experimental data. Discussions with the supervisor of the researcher who conducted the experiment (A. Papastefanou, 2011), has suggested that, determining the absolute levels of the leak noise signals was not important to the project at that time, and therefore little effort was spent in correctly calibrating the hydrophones and subsequent processing software. The aim of A. Papastefanou (2011) was simply to establish the scaling laws of the leak noise signals with leak parameters, such as the leak flow rate and leak size.

c. Incorrect noise generation mechanism

The basis of the model presented in this thesis is based on the assumption that leak noise is generated by the fluctuating mass flux of turbulent kinetic energy in the leak orifice. This assumption was made as it is consistent with the U^2 and a^4 scaling laws observed in both water (A. Papastefanou, 2011) and in gas pipes (Xiao et al., 2020). However, it is possible that this assumed noise generation mechanism is not ideally valid for leak noise generation in fluid pipes. Again, more work is needed, both experimentally and numerically, to establish more clearly, the precise noise generation mechanism for leak noise.

d. Wall thickness

Wall thickness is not a reason for the discrepancy in the predicted data as it was not modelled and therefore not included in CFD calculations. Computational domain was only made up of fluid in the pipe, as stated in section (3.2.2). Wall thickness was not modelled nor included in the CFD calculations because of the high mesh density required, which was computationally too expensive for this work.

e. Assumption of radiation efficiency

Another possible reason for the discrepancy between predictions and measurements is the assumption of perfect radiation efficiency $\sigma_{rad} = 1$ in the predicted data, which is only true at sufficiently high frequency (Joseph, 2024). At high frequency:

$$ka = {}^{\omega a}/_{c} > 1 \qquad (91)$$

where a is the leak radius, k is the wave number and c is the flow speed. Since very small leak diameters, where $5e^{-4} < a < 4e^{-3}$, are considered in this study, this corresponds to frequency of about 0.1 KHz. As leak noise is a low frequency signal, ka in equation (91) should be less than 1 (Blackstock, 2000; Joseph, 2024)

Assuming that the efficiency of monopole radiation varies as $\sigma_{rad} \sim (ka)^2$, the efficiency for the largest leak size considered, a = 0.004 m at a high frequency f = 1 kHz, corresponds to a noise reduction of $20 \log_{10} \sigma_{rad} \sim 20dB$.

The RANS simulations adopted in this study cannot be used to compute radiation efficiency σ_{rad}, since noise cannot be predicted from the RANS model as this is not time resolved. However, as suggested above, increased radiation efficiency of $\sigma_{rad} = 1$ could be a possible reason for the discrepancy between measurement and prediction. Therefore, the radiation efficiency of the leak orifice could be added theoretically, based on the assumption of monopole radiation as indicated above.

$$\sigma_{rad} = {(ka)^2}\Big/{(1 + (ka)^2\ )} \tag{92}$$

In Eq. (92), it is evident that at low frequencies, σ_{rad} behaves as $(ka)^2$ while at high frequencies, it behaves as 1. This study erroneously assumed high frequencies, where $\sigma_{rad} = 1$ (sections 6.2 & 6.4) and thus a possible reason for the overprediction of noise levels.

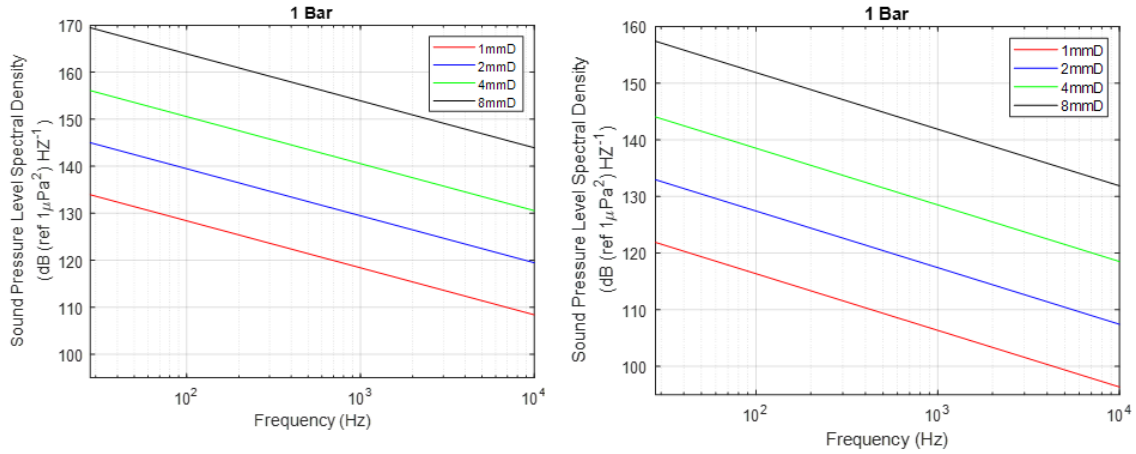

a. 25 mm diameter pipe

b. 50 mm diameter pipe

Figure 78 – Estimated leak spectra in 25 mm and 50 mm diameter pipes at *P* = 1 Bar.

In the predicted spectra presented in (Figure 78), it was found that, for the same pressure, leak noise increased just as leak sizes increased. This indicated that at constant pressure, increased noise levels could be used to estimate the size of the leak and this information could be used to prioritise repair operations and minimise water loss due to leakage. In addition, for all leak sizes at constant pressure, magnitudes of leak noise spectrum in 25 mm diameter pipe was found to be higher than that of 50 mm diameter pipe. Gupta, Sharma, Singh, and Verma (2017) investigated leak noise intensity in different pipe sizes and reported that leak noise was generally louder in small pipes. The fluid velocity in small pipes is typically higher for the same flow rate compared to larger pipes (Brown, Johnson, Smith, & Williams, 2018). As the fluid rushes through the leak, the increase in velocity leads to higher turbulence and greater energy dissipation, resulting in louder leak noise.

When pressure was increased to 5 Bar (Figure 79), levels of leak noise in both pipes increased accordingly. However, the rate of change of leak noise level in response to pressure increment indicated that leak noise was not significantly sensitive to pressure change. When pressure was increased by 400 percent from 1 Bar to 5 Bar, for 1 mm diameter leaks, noise in the pipe only responded by rising to 4.6 % in 25 mm diameter pipe and 5.1 % in 50 mm diameter pipe. Similarly, for 8 mm diameter leaks, leak noise rose by 2.8 % in 25 mm diameter pipe and 3 % in 50 mm diameter pipe.

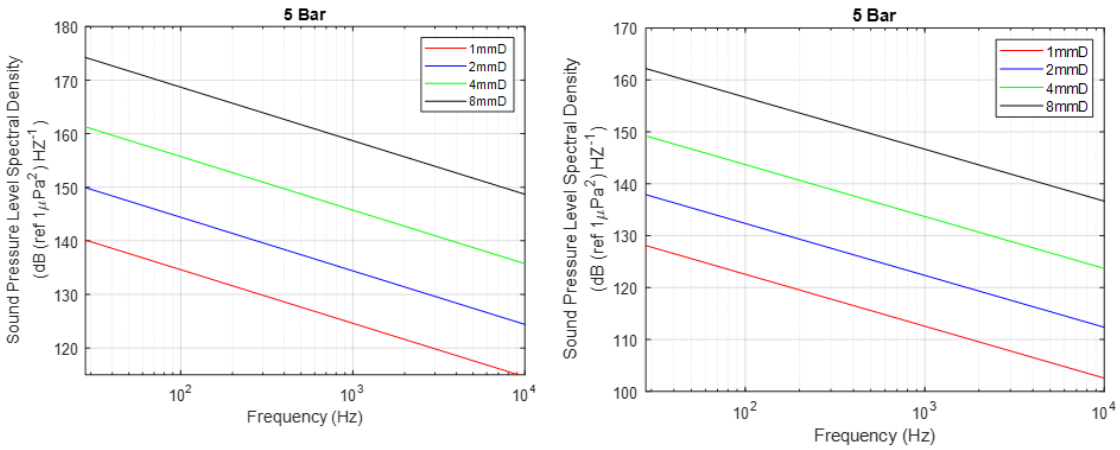

a. 25 mm diameter pipe

b. 50 mm diameter pipe

Figure 79 - Estimated leak spectra in 25 mm and 50 mm diameter pipes at *P* = 5 Bar

On the contrary, at constant leak size of 1 mm diameter leaks, increase in pressure resulted in corresponding increase in leak noise level (Figure 80). Again, for all pressures, noise in smaller diameter pipe is louder than in larger diameter pipe for reasons discussed previously.

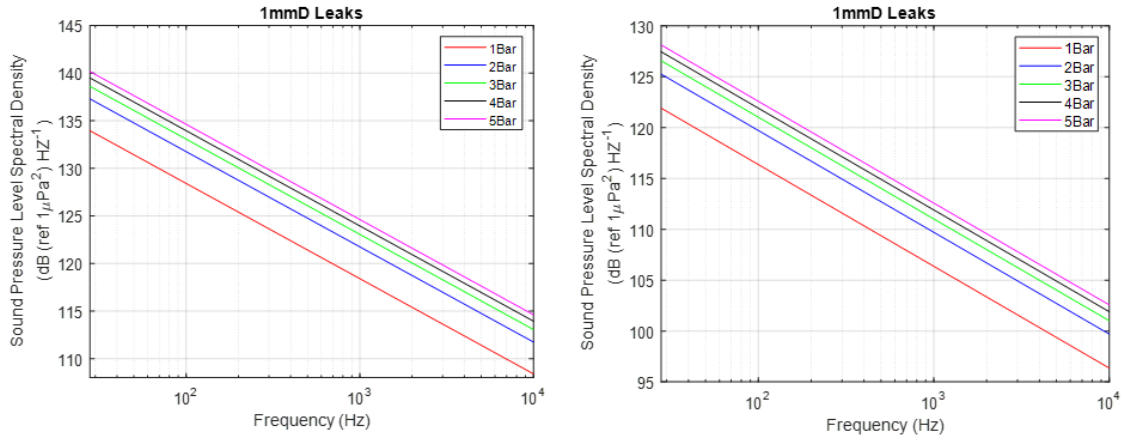

a. 25 mm diameter pipe

b. 50 mm diameter pipe

Figure 80 - Estimated leak spectra in 25 mm and 50 mm diameter pipes for 1 mm diameter leaks

To investigate the sensitivity of leak noise to leak size, noise levels were observed for constant leak size of 8 mm diameter leak at varying pressures, and they were found to increase in response to pressure increase (Figure 81). However, for smaller diameter pipe at 1 Bar pressure, 700 % increase in leak size, from 1 mm diameter leak to 8 mm diameter leak, has resulted in 26.5 %

increment in leak noise level while for a larger diameter pipe, increment of 29 % was estimated. At a pressure increase of 5 Bar, noise levels rose to 24 % in a smaller diameter pipe and for a larger diameter pipe, 27 %. These findings suggest that leak noise is clearly more sensitive to leak size than pressure. This agrees with leak noise analytical models in the works (equations 83 & 84) where leak noise was predicted to be proportional to the fourth power of leak radii (a^4) and pressure (P) respectively. A. S. Papastefanou et al. (2012) and Xiao et al. (2020) also reported in their works that leak noise was proportional to the third power ($S_{PP} \propto a^3$) and fourth power leak radii ($S_{PP} \propto a^4$) respectively.

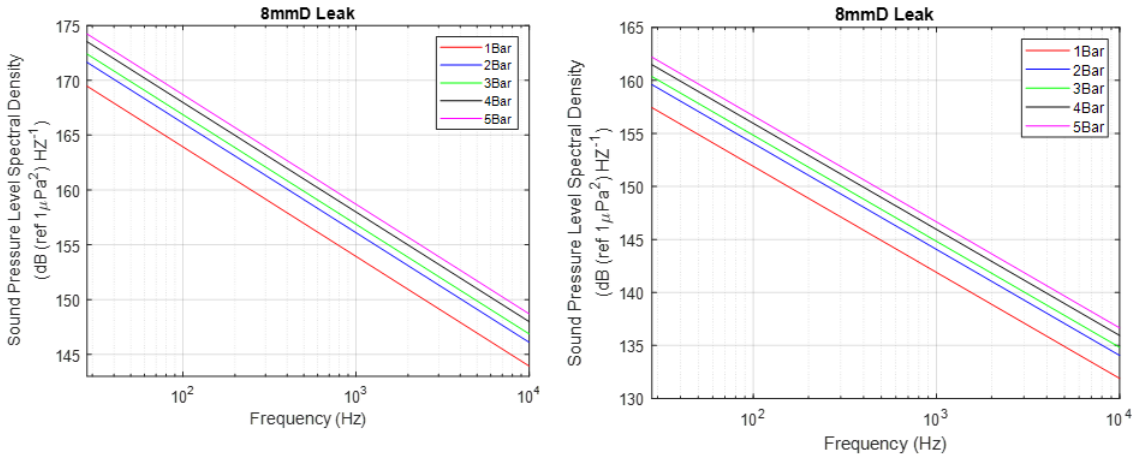

a. 25 mm diameter pipe

b. 50 mm diameter pipe

Figure 81 - Estimated leak spectra in 25 mm and 50 mm diameter pipes for 8 mm diameter leaks.

6.5.2 Effect of volumetric flow rate on over all sound pressure levels (OASPLs)

Overall sound pressure level represents the total noise level obtained by integrating individual sound pressure levels (Figure 78 - Figure 81) across all frequencies. When leak occurs in pipes, it gives off noise, which is received and presented as sound pressure level or overall sound pressure level. Some details about the leak, such as leak size and leak flow rate, can be derived from leak noise signatures. These details can, in turn, be used to detect and localise the leak. Overall sound pressure level was plotted against volumetric leak flow rates of all leaks and the results revealed that for both small and large diameter pipes, leak noise levels increased as leak flow rates were increased (Figure 82). It was shown in the semi-analytical expression in equation 83 and section (5.7) that leak noise is proportional to the square of leak flow rate.

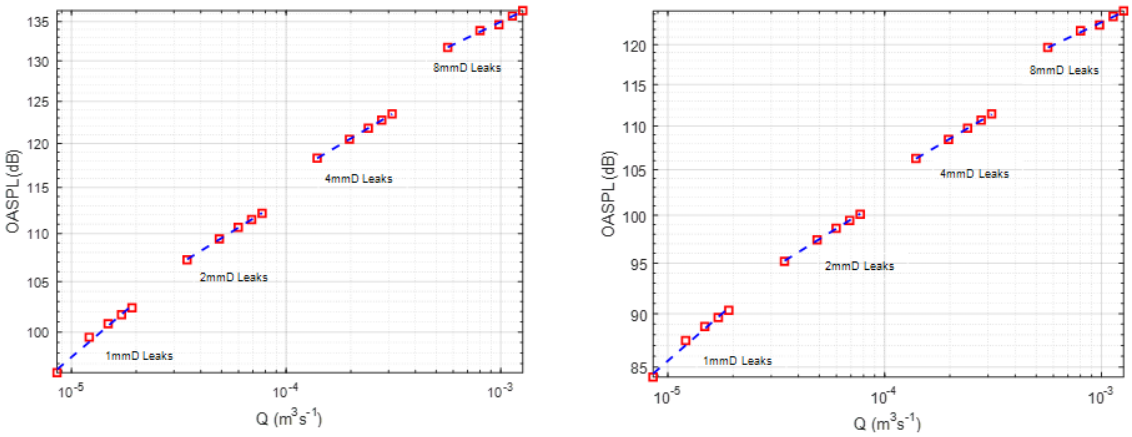

a. 25 mm diameter pipe

b. 50 mm diameter pipe

Figure 82 – Effect of volumetric flow rate on OASPL in 25 mm and 50 mm diameter pipes.

6.5.3 Effects of flow velocities on overall sound pressure levels

To understand how leak noise varies with leak flow velocities, leak spectra obtained from this study were integrated across all frequencies and plotted against their discharge velocities. It was found that for all leak diameters, the overall sound pressure levels (OASPL) in small and large diameter pipes varied as leak flow velocity to the power of 2 (Figure 83). The finding was consistent with the semi-analytical leak noise prediction model in equation 83 and in the works of A. Papastefanou (2011) and Xiao et al. (2020).

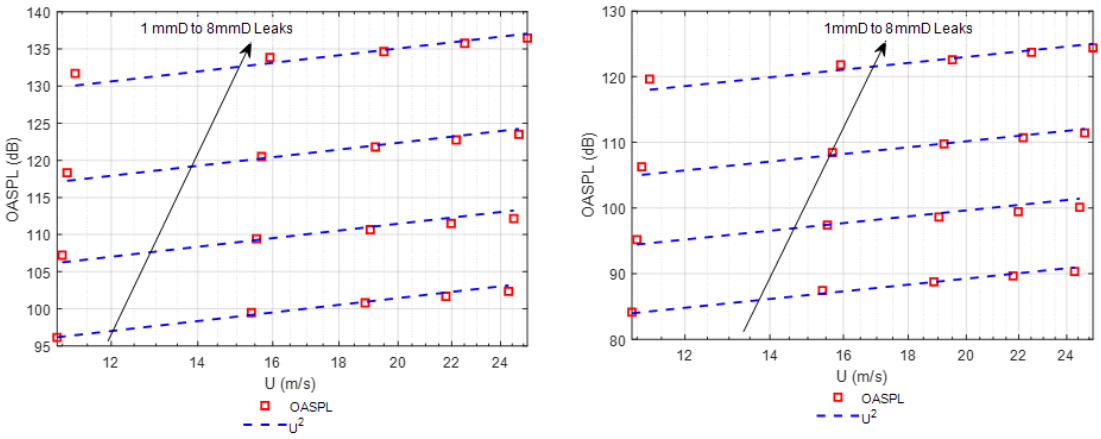

a. 25 mm diameter pipe

b. 50 mm diameter pipe

Figure 83 – Variations of overall sound pressure levels with leak flow velocities for small and large diameter pipes

The trends (Figure 83) were in perfect agreement with the work of Xiao et al. (2020) where it was predicted, using velocity scaling law, the fluctuating mass flux of monopole order was responsible for leak noise generation at the orifice. Similar trend was reported for small diameter leaks in the experimental work of A. Papastefanou (2011). For large diameter leaks, mean square pressure in the work of A. Papastefanou (2011) varied as flow speed power law of U^8, which was suggested to have been caused by a change in leak noise generation mechanism. With the findings in this study, U^2 velocity scaling law variation with leak noise suggests that it would be relatively easier to detect leaks of higher leak flow rates than leaks of lower leak flow rates.

6.5.4 Effects of leak orifice radius on overall sound pressure levels

To understand how the leak noise scaled with leak orifice radius, overall sound pressure levels of all leak spectra were plotted against orifice radii of all leak sizes for different line pressures and pipe diameters. The plots revealed leak noise to vary as leak orifice radii to the power of 4 (a^4) (Figure 84 & Figure 85) and this was in very perfect agreement with the semi-analytical noise prediction model in equation 83.

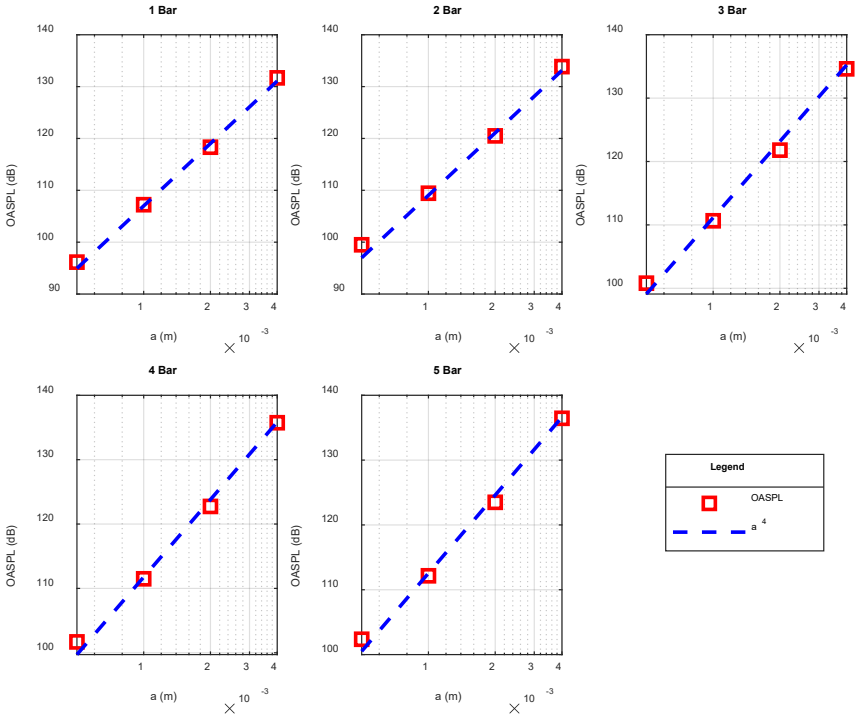

Figure 84 - Variations overall sound pressure levels with of leak orifice radii for 25 mm diameter pipes at different line pressures.

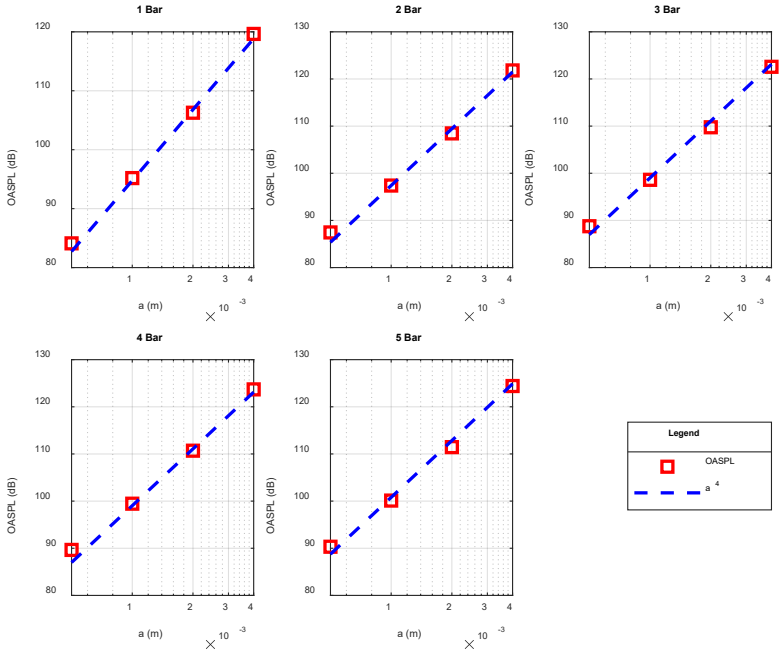

Figure 85 - Variations overall sound pressure levels with of leak orifice radii for 50 mm diameter pipes at different line pressures.

The findings were in good agreement with the work of Xiao et al. (2020), where leak noise was reported to vary as the fourth power of leak orifice radius (a^4) and it was stated that large leaks were relatively more easily detected than small leaks while in the work of A. Papastefanou (2011), the spectra varied as a^3.

6.5.5 Effect of pressure and velocity on area-averaged mean square turbulent velocity fluctuations ($\overline{u'^2}$) at the leak orifice.

It was shown in the semi-analytical model (equation 83) that leak noise in the pipe is related to the velocity spectrum at the leak orifice and the main source of noise at the leak is due to turbulent velocity fluctuations (Xiao et al., 2020). To understand how pressure and velocity are related to the turbulent velocity fluctuations, mean square turbulent velocity fluctuations were integrated over the leak holes and the numerical results were area-averaged, in order to remove the effect of leak size, and results were then plotted against pressure. Results revealed that when leak size is fixed, mean square turbulent velocity fluctuations increased with pressure *P* to the power of ≈ 1. The direct proportionality relationship between mean square turbulent velocity fluctuations and pressure is evident in Figure 86 where it was shown that fluctuating velocity is a product of turbulent intensity and mean flow velocity and squaring both sides of the equation gives:

$$\overline{u'^2} = (I\overline{U})^2 = I^2 P \tag{93}$$

where $\overline{u'^2}$ is the mean square turbulent velocity fluctuations, I is turbulent intensity, $\overline{U}$ is leak mean flow velocity and P is pressure. In equation (93), it was evident that mean square turbulent velocity fluctuations is proportional to pressure, because $\overline{U}^{\,2} = P$.

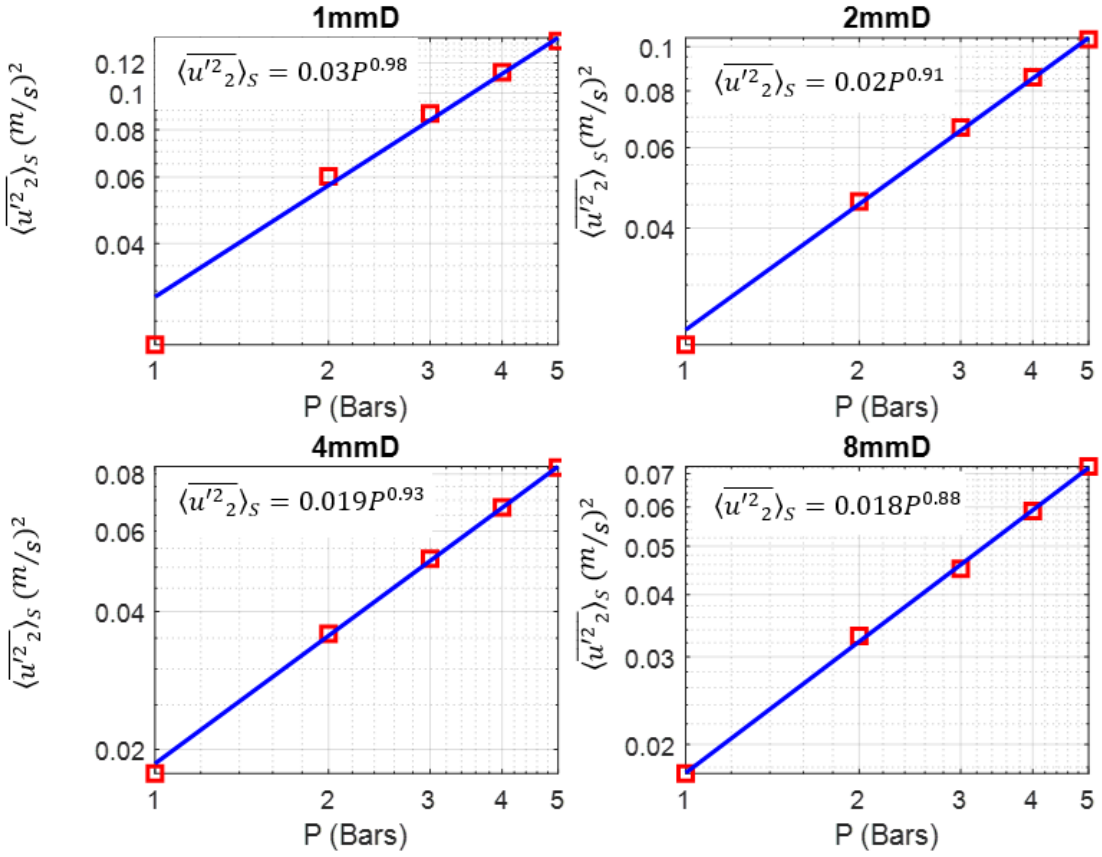

Figure 86 – Effect of pressure on mean square turbulent velocity fluctuations

In Figure 87, numerical simulation results revealed that mean square turbulent velocity fluctuations increased with mean velocity to the power of ≈ 2. This was in very good agreement with the analytical expression in equation (93) and indicated that the generation and maintenance of turbulence at the leak orifice is driven by mean flow velocity, rather than pressure.

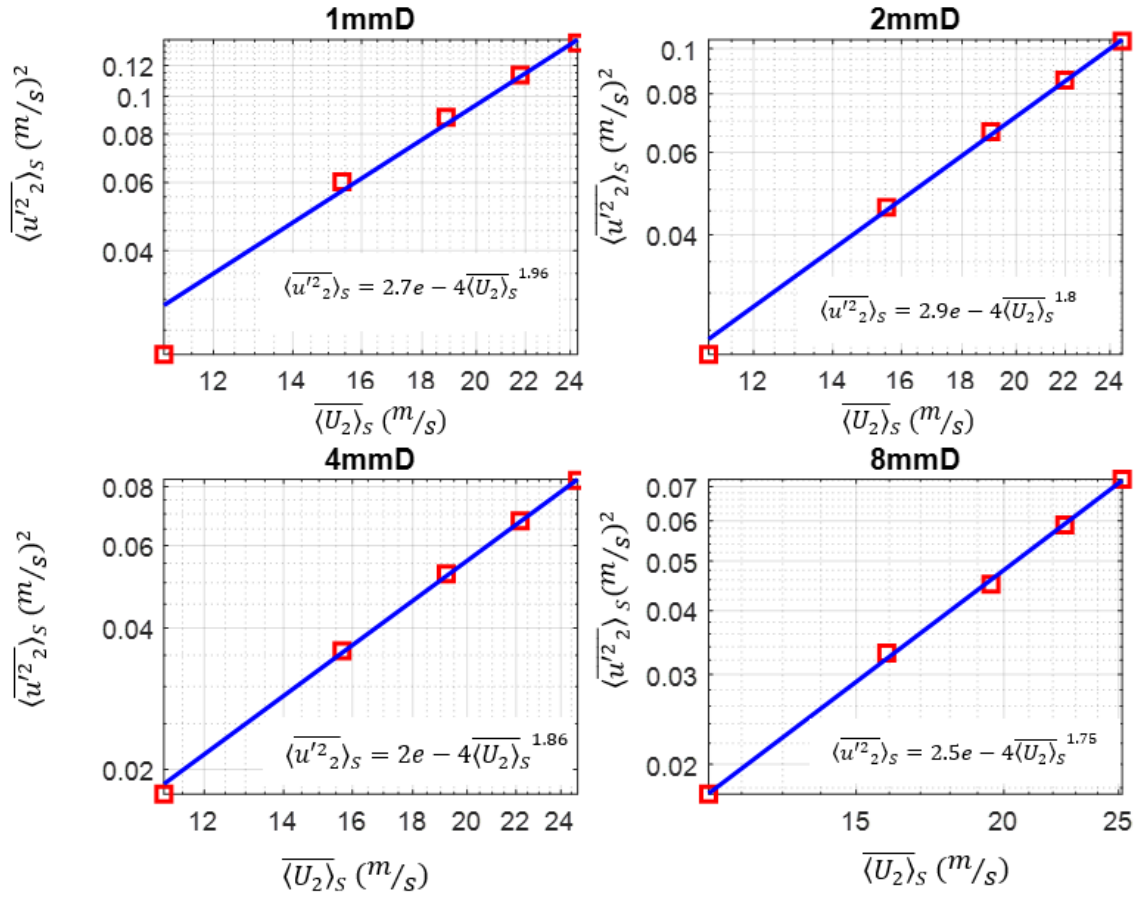

Figure 87 - Effect of mean flow velocity on mean square turbulent velocity fluctuations

6.5.6 Effect of leak noise source strength on overall sound pressure levels

To investigate the effect of the source strength at the leak on the overall sound pressure levels in the pipe, source strengths from different leak sizes were plotted against their OASPLs and it was found that leak noise increased with source strength (Figure 88). As the source strength of a noise source increases, the resulting noise becomes louder (section 5.7) and contributes more significantly to the overall noise level.

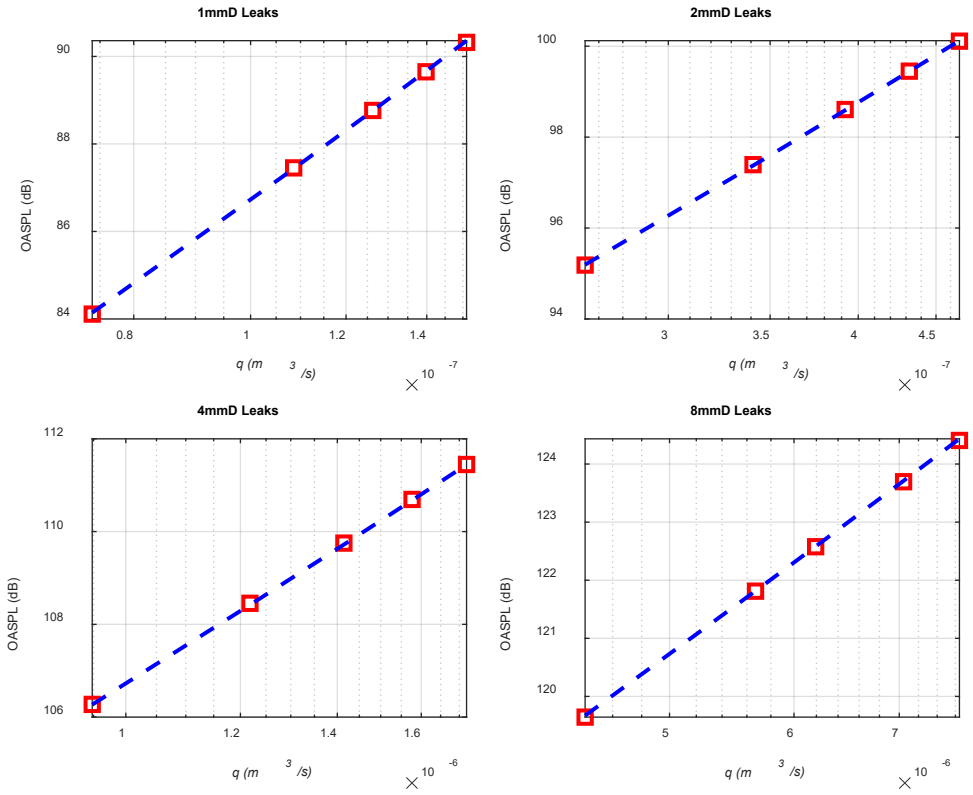

Figure 88 – Effect of source strengths from different leak sizes on over all sound pressure levels

6.5.7 Effect of leak shape on leak noise signatures

It was reported in the experimental studies conducted in gas pipelines by Xiao, Hu, et al. (2022) and in water pipeline by J. D. Butterfield (2018), that very few experimental studies but no known theoretical studies have numerically reported the effect of leak shape on leak noise signatures. This study have identified the gap and have thereby numerically investigated the effects of circular, square, longitudinal slit and transverse slit leaks on their leak noise signatures. All the leak shapes were modelled to have the same leak area as a 2mm diameter circular leak and leak noise in the pipe was predicted using the semi-analytical model in equation (83). Results showed no significant difference in the noise levels of all the leak shapes. However, circular leak produced the least noise while transverse slit leak produced the loudest noise (Figure 89). The reason could be due to differences in their perimeters, as previously discussed. These findings were very similar to the work of Xiao, Hu, et al. (2022), where, it was reported that, from 100 Hz to 1000 Hz, leak noise amplitude of circular leak was slightly lower than that of rectangular leak by only 1.5 dB (Figure 90). These findings however suggest that leak shape has negligible effect on leak noise signature.

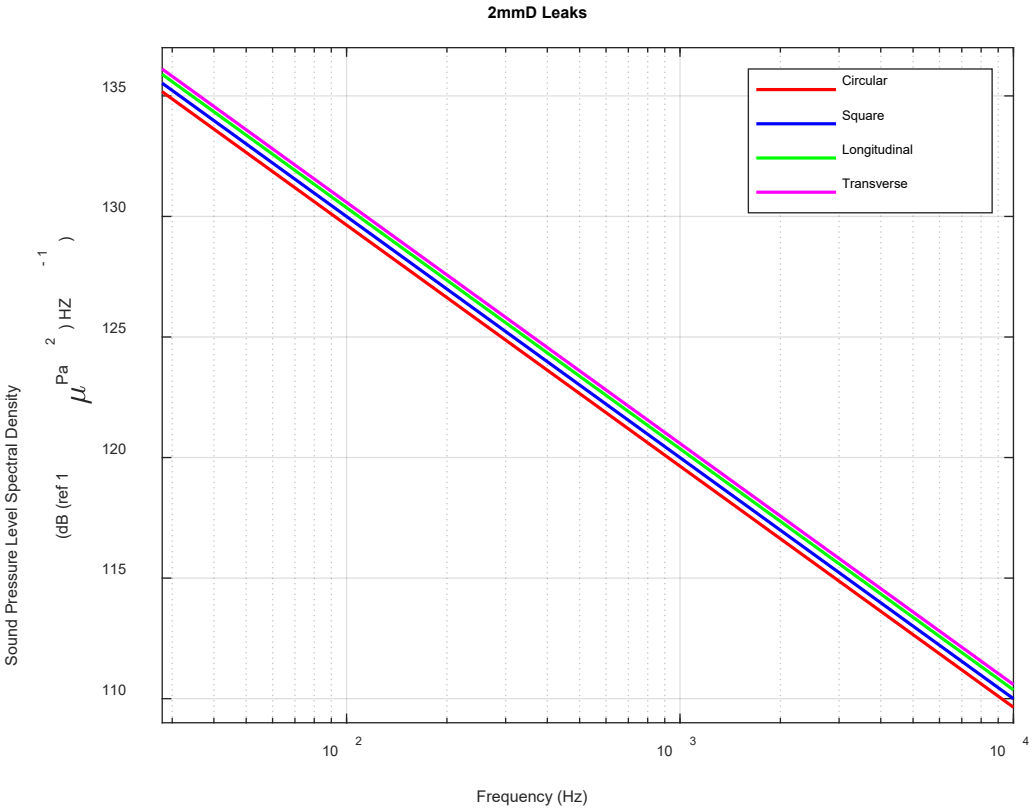

Figure 89 – Effect of leak shape on leak noise signatures

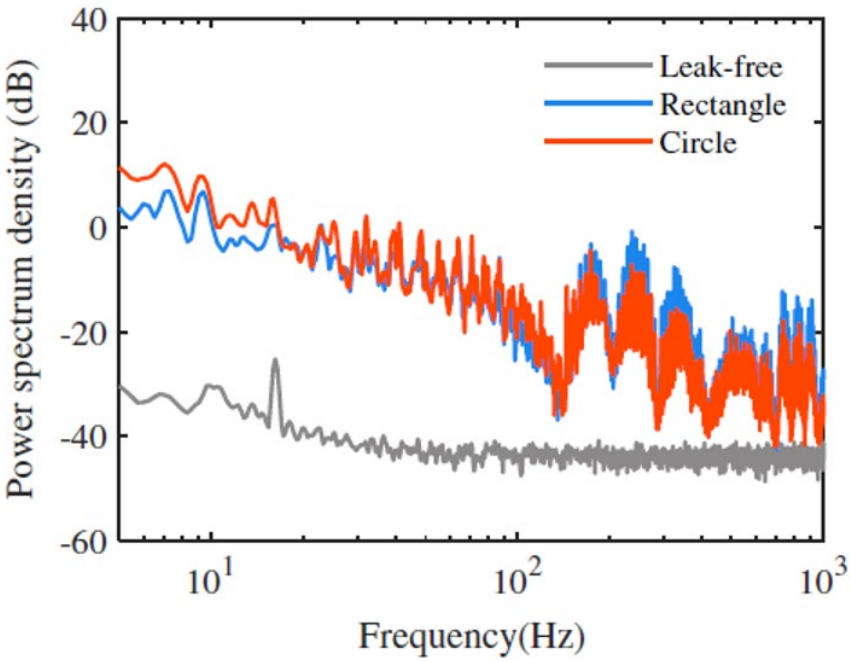

Figure 90 - Effect of leak shape on leak noise signatures (Xiao, Hu, et al., 2022).

However, in the work of J. D. Butterfield (2018), leak noise was measured for circular, longitudinal slit and electrofusion joint leaks, all of the same area and flow rate and it was concluded that at high frequencies, circular and electrofusion joint leaks produced the loudest and lowest noise respectively (Figure 91).

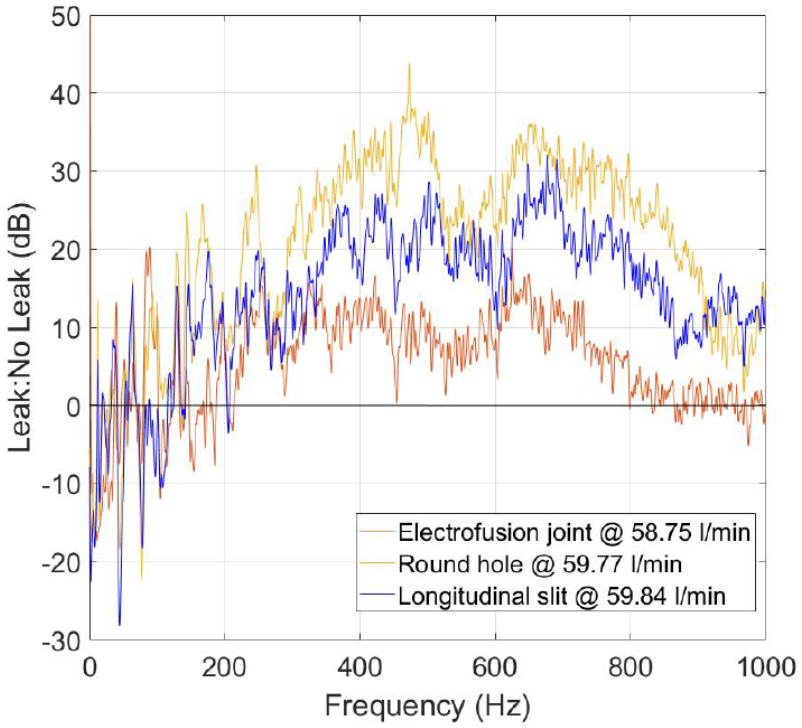

Figure 91 – Effect of leak shape on leak noise signature (J. D. Butterfield, 2018).

The finding contradicted the similar results obtained from the duo of Xiao, Hu, et al. (2022) and this current work. As very limited work is done in this area, there is yet no universally accepted conclusion on the effect of leak shape on leak noise. This work therefore keenly recommends a future work that will accurately measure the effect of leak shape on leak noise signature

6.5.8 Effect of volumetric leak flow rate on leak noise signatures

It was already shown in the semi-analytical expression that leak noise is proportional to the square of volumetric leal flow rate. However, it is important to also know how the result is influenced by different shapes of leaks. Volumetric flow rate was plotted against leak noise signatures for leaks of different shapes but the same sizes.

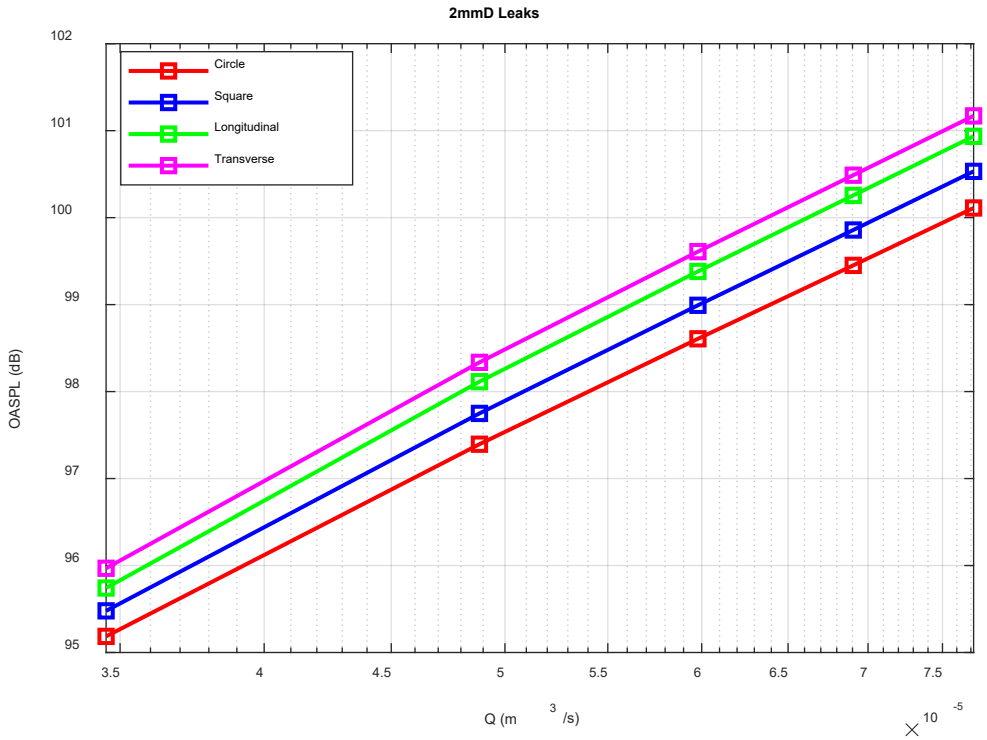

Figure 92 – Effect of volumetric leak flow rate on leak noise signatures

Results (Figure 92) showed leak noise to increase with volumetric leak flow rates as pressures increased. However, for the same pressure and volumetric leak flow rate, transverse slit and circular leaks produced the loudest and weakest noise respectively. It is worthy to note that there was no significant difference in the noise levels. For instance, at 2 bar pressure and for the same leak flow rate of 4.9 e-5 m^3/s, transverse slit, and circular leaks produced 98.3 dB and 97.4 dB of noise, with only a difference of 0.9 dB. The difference is assumed to be insignificant, and this study therefore suggests that the effect of leak shape on leak noise signature is negligible. However, the only proven reason for this behaviour is the differences in the leak perimeters, as shown in Table 7, with the exception of longitudinal leak.

6.5.9 Effects of leak size, shape and pressure on noise to flow ratio

It is known that volumetric leak flow rate is related to the amount of water lost and leak noise relates to how the leak is detected. Water companies in the UK are very keen to understand the ratio of noise to flow for different leak shapes and for all the leak sizes, in order to better optimise

leakages in their network. To investigate this, the OASPL was averaged by volumetric leak flow rate and the ratio was plotted for all leak shapes and sizes.

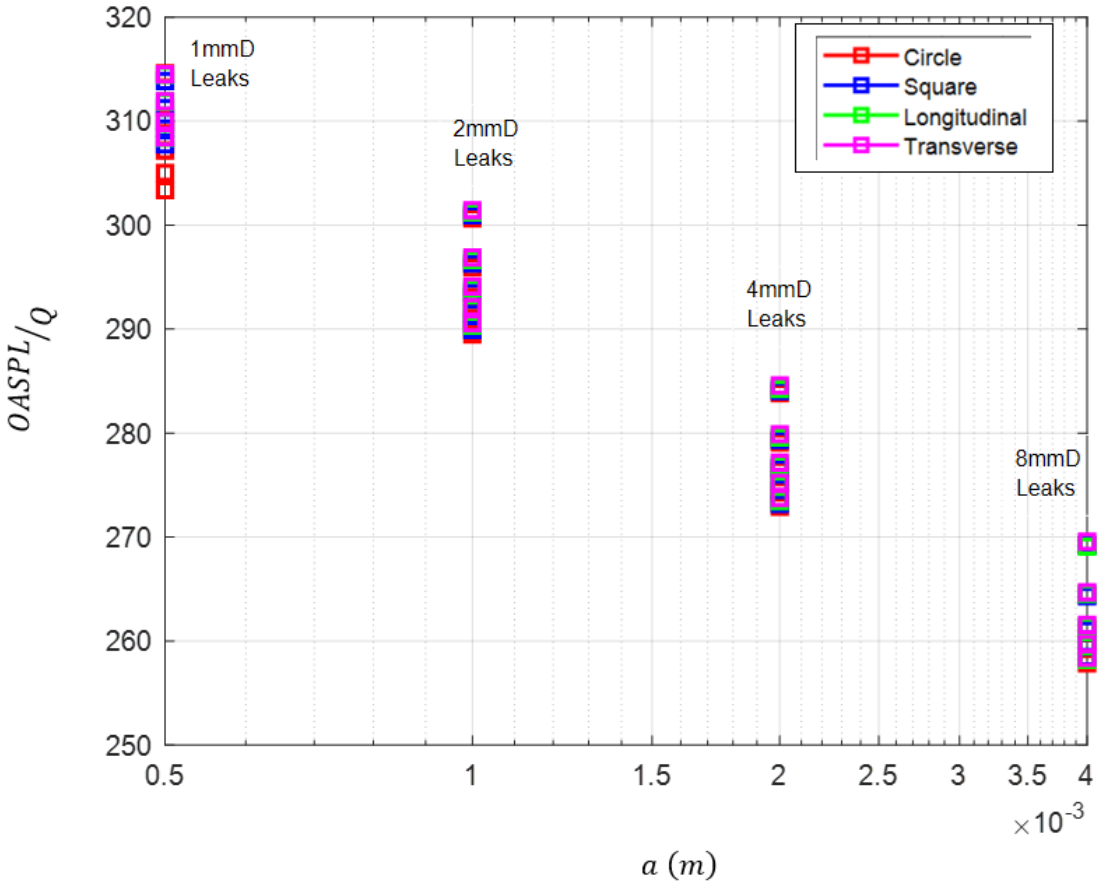

Figure 93 – Effect of leak size on noise to flow ratio

The averaging was carried out in order to remove the contribution of leak flow rate from leak noise so that the effects of leak shapes and sizes on leak noise can be better understood. For all the leaks shapes, leak noise, as discussed previously, is proportional to the square of leak flow rate and as Figure 89 & Figure 90 showed no much difference in the leak noise from different shapes, it was concluded that the effect of leak shape on leak noise amplitude is negligible. However, the ratio of noise to flow (Figure 93), decays as leak sizes increase and this implies that, devoid of volumetric leak flow rate, leak noise is inversely proportional to leak size. This result again, reiterated the importance of leak flow rate in leak noise generation, as $S_{PP} \propto Q^2$.

For the same size of 4 mm diameter leak and at constant pressure, the effect of leak shape on noise to flow ratio (Figure 94) was not significant, though transverse and circular leaks produced the largest and smallest ratio due to reasons explained previously. However, it was observed that the ratio increased with pressure and as explained in section (5.8) and Figure 73, the effect of leak

shape on noise would be significant if pressure was increased. It could be concluded that for the same leak size, noise to flow ratio would only increase if pressure was increased.

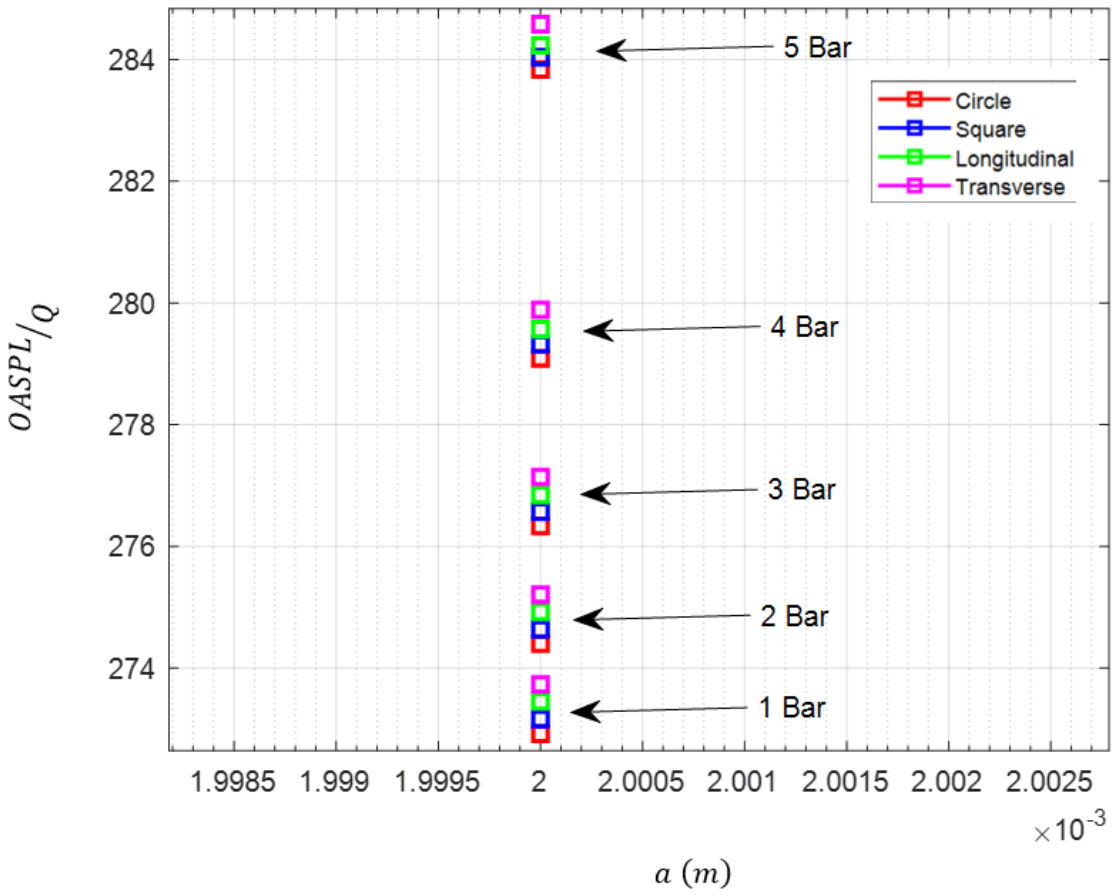

Figure 94 – The effects of leak shape and pressure on noise to flow ratio

Chapter 7 Conclusions and future work

7.1 Conclusions

This chapter highlights the general conclusions of this work and the challenges faced in the course of carrying out the study. Recommendations were provided for future work opportunities. This work focused mainly on investigating and modelling turbulent kinetic energy as a source of leak noise in water pipes. Computational fluid dynamics approach was employed in modelling and simulating water flow in the pipes and at the leaks of different shapes and dimensions. Numerical flow data were subsequently used to predicting and characterise leak noise.

In this work, the challenges of having to model and simulate the flow using long pipes were defeated by importing fully developed flow from a long pipe into a short pipe that is sliced into two equal parts along symmetry plane. One of the advantages of simulating the flow from a short pipe was that the domain was adequately and optimally meshed with about 30 Million cells and HPC supercomputer was employed to run the simulation due to its high speed and vast memory.

The main conclusions can be summarized as follows:

a) The sources of leak noise generation was investigated by simulating leaks of different shapes and sizes and peaks of turbulent kinetic energy, found around the circumference of the leaks, was identified as one of leak noise sources. Although turbulent kinetic energy did not change much around the edges of the leak geometries, it decays from maximum at the edge to minimum values around the centre of the leak and this suggests that all the leak noise energy is concentrated at the edge. In addition, edge turbulence is the most important region of interest in detecting, localising and predicting leaks in fluid pipes. This information would be useful in improving the effectiveness of leak detection technologies such as noise correlators and leak noise detection robots.

b) Quantitative and qualitative analyses was carried out on the turbulent kinetic energy, to further understand it's behaviour with pressure, velocity, flow rate, leak shapes and sizes. It was found that, for all the leak shapes, sizes, and under all pressure and velocity conditions, turbulent kinetic energy was maximum at the edge and minimum at the centre of the leak geometries. When turbulent kinetic energy is normalised by its edge turbulence, a universal behaviour existed for the smallest leaks, that is independent of

pressure, which follows a Gaussian function. As the leaks get bigger, the behaviour changed and the bigger leaks, instead, exhibited a universal behaviour that follows an exponential function. The change of universal behaviour between large and small leaks could be attributed to high influence of viscous effects on small leaks, which changed as fluids become more turbulent for bigger leaks.

c) Torricelli equation was used to predict leak flow rate of different sizes and shapes

d) Leak noise source strength was estimated for different leak sizes and shapes by numerically integrating source strengths over the leak holes. For all leak sizes and shapes and under varying pressures, source strength was found to increase as a square of leak radii ($q \approx a^2$). This indicated that the size of the leak plays a very vital role in the generation of source strength, more than the shape, and that, smaller leaks are disproportionately weaker in leak noise source strength, compared to bigger leaks. In addition, mean flow speed ($\overline{U}$) at the leak was found to better influence the strength of leak noise source, in comparison to pressure (P). In addition, source strength for all the leak shapes were plotted against their leak flow rates and an important expression was obtained from the relationship, which showed source strength to be proportional to 0.7 % of the volumetric leak flow rate, with longitudinal and circular leaks having the largest and smallest source strength respectively, due to the differences in their perimeters.

e) Numerical modelling of the mean flow speed at the leak orifice revealed the mean flow speed to exhibit a highly directional behaviour, comprising of components that display strong variations of velocity distributions in the radial and circumferential directions, unlike the mean flow speed which vary only in the radial direction.

f) A semi-analytical model was developed to predict leak noise in water pipes, using source strength at the leak orifice, which was predicted to be proportional to the square of leak radii ($q \propto a^2$). Leak noise prediction semi-analytical model was also obtained as functions of pressure and discharge velocity. Leak noise was estimated from leaks of different shapes of the same leak areas and transverse and circular leaks produced the loudest and least noise respectively, but the study however concluded that leak shape played no significant role in the noise estimation.

7.2 Recommendation for future work

Steady-state computational fluid dynamics numerical simulation approach was employed in this study, which provides only estimates of flow parameters, including turbulent quantities, under varying pressure and velocity. However, the approach was time independent and as such, was unable to capture the behaviour of flow as it changes with time. This work therefore recommends that future work be conducted on leak noise characterisation using transient numerical simulation of different leak shapes, so as to better understand the time-dependent behaviour of fluid in the vicinity of the leak.

As this work focussed on investigating leak noise generation mechanisms and characterisation on surface pipes, it will be beneficial to also carry out future work on numerical and experimental characterisation of leak noise from buried pipes containing leaks of different geometries so as to understand the effects and impacts of soil type and burial depth on leak noise generation, propagation and characterisation.

As the finding in this study and that of Xiao, Hu, et al. (2022) contradict the result reported in the work of J. D. Butterfield (2018) about the effect of leak shape on leak noise, a future work, of which outcome will be universally accepted, is recommended to accurately measure the effect of leak shapes, as suggested by J. D. Butterfield (2018), on leak noise signature

Bibliography

Absi, K. S. R. (2021). Turbulent kinetic energy estimate in the near wall region of smooth turbulent channel flows. *Meccanica*. doi:56:2533–2545

Acharya, R. (2016). Investigation of differences in Ansys solvers CFX and fluent. In.

Ahmad, S., Ahmad, Z., Kim, C.-H., & Kim, J.-M. (2022). A method for pipeline leak detection based on acoustic imaging and deep learning. *Sensors, 22*(4), 1562.

Ahsan, M. (2014). Numerical analysis of friction factor for a fully developed turbulent flow using k–ε turbulence model with enhanced wall treatment. *Beni-Suef University journal of basic and applied sciences, 3*(4), 269-277.

Alauzet, F., Loseille, A., & Marcum, D. (2017). *On a robust boundary layer mesh generation process.* Paper presented at the 55th AIAA Aerospace Sciences Meeting, AIAA Paper2017-0585, Grapevine, TX, USA.

Alfonsi, G. (2009). Reynolds-averaged Navier–Stokes equations for turbulence modeling. *Applied Mechanics Reviews, 62*(4).

Ali, S., Hawwa, M. A., & Baroudi, U. (2022). Effect of Leak Geometry on Water Characteristics Inside Pipes. *Sustainability, 14*(9), 5224.

Allwright, D. (2001). Noise Generation by Water Pipe Leaks. Retrieved from chrome-extension://efaidnbmnnnibpcajpcglclefindmkaj/https://core.ac.uk/download/pdf/17075.pdf

Anderson Jr, J. D., & Anderson, J. D. (1998). *A history of aerodynamics: and its impact on flying machines*: Cambridge university press.

Andersson, B., Andersson, R., Håkansson, L., Mortensen, M., Sudiyo, R., & Van Wachem, B. (2011). *Turbulent-flow modelling. In Computational Fluid Dynamics for Engineers*. Cambridge: Cambridge University Press.

Ansys-Fluent-4. (2021). Using flow boundary conditions. Retrieved from https://www.afs.enea.it/project/neptunius/docs/fluent/html/ug/node238.htm

Ansys-Fluent-11. (2023). 26.13.1 Monitoring Residuals

Ansys-Fluent, M. (2022). Shear-Stress Transport (SST) K-Omega Model. Retrieved from https://www.afs.enea.it/project/neptunius/docs/fluent/html/th/node67.htm

Ansys-Fluent_manual. (2023). Judging Convergence. Retrieved from https://www.afs.enea.it/project/neptunius/docs/fluent/html/ug/node833.htm#sec-judging-convergence

Ansys. (2006). Modeling turbulent flows: Introductory turbulent training. *Introductory FLUENT Notes FLUENT v6.3 December 2006.* Retrieved from chrome-extension://efaidnbmnnnibpcajpcglclefindmkaj/https://www.southampton.ac.uk/~nwb/lectures/GoodPracticeCFD/Articles/Turbulence_Notes_Fluent-v6.3.06.pdf

ANSYS. (2010). Solver settings.

Introduction to Ansys Flent

Retrieved from chrome-extension://efaidnbmnnnibpcajpcglclefindmkaj/https://imechanica.org/files/fluent_13.0_lecture05-solver-settings.pdf

Ansys. (2013). *Ansys Meshing User's Guide*(Release 15.0

November 2013 ed., Vol. 2020).

ANSYS. (2021). Modeling Turbulent Flows. Retrieved from https://www.southampton.ac.uk/~nwb/lectures/GoodPracticeCFD/Articles/Turbulence_Notes_Fluent-v6.3.06.pdf

ANSYS. (2023). Near wall meshing guidelines. Retrieved from https://www.afs.enea.it/project/neptunius/docs/fluent/html/ug/node410.htm

ANSYS_FLUENT. (2009a). Choosing the Relative or Absolute Velocity Formulation. Retrieved from https://www.afs.enea.it/project/neptunius/docs/fluent/html/ug/node376.htm#:~:text=The%20absolute%20velocity%20formulation%20is,impeller%20in%20a%20mixing%20tank.

ANSYS_FLUENT. (2009b). First-Order Accuracy vs. Second-Order Accuracy. Retrieved from https://www.afs.enea.it/project/neptunius/docs/fluent/html/ug/node779.htm

Ansys_Fluent. (2021, 20 December 2021). Evaluation of Gradients and Derivatives. Retrieved from https://www.afs.enea.it/project/neptunius/docs/fluent/html/th/node368.htm

Ansys_Fluent. (2023). Ansys Innovation Courses. Retrieved from https://courses.ansys.com/index.php/courses/steady-flow-past-a-cylinder/lessons/physics-setup-lesson-5-18/

Ansys_Fluent_precision_solvers_manual. (2021). Single-Precision and Double-Precision Solvers. Retrieved from https://www.afs.enea.it/project/neptunius/docs/fluent/html/ug/node11.htm

AnsysFluent. (2021). Pressure-Velocity Coupling. Retrieved from https://www.afs.enea.it/project/neptunius/docs/fluent/html/th/node373.htm

Bais, S. (2021). Hydrodynamics: The Navier-Stokes Equations. from Amsterdam University Press

Ben-Mansour, R., Habib, M., Khalifa, A., Youcef-Toumi, K., & Chatzigeorgiou, D. (2012). Computational fluid dynamic simulation of small leaks in water pipelines for direct leak pressure transduction. *Computers & Fluids, 57*, 110-123.

Bhandari, D., & Singh, S. (2012). Analysis of fully developed turbulent flow in a pipe using computational fluid Dynamics. *International Journal of Engineering Research and Technology, 1*(5), 1-8.

Blackstock, D. (2000). *Fundamentals of Physical Acoustics*: Wiley-Interscience.

Braga, A. S., Fernandes, C. V. S., & Braga, S. (2018). *Leakage Modeling Through Empirical Equations: An Experimental Approach:(021).* Paper presented at the WDSA/CCWI Joint Conference Proceedings.

Brennan, M., Karimi, M., Muggleton, J., Almeida, F., de Lima, F. K., Ayala, P., . . . Kessissoglou, N. (2018). On the effects of soil properties on leak noise propagation in plastic water distribution pipes. *Journal of Sound and Vibration, 427*, 120-133.

Brown, J., Johnson, D., Smith, M., & Williams, L. (2018). Influence of Fluid Flow Rate on Leak Noise Loudness: A Comparative Study of Small and Large Pipes. *Journal of Acoustical Engineering, 45(3), 201-208.*

Butterfield, J. (2018). *Deriving further information from the leak signal in water distribution pipes.* University of Sheffield,

Butterfield, J. D. (2018). *Deriving further information from the leak signal in water distribution pipes.* (EngD eTHESIS). The University of Sheffield, United Kingdom.

Butterfield, J. D., Collins, R. P., Krynkin, A., & Beck, S. B. (2017). Experimental investigation into the influence of backfill types on the vibro-acoustic characteristics of leaks in MDPE pipe. *Procedia Engineering, 186*, 311-318.

Butterfield, J. D., Meyers, G., Meruane, V., Collins, R. P., & Beck, S. B. M. (2018). Experimental investigation into techniques to predict leak shapes in water distribution systems using vibration measurements. *Journal of Hydroinformatics, 20*(4), 815-828. doi:10.2166/hydro.2018.117

Cassa, A., Van Zyl, J., & Laubscher, R. (2010). A numerical investigation into the effect of pressure on holes and cracks in water supply pipes. *Urban Water Journal, 7*(2), 109-120.

Cassa, A. M., & van Zyl, J. E. (2013). Predicting the head-leakage slope of cracks in pipes subject to elastic deformations. *Journal of Water Supply: Research and Technology—AQUA, 62*(4), 214-223.

Cengel, Y., & Cimbala, J. (2013). *EBOOK: Fluid Mechanics Fundamentals and Applications (SI units)*: McGraw Hill.

CFD-Online-1. (11 November, 2021). Pressure based and density based solver. Retrieved from https://www.cfd-online.com/Forums/main/8398-pressure-based-density-based-solver.html

CFD-Online. (2021, 18 November, 2021). SST k-omega model. Retrieved from https://www.cfd-online.com/Wiki/SST_k-omega_model

CFD, C. (2023). The Reynolds-Averaged Navier-Stokes (RANS) Equations and Models. Retrieved from https://resources.system-analysis.cadence.com/blog/msa2021-the-reynolds-averaged-navier-stokes-rans-equations-and-models

CIWEM. (2020, 17 March 2020). Water Distribution System Leakage in The UK. Retrieved from https://www.ciwem.org/assets/pdf/Policy/Policy%20Position%20Statement/Water-distribution-network-leakage-in-the-UK.pdf

Cody, R. (2020). Acoustic Monitoring for Leaks in Water Distribution Networks.

de Almeida, F., Joseph, P., Brennan, M., Whitfield, S., & Dray, S. (2013). *The dynamic behaviour of a buried water pipe and its effect on leak location using acoustic methods.* Paper presented at the Key Engineering Materials.

De Marchis, M., & Milici, B. (2019). Leakage estimation in water distribution network: effect of the shape and size cracks. *Water Resources Management, 33*(3), 1167-1183.

Ebrahimi-Moghadam, A., Farzaneh-Gord, M., Arabkoohsar, A., & Moghadam, A. J. (2018). CFD analysis of natural gas emission from damaged pipelines: Correlation development for leakage estimation. *Journal of Cleaner Production, 199*, 257-271.

Ekmekcioğlu, Ö., BAŞAKIN, E. E., & Özger, M. (2020). Discharge coefficient equation to calculate the leakage from pipe networks. *Journal of the Institute of Science and Technology, 10*(3), 1737-1746.

Elmekawi, A. N. (2012). Fluent Solver Settings. Retrieved from chrome-extension://efaidnbmnnnibpcajpcglclefindmkaj/https://drahmednagib.com/CAD_2018/Lecture_7_Fluent_Solver_Settings.pdf

Eriksson, L. J. (1980). Higher order mode effects in circular ducts and expansion chambers. *The Journal of the Acoustical Society of America, 68*(2), 545-550.

Faerman, V., Sharkova, S., Avramchuk, V., & Shkunenko, V. (2022). *Towards applicability of wavelet-based cross-correlation in locating leaks in steel water supply pipes.* Paper presented at the Journal of Physics: Conference Series.

Fan, H., Tariq, S., & Zayed, T. (2022). Acoustic leak detection approaches for water pipelines. *Automation in Construction, 138*, 104226.

Farrow, J., Jesson, D., Mulheron, M., Nensi, T., Smith, P,. (2016). *<Zero Leakage By 2050 The Basic Mechanisms of Bursts and Leakage. Water Mains & Services.pdf>*. Retrieved from University of Surrey, United Kingdom:

Fatchurrohman, N., & Chia, S. (2017). *Performance of hybrid nano-micro reinforced mg metal matrix composites brake calliper: simulation approach.* Paper presented at the IOP Conference Series: Materials Science and Engineering.

Ferraiuolo, R., De Paola, F., Fiorillo, D., Caroppi, G., & Pugliese, F. (2020). Experimental and Numerical Assessment of Water Leakages in a PVC-A Pipe. *Water, 12*(6), 1804.

Ferrante, M., Brunone, B., Meniconi, S., Capponi, C., & Massari, C. (2014). The leak law: From local to global scale. *Procedia Engineering, 70*, 651-659.

Ferrante, M., Massari, C., Brunone, B., & Meniconi, S. (2010). Leakage and pipe materials. In *Water Distribution Systems Analysis 2010* (pp. 1140-1145).

Fluent-Ansys. (2023). Mesh Quality. Retrieved from https://www.afs.enea.it/project/neptunius/docs/fluent/html/ug/node167.htm

Fluent, A. (2023). Symmetry Boundary Conditions. Retrieved from https://www.afs.enea.it/project/neptunius/docs/fluent/html/ug/node251.htm

Fox, S. (2016). *<Understanding the Dynamic Leakage Behaviour of Longitudinal Slits In Viscoelastic Pipes.pdf>.* (PhD eThesis). The University of Sheffield, United Kingdom.

Franchini, M., & Lanza, L. (2014). Use of Torricelli's equation for describing leakages in pipes of different elastic materials, diameters and orifice shape and dimensions. *Procedia Engineering, 89*, 290-297.

Fuchs, H. V., & Riehle, R. (1991). Ten years of experience with leak detection by acoustic signal analysis. *Applied Acoustics, 33*(1), 1-19.

Gao, Y., Brennan, M. J., Joseph, P., Muggleton, J., & Hunaidi, O. (2005). On the selection of acoustic/vibration sensors for leak detection in plastic water pipes. *Journal of Sound and Vibration, 283*(3-5), 927-941.

Gao, Y., Brennan, M. J., Joseph, P. F., Muggleton, J. M., & Hunaidi, O. (2004). A model of the correlation function of leak noise in buried plastic pipes. *Journal of Sound and Vibration, 277*(1-2), 133-148. doi:10.1016/j.jsv.2003.08.045

George, P. W. K. (2021). Introduction to turbulence / Reynolds averaged equations. Retrieved from https://www.cfd-online.com/Wiki/Introduction_to_turbulence/Reynolds_averaged_equations

Gupta, R., Sharma, A., Singh, V., & Verma, S. (2017). Leak Noise Intensity in Different Pipe Sizes: A Comparative Study. *Proceedings of the International Conference on Acoustics, 112, 289-294.*

Harsha, P., & Lee, S. (1970). Correlation between turbulent shear stress and turbulent kinetic energy. *AIAA Journal, 8*(8), 1508-1510.

Hodasalu Sadananda, B. (2019). *Design and Implementation of Google Cloud Framework for Monitoring Water Distribution Networks.* University of Waterloo,

Hunaidi, O., & Chu, W. T. (1999). Acoustical characteristics of leak signals in plastic water distribution pipes. *Applied Acoustics, 58*(3), 235-254.

Hunaidi, O., Wang, A., Bracken, M., Gambino, T., & Fricke, C. (2004). *Acoustic methods for locating leaks in municipal water pipe networks.* Paper presented at the International conference on water demand management.

Hunaidi, O., Wang, A., Bracken, M., Gambino, T., & Fricke, C. (2005). Detecting leaks in water distribution pipes. *Arab Water World, 29*(4), 52-55.

Jin, H., Zhang, L., Liang, W., & Ding, Q. (2014). Integrated leakage detection and localization model for gas pipelines based on the acoustic wave method. *journal of Loss Prevention in the Process Industries, 27*, 74-88.

Johnson, R. W. (2016). *Handbook of fluid dynamics*: Crc Press.

Joseph, P. (2024). Sound radiation and transmission. Retrieved from chrome-extension://efaidnbmnnnibpcajpcglclefindmkaj/https://www.feis.unesp.br/Home/departamentos/engenhariamecanica/gmsint/8-sound-radiation-and-transmission.pdf

Jujuly, M., Thodi, P., Rahman, A., & Khan, F. (2016). *Computational fluid dynamics modeling of subsea pipeline leaks in arctic conditions.* Paper presented at the Arctic Technology Conference.

Jujuly, M. M. (2016). *Computational fluid dynamics (CFD) based approach to consequence assessment of accidental release of hydrocarbon during storage and transportation.* Memorial University of Newfoundland,

K.A.U. (2004). Flow in pipes. Retrieved from https://www.kau.edu.sa/Files/0057863/Subjects/Chapter%208.pdf

Kabaasha, A. M., Piller, O., & van Zyl, J. E. (2018). Incorporating the modified orifice equation into pipe network solvers for more realistic leakage modeling. *Journal of Hydraulic Engineering, 144*(2), 04017064.

Kabaasha, A. M., van Zyl, J. E., & Piller, O. (2016). *Modelling pressure: Leakage response in water distribution systems considering leak area variation.* Paper presented at the 14th CCWI international conference, Computing and Control in Water Industry.

KAHRAMANOĞLU, E., Sezen, S., & Bayraktar, S. (2017). Computational fluid dynamics analyses on the hydrodynamic entry length in internal flows. *Pamukkale University Journal of Engineering Sciences, 23*(4).

Khalifa, A. E., Ben-Mansour, R., Youcef-Toumi, K., & Choi, C. (2011). *Characterization of in-pipe acoustic wave for water leak detection.* Paper presented at the ASME International Mechanical Engineering Congress and Exposition.

Khulief, Y., Khalifa, A., Mansour, R. B., & Habib, M. (2012). Acoustic detection of leaks in water pipelines using measurements inside pipe. *Journal of Pipeline Systems Engineering and Practice, 3*(2), 47-54.

Kim, M.-S., & Lee, S.-K. (2009). Detection of leak acoustic signal in buried gas pipe based on the time–frequency analysis. *journal of Loss Prevention in the Process Industries, 22*(6), 990-994.

Kudela, H. (2010). Turbulent flow. In: Faculty Mech. Power Eng., Wrocław Univ. Sci. Technol. Wrocław, Poland.

Lambert, A. (2001). *What do we know about pressure-leakage relationships in distribution systems.* Paper presented at the IWA Conf. n Systems approach to leakage control and water distribution system management.

Lansigan, D. L. (2021). Critical Comparison of k − ϵ and k − ω SST Turbulence Models in 2D Backward Facing Step Simulations. Retrieved from chrome-extension://efaidnbmnnnibpcajpcglclefindmkaj/http://stanford.edu/~dlol/assets/docs/ME461-report-dlavacot.pdf

Liu, C., Li, Y., Meng, L., Wang, W., & Zhang, F. (2014). Study on leak-acoustics generation mechanism for natural gas pipelines. *journal of Loss Prevention in the Process Industries, 32*, 174-181.

Mali, V., & Dange, S. (2010). Basics of Y Plus, Boundary Layer and Wall Function in Turbulent Flows. *LearnCAx,[Online]. Available: https://www. learncax. com/knowledge-base/blog/by-category/cfd/basics-of-y-plusboundary-layer-and-wall-function-in-turbulent-flows.[Accessed 15 February 2016]*.

Mangani, L., Sanz, W., & Darwish, M. (2016). *Comparing the performance and accuracy of a pressure-based and a density-based coupled solver.* Paper presented at the 16th International Symposium on Transport Phenomena and Dynamics of Rotating Machinery.

Mashford, J., De Silva, D., Burn, S., & Marney, D. (2012). Leak detection in simulated water pipe networks using SVM. *Applied Artificial Intelligence, 26*(5), 429-444.

Meng, L., Yuxing, L., Wuchang, W., & Juntao, F. (2012). Experimental study on leak detection and location for gas pipeline based on acoustic method. *journal of Loss Prevention in the Process Industries, 25*(1), 90-102.

Menge, B. K. (2015). *Analysis of Turbulent Flow in a Pipe at Constant Reynolds Number using Computational Fluid Dynamics.*

Menter, F., Lechner, R., & Matyushenko, A. (2021). Best Practice: RANS Turbulence Modeling in Ansys CFD. *ANSYS Inc.: Canonsburg, PA, USA*.

Menter, F. R. (1994). Two-equation eddy-viscosity turbulence models for engineering applications. *AIAA Journal, 32*(8), 1598-1605.

microflown.com. (2023). *Monopole sound sources*. Retrieved from chrome-extension://efaidnbmnnnibpcajpcglclefindmkaj/https://www.microflown.com/assets/uploads/Publications/ebook_11_monopole.pdf

Midtun, B. (2011). *Evaluation of hydro acoustic condition monitoring of subsea processing equipment.* University of Stavanger, Norway,

Miedema, S. A. (2020). *3: Pressure Losses with Homogeneous Liquid Flow*. Delft University of Technology: Delft University of Technology

Morse, P. M., & Ingard, K. U. (1986). *Theoretical acoustics*: Princeton university press.

Muggleton, J., Scussel, O., Rustighi, E., Brennan, M., Almeida, F., Karimi, M., & Joseph, P. (2023). *A Simplified Model of the Ground Surface Vibration Arising from a Leaking Pipe.* Paper presented at the International Conference on Wave Mechanics and Vibrations.

Muggleton, J. M., & Brennan, M. J. (2004). Leak noise propagation and attenuation in submerged plastic water pipes. *Journal of Sound and Vibration, 278*(3), 527-537.

Muggleton, J. M., Brennan, M. and Pinnington, R. (2002). Wavenumber Prediction of Waves in Buried Pipes for Water Leak Detection. Journal of Sound and Vibration. *Journal of Sound and Vibration, 249(5)*, 939-954.

Muggleton, J. M., Yan J. (2013). Wavenumber prediction and measurement of axisymmetric waves in buried fluid-filled pipes: Inclusion of shear coupling at a lubricated pipe/soil interface. *", Journal of Sound and Vibration, 332*(1216-1230).

NASA. (2021). Turbulence Modeling Resource. Retrieved from https://turbmodels.larc.nasa.gov/sst.html

Okoyenta, A. R., Wu, H., Liu, X., & Jiang, W. (2020). A short survey on Green's function for acoustic problems. *Journal of Theoretical and Computational Acoustics, 28*(02), 1950025.

Papastefanou, A. (2011). *An experimental investigation of leak noise from water filled plastic pipes.* (Thesis (Ph D) - University of Southampton, Institute of Sound and Vibration Research, 2011). Original typescript,, Retrieved from http://eprints.soton.ac.uk/190853/

Papastefanou, A. S., Joseph, P. F., & Brennan, M. J. (2012). Experimental Investigation into the Characteristics of In-Pipe Leak Noise in Plastic Water Filled Pipes. *Acta Acustica United with Acustica, 98*(6), 847-856. doi:10.3813/Aaa.918568

Piest, J. (2018). Mean velocity equation for fluctuating flow. *European Journal of Mechanics / B Fluids*, 137-157.

Pijush K. Kundu, I. M. C., David R. Dowling. (2016). *Boundary Layes and Related Topics*: Academic Press.

Prisutova, J., Krynkin, A., Tait, S., & Horoshenkov, K. (2022). Use of fibre-optic sensors for pipe condition and hydraulics measurements: A review. *CivilEng, 3*(1), 85-113.

Reethof, G. (1978). Turbulence-generated noise in pipe flow. *Annual Review of Fluid Mechanics, 10*(1), 333-367.

Rucka, M., Kaczmarek, M., & Podraza, P. (2017). The influence of leak size on the spectral characteristics of leak noise. *Archives of Acoustics, 42(2), 235-242*.

Russell, D. A., Titlow, J. P., & Bemmen, Y.-J. (1999). Acoustic monopoles, dipoles, and quadrupoles: An experiment revisited. *American Journal of Physics, 67*(8), 660-664.

Salama, A. (2021). Velocity profile representation for fully developed turbulent flows in pipes: a modified power law. *Fluids, 6*(10), 369.

Schlichting, H., Gersten, K., Schlichting, H., & Gersten, K. (2000). Fundamentals of boundary-layer theory. *Boundary-layer theory*, 29-49.

Schwaller, J., Van Zyl, J., & Kabaasha, A. (2015). Characterising the pressure-leakage response of pipe networks using the FAVAD equation. *Water Science and Technology: Water Supply, 15*(6), 1373-1382.

Scussel, O., Brennan, M.J., Almeida, F.C.L., Muggleton, J.M., Rustighi, E., Joseph, P.F. (2020). Estimating the Spectrum of Leak Noise in Buried Plastic Water Distribution Pipes using Acoustic or Vibration Measurements Remote from the Leak. *Mechanical Systems and Signal Processing*, 21.

Siddique, M. F., Ahmad, Z., Ullah, N., & Kim, J. (2023). A Hybrid Deep Learning Approach: Integrating Short-Time Fourier Transform and Continuous Wavelet Transform for Improved Pipeline Leak Detection. *Sensors, 23*(19), 8079.

SIMSCALE. (2023a). K-Epsilon Turbulence Models. Retrieved from https://www.simscale.com/docs/simulation-setup/global-settings/k-epsilon/

SIMSCALE. (2023b). What is y+ (yplus)? Retrieved from https://www.simscale.com/forum/t/what-is-y-yplus/82394

Ssozi, E., Reddy, B., & Van Zyl, J. (2016). Numerical investigation of the influence of viscoelastic deformation on the pressure-leakage behavior of plastic pipes. *Journal of Hydraulic Engineering, 142*(3), 04015057.

Strasser, W. (2007). CFD investigation of gear pump mixing using deforming/agglomerating mesh.

Thames-Water (Producer). (2023). Our Leakage Performance. Retrieved from https://www.thameswater.co.uk/about-us/performance/leakage-performance

Thompson, M., Chapman, C., Howison, S., & Ockendon, J. (2001a). Noise generation by water pipe leaks. *Study report of 40th European Study group with industry*, D1-D6.

Thompson, M., Chapman, C., Howison, S., & Ockendon, J. (2001b). Noise generation by water pipe leaks. 40th European Study Group with Industry. In: Keele.

Tran, V. Q., Le, D. V., Yntema, D. R., & Havinga, P. J. (2021). A review of inspection methods for continuously monitoring PVC drinking water mains. *IEEE Internet of Things Journal, 9*(16), 14336-14354.

UK Water Industry Research. (2020). <UKWIR - Big Question No. 2; Route Map to Achieve the Vision.pdf>. Retrieved from https://ukwir.org/How-will-we-achieve-zero-leakage-in-a-sustainable-way-by-2050

Wei, O. Y., & Masuri, S. U. (2019). Computational Fluid Dynamics Analysis on Single Leak and Double Leaks Subsea Pipeline Leakage. *CFD Letters, 11*, 95-107.

Wei, T. (2018). Integral properties of turbulent-kinetic-energy production and dissipation in turbulent wall-bounded flows. *Journal of Fluid Mechanics, 854*, 449-473.

Wieselquist, W. A. (2002). *One Validation Case of the CFD Software Fluent: Part of the Development Effort of a New Reactor Analysis Tool.* Paper presented at the International Conference on Nuclear Engineering.

Wu, D., Burton, R., & Schoenau, G. (2002). An empirical discharge coefficient model for orifice flow. *International journal of fluid power, 3*(3), 13-19.

Xiao, R., Hu, Q., & Li, J. (2019). Leak detection of gas pipelines using acoustic signals based on wavelet transform and Support Vector Machine. *Measurement, 146*, 479-489.

Xiao, R., Hu, Q., & Li, J. (2022). Experimental investigation on characteristics of leak noise in gas pipeline systems. *Journal of Pipeline Systems Engineering and Practice, 13*(1), 04021070.

Xiao, R., Joseph, P., & Li, J. (2020). The leak Noise Spectrum in Gas pipeline systems: Theoretical and Experimental Investigation. *Journal of Sound and Vibration*, 115646.

Xiao, R., Joseph, P. F., Muggleton, J. M., & Li, J. (2022). Limits for leak noise detection in gas pipes using cross correlation. *Journal of Sound and Vibration, 520*, 116639.

Xu, W., Fan, S., Wang, C., Wu, J., Yao, Y., & Wu, J. (2022). Leakage identification in water pipes using explainable ensemble tree model of vibration signals. *Measurement, 194*, 110996.

Xue, Z., Tao, L., Fuchun, J., Riehle, E., Xiang, H., Bowen, N., & Singh, R. P. (2020). Application of acoustic intelligent leak detection in an urban water supply pipe network. *Journal of Water Supply: Research and Technology—AQUA, 69*(5), 512-520.

Yang, J., Wen, Y., & Li, P. (2008). *Leak acoustic detection in water distribution pipelines.* Paper presented at the 2008 7th World Congress on Intelligent Control and Automation.

Yusuf, S. N. A., Asako, Y., Sidik, N. A. C., Mohamed, S. B., & Japar, W. M. A. A. (2020). A short review on rans turbulence models. *CFD Letters, 12*(11), 83-96.

Zeng, Y., & Luo, R. (2019). Numerical Analysis on Pipeline Leakage Characteristics for Incompressible Flow. *Journal of Applied Fluid Mechanics, 12*(2), 485-494.

Zhao, X., Wu, X., Sun, H., Zhang, P., Lai, W., Lin, F., . . . Gao, C. (2022). *Pipeline leak audio detection system based on machine learning.* Paper presented at the Proceedings of the 2022 5th International Conference on Telecommunications and Communication Engineering.

Zhu, H.-H., Liu, W., Wang, T., Su, J.-W., & Shi, B. (2022). Distributed acoustic sensing for monitoring linear infrastructures: Current status and trends. *Sensors, 22*(19), 7550.

Zohora, F. (2021). *Study of pipe leak fluid dynamic characteristics and their influences on acoustic emission generation.* Queensland University of Technology,